Gallium Arsenide Radiation Detectors for the ATLAS Experiment

Richard L. Bates

Department of Physics & Astronomy
The University
Glasgow

Thesis submitted for the degree of
Doctor of Philosophy

June 1997

Abstract

Results obtained with Gallium Arsenide (GaAs) Schottky barrier particle detectors are presented. Semi-insulating undoped (SI-U), semi-insulating indium doped, (SI-In doped), and vapour phase epitaxial (VPE) substrates were investigated.

Details of the fabrication techniques utilised at Glasgow University for detector realisation are given as well as the characterisation methods used. Two detector types were fabricated: the simple pad device and the microstrip detector. The pad detector was used to investigate the electrical and charge collection characteristics of the device both before and after neutron and charged particle irradiation. The microstrip detectors enabled the spatial resolution of GaAs devices to be obtained.

The electrical measurements performed on the semi-insulating diodes revealed a low voltage Schottky region and a high voltage trap-controlled current characteristic. From the low voltage measurements a barrier height of 0.91 ± 0.02 V and a bulk resistivity of 6.4×10^7 Ωcm were determined for a measurement temperature of 20°C. For high bias (~10V) the reverse current was attributed to generation current which was observed to saturate at a reverse bias above ~ 50 V. A field-enhanced capture cross-section of the native EL2 deep donor level was proposed as the cause of this behaviour. The electric field at high bias was not uniform across the device and divided it into two distinct regions: a high and a low field region. This effect has also been attributed to the EL2 defect. The extension of the high field region increased linearly with applied reverse bias at a rate of ~ 1 μm/V.

The charge collection of the SI-U detectors were measured to be less than 100% due to the trapping of both carriers, with the electrons affected to a greater extent.

The VPE material was found to have a low trap density and behaved as expected from Schottky theory, with a barrier height of 0.81 V and a reverse current dominated by generation current. 60 keV gamma and front illumination from a 5.45 MeV alpha source demonstrated that the detectors had a charge collection efficiency close to 100%.

The performance of SI-U detectors after 1MeV neutron, 300 MeV/c pion and 24 GeV/c proton radiation showed a slight increase in the current above 50 V reverse bias. The charge collection efficiency, however, fell with fluence. The mean free absorption length of both carriers was observed to fall with fluence with the value for the holes falling at a faster rate than that for the electrons. For a 200μm thick detector at a reverse bias of 200 V a 10000 electron signal response to a minimum ionising particle was obtained after 1.4×10^{14} n/cm^2, 6.0×10^{13} p/cm^2, and only 3.0×10^{13} π/cm^2. An electron signal of at least this magnitude is required to guarantee a signal-to-noise ratio of 10:1 with the proposed electronics for the ATLAS experiment. Both the reverse current and charge collection changed rapidly with initial flux but more slowly with increased fluence. A correlation between the charge collection and particle type and energy was obtained using calculated values for the non-ionising energy loss of the incident radiation in GaAs.

The VPE diodes demonstrate a much better post-irradiation electron collection but suffered from an increase in reverse current of over an order of magnitude after a fluence of 1.25×10^{14} 24GeV/c protons/cm^2.

The spatial resolution of GaAs microstrip detectors was measured in a 70 GeV/c π beam at CERN. The detectors utilised a combination of integrated biasing structures and decoupling capacitors. Both rectifying and ohmic strips were investigated. The best performance gave a spatial resolution of 10.83 μm, (with a 50μm pitch), a signal-to-noise of 14.8, (with a peaking time of 300 ns), and a detection efficiency of 94%.

Contents

List of Figures

List of Tables

Preface

The development of position sensitive detectors fabricated on a gallium arsenide substrate are described in this thesis. This work has been performed within the RD8[8] collaboration. The objective of the collaboration was to investigate the possibility of developing radiation hard position sensitive particle detectors from GaAs to be included in the new experiments approved for the p-p collider (LHC) at CERN. The work has been performed as part of the Glasgow GaAs research effort and with many people in the RD8 collaboration and the particle physics community.

The low voltage electrical characterisation work was performed in collaboration with Professor J. Vaitkus of Vilnius University, Lithuania, in his capacity as visiting professor at Glasgow University. The spectral noise measurements of section 4.2 were performed at the Politecnico di Milano, Italy, under the guidance of Dr. G. Bertuccio.

The exposure of the detectors to neutron irradiation at R.A.L. was carried out by Dr. M. Edwards, without whom this portion of the work would not have been possible. The proton irradiations were performed with the aid of members of the RD2 collaboration at CERN. Dr. M. Glaser produced the measurement of the proton beam profile illustrated in figure 5.5. The NIEL analysis of chapter 5 was performed by Prof. T. Sloan of Lancaster University using data collected in the Glasgow GaAs laboratory over the past three years.

No portion of the research by the author referred to in this thesis has been submitted in support of an application for another degree or qualification in this, or any other institute of learning.

Acknowledgements

I would like to thank the Rutherford and Appleton Laboratory for the CASE award which enabled me to undertake my studies at the University of Glasgow; without it the Particle Physics & Astronomy Research Council would not have funded my position. At RAL I would like to thank Peter Sharp, and Steve Thomas, one of the brightest guys I have met in the last three years.

My supervisor deserves a BIG mention for all the effort that he has put in to motivate me over the past three years - not an easy job at the best of times - and for providing an abundance of research ideas.

Catherine has been really smashing and a huge help in dealing with all those nasty people up the hill and in Swindon.

Among those with whom I have work over the past three years; Colin, Val, Saverio, Drew, Fred and Frank must be mentioned. They have all helped in their own way to make the time quite enjoyable. Mention of the PS blues, giant pots of mustard and bacon in peas will always remind me of Drew.

Martin with a sharp foil, and tongue to match, made life fun if not a little dangerous at times, especially on a Thursday evenings. Simon has been outstanding entertainment from start to finish and Fiona has to be thanked for keeping us going over the last few hurdles, as well as the fun times before the writing up started. Jane also deserves a special mention - special mention to Jane.

Michayla, Manny, Constantin and Euan have all had the experience of sharing flats with me over the past three years. Is it too late to apologise for never vacuuming, cleaning and so forth? I don't think I could have asked for better flat mates. Thanks.

Mairi, Simon and all at Partick South have, in their own special ways, helped me along over the past few years.

I had better not miss out Allan, Spyros, Steve, Andrew, Andy and Stanley.

Apologies to all the guys from Manchester for neglecting everybody over the past few months; probably more like years now.

I guess that I have not mentioned everybody, however, it is one o'clock in the am and I had better get this thing finished.

Finally,

To Mum, Dad, George and Vicky I dedicate this document.

(Vicky, I bet you are glad that I did that aren't you.)

Thank you for all the support that you have shown over the past three years and, well, for as long as I can remember.

To all who read this I wish all the best, while to those who use it as a book end I am happy in the knowledge that it found some purpose.

Chapter 1

Introduction

1.1 Introduction

The particle physics experiments operated on the LEP collider at CERN have tested the standard model vigorously since the start of their operation in 1989. However, for the knowledge of physics to be extended, higher energy machines and new experiments must be constructed. The Large Hadron Collider (the LHC) to be built at CERN is such a machine. It will collide protons at a centre of mass energy of 14 TeV. Due to the low cross-sections of the interesting physics events at these energies high luminosity will be required in order to obtain reasonable statistics over the 10 year lifetime of the experiment. Therefore the time between bunch crossings will be very small, around 25ns, imposing a stringent requirement on the trigger and data acquisition speed of the new experiments. The radiation environment from a high energy p-p collision is much greater than that produced in the present electron-positron collider operated at CERN where synchrotron radiation, beam loss and beam-gas interaction are the main radiation sources. At an LHC experiment the radiation level will be dominated by particles from the proton proton interactions themselves and from background neutrons created in the calorimeters.

Tracking detectors for the LHC experiments must be capable of meeting the above requirements of high speed and high radiation tolerance. An additional requirement of high detector granularity, to reduce occupancy, results from the large multiplicity of an event, due to the high number of available channels from the p-p interaction.

The research presented here is concerned with the development of radiation hard Gallium Arsenide semiconductor tracking detectors for the ATLAS[9] experiment at the LHC. The rest of this chapter outlines the basic principles of semiconductor detector operation and the ATLAS experiment with relation to its design and physics objectives. The chapter closes with the motivation for investigating GaAs over silicon based semiconductor detectors for the forward wheels of the ATLAS inner tracker.

The thesis contains work on characterising Schottky barrier diodes both electrically and as charge collection devices. The theory of the Schottky barrier is explained in depth to aid the understanding of the results. The aim of this work was to understand the depletion mechanism, the source of the leakage current, the noise sources and the nature of the traps in the material and ultimately to be able to fabricate devices with a 100% charge collection efficiency. The desire to produce radiation hard detectors motivated an extensive investigation of the effects of radiation on GaAs devices. Chapter 5 reports the results of these experiments.

The detectors were shown to perform well as position sensitive devices in a pion test beam at the X1 beam line, CERN. Results from the test beam are reported in chapter 6.

1.2 What is a semiconductor detector?

Semiconductor devices fabricated on silicon substrates have been used in high energy physics since the 1970's [10]. The first detectors operated as ionisation chambers and were used only to separate signals from background events. Only after the introduction in 1980 of the planar technique[11] for the fabrication of large scale silicon detectors did position measurements begin. Since then the use of semiconductor detectors for tracking and vertexing has been extensive and at present all four experiments on the LEP collider at CERN use silicon-based microstrip vertex detectors.

A position sensitive microstrip detector is formed by dividing the contact on the semiconductor into thin, generally parallel strips. When signals from each of these strips are read out the position of the incoming particle can be deduced. Semiconductors have many advantages over gaseous detectors, which they have largely superseded for accurate position measurements, where large volume detectors are not required. Listed below are the major advantages for experimental high energy physics applications:

- **Low energy required to create an electron hole pair.** In GaAs only 4.2 eV are required to liberate an electron hole pair while a gas detector typically requires 30 eV and a photo-cathode coupled to a scintillator needs 300 eV. As a result more carriers are liberated for the same amount of energy deposition and the associated reduction in statistical fluctuations implies that good intrinsic energy resolution results.
- **High density and atomic number.** Semiconductors therefore have a higher specific energy loss ($\frac{dE}{dx}$) than gases and thus thinner detectors may be used. The higher density of the material reduces the range of energetic secondary electrons, (delta electrons), produced inside the material, leading to better spatial resolution.
- **High mobility.** Semiconductor detectors are much faster than gas filled devices due to the higher mobility of both carriers over those in gaseous detectors.
- **Fabrication Techniques.** Lithographic technology is utilised in detector fabrication. This enables aspect ratios (strip width to width plus strip spacing) of order 10:25 μm to be obtained. Spatial resolutions of 3 μm are achievable with these dimensions with the inclusion of measurements of charge sharing between strips (see chapter 6).

The major drawbacks to the implementation of semiconductor detectors are: their cost for large area coverage is significantly greater than for gaseous devices, and they add material between the interaction point and the calorimeters which degrades the impact parameter measurement. Therefore semiconductors are generally found only in the small volume around the interaction vertex where the best position resolution is essential. To reduce material and therefore scattering, semiconductor detectors are made as thin as possible. The lower limit is set by the signal-to-noise ratio of the detector because the signal is proportional to the thickness of the semiconductor. Typical silicon detectors are 300 μm thick.

A semiconductor detector works by separating, via an electric field, the electron and hole pairs created by the passage of ionising radiation through the material. The average number of electron hole pairs created in a 300μm thick silicon detector traversed by a minimum ionising particle is 3.2×10^4, while for intrinsic silicon the number of free carriers (n_i) in a 1 cm^2 area of the same thickness is four orders of magnitude higher. It is obvious that the signal would be swamped if simple conducting electrodes were placed on either side of the material. For diamond detectors, on the other hand, the number of free charge carriers is so small that such an arrangement is in fact feasible, but both GaAs and silicon must be depleted of their free carriers by the use of a reverse biased rectifying junction. Normally, p-n junctions are used for silicon detectors while the GaAs devices described in this work are Schottky barrier diodes. The major cause of leakage current for a fully depleted silicon diode is the generation current (J_{gen})[12], given by:

$$J_{gen} = \frac{1}{2}\frac{qn_iw}{\tau_0} \tag{1.1}$$

where q is the elementary charge, τ_0 is the mean carrier lifetime in the depletion region of thickness w, which is approximately equal to the thickness of the device. To reduce J_{gen} the lifetime must be maximised, which is achieved by reducing the number of defects in the crystal. The intrinsic carrier concentration has an exponential dependence upon temperature, resulting in a doubling of the current for an increase of 8 K in the temperature. For successful application of semiconductor detectors in physics experiments the temperature must therefore be kept constant so that the signal-to-noise ratio does not change and cause an alteration in the resolution of the detector.

Section 2.5.2 states that the depletion depth is proportional to the square root of the product of the applied reverse bias (V) and the semiconductor resistivity (ρ). For detectors operated at full depletion the product $V_{fd}\rho$ remains constant. As the charge carriers created in the detector bulk drift, they diffuse laterally and are deposited on more than one strip. If the charge is shared between two strips then the resolution is improved from the situation where only one strip has a signal[13]. The lower the applied voltage the lower the electric field and the longer the carriers take to drift through the material. Thus a greater amount of charge sharing takes

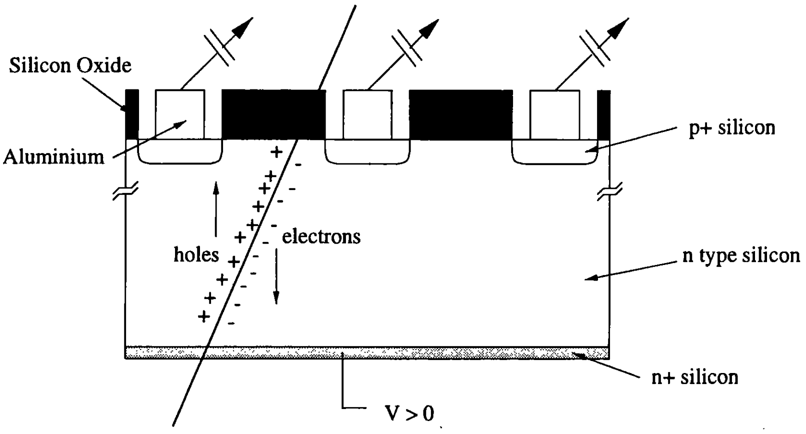

Figure 1.1: The cross-section of a silicon microstrip detector.

place. It is for this reason that detectors are made from high resistivity material.

Figure 1.1 is a representation of a silicon microstrip detector in cross-section. The depletion layer is produced through the reverse biased p^+n junction. The p^+ implant is segmented to produce the microstrip pattern while an n^+ layer is grown on the opposite side of the silicon to prevent the depletion layer reaching the back surface. The n^+ side can be patterned with the strips running in the orthogonal direction to those on the p^+ side to produce a double-sided device. Aluminium is evaporated onto the implants and the strips are wire bonded to external electronics. The silicon oxide layer is present to protect the surface of the detector.

1.3 The ATLAS experiments

The radiation environment of the ATLAS inner detector is discussed in this section after an outline of the physics expectations of the ATLAS experiment and an overview of the detector design.

1.3.1 Physics with the ATLAS detector at the LHC

The LHC machine has very high collision and event rates. A bunch crossing will take place every 25 ns with an estimated 20 proton-proton interactions per crossing, resulting in pile-up problems even in a single bunch crossing. To compound the problems of the detector physicist, the events of interest are very rare indeed, which means that the experiment must have high selectivity. The radiation problem will be severe, with contributions from both charged hadrons from the interaction point and neutrons from the calorimeters. Large coverage in pseudo-rapidity ($\eta = -\ln(tan\phi/2)$ where ϕ is the angle between the beam directions and the emitted particle) is desired due to the number of interesting physics events that occur at high pseudo-rapidity. Thus the vertex detector must be as close to the beam pipe and as long as possible.

The ATLAS experiment, one of two 'general purpose' experiments to be situated on the LHC ring, will have to cope with a broad variety of possible physics processes as well as have the maximum possible potential for the discovery of new, unexpected physics at the high operating energies. It must be sensitive to the largest expected value of the Higgs mass ($\sim$ 1 TeV) and its expected decay products, be able to perform super-symmetric particle searches, investigate CP-violating B-decays and perform detailed studies of the top quark.

The Higgs search, however, will be the bench mark of the detector optimisation. The Standard Model assumes that it is through interactions with the Higgs field mediated by the Higgs boson that particles obtain mass. The discovery of such a particle is therefore of great importance. At the LHC Higgs bosons, produced through gluon-gluon fusion in the proton interactions, will decay through various channels depending upon the Higgs mass[9]:

H →	$b\bar{b}$	80 GeV $< m_H <$ 100 GeV
H →	$\gamma\gamma$	90 GeV $< m_H <$ 150 GeV
H →	$ZZ^* \to 4l^\pm$	130 GeV $< m_H < 2m_Z$
H →	$ZZ \to 4l^\pm, 2l^\pm 2\nu$	$m_H > 2m_Z$
H →	$WW,ZZ \to l^\pm\nu$ 2jets, $2l^\pm$ 2jets	m_H up to 1TeV

which must all be identifiable by an LHC experiment.

The minimal super-symmetric extension to the standard model (MSSM) is the simplest extension and requires additional Higgs searches for processes such as:

$$\begin{aligned} A \quad &\to \tau^+\tau^- \quad \to e\mu \text{ plus } \nu\text{'s} \\ &\qquad\qquad\; \to l^\pm \text{ plus hadrons plus } \nu\text{'s} \\ H^\pm \quad &\to \tau^\pm\nu \\ &\to 2 \text{ jets} \quad \text{using a } l^\pm \text{ tag and b-tagging} \end{aligned} \tag{1.2}$$

where A and $H^{\pm}$ are MSSM Higgs particles. The search for other physics during both the initial low- and later high-luminosity periods places other constraints on the detector design.

The final detector design considerations for any general purpose detector operating at the LHC are:

- **Very good electromagnetic calorimeters.** These are required to perform electron and gamma identification and energy measurements. The calorimeters should be hermetic so that any missing transverse energy can be assigned to neutrinos.
- **Efficient tracking.** At high luminosity this is required for lepton momentum measurements, pattern recognition, b-quark tagging and enhanced electron and gamma identification from Higgs decays. At low luminosity, tracking is required for tau and heavy flavour vertexing and the reconstruction of some B-decay final states.
- **Stand-alone muon momentum measurement.** To reconstruct Higgs decays at high luminosity, precision muon momentum measurements are vital to overcome the background events, while at low luminosity low transverse momentum triggering is required for heavy flavour physics. The stand-alone muon measurements guarantee radiation hardness operation for the identification of the Higgs to two muon decay channel.
- **Large pseudo-rapidity acceptance.**
- **Triggering and measurements of low transverse momentum particles.**

The last two items are necessary in order to maximise the potential physics reach of the experiment.

1.3.2 Detector overview

The ATLAS detector is shown in figure 1.2. The detector consists of the muon spectrometer, the hadronic and electromagnetic calorimeters and the inner tracking detector (described in detail in the next section). The muon spectrometer consists

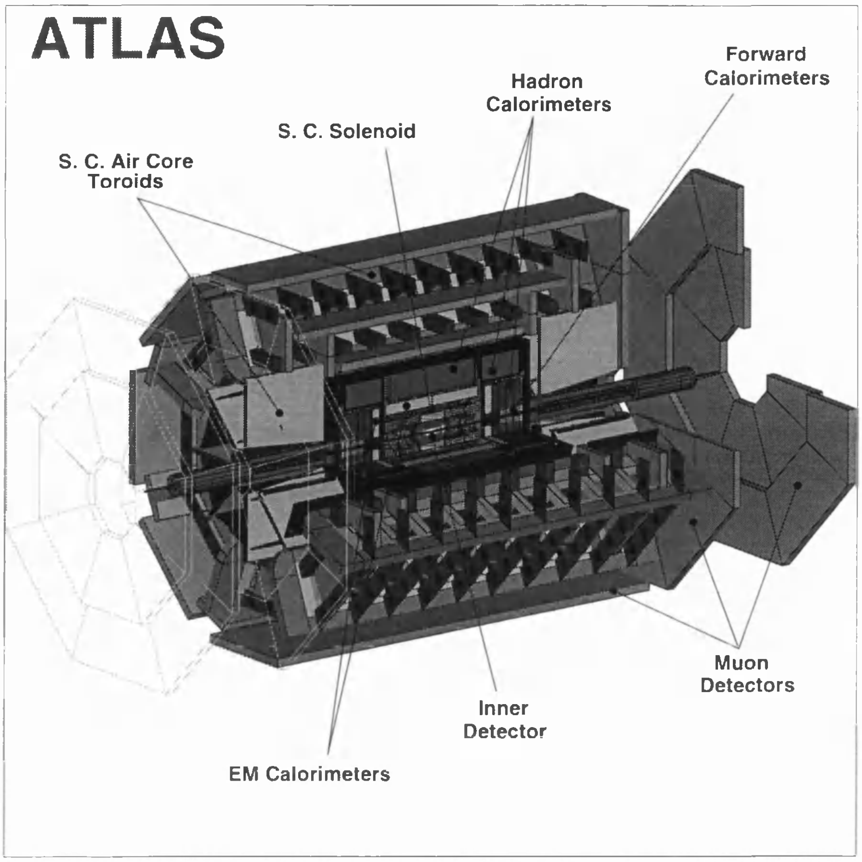

Figure 1.2: A 3-D picture of the ATLAS detector.

of three muon chambers before, inside and after a set of air core toroids. A toroidal magnetic system was chosen to provide large pseudo-rapidity coverage, the best possible transverse muon momentum resolution and robust pattern recognition. The spectrometer will provide the first level trigger for a physics event. The toroids do not provide magnetic fields in the inner detector for inner tracking and therefore a solenoid is present in front of the electromagnetic calorimeters where it produces a homogeneous magnetic field for this purpose. A drawback to the solenoid in this position is that its extra mass degrades the energy and position measurements of the electromagnetic calorimeter. This effect is minimised by placing the solenoid inside the inner cryostat wall of the liquid argon calorimeter where it acts as part of the pre-shower radiator of the calorimeters.

1.3.3 The inner detector

The main objectives of the inner detector are tracking and pattern recognition. While the inner detector is vital for photon identification, for example in the identification of the Higgs decay $H \rightarrow \gamma\gamma$, its ability to perform lepton energy measurements will be less than that of the muon system and the electromagnetic calorimeter. Pattern recognition is enhanced by the ability of the inner detector to perform efficient rejection of π^0s and hadrons that 'fake' electrons in the electromagnetic calorimeter.

In order to have the best acceptance of physics channels the largest possible coverage is required. The inner detector has been designed to cover the pseudo-rapidity range $|\eta| < 2.5$ as a compromise between maximum angular coverage and the practical difficulty of implementing high precision tracking at ever increasing pseudo-rapidity.

The inner tracker will consist of two distinct types of detectors; the precision tracking semiconductor layers and the continuous transition radiation tracker (the TRT). The TRT has a lower individual space point resolution but allows a larger number of points to be obtained for tracking purposes. This is achievable due to its lower material requirement per point and its lower cost with respect to semiconductor detectors.

The ATLAS performance specifications [9] require the number of precision tracking points over the whole pseudo-rapidity range to be ≥ 5. Robust precision tracking is thereby achieved without the need to know the interaction point and with the possibility of some of the inner layers becoming damaged due to the effects of radiation. The TRTs will be used for tracking and the second level trigger, both of which improve with a greater number of points and a larger radial coverage. The specification of the continuous tracker is to deliver 36 measured points for $|\eta| < 2.5$. This may fall to 25 points for a pseudo-rapidity close to 2.5.

The specifications imposed on the efficiency in tracking and pattern recognition of charged tracks are due to four main track categories, three from high luminosity physics and one from the low luminosity B-physics requirements. The most important of these is the identification of high p_T, isolated tracks which are likely to be leptons from interesting physics. The four categories of tracks and the associated

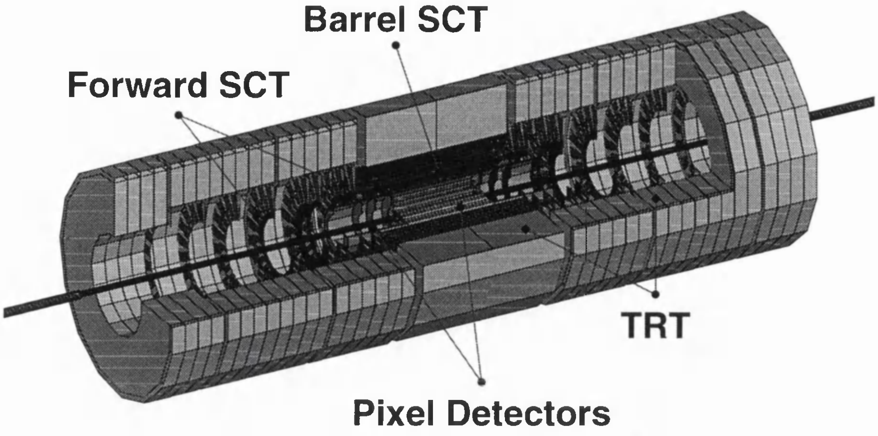

Figure 1.3: The inner detector of ATLAS.

tracking efficiencies imposed on the inner detector are discussed by D. Froidevaux [14].

At low momentum (below 30GeV) the momentum resolution of the inner detector is limited by its own material: muons will undergo multiple scattering in the tracker material itself and bremsstrahlung radiation will limit electron measurements. The momentum resolution specifications of the inner detector are $\Delta\ p_T/p_T < 30\%$ for $p_T = 500$ GeV with $|\eta| < 2$, and $\Delta\ p_T/p_T < 50\%$ for $p_T = 500$ GeV for $|\eta| < 2.5$ due to the reduction in the magnetic field above $|\eta| = 2$.

Figure 1.3 shows a three-dimensional view of the inner detector. The high resolution required for momentum and vertex measurements is provided by the semiconductor tracker (SCT) which must be made from high granularity detectors to cope with the large track density. Closest to the beam pipe, where the track density is greatest, pixel detectors will be installed. The number of pixel layers is limited by the tolerable amount of material in the region, the power dissipation and the cost. The TRTs surrounding the semiconductor detectors provide the necessary number of points for reliable tracking and pattern recognition. The electron identification is enhanced by the TRTs through the detection of transition radiation photons produced inside the foam and straw tubes of the detectors.

Figure 1.4 is a 2-D diagram of one quarter of the inner detector. The precision tracker consists of a barrel region of two pixel detector layers and four layers of

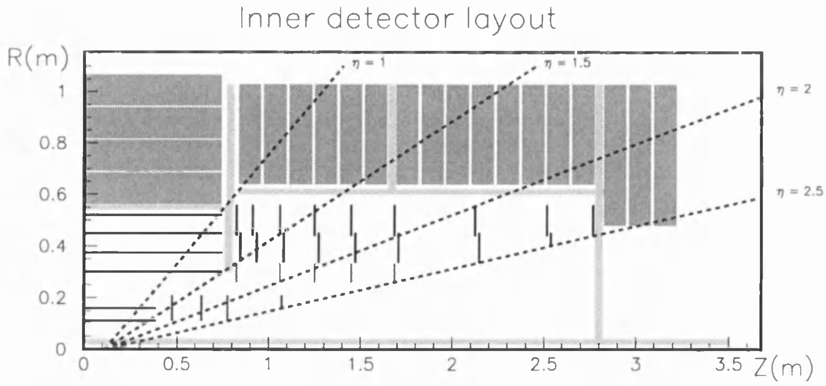

Figure 1.4: A cross-section of the ATLAS inner detector. The colour code is: magenta - pixels; dark blue - silicon strip detectors; green - GaAs strip detectors; light blue - active area of TRT detectors; yellow - additional inactive material.

strips. The region is 74.5 cm long with a radius of 52 cm. During low luminosity operation an extra layer of pixel detectors will be placed as close to the beam pipe as possible to enhance vertex measurements. The continuous tracking detectors surround the precision trackers with the support structures and service areas at the outermost radius. A forward region of precision detectors consists of four planes of pixels and nine strip planes (the semiconductor wheels). Inside the barrel the semiconductor detectors are arranged in concentric cylinders around the beam axis while the forward detectors are planes perpendicular to the beam axis, with stereo strips which run in almost radial directions. The TRT straws are parallel to the beam direction in the barrel region and radial in the forward region. This geometry has been chosen to optimise the Rϕ resolution of the inner detector. Figure 1.5 shows the design of a wheel with the lowest section, highest eta, made from GaAs.

The inner detector design will give 6 precision space points for $|\eta| < 2.5$, one more than the design specifications. Over this region 36 space points will be given by the TRTs, with a slight degradation in the transition region from barrel to forward region.

The material distribution has been a major design criterion. The amount of material must be kept to a minimum and away from the beam pipe where photon conversions are most difficult to veto and where the impact of bremsstrahlung, and thus inefficiency in electron reconstruction, is most severe. The material budget for

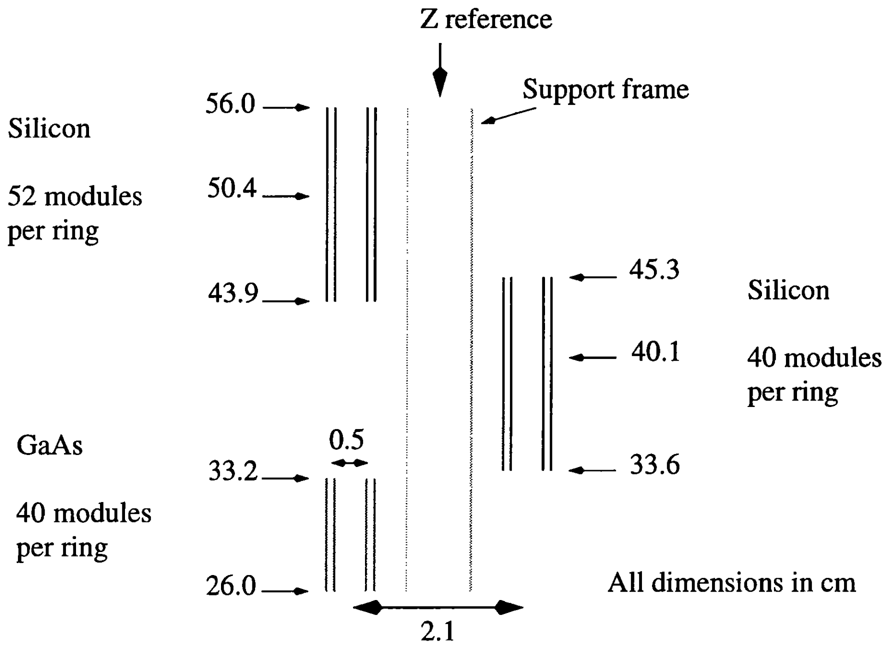

Figure 1.5: Cross-section of an ATLAS wheel.

each layer in radiation lengths (X_0), which is defined as the distance over which the energy of an electron of initial energy E_0 falls to E_0/e, are:

- Pixel layer: 1.3% X_0 at normal incidence
- Barrel SCT layer: 1.6% X_0 at normal incidence
- Forward SCT wheel: 1.9% (2.5%) X_0 at normal incidence for silicon (GaAs)

Due to the smaller radiation length of GaAs (X_0 = 2.3 cm) the ATLAS experiment requires that the GaAs microstrip detectors must be fabricated from 200 μm thick substrate material compared to the 300 μm substrates used for the silicon detectors.

Additional material is present in the beam pipe, supports, services and the TRTs. The material distribution of the inner detector is shown in figure 1.6.

1.3.4 The radiation environment at the ATLAS experiment

The major source of radiation from the LHC is due to proton-proton interactions. At the design luminosity of 1.0×10^{34} $cm^{-2}s^{-1}$ with a cross-section for inelastic p-p interactions of σ_{in} = 80 mb there will be of the order of 10^9 such p-p events per second. The severe radiation load is obvious. The production of particles from the interaction has been simulated with the use of the DTUJET [15] code and

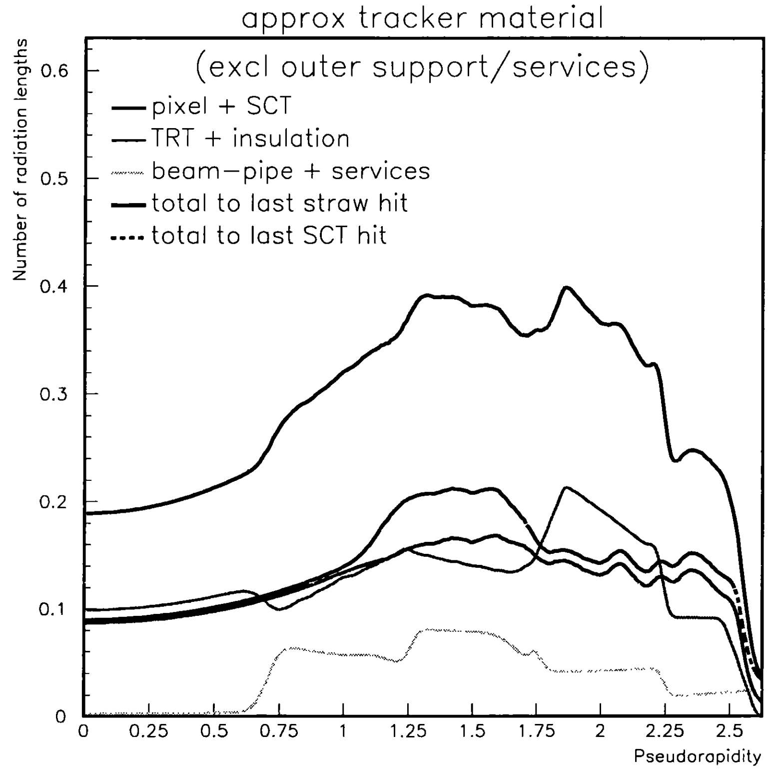

Figure 1.6: Material distribution in the inner detector.

transported through the detector medium with the FLUKA93 [16] code in which the particles are allowed to interact to produce showers. When a high energy particle enters a detector material it showers and, if the material is thick enough, the charged particle is absorbed. During this process neutrons and photons are produced which can escape from the detector medium. In the electromagnetic calorimeters the incident particles will undergo a long shower process to produce neutrons which are scattered many times before either being absorbed or leaving the calorimeters. The neutrons formed through this process are low energy background particles with no time structure and a relatively uniform and isotropic distribution.

The results of the simulation performed by G. Gorfine et al. [17] for the inner detector showed that hadrons from the interaction point dominate the radiation environment at small radii (r) and demonstrate a $1/r^2$ dependence in flux. It was also shown that the inclusion of a polyethylene moderator placed on the inside of the calorimeters reduced the neutron fluence in the inner detector by a factor of between two and three when a thickness of 10 cm was used. The TRTs in the barrel region were also shown to act as neutron moderators.

For an LHC year of 10^7 s the annual particle fluxes calculated for the silicon barrel and the GaAs wheel region are given in table 1.1. Here the simulation assumed seven silicon layers and four GaAs wheels however the position of the layers do not directly correspond to those shown in figure 1.4 due to alterations in the layout of the inner detector since the simulation was performed. Silicon layers S1 and S2 are pixel layers while the five other barrel layers are microstrip detectors. The neutron fluxes calculated with and without a moderator are shown is table 1.2. The moderator was 10 cm thick in the end-cap region and only 5 cm thick in the barrel of the detector.

The GaAs wheels will be exposed to a higher radiation field than any of the silicon strip detectors. From the tables it can be seen that the GaAs wheels will receive 0.30×10^{14} π/cm^2 per year. The neutron flux will be of the order of 3 to 8 times less that this depending on whether a moderator is used. The contributions from other charged hadrons are an order of magnitude less than from pions.

It must be noted that the layout of the inner detector has changed since the simulation was performed and the figures given here are no more than a rough guide to what can be expected at ATLAS with the final detector design.

1.4 Why choose GaAs?

The radiation levels described above will cause significant damage to all the components of the inner detector, including the silicon microstrip detectors. During the operation of the experiment the leakage current of such devices will increase by several orders of magnitude. This will lead to an increase in noise and extra heating effects inside the barrel. As the temperature of semiconductor detectors must be kept constant to prevent instabilities in the leakage current, as noted in section 1.2, extra cooling will be required to remove this additional heat. The silicon bulk will also become doped with radiation-induced defects and undergo type inversion from n- to p-type. The effective doping density will continue to rise with time and therefore the bias required to deplete the detector fully will increase. A 300 μm thick detector will require a reverse bias of over 300 V for full depletion after the ten year

Region			p	$\overline{p}$	$\pi^{\pm}$	$K^{\pm}$	K^0_L
	r (cm)	z (cm)	Flux	Flux	Flux	Flux	Flux
S1 Si	11.5	±35	0.42	0.34	7.3	0.53	0.30
S2 Si	14.5	±40	0.30	0.21	4.8	0.34	0.19
S3 Si	20	±55	0.16	0.11	2.7	0.17	0.099
S4 Si	30	±95	0.087	0.050	1.5	0.076	0.045
S5 Si	50	±95	0.032	0.017	0.58	0.024	0.014
S6 Si	60	±95	0.026	0.011	0.4	0.017	0.0098
S7 Si	69	±95	0.016	0.0084	0.28	0.013	0.0076
G1 GaAs	15-22.5	58.5	0.25	0.16	3.4	0.23	0.14
G2 GaAs	15-22.5	70	0.28	0.18	3.2	0.23	0.14
G3 GaAs	15-25	96	0.24	0.15	2.9	0.21	0.12
G4 GaAs	15-25	109	0.23	0.15	3.0	0.22	0.12

Table 1.1: Annual particle fluxes for different particle species in the inner detector. Units are 10^{13} particles/cm^2/year.

Region	no moderator	with moderator
S1 Si r = 11.5 cm	1.6	1.0
S2 Si r = 14.5 cm	1.2	0.63
S3 Si r = 20 cm	1.0	0.42
S4 Si r = 30 cm	0.77	0.36
S5 Si r = 50 cm	0.73	0.19
S6 Si r = 60 cm	0.66	0.18
S7 Si r = 69 cm	0.61	0.16
G1 GaAs z = 58.5 cm	0.92	0.43
G2 GaAs z = 70 cm	1.0	0.48
G3 GaAs z = 96 cm	1.0	0.47
G4 GaAs z = 109 cm	1.2	0.45

Table 1.2: Annual neutron fluxes in the inner detector with and without a 10cm thick polyethylene moderator. Units are 10^{13} particles/cm^2/year.

lifetime of LHC if it is operated at 20°C. This high bias is not acceptable for the running of such an experiment. If the inner detector can be cooled to -10°C then the formation of deep level defects is slowed down and full depletion is possible at lower biases. However the uniform cooling of such a large volume without the addition of significant extra material is very difficult. If the detector is not fully depleted then the capacitance of the device will be higher, resulting in an increase in the noise. The signal shape will also change with the addition of a slow component which will lead to signal loss due to the fast shaping time of the readout electronics.

An alternative to silicon is required for construction of the forward wheels where the radiation damage will be most acute. Semi-insulating undoped gallium arsenide (SI-U GaAs) has been proposed. SI-U GaAs has a very low level of naturally-occurring free charge carriers at room temperature, which explains its insulating properties. However, the material has a high concentration of deep levels, the EL2 trap for example, even before exposure to radiation. Recalling the equation for the generation current, J_g, in section 1.2 and because the carrier lifetime is inversely proportional to the trap concentration N_T, J_g may be expressed as:

$$J_g \propto N_T n_i \tag{1.3}$$

where n_i the intrinsic concentration of free carriers in the material. SI-U GaAs has a free carrier concentration four orders of magnitude less than that of silicon. It is therefore expected to be able to withstand a higher level of trap production and hence a higher level of radiation fluence than silicon before the leakage current becomes excessive. GaAs electronic devices have also demonstrated a higher radiation tolerance than those fabricated in silicon, for example, no noticeable degradation in FET gain has been observed to occur before fluences of order 10^{15} n/cm^2[18]. For these reasons GaAs has been pursued as a viable alternative to silicon in the forward region.

Chapter 2

Semiconductor Theory.

2.1 The simple semiconductor model

Semiconductor theory is explained in this chapter with emphasis placed on that relating to Schottky barriers. The initial theory for an ideal semiconductor such as silicon or germanium is later extended to the special case of deep levels in semi-insulating undoped GaAs.

2.1.1 Crystal structure

A crystalline semiconductor is a regular assembly of atoms which are held together by covalent bonds. In GaAs the bonds in fact have a slight ionic component. Atomic arrangement is possible in many ways with five of the most common illustrated in figure 2.1. As can be seen, the crystal structure may be very simple, as in the simple cubic and the body-faced cubic structures, however the three main semiconductors have a slightly more complex structure. Silicon and germanium have diamond crystalline structures and GaAs is of the zincblende type. These two structures can be visualised as two inter-penetrating face-centred cubic lattices, where in GaAs one sub-lattice is gallium and the other is arsenic. Since gallium is in group III of the periodic table and arsenic is in group V, GaAs belongs to the III-V family of semiconductors.

Miller indices define the crystal planes of a semiconductor using the direct basis vector coordinate system. The procedure to define a plane is to find the intercept of the plane with the three basis axis in units of the lattice constants. The reciprocals

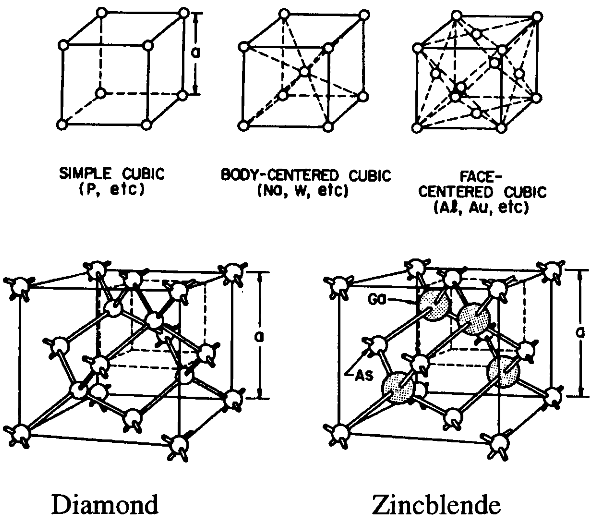

Figure 2.1: Semiconductor crystal structures.

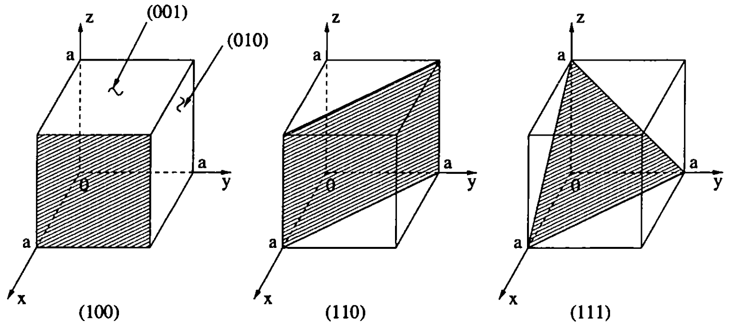

Figure 2.2: Miller planes in a crystal.

of these numbers are reduced to the smallest three integers having the same ratio. For example, in figure 2.2, the plane (100) crosses the x-axis at a, and the y and z axis at infinity. Taking the reciprocals of these gives 1/a, 0 and 0 which has 1, 0, 0 as the smallest set of integers with the same ratio. A set of planes with an equivalent symmetry are enclosed in curly brackets, for example in a simple cubic crystal {100} represents the set of planes (100), (010), (001), $(\bar{1}00)$, $(0\bar{1}0)$ and $(00\bar{1})$, where the over-line implies that the plane crosses the axis at a negative coordinate. Directions in the crystal can be expressed in a similar fashion with the integers being enclosed in square bracket, for example the x-axis, which is normal to (100), is [100].

Semiconductor crystals have preferred cleavage planes. For silicon and germanium this is the {111} set of planes, while in GaAs it is {110}.

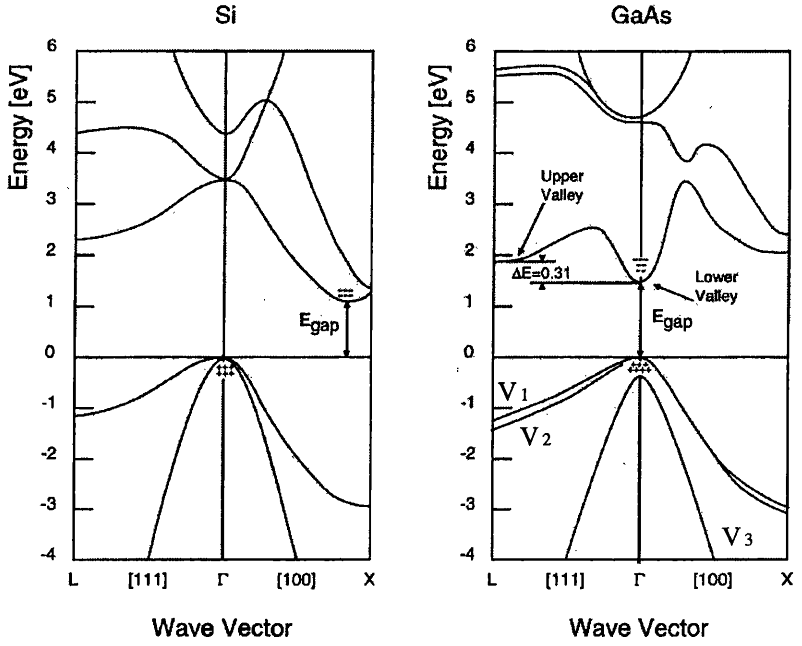

Figure 2.3: The energy band structure in silicon and gallium arsenide. The three lowest bands in GaAs are the valence bands labled V_1 V_2 and V_3, the upper bands are the conduction bands and E_{gap} is the energy bandgap. The minus (-) signs indicate electrons in the conduction band and the plus (+) signs indicate holes in the valence bands[1].

2.1.2 Energy levels

The allowed energy of the electrons in a semiconductor can be found by solving the Schrodinger equation for a crystal in which the atoms are completely ionised and the electrons do not interact with the ions of the crystal. This is the free electron model. When the electrons are allowed to interact with the ions of the crystal lattice, energy bands for the electrons result with a forbidden band in their energy-momentum (**k**) diagram.

The real energy states in a semiconductor are in fact more complex than the nearly free electron model describes. The energy band structures, that is the energy-momentum relationship, for silicon and GaAs are shown in figure 2.3. The value $\mathbf{k} = \Gamma$ corresponds to $\mathbf{k} = 0$. The energy gap at 300 K of $E_g = 1.11$ eV for silicon and 1.42 eV for GaAs.

The properties of the semiconductor depend principally on the interaction between the lowest, nearly filled energy band states, defined as the valence band,

and the next, nearly empty, energy band states immediately above the valence band - the conduction band. When an electron is excited from the valence band to the conduction band a vacancy remains in the valence band. It is mathematically convenient to treat this vacancy as another particle, the hole. A hole has a similar mass, as well as other low energy properties of the electron, except for its charge which is positive. The electron and hole are known as charge carriers.

The rest of semiconductor theory is occupied with the determination of the distribution and motion of the carriers.

Several points should now be made about the energy-momentum relationships in GaAs and silicon. The energy band gap in GaAs is larger than that in silicon. This should result in more thermal energy being required to excite the electrons from the valence band to the conduction band. In other words, at a given temperature the number of electrons in the conduction band should be less for GaAs than for silicon. Another feature of the energy-momentum relationships is that GaAs is a direct band gap material. That is, the minimum in the conduction band and the maximum in the valence band have the same momentum. Silicon, on the other hand, is an indirect band gap material as the conduction band minima and the valence band maxima do not occur at the same value of momentum, which is illustrated in figure 2.3. In GaAs a photon may therefore be emitted when an electron undergoes a transition from the conduction band to the valence band, as no change in electron momentum occurs. This allows optical modulators to be fabricated from GaAs. Finally a second minimum, the 'upper valley', is present in the conduction band 0.31 eV above the lower valley. In high electric fields ($> 3 \times 10^3$ Vcm^{-1}) in GaAs, electrons can be excited into this valley where their transport is affected. A short discussion of this point is contained in section 2.3 on mobility.

2.2 Carrier concentration at thermal equilibrium

In this section the ideas of carrier concentration in the conduction band and the valence band are discussed, requiring the introduction of the concept of the effective mass of the carriers. The carrier concentrations are found for a very pure (intrinsic) semiconductor and then for materials with impurities (extrinsic).

Two families of impurities exist, called donors and acceptors. A donor has an extra valence electron, with respect to the intrinsic material, which is donated to the electron gas. Phosphorus is a donor in silicon. The semiconductor is now n-type because of the addition of negative electrons. Electrons are known as the majority carriers and holes the minority carriers in n-type semiconductors. Similarly, with incorporation in silicon of an impurity that has only three valence electrons, for example boron, an electron is accepted by the impurity atom to form four covalent bonds and thus the impurity is called an acceptor. A vacancy, or 'hole', is created in the valence band and the semiconductor is p-type due to the addition of positive charge; holes are the majority carriers in this case. The energy level of a donor is measured down from the conduction band while that of an acceptor is measured up from the valence band.

In GaAs silicon and carbon (both group IV) may be either a donor or an acceptor depending upon the atom that they displace. In the GaAs used for this work silicon is a donor and carbon an acceptor (see section 2.9.1).

2.2.1 Carrier effective mass

Because the carriers in a semiconductor are not free particles, to treat them as classical charged particles the concept of an effective mass must be introduced. The effective mass is defined by the band curvature, as:

$$m_c^* = (\hbar)^2 \left(\frac{d^2E}{d\mathbf{k}^2}\right)^{-1} \tag{2.1}$$

where $\hbar$ is the Planck constant, E the band energy and $\mathbf{k}$ the wave vector. Therefore the effective mass of a carrier depends upon the band that the carrier is in. In GaAs, for example, the effective mass of an electron in the lowest valley of the conduction band (m_Γ^*) is $0.063m_0$ at room temperature, where m_0 is the mass of the free electron. Electrons in the upper valley have two effective masses: m_l^* (the longitudinal mass) along the symmetry axes of the constant energy surfaces in the crystal and m_t^* (the transverse mass) perpendicular to the symmetry axes. Appendix A gives these values. A low temperature overall electron effective mass for this valley is:

$$m_L^* = (16m_l^*(m_t^*)^2)^{\frac{1}{3}} \approx 0.56m_0 \tag{2.2}$$

The temperature dependence is slight and at 300K $m_L^* = 0.55m_0$.

There are three valence bands in GaAs which all have their maxima at $\mathbf{k} = 0$, as shown in figure 2.3. The heavy hole (V_1) and light hole (V_2) bands are degenerate at their maxima while the split-off valence band (V_3) is separated by 0.34 eV. This lower band is ignored for calculations at room temperature because its hole occupancy is negligible. Due to the difference in curvature of the two degenerate bands, different hole effective masses arise. For the heavy hole band, (V_1), $m_{hh}^* = 0.45m_0$ and for the light band, (V_2), $m_{lh}^* = 0.082m_0$, at 300K. An overall effective mass, know as the density of states effective mass, is defined as:

$$m_h^* = \left[(m_{lh}^*)^{\frac{3}{2}} + (m_{hh}^*)^{\frac{3}{2}}\right]^{\frac{2}{3}} = 0.524m_0 \tag{2.3}$$

2.2.2 Density of states

The number of electrons per unit volume in the conduction band (n) is given by the probability of there being an electron in a state of energy E ($f(E)$) integrated over all the available states. This probability is governed by Fermi-Dirac statistics and is therefore given by the Fermi-Dirac function:

$$f(E) = \frac{1}{1 + \exp\left(\frac{E-E_F}{k_BT}\right)} \approx \exp\left(-\frac{E - E_F}{k_BT}\right) \tag{2.4}$$

where k_B is the Boltzmann constant, T is the temperature and E_F is the energy of the Fermi-level. At temperatures above absolute zero the Fermi level is the energy level which has a 50% probability of being occupied by an electron. For the condition $E - E_F > k_BT$ the approximation in equation (2.4) is valid. The energy of an electron is taken to be zero at the bottom of the conduction band and increases upwards, while that for a hole is zero at the top of the valence band and increases downwards.

Integrating over all available states gives:

$$n = N_C \exp\left(-\frac{E_C - E_F}{k_BT}\right) \tag{2.5}$$

where

$$N_C = 2\left(\frac{m_\Gamma^* k_BT}{2\pi\hbar^2}\right)^{\frac{3}{2}} \tag{2.6}$$

is the effective density of states in the conduction band and $\hbar$ is Planck's constant.

The probability of finding a hole in the valence band is simply the probability of not finding an electron and therefore the density of holes in the valence band (p) is:

$$p = N_V \exp\left(-\frac{E_F - E_V}{k_B T}\right) \tag{2.7}$$

where

$$N_V = 2\left(\frac{m_h^* k_B T}{2\pi\hbar^2}\right)^{\frac{3}{2}} \tag{2.8}$$

is the effective density of states in the valence band.

In an intrinsic semiconductor in thermal equilibrium the electrons are continuously excited from the valence into the conduction band. This process is balanced by the recombination of the electrons in the conduction band with holes in the valence band. Equal and constant values for n and p therefore exist, that is $p = n = n_i$, where n_i is the intrinsic carrier density. The intrinsic semiconductor has a Fermi level (E_i) given by:

$$E_F = E_i = \frac{E_C + E_V}{2} + \frac{k_B T}{2}\ln\left(\frac{N_V}{N_C}\right) \tag{2.9}$$

derived by equating equations (2.5) and (2.7). It can be seen that the Fermi level of an intrinsic semiconductor lies close to the middle of the band gap. The Fermi level of an extrinsic semiconductor is calculated at the end of this section.

Equations (2.5) and (2.7) may now be re-written in terms of n_i and E_i:

$$n = N_C \exp\left(-\frac{E_C - E_i}{k_B T}\right)\exp\left(\frac{E_F - E_i}{k_B T}\right) = n_i \exp\left(\frac{E_F - E_i}{k_B T}\right) \tag{2.10}$$

$$p = N_V \exp\left(-\frac{E_i - E_V}{k_B T}\right)\exp\left(\frac{E_i - E_F}{k_B T}\right) = n_i \exp\left(\frac{E_i - E_F}{k_B T}\right) \tag{2.11}$$

Now it is possible to obtain an expression for n_i in terms of the band gap energy ($E_g = E_C$ - E_V) and the effective density of states in the conduction and valence bands:

$$n_i = \sqrt{np} = \sqrt{N_C N_V}\exp\left(-\frac{E_g}{2k_B T}\right) \tag{2.12}$$

This clearly demonstrates that it is the band gap energy that predominates in the determination of the free carrier concentration.

The addition of either donor or acceptor atoms into the semiconductor will alter the position of the Fermi level. Some of the donors and acceptors will become ionised by either donating an electron to the conduction band (donor) or by accepting an electron from the valence band (acceptor). The Fermi level will adjust to the addition of the impurities so that charge neutrality in the crystal is preserved. Charge neutrality demands for a crystal with a density N_A of acceptor atoms and a donor density N_D:

$$n + N_A^- = p + N_D^+ \tag{2.13}$$

The concentration of ionised donors and acceptors are given by equations (2.14) and (2.15) where E_A and E_D are the acceptor and donor energy levels, respectively. Each equation has a factor g which is the ground state degeneracy of the impurities. For the donor g = 2 due to the Pauli exclusion principle. However, for the acceptor level g = 4 because the level is doubly degenerate at **k** = 0 as a result of the two valence bands V$_1$ and V$_2$[1].

$$N_A^- = \frac{N_A}{1 + g\exp\left(\frac{E_A - E_F}{k_B T}\right)} \tag{2.14}$$

$$\begin{aligned} N_D^+ &= N_D\left[1 - \frac{1}{1 + \frac{1}{g}\exp\left(\frac{E_D - E_F}{k_B T}\right)}\right] \\ &= \frac{N_D}{1 + g\exp\left(\frac{E_F - E_D}{k_B T}\right)} \end{aligned} \tag{2.15}$$

For a given semiconductor (thus a known E_g) with a known concentration of donors, N_D, of a given energy E_D and acceptors, N_A, at an energy E_A at a given temperature, T, the Fermi level can be found from equations (2.13), (2.14) and (2.15), the values of n and p being given previously by equations (2.5) and (2.7).

It should be noted that when impurities are added to a semiconductor, the relationship given by equation (2.12) for the product np still holds, and the product is independent of the added impurities. Therefore from equations (2.13) and (2.12) the electron concentration in a n-type material with only shallow dopants is:

$$n = \frac{1}{2}\left(N_D - N_A + \sqrt{(N_D - N_A)^2 + 4n_i^2}\right) \tag{2.16}$$

2.3 Carrier transport

The carrier distributions have been defined and the above formulation put in place so that the Fermi level can be calculated from a basic knowledge of the semiconductor type and doping. The transport properties of the carriers must now be explained if practical devices are to be understood.

Electrons in the conduction band have a random thermal velocity, v_{th}, given by:

$$\frac{1}{2}m_n^* v_{th}^2 = \frac{3}{2}k_B T \tag{2.17}$$

At room temperature the electron thermal velocity is of the order of 10^4 ms^{-1}. A corresponding relationship also applies for holes.

Under the application of an external electric field ($\mathcal{E}$) a drift component is added to the carrier motion. The low field drift velocities for electrons (v_n) and holes (v_p) are:

$$v_n = -\mu_n \mathcal{E} \tag{2.18}$$

$$v_p = \mu_p \mathcal{E} \tag{2.19}$$

where the constant of proportionality is the mobility ($\mu_{n,p}$) of the carriers which is both carrier and material dependent. The negative sign is present as the carriers move in opposite directions. The drift velocity gives rise to a drift current (J):

$$J = nqv = nq\mu\mathcal{E} \tag{2.20}$$

The mobility depends on the effective mass and temperature of the carrier. With decreasing mass the mobility increases, thus in GaAs electrons have a much higher mobility than holes. For high electric fields the above relationships are no longer valid as the mobilities are affected by the scattering of carriers in the material and by the transfer of electrons into the upper valley in the conduction band, (see figure 2.3). Electrons in the direct band, lower valley, have very high mobilities (8500 cm^{2}V^{-1}s^{-1} at 300 K) resulting in high velocities at low electric fields. As the electric field is increased the electrons are scattered into the indirect upper valley where the mobility is reduced due to the increase in effective mass. This is known as the 'transferred electron' effect. As a result the average group velocity of the electrons begins to fall,

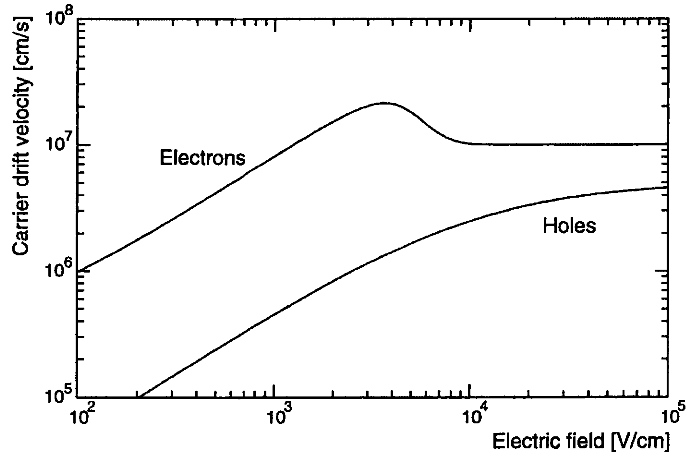

Figure 2.4: Carrier drift velocities as a function of electric field in GaAs.

(noticeably for fields above 3×10^3 Vcm^{-1}), as the population of electrons in the upper valley rises. The drift velocity as a function of electric field for the carriers in GaAs is shown in figure 2.4.

Evident from figure 2.4 is the low hole velocity due to its low field mobility of only 400 cm^{2}V^{-1}s^{-1} at 300K. To increase the average hole velocity the electric field must be increased. Similar electron and hole velocities can be achieved at fields greater than 1×10^4 Vcm^{-1} but only at the expense of the electron velocity.

The resistivity (ρ) of a semiconductor is defined as the proportionality constant between the electric field and the drift current, which at low fields depends upon the mobility of the carriers:

$$\rho = \frac{\mathcal{E}}{J} = \frac{1}{q(n\mu_n + p\mu_p)} \tag{2.21}$$

The conductivity (σ) of the sample is defined as the reciprocal of the resistivity:

$$\sigma = q(n\mu_n + p\mu_p) \tag{2.22}$$

For intrinsic GaAs at room temperature the value of the resistivity can now be calculated. The intrinsic carrier concentration is found with equation (2.12) and the values of the effective density of states are given in appendix A. With a band gap energy of 1.423 eV at room temperature equation (2.12) yields 2.4×10^6 cm^{-3} for the intrinsic carrier concentration. For the low field mobilities a resistivity of

3.9×10^8 Ωcm follows from equation (2.21). For an n-type material, where $N_D \gg n_i$ and $N_D \gg N_A$, the resistivity from equations (2.21) and (2.16) is:

$$\rho = \frac{1}{q\mu N_D} \tag{2.23}$$

A high resistivity has implications for the extension of the depletion region inside a device and therefore for detector operation, as will be explained in section 2.5.2.

Carriers in a semiconductor diffuse as well as drift, a fact which is very important in the processes that result in the equilibrium of many devices. The carriers diffuse with a flux that is proportional to the carrier concentration gradient. As the current density is simply the flux of carriers multiplied by the electron charge (q) then the diffusion currents are:

$$J_n = qD_n\frac{dn}{dx} \tag{2.24}$$

$$J_p = -qD_p\frac{dp}{dx} \tag{2.25}$$

where D_n and D_p are the diffusion coefficients for electrons and holes respectively. Again the negative sign arises due to the relative motion of the electrons and holes.

The diffusion of electrons results in a change in the carrier concentration and therefore the electric field distribution will be altered. The movement of charge from point A to B due to diffusion will create an electric field that will oppose this motion and tend to cause electrons to drift from B back to A. In equilibrium these balance:

$$J_{\text{drift}} = J_{\text{diffusion}} \rightarrow qn\mu_n\mathcal{E}_x = qD_n\frac{dn}{dx} \tag{2.26}$$

If the concentration gradient is described by $n = n_0\exp(\frac{qV}{k_BT})$, as it often is, then Einstein's relationship between the mobility and diffusion constant follow:

$$D_n = \left(\frac{k_BT}{q}\right)\mu_n \tag{2.27}$$

$$D_p = \left(\frac{k_BT}{q}\right)\mu_p \tag{2.28}$$

2.4 Recombination processes - carrier lifetimes

An ideal radiation detector is required to collect all the charge that is deposited in the material by an ionising particle. To do this the charge carriers must be

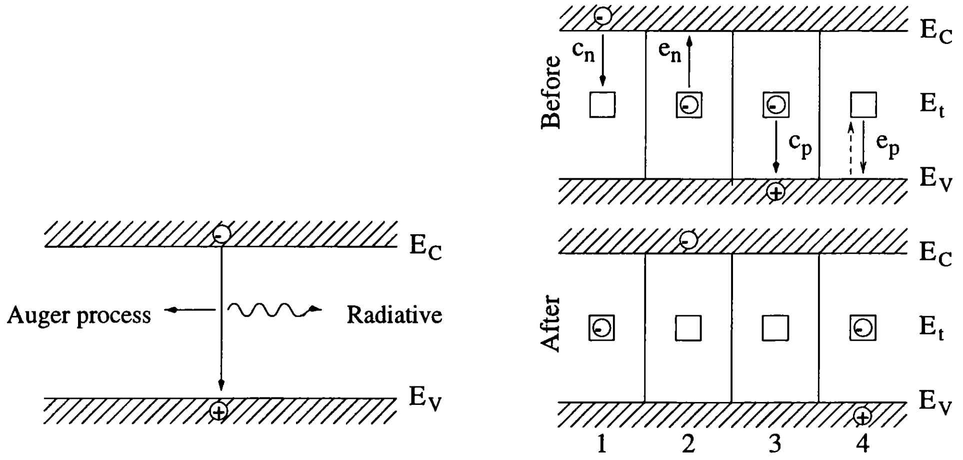

(a) Band to band.

(b) Single level. The process are: 1 - electron capture, 2 - electron emission, 3 - hole capture and 4 - hole emission.

Figure 2.5: Recombination processes in gallium arsenide.

able to travel through the volume of the detector and reach the contacts without being stopped. The carriers will not do this if they recombine with each other or are trapped in an energy level in the forbidden energy gap, that is if electrons are removed from the conduction band and holes from the valence band. The carrier constant that characterises this removal is the carrier lifetime. This section will discuss the recombination processes that occur in a semiconductor and the effect of these on the carrier lifetimes, drawing on GaAs for examples.

In thermal equilibrium the product of electron and hole concentration is equal to the square of the intrinsic carrier concentration, as stated earlier. When a process occurs that changes this, for example the liberation of electron hole pairs by an ionising particle, $np \neq n_i^2$ and restoration processes occur in the semiconductor. Figure 2.5 shows the two main processes. The first is a band-to-band process where an electron in the conduction band recombines directly with a hole in the valence band. The energy is liberated either as a photon (radiative recombination) or directly to another electron or hole, the Auger process.

For direct band gap semiconductors radiative recombination should dominate. This process will result in a shorter carrier lifetime in pure GaAs than in silicon and germanium which are not direct band gap materials. The radiative recombination lifetime for minority carriers (τ_c), holes in an n-type semiconductor, can be expressed as:

$$\tau_c = \frac{1}{Bn_m} \tag{2.29}$$

where B is the probability of radiative recombination with units of cm^3s^{-1}, and n_m is the majority carrier concentration (electrons for n-type material), with units of cm^{-3}.

The net recombination rate (R_r in Hz) is:

$$R_r = B(np - n_i^2) \tag{2.30}$$

where the difference between the product of the non-equilibrium carrier concentration and the square of the intrinsic carrier concentration is zero at equilibrium.

In GaAs B has been calculated to be 1.74×10^{-10} cm^{3}s^{-1}[19]. Very pure material should have a reasonably long carrier lifetime, according to equation (2.30). For n-type GaAs with a carrier concentration of 1×10^{14} cm^{-3}, a hole (minority carrier) lifetime of 57.5 μs is predicted which gives a mean absorption length of order 1000 μm for a electric field of order 1 V/μm.

Chapter 4 will show that such values have not been observed in bulk SI-U GaAs. Other processes must therefore be present that reduce the carrier lifetime. Other evidence to this effect is that radiative recombination lifetimes are inversely proportional to the doping concentration so that, as the doping concentration changes in n-type material, the hole lifetime should alter. However, for concentrations below 10^{18} cm^{-3} the lifetime has been shown to remain constant[20]. Radiative recombination is therefore not the major process.

GaAs that has undergone irradiation shows reduced mean carrier absorption lengths and therefore lifetimes (see chapter 5). As radiation introduces traps in the material it is therefore expected that traps will explain the observed carrier lifetimes even in the unirradiated material.

Such a method of carrier recombination is shown as the second process of figure 2.5. In this figure a deep energy level (E_t) is present close to the intrinsic Fermi level of the semiconductor, that is close to mid-gap. Four processes are allowed to occur between the conduction and valence bands and the deep level. An electron in the conduction band can be captured by the level, described by the electron capture coefficient of the level (c_n). An electron may be emitted from the level to the conduction band, characterised by an electron emission rate e_n. The third process is the capture of a hole from the valence band by the level, and the level will therefore also have a hole capture coefficient (c_p), while the fourth process is the emission of the hole back to the valence band, with emission rate e_p. This can be thought of as electron emission from the valence band as represented by the dashed line in the figure. Figure 2.5 shows the state of the bands and the deep level both before and after these processes.

In a recombination event, the first and third processes occur and a generation event occurs when the fourth process follows the second. A final event type is trapping, which is neither generation nor recombination. This happens when the first and second processes follow each other (the capture of an electron and then, at some time later, its re-emission back to the conduction band) or when the third and fourth processes occur - hole trapping. Trapping events only involve the deep level and one of the bands. Whether a deep level is a trap or a generation-recombination centre depends upon the energy level with respect to the Fermi level, the temperature and the capture cross-sections of the level. Generally a generation-recombination centre is close to the middle of the band gap, while a trap is closer to one of the bands.

Normally only one of the carrier emission rates dominates. If the level is in the upper half of the band the electron emission rate is often larger than the hole rate and hole emission can be neglected. For levels in the lower half of the band the situation is reversed. It should be noted that recombination is more likely when there is an excess of carriers in the semiconductor and generation will occur in situations where the carrier density is low. An example of this is given in the section on generation current in the space charge region (see section 2.6.5).

The recombination process will now be considered. Shockley-Read-Hall[1] statistics describe the single-level recombination rate (R_{srh}) as:

$$R_{srh} = \frac{np - n_i^2}{\tau_p(n + n_1) + \tau_n(p + p_1)} \tag{2.31}$$

for a concentration N_T of deep levels at an energy E_T, where

$$n_1 = n_i \exp\left(\frac{E_i - E_T}{k_B T}\right) \tag{2.32}$$

and

$$p_1 = n_i \exp\left(\frac{E_T - E_i}{k_B T}\right) \tag{2.33}$$

$\tau_{n,p}$ are the minority carrier lifetimes for electrons and holes defined by:

$$\tau_{n,p} = \frac{1}{c_{n,p} N_T} = \frac{1}{\sigma_{n,p} v_{th(n,p)} N_T} \tag{2.34}$$

where $c_{n,p}$ are the carrier capture coefficients, $\sigma_{n,p}$ the carrier capture cross-sections and $v_{th(n,p)}$ the carrier thermal velocities. The deep level recombination rate will be zero under equilibrium conditions, that is when $np = n_i^2$.

If both lifetimes are equal, simplification of this expression occurs:

$$R_{srh} = \frac{np - n_i^2}{\tau\left(n + p + 2n_i \cosh\left(\frac{E_T - E_i}{k_B T}\right)\right)} \tag{2.35}$$

It follows that recombination will be a maximum for a value of $E_T \sim E_i$, that is an energy level near mid gap.

It can be seen that for an n-type semiconductor, where $n_n \approx n_{n0}$, $n_n \gg n_i$ and $n_n \gg p_n$, the recombination rate is determined by the lifetime of the minority carrier (holes) and is given by:

$$R_{srh} = \frac{p_n - p_{n0}}{\tau_p} \tag{2.36}$$

Here the subscripts n and 0 denote the n-type semiconductor and the equilibrium value of the carrier concentrations, respectively. This expression is only valid when the number of injected carriers is much smaller than the number of majority carriers.

Charge injection into the material by a high energy particle or electrical biasing of the device will increase both the radiative and the single level recombination terms of equations (2.30) and (2.35). The higher rate will be the dominant process. As already stated, the dominant process in GaAs is most likely the single level recombination rate even though the radiative rate is higher in this material than in silicon or germanium.

An operational particle detector is not in thermal equilibrium due to the large external electric field applied to the bulk of the device. Therefore the measured carrier lifetimes in GaAs in thermal equilibrium do not represent the correct lifetimes when charge collection is being considered. Due to the large electric field the concentration of electrons in the conduction band is small and therefore recombination is unlikely. Trapping is therefore the most probable carrier loss mechanism. At the instant of electron hole pair creation by the ionising particle, however, both carriers are in close proximity. This is termed the detector plasma time. Before carrier separation has taken place, recombination may occur in the plasma which will be dominated by deep level recombination in GaAs. The overall detector carrier lifetimes are therefore a combination of the plasma recombination lifetime and the trapping lifetime during the collection period.

2.5 Metal-semiconductor contacts

GaAs particle detectors are diodes operated in reverse bias. The diodes are realised in one of three ways: the p-i-n structure, a p-π-ν-n in-diffusion gradient, where π and ν are lightly doped p- and n-type material, or with the use of a metal-semiconductor Schottky contact. As the work detailed in this thesis is concerned primarily with detectors fabricated with the metal-semiconductor contact, only the theory relevant to this device structure will be discussed. Details of p-i-n contacts and detectors can be found in reference [21] while reference [22] contains details of the in-diffusion gradient type of detector. This section and the next are primarily concerned with the theory of ideal Schottky contacts, as formed on semiconductors with no deep defects. Section 2.9 details the effects that deep defects have on such devices. The equipment used to characterise the barrier is described in chapter 3, while chapters 4 and 5 report on the measurements actually made.

2.5.1 The Schottky barrier

Barrier formation is discussed first followed by the process of field penetration into the semiconductor. Field penetration creates a space-charge region which is vital for particle detectors as only carriers deposited by ionising particles in this region are separated and collected. The effect of surface states on the barrier are outlined and an examination of image-force lowering of the barrier closes this section.

Barrier formation

The rectifying barrier is formed when a metal and a semiconductor are brought into direct contact with each other. Free passage of current is allowed by the barrier in one direction while the flow in the other direction is inhibited; this constitutes the rectifying nature of the contact.

A semiconductor has an electron affinity (χ_s) which is the difference in energy between the bottom of the conduction band and the vacuum state. For a semiconductor in which the bands are flat, that is without the presence of any electric fields, the work function (ϕ_s) and the electron affinity are related by:

$$q\phi_s = q(\chi_s + V_n) \tag{2.37}$$

where qV_n is the energy difference between E_C and E_F and is equal to:

$$V_n = \frac{k_B T}{q} \ln\left(\frac{N_C}{N_D}\right) \tag{2.38}$$

for an n-type semiconductor where $N_D \gg n_i$ and $N_D \gg N_A$.

The formation of a barrier without surface states on n-type material is shown schematically in figure 2.6. At the start both metal and semiconductor are electrically neutral and separate from each other. They are then connected electrically and because the semiconductor work function is lower than that of the metal electrons will enter the metal from the semiconductor and the two Fermi levels will line up (figure 2.6(b)). Due to the lowering of the semiconductor Fermi level, the energy of electrons that have entered the vacuum state from either material will be different, therefore an electric field directed towards the metal will exist across the gap. A negative charge is produced on the metal which is balanced by a positive charge in the semiconductor. Positive charge is produced in the semiconductor by electrons receding from the contact to leave uncompensated positive donor ions, known as the depletion or space charge region. As donor densities are much less than the electron concentration in a metal, a relatively large positively charged area will be produced in the semiconductor while the extra charge in the metal is contained in a thickness of approximately $0.5\mathring{A}$.

Due to the removal of electrons, the Fermi level in the semiconductor changes position relative to the bands, resulting in the bands being bent upwards as the

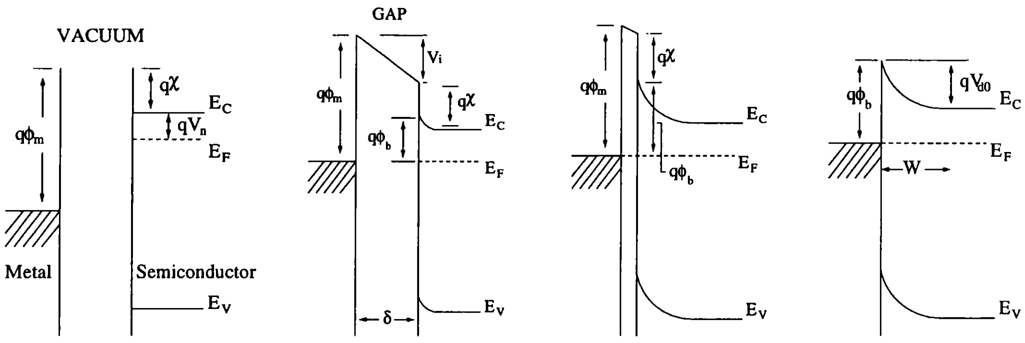

(a) Isolated (b) Electrical connection (c) Separated by a narrow gap (d) In perfect contact

Figure 2.6: The formation of a barrier at a metal-semiconductor interface.

Fermi levels of the two materials must remain the same (shown in figure 2.6). The difference in the vacuum states for the metal and semiconductor (V_i) is given by the product of the separation distance (δ) and the electric field in the gap ($\mathcal{E}$). As the two are brought into closer contact δ is reduced and therefore V_i must tend to zero to keep $\mathcal{E}$ finite. When $\delta = 0$ the barrier height (ϕ_b) for a perfect metal-semiconductor contact is:

$$\phi_b = \phi_m - \chi_s \tag{2.39}$$

The diffusion potential ($V_d = V_{d0}$ for zero external potential) is defined as the difference in potential across the depletion region, that is the difference between the barrier height and V_n:

$$V_{d0} = \phi_b - V_n \tag{2.40}$$

The shape of the potential barrier depends on the charge distribution in the depletion region. The barrier can raise the bottom of the conduction band by a few times k_BT/q which causes the electron density to be reduced by an order of magnitude, implying that the space-charge is entirely due to the uncompensated donors. If the donor concentration is homogeneous up to the barrier then the Schottky barrier is produced. The electric field increases linearly with distance from the edge of the depletion region, and the potential increases quadratically, as will be discussed in section 2.5.2.

However, if at the surface the donor density is negligible the electric field would

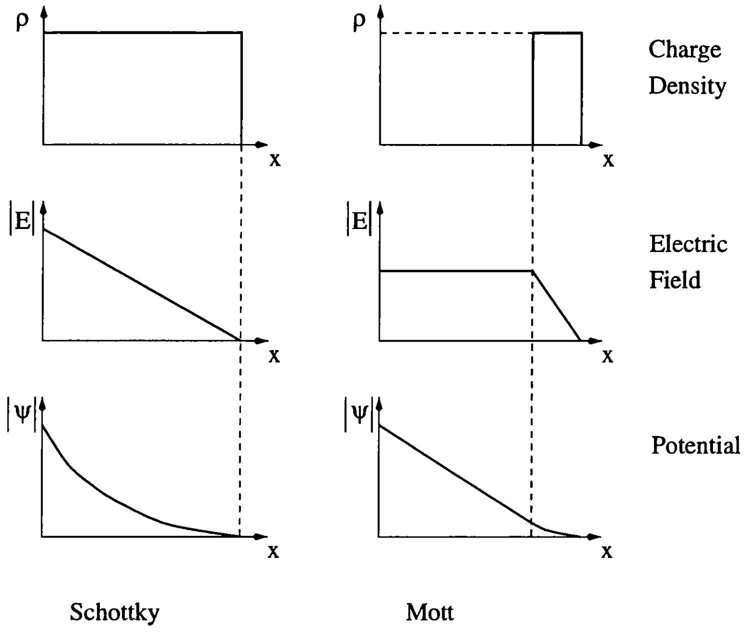

Figure 2.7: The Schottky and Mott barriers for an n-type semiconductor.

be constant over this layer. A linear potential will arise in this area and become quadratic only in the area of significant donor concentration, as shown in figure 2.7. This is the Mott barrier. A similar potential distribution has been found in GaAs devices under high bias but the reason is quite complex and is discussed in section 2.9.3. Mott barriers are not common and only the Schottky barrier is considered further.

Figure 2.8 shows the second situation which occurs at a metal- n-type semiconductor contact when the metal work function is less that that of the semiconductor. Here electrons will encounter no barrier from the semiconductor to the metal. If the junction is forward biased the bands are bent down still further and the current is determined by the bulk resistance of the semiconductor and not the contact properties. This is the ohmic contact, discussed in more detail in section 2.7 and in section 3.1.3.

2.5.2 Depletion approximation

The definite energy relationship between the conduction and valence bands of the semiconductor and the metal Fermi level at a metal-semiconductor junction make it possible to find expressions for the depletion width, the electric field strength

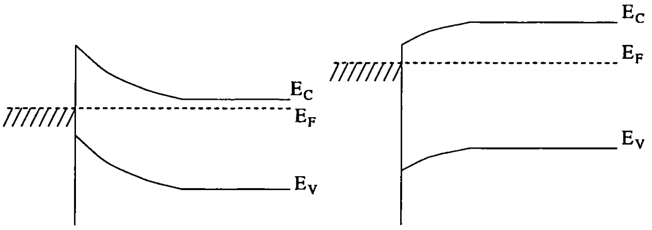

(a) $\phi_m > \phi_s$ rectifying (b) $\phi_m < \phi_s$ ohmic

Figure 2.8: The metal barrier on an n-type substrate for different metal-work functions.

and the electrostatic potential of the barrier as functions of the barrier height, bias voltage and semiconductor impurity concentration. The depletion approximation states that the free carrier density at the edge of the depletion region has an abrupt fall from its bulk value to a negligible one with respect to the donor or acceptor concentration. In reality the transition occurs smoothly over the distance in which the bands are bent by about $3k_BT/q$.

Assuming only shallow dopants, the charge density of an n-type semiconductor of donor density N_D equals qN_D in the depleted region and is zero in the neutral region. For a semiconductor with both donors, with a density N_D, and acceptors, of density N_A, the net charge density is $q(N_D - N_A)$. The potential due to this charge is dropped entirely across the depleted part of the semiconductor, of width w, resulting in an electric field given by Gauss's theorem of:

$$\frac{d\mathcal{E}}{dx} = \frac{qN_D}{\epsilon_s} \tag{2.41}$$

where ϵ_s is the permittivity of the semiconductor. The boundary conditions on the field are that it equals zero for $x > w$ and $x < 0$, where x is zero at the metal-semiconductor interface and increases into the semiconductor. The electric field strength as a function of x is therefore:

$$\mathcal{E}(x) = -\frac{qN_D}{\epsilon_s}(w - x) \tag{2.42}$$

with a maximum ($\mathcal{E}_{max}$) at the interface of:

$$\mathcal{E}_{max} = -\frac{qN_D w}{\epsilon_s} = \frac{Q_D}{\epsilon_s} \tag{2.43}$$

where Q_D is the total charge per unit area of the uncompensated donors in the depletion region. As the electric field varies linearly with x between $x = 0$ and $x = w$ the average field is:

$$\mathcal{E}_{ave} = \frac{1}{2}|\mathcal{E}_{max}| = \frac{1}{2}\frac{qN_D w}{\epsilon_s} \tag{2.44}$$

Due to the fact that the potential is zero outside the depletion region the potential in the region ($\phi(x)$) may be found as follows:

$$\begin{aligned} \phi(x) &= \int_x^w \mathcal{E} dx \\ &= -\int_x^w \frac{qN_D(x)}{\epsilon_s}(w-x)dx \\ &= -\frac{qN_D}{2\epsilon_s}(w-x)^2 \end{aligned} \tag{2.45}$$

This has a quadratic dependence on x with a maximum value at $x = 0$ of:

$$\phi(x)_{max} = \frac{qN_D w^2}{2\epsilon_s} \tag{2.46}$$

which is the difference in potential across the depletion region (the diffusion potential, V_d). Combining equations (2.43) and (2.46) allows V_d to be expressed as:

$$\begin{aligned} V_d &= \frac{\epsilon_s \mathcal{E}_{max}^2}{2qN_D} \\ V_d &= \frac{Q_D^2}{2\epsilon_s q N_D} \end{aligned} \tag{2.47}$$

From equation (2.47) the differential capacitance per unit area is given by:

$$C = \frac{dQ_D}{dV_d} = \left(\frac{\epsilon_s q N_D}{2V_d}\right)^{\frac{1}{2}} = \frac{\epsilon_s}{w} \tag{2.48}$$

It is clear that the capacitance and V_d are related by the doping density, and it will be shown in section 2.8 that N_D can be determined from capacitance voltage measurements.

The energy of the bottom of the conduction band relative to the metal Fermi level is:

$$\begin{aligned} E_C(x) &= q\phi_b + q(\phi(0) - \phi(x)) \\ &= q\phi_b + \frac{q^2 N_D}{2\epsilon_s}(x^2 - 2wx) \end{aligned} \tag{2.49}$$

which is a result used in section 2.6.1.

If the depletion approximation is extended to take into account the transition zone at the edge of the depletion region, expression (2.50) follows for the depletion width, which can then be substituted into the expressions for the electric field strength and the electric potential.

$$w = \sqrt{\frac{2\epsilon_s}{qN_D}\left(V_d - \frac{k_B T}{q}\right)} \tag{2.50}$$

The differential capacitance is still given by ϵ_s/w. The depletion width is inversely proportional to N_D and therefore for a very high density ($N_D > 10^{18}$ cm^{-3}) the depletion layer will be much less than 1μm. This result is very important in the construction of ohmic contacts, see section 2.7.

The depletion width for an n-type semiconductor, for which $N_D \gg n_i$, can be expressed in terms of resistivity (equation (2.23)) as:

$$w = \sqrt{2\epsilon_s \mu_n \rho \left(V_d - \frac{k_B T}{q}\right)} \tag{2.51}$$

On the application of an external bias (V) the diffusion potential of equation (2.40) becomes:

$$V_d = \phi_b - V - V_n \tag{2.52}$$

The barriers considered so far are for the ideal case with no surface states. Surface states, however, are present for all semiconductors, and for GaAs in particular, so their effect must be included in barrier formation.

2.5.3 Surface states

Barrier heights have been found to be less sensitive to the metal work function than implied by equation (2.39), and in some cases almost completely insensitive. Surface states are responsible for this effect.

The model assumes that the metal and the semiconductor remain separated by a thin insulator, the interfacial layer $\sim 10\text{Å}$ thick, and that at the surface there is a continuous distribution of surface (interface) states. Electrons can easily tunnel through the interfacial layer and therefore the barrier is due to the band bending in the semiconductor, as before. Figure 2.9 shows a junction with such a layer under

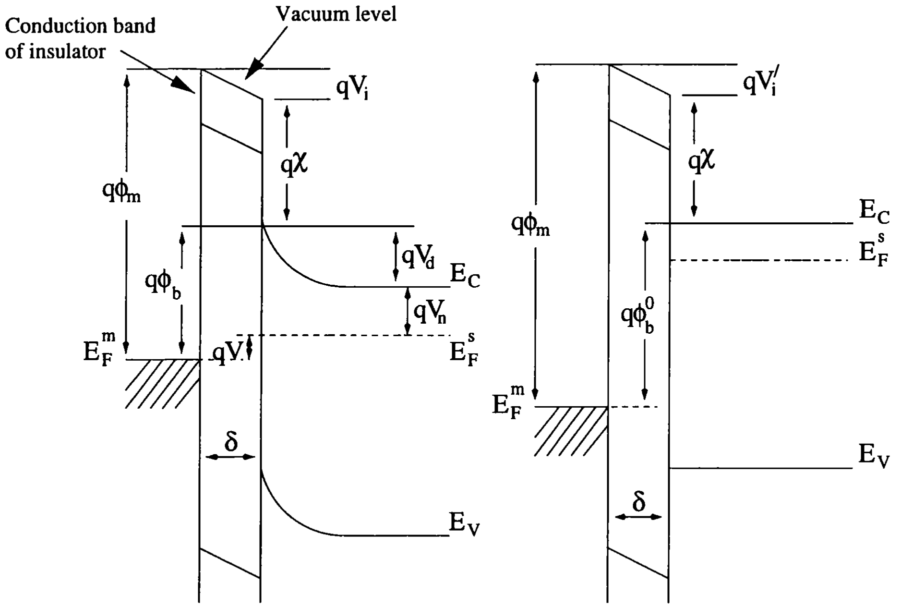

(a) Forward bias (b) Flat band

Figure 2.9: The metal-semiconductor barrier with an interfacial layer under forward bias V_f and in the flat band state.

a forward bias (V_f) and in the 'flat band' state, corresponding to a large forward bias. Listed below are the three sources of charge in the barrier and the property that governs them.

- Q_m - charge on the surface of the metal:
  determined by the electric field strength in the insulator.
- Q_D - charge due to uncompensated donor ions in the depletion region:
  depends on the depletion region width and donor density.
- Q_{ss} - charge in the surface (interface) states:
  defined by the density of surface states and their occupation probability.

As no electric field is present in the bulk of either the metal or semiconductor, charge neutrality is obtained when the sum of these three sources of charge equals zero. With no surface states the negative charge at the metal surface equals the positive charge of the uncompensated donors.

The size and sign of the surface charge will depend upon the relative values of

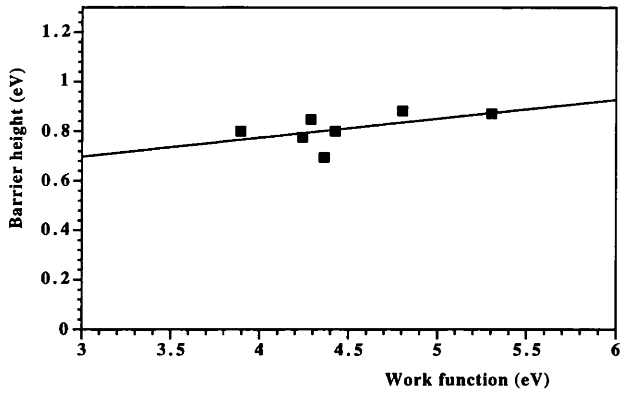

Figure 2.10: The barrier height measured on n-type GaAs as a function of metal work function[2].

the Fermi level and the surface states neutral level ($q\phi_0$) which is the energy level defined so that surface neutrality exists when the surface states up to this level are full. If the density of surface states is very large then the Fermi level and the neutral level will approach each other, that is $q\phi_0 \approx E_F$. As $q\phi_0$ is measured from the top of the valence band, the barrier height is:

$$q\phi_b \approx E_g - q\phi_0 \tag{2.53}$$

The barrier is 'pinned' by the high density of surface states and is effectively independent of the work function of the metal.

GaAs has a high density of surface states and it is expected that the barrier height will be pinned at the Fermi level in this material. The barrier height on n-type GaAs is shown as a function of work function in figure 2.10. It is clear from the figure that the barrier height has a slight dependence on the work function but less than that given by equation (2.39). The barrier height of titanium on GaAs ($q\phi_b^{Ti}$) is 0.83eV[23].

Due to the presence of surface charge the barrier height has a dependence on the applied bias and therefore the magnitude of the electric field in the barrier.

The barrier height with an arbitrary applied bias is[2]:

$$\phi_b = \phi_b^0 - \alpha\mathcal{E}_{max} = \phi_b^0 - \Delta\phi_b \tag{2.54}$$

where:

$$\alpha = \frac{\delta \epsilon_s}{\epsilon_i + q\delta D_s} \tag{2.55}$$

and ϵ_i and ϵ_s are the permittivity of the interfacial layer and semiconductor respectively, given in appendix A for GaAs. D_s is the density of interface states per unit area per eV, and ϕ_b^0 is the flat band barrier height. The 'flat band' situation is when a large forward bias is applied, causing the depletion region to disappear; that is, the bands in the semiconductor are no longer bent, see figure 2.9. The flat band barrier height is[2]:

$$\phi_b^0 = \frac{\alpha\epsilon_i}{\delta\epsilon_s}(\phi_m - \chi_s) + (1 - \frac{\alpha\epsilon_i}{\delta\epsilon_s})(E_g/q - \phi_0) \tag{2.56}$$

As D$_s$ approaches zero the flat band barrier height approaches ϕ_m - χ_s, that is the barrier height predicted for a perfect contact, as expected. For an infinite density of surface states $q\phi_b^0 \rightarrow E_g - q\phi_0$ and the barrier is 'pinned' as discussed previously. The density of surface states has been assumed to be field independent which is true up to very high values of field and thus large values of $q\Delta\phi_b$ ($>$ 0.1 eV).

The barrier height may be expressed in terms of the applied bias and doping concentration as:

$$\phi_b = \phi_b^0 - \alpha\left(\frac{2qN_D}{\epsilon_s}\right)^{\frac{1}{2}}\left(V_d - \frac{k_BT}{q}\right)^{\frac{1}{2}} \tag{2.57}$$

or

$$\phi_b = \phi_b^0 - \left[\frac{\alpha^2 2qN_D}{\epsilon_s}\left(\phi_b^0 - V - V_n - \frac{k_BT}{q}\right)\right]^{\frac{1}{2}} \tag{2.58}$$

The barrier is thus a decreasing function of external reverse bias and N_D.

With thin interfacial layers and moderate values of surface state density ($D_s <$ 1×10^{13} eV^{-1}cm^{-2}), a barrier lowering of less than 0.02 V occurs for a diffusion potential of 0.5 V and a donor density of less than 1×10^{16} cm^{-3}. Due to the larger biases applied the effect is more pronounced under reverse bias, see section 2.6.5.

2.5.4 Barrier image force lowering

The charge carrier image-force induced lowering of the barrier is now considered.

When an electron approaches a metal surface a positive charge will be induced on that metal surface, resulting in an electron at a distance x from the surface experiencing a force $q^2/4\pi\epsilon_s(2x)^2$. Because of this attractive force the electron has the negative image potential energy $-qV_I$:

$$\begin{aligned} V_I &= \frac{q}{16\pi\epsilon_s}\int_x^\infty \frac{dx}{x^2} \\ &= \frac{q}{16\pi\epsilon_s x} \end{aligned} \tag{2.59}$$

relative to that of the electron at infinity.

The image potential field must be superimposed on the potential of the Schottky barrier. The image potential field is non-negligible only near the surface, where the field due to the Schottky barrier can be considered to be constant at a value $\mathcal{E}_{max}$. Using the depletion approximation of the previous section for $\mathcal{E}_{max}$ and including the transition region at the edge of the depletion region:

$$\mathcal{E}_{max} = \left(\frac{2qN_D}{\epsilon_s}\right)^{\frac{1}{2}}\left(V_d - \frac{k_BT}{q}\right)^{\frac{1}{2}} \tag{2.60}$$

The maximum potential energy occurs at a distance x_m where the resultant electric field vanishes; that is where the image potential field and the field in the depletion region are equal and opposite, so:

$$\frac{q}{16\pi\epsilon_s x_m^2} = \mathcal{E}_{max} \tag{2.61}$$

The barrier is lowered due to the image force by an amount $\Delta\phi_{bi}$:

$$\begin{aligned} \Delta\phi_{bi} &= x_m\mathcal{E}_{max} + \frac{q}{16\pi\epsilon_s x_m} = 2x_m\mathcal{E}_{max} \\ &= \left(\frac{q\mathcal{E}_{max}}{4\pi\epsilon_s}\right)^{\frac{1}{2}} \end{aligned} \tag{2.62}$$

Substituting for $\mathcal{E}_{max}$ (equation (2.60)) and V$_d$ (equation (2.40)) gives:

$$\Delta\phi_{bi} = \left[\frac{q^3N_D}{8\pi{\epsilon_s}^3}\left(\phi_b - V - V_n - \frac{k_BT}{q}\right)\right]^{\frac{1}{4}} \tag{2.63}$$

$$x_m = \frac{1}{4}\left(\frac{q\epsilon_s}{2\pi^2{\epsilon_s}^2N_D}\right)^{\frac{1}{4}}\left(\phi_b - V - V_n - \frac{k_BT}{q}\right)^{-\frac{1}{4}} \tag{2.64}$$

The image force lowering of the barrier can now be calculated from either $\mathcal{E}_{max}$ or the external bias (V) applied to the barrier. For GaAs with $\mathcal{E}_{max} = 1 \times 10^5$ Vcm^{-1} a barrier lowering of 0.036 V is obtained.

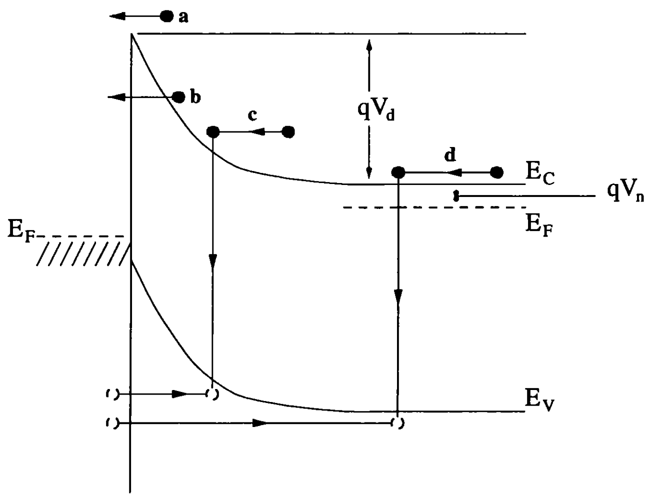

Figure 2.11: Transport processes in a forward-biased barrier.

Taking into account all the mentioned effects that affect the barrier height, the variation of barrier height as a function of metal work function for n-type GaAs shown in figure 2.10 can be explained well theoretically.

2.6 Current transport in metal-semiconductor contacts

The current transport mechanisms of both forward and reverse biased contacts will now be discussed.

Electrons may cross a forward biased metal-semiconductor barrier in the four ways shown in figure 2.11, with the inverse processes taking place in a reverse biased barrier. The four processes shown in the figure are:

- a: emission of electrons over the top of the barrier into the metal.
- b: quantum-mechanical tunnelling of an electron through the barrier.
- c: recombination in the space charge region.
- d: recombination in the neutral region - hole injection.

Schottky barriers for which the first process is dominant are referred to as ideal. This process will be described first. SI-U GaAs diodes will be shown subsequently not to exhibit an ideal behaviour at operational biases.

2.6.1 Emission over the barrier

There are two models which describe the emission of electrons over a Schottky barrier. They arise from the initial limiting assumptions on the electron transport from the semiconductor into the metal. Neither is correct and a combined theory is necessary.

The transport of electrons may be limited either by the transport processes of drift and diffusion of the carriers across the depletion region or by the emission into the metal. The first case gives rise to the diffusion theory of current transport while the latter is the thermionic emission theory of Bethe[24]. Both theories make use of hypothetical energy levels known as the quasi-Fermi levels (ζ_n and ζ_p) which are used to predict the non-equilibrium behaviour of the carriers. When ζ_n is used in place of the Fermi level in the Fermi-Dirac equation the correct concentration of electrons in the conduction band is determined.

Diffusion theory

Diffusion theory states that the boundary condition on the electron density in the conduction band at the metal interface is that the density remains unchanged with applied bias. This corresponds to the electron quasi-Fermi level in the semiconductor and the Fermi level in the metal being equal. The quasi-Fermi level must therefore drop down from the level in the depletion region to that at the barrier.

For the rectifying junction the current dependence on bias voltage from diffusion theory is:

$$J = qN_C\mu\mathcal{E}_{max}\exp\left(\frac{-\phi_B}{k_BT}\right)\left[\exp\left(\frac{qV}{k_BT}\right)-1\right] \tag{2.65}$$

a form close to that of an ideal rectifier:

$$J = J_0\left[\exp\left(\frac{qV}{k_BT}\right)-1\right] \tag{2.66}$$

with the difference that $\mathcal{E}_{max}$ has an applied bias dependence, as shown by equation (2.60), and is proportional to $V_d^{\frac{1}{2}}$. At very large values of reverse bias, the current does not saturate therefore but increases as $V^{\frac{1}{2}}$.

Thermionic-emission theory

The current limiting process in thermionic-emission theory is the rate of transfer of electrons across the interface. The current consists of two components: the flow of electrons from the semiconductor into the metal and the electron flow in the reverse direction. The effect on the transport process due to drift and diffusion is assumed to be negligible, which implies that the mobility is infinite.The quasi-Fermi level is flat in the depletion region and must coincide with the Fermi level in the bulk of the semiconductor, q$\zeta_n = E_F$.The current density from the semiconductor to the metal is:

$$\begin{aligned} J_{sm} &= \frac{v_{th} n q}{4} \\ J_{sm} &= \frac{q N_C v_{th}}{4} \exp\left(\frac{-q(\phi_b - V)}{k_B T}\right) \end{aligned} \tag{2.67}$$

for a semiconductor with an isotropic distribution of electron velocities, where v_{th} is the average electron thermal velocity.

The current due to electron flow from the metal to the semiconductor (J_{ms}) is analogous to thermionic emission from the metal with the barrier ϕ_b replacing the work function, which at present will be assumed to be bias independent. With no external bias there is no net current flow and therefore:

$$J_{ms} = J_{sm}(V = 0) = \frac{q N_C v_{th}}{4} \exp\left(\frac{-q\phi_b}{k_B T}\right) \tag{2.68}$$

With an external bias the net current flow is the difference in the currents J_{sm} and J_{ms}, thus:

$$J = \frac{q N_C v_{th}}{4} \exp\left(-\frac{q\phi_b}{k_B T}\right) \left[\exp\left(\frac{qV}{k_B T}\right) - 1\right] \tag{2.69}$$

For a Maxwellian distribution of electron velocities in the semiconductor with an effective mass m^*:

$$v_{th} = \left(\frac{8 k_B T}{\pi m^*}\right)^{\frac{1}{2}} \tag{2.70}$$

Substituting for v_{th} and N_C (equation (2.6)) into equation (2.69) gives equation (2.71) for the thermionic-emission current for a metal-semiconductor junction, where J_0 is the reverse bias saturation current, A* is the Richardson constant given in equation (2.72) and m_0 is the free electron mass.

$$\begin{aligned} J &= J_0 \left[\exp\left(\frac{qV}{k_BT}\right) - 1 \right] \\ J_0 &= A^*T^2 \exp\left(-\frac{q\phi_b}{k_BT}\right) \end{aligned} \tag{2.71}$$

$$A^* = \frac{4\pi m^* q k_B^2}{h^3} = 120 \left(\frac{m^*}{m_0}\right) \text{Acm}^{-2}\text{K}^{-2} \tag{2.72}$$

In deriving equation (2.71) the barrier height was assumed to be bias independent which resulted in an ideal rectifier. However, in practice, the barrier height is a function of bias. Even in the perfect contact the barrier will be reduced by $\Delta\phi_{bi}$ due to the image force (see section 2.5.4) and the effective barrier (ϕ_e) is:

$$\phi_e = \phi_b - \Delta\phi_{bi} \tag{2.73}$$

Section (2.5.3) showed that for practical devices with an interfacial layer ϕ_b is actually bias dependent. The effective barrier height is therefore a function of bias for two reasons which will alter the current voltage characteristic found above.

If the variation of effective barrier height with bias is assumed to be constant then the barrier may be expressed as:

$$\phi_e = \phi_{b0} - \Delta\phi_{bi0} + \beta V \tag{2.74}$$

where the 0 represents the zero bias values. As the barrier increases with increasing forward bias β is a positive constant. The expression for the current given by equation (2.71) may now be written as:

$$\begin{aligned} J &= A^*T^2 \exp\left(-\frac{q(\phi_{b0} - \Delta\phi_{bi0} + \beta V)}{k_BT}\right) \left[\exp\left(\frac{qV}{k_BT}\right) - 1 \right] \\ J &= J_0 \exp\left(-\frac{\beta qV}{k_BT}\right) \left[\exp\left(\frac{qV}{k_BT}\right) - 1 \right] \end{aligned} \tag{2.75}$$

where

$$J_0 = A^*T^2 \exp\left(\frac{-q(\phi_{b0} - \Delta\phi_{bi0})}{k_BT}\right) \tag{2.76}$$

The junction is no longer an ideal rectifier. The ideality factor (n) given by:

$$\frac{1}{n} = 1 - \beta = 1 - \frac{\partial\phi_e}{\partial V} \tag{2.77}$$

may be introduced to re-express the current as:

$$J = J_0 \exp\left(\frac{qV}{nk_BT}\right)\left[1 - \exp\left(\frac{-qV}{k_BT}\right)\right] \tag{2.78}$$

For an applied bias $V > 3k_BT/q$ this expression simplifies to:

$$J = J_0 \left[\exp\left(\frac{qV}{nk_BT}\right) - 1\right] \tag{2.79}$$

Experimentally the value of the ideality factor may be obtained by plotting $\ln(J/[1 - \exp(-qV/k_BT)])$ against V. The gradient of the curve is $\frac{q}{nk_BT}$. It should be noted the n is normally a function of bias and the curve will not be a straight line. For an ideal barrier n is close to unity and deviations from this are a measure of the difference between the experimental junction and the ideal situation.

Combined theory

The two theories may be combined by placing the thermionic and diffusion currents in series. A quasi-Fermi level at the metal-semiconductor interface is defined that results in both currents being equal and a thermionic recombination velocity (v_r) at the top of the barrier is introduced, defined using the net electron current into the metal (J), as:

$$J = v_r(n - n_0) \tag{2.80}$$

where n_0 is the equilibrium electron density at the top of the barrier at zero bias. The first term represents the current from the semiconductor into the metal while the latter is that into the semiconductor. For the thermionic-emission theory, where all the electrons that pass over the maximum of the barrier are said to enter the metal, $v_r = v_{th}/4$.

The current is given by:

$$J = \frac{qN_Cv_r}{1 + \frac{v_r}{v_d}} \exp\left(\frac{-q\phi_b}{k_BT}\right)\left[\exp\left(\frac{qV}{k_BT}\right) - 1\right] \tag{2.81}$$

where v_d is the effective diffusion velocity associated with the transport of electrons from the edge of the depletion layer ($x = w$) to the potential maximum. Making the approximation that the electric field is constant and equal to $\mathcal{E}_{max}$ implies $\mathrm{v}_d = \mu\mathcal{E}_{max}$.

If $v_d >> v_r$ the thermionic current dominates, that is to say that the limiting current is that of the emission of the electrons over the barrier into the metal. If $v_d << v_r$ then the limiting factor is the drift and diffusion of the electrons and diffusion theory now applies.

So far it has been assumed that all the electrons which cross the top of the barrier will enter the metal and not return. However, the electrons can be scattered back by a process involving phonon emission or they may be quantum mechanically reflected by the barrier. Including these effects leads to the inclusion of two probability factors. The first (f_p) is the probability of the electron reaching the metal without being scattered back into the semiconductor. A field dependence exists for f_p as the reflections occur in the region between $x = 0$ and $x = x_m$. As the field increases x_m is reduced and f_p asymptotically approaches 1. In GaAs $f_p = 0.85$ for T = 300K and $\mathcal{E}_{max} = 4 \times 10^4$ Vcm^{-1}. The second probability factor (f_q) is related to quantum mechanical reflections and tunnelling through the top of the barrier. This is field and temperature dependent due to the temperature dependence of the electron energy. For high fields $f_q > 1$ due to tunnelling effects, at low fields f_q approaches 0.6 in GaAs at room temperature[2].

The complete expression for the current, taking into account these effects, is:

$$\begin{aligned} J &= J_s\left[\exp\left(\frac{qV}{k_BT}\right) - 1\right] \\ J_s &= A^{**}T^2\exp\left(\frac{-q\phi_b}{k_BT}\right) \end{aligned} \tag{2.82}$$

where

$$A^{**} = \frac{f_pf_qA^*}{1+\frac{f_pf_qv_r}{v_d}} \tag{2.83}$$

which does in fact have a bias dependence. This is masked, however, by the image force lowering of the barrier.

Sze states [1] that for most Ge, Si and GaAs Schottky barrier diodes the current is due to the thermionic emission of majority carriers, that is the diffusion current does not play an important role in the current characteristics.

2.6.2 Tunnelling current

For semiconductors that are either heavily doped or operated at low temperatures the current can become dominated by electrons that quantum mechanically tunnel through the barrier. Two additional sources of current are possible: field emission and thermionic-field emission currents.

Field-emission is the current that results from electrons with energies close to the Fermi level of the semiconductor tunnelling through the barrier. As the temperature is raised the electrons are excited to higher energies and therefore see a thinner and lower barrier with the result that the tunnelling probability increases. The actual number of electrons with a given energy decreases with increasing energy and thus there is a maximum current for electrons at an energy E_m above the conduction band. This is thermionic-field emission. As the temperature is raised still further the number of electrons that have sufficient energy to go over the top of the barrier increases and thus pure thermionic emission results as the contribution from tunnelling becomes negligible.

At a temperature of 300K the contribution to the current from tunnelling for an n-type GaAs barrier is only significant for doping concentrations above 10^{17} cm^{-3} and is seen experimentally as the departure of the ideality factor from unity[2].

If the tunnelling component dominates then the current is given by[2]:

$$J_t \sim \exp\left(\frac{-q\phi_b}{E_{00}}\right) \tag{2.84}$$

where

$$E_{00} = \frac{q\hbar}{2}\sqrt{\left(\frac{N_D}{\epsilon_s m^*}\right)} \tag{2.85}$$

It can be seen that the tunnelling current will increase exponentially with $\sqrt{N_D}$.

Field emission becomes important for ohmic contacts which are usually fabricated as a Schottky barrier upon a highly doped layer.

2.6.3 Recombination current

The third source of current shown in figure 2.11 is the recombination current. Recombination has been discussed in section 2.4. The theory of recombination current is the same here as that for p-n junction diodes where the product np maybe expressed as:

$$np = n_i^2 \exp\left(\frac{q(\zeta_p - \zeta_n)}{k_B T}\right) \tag{2.86}$$

for a forward biased diode, where ζ_n and ζ_p are the quasi-Fermi levels for electrons and holes respectively. Substitution into the recombination rate derived from Shockley-Reed-Hall statistics, given in equation (2.31), results in an expression for the recombination rate under forward bias which implies that the maximum rate occurs when the trap is at the energy at the middle of the band gap. Integration of the recombination rate with respect to x over the depletion region results in the recombination current:

$$J_r = J_{r0}\left[\exp\left(\frac{qV}{2k_B T}\right) - 1\right] \tag{2.87}$$

where:

$$J_{r0} = \frac{q n_i w}{2\tau_r} \tag{2.88}$$

and w is the thickness of the space charge region, n_i is the intrinsic carrier concentration, which is proportional to $\exp(\frac{-E_g}{2k_B T})$, and τ_r is the lifetime in the depletion region. The total current is simply given as the sum of the thermionic-emission and the recombination currents:

$$J = J_{te} + J_r = J_{t0}\left[\exp\left(\frac{qV}{k_B T}\right) - 1\right] + J_{r0}\left[\exp\left(\frac{qV}{2k_B T}\right) - 1\right] \tag{2.89}$$

For bias voltages above $4k_B T/q$ the ratio of thermionic and recombination current becomes:

$$\frac{J_{te}}{J_r} \propto \tau_r \exp\left(\frac{E_g + qV - 2q\phi_b}{2k_B T}\right) \tag{2.90}$$

Therefore for increasing values of τ_r, V and E_g the contribution from the recombination current is reduced, while for increasing barrier height it is increased. The current becomes important for GaAs diodes because: the lifetimes are short, the barrier heights are all reasonably large due to surface state pinning, and the high concentration of mid gap energy states.The ideality factor lies between 1 and 2 with values closer to 2 implying a larger contribution from the recombination current.

2.6.4 Hole injection

If the barrier height on an n-type semiconductor is larger than half the band gap, which it often is, the barrier to hole injection is small enough to allow a high density of holes to build up in the region of the semiconductor adjacent to the metal and here the semiconductor becomes p-type. The holes may now diffuse into the neutral region of the semiconductor.

If the hole quasi-Fermi level is assumed to be flat in the depletion region and equal to the Fermi level in the metal then the hole transport to the space charge region via drift and diffusion in the neutral n-type region may be expressed with the same equations that apply for pn junctions. Consider a junction with a depletion region of depth x_n and a neutral region which extends from $x = x_n$ to $x = x_n + \mathrm{L}$, where x is zero at the metal interface and increases into the semiconductor. The hole current is:

$$J_p = qv_T p_n \tag{2.91}$$

where v_T is a transport velocity which equals the ratio of the diffusion constant and the diffusion length ($= \mathrm{D}_p/\mathrm{L}_p$). The diffusion constant was given previously by equation (2.24), while the diffusion length is the square root of the diffusion constant multiplied by the hole lifetime in the neutral region. Using this expression for the velocity and the expression:

$$p - p_0 = p_{n0}\left[\exp\left(\frac{qV}{k_BT}\right) - 1\right]\exp\left(\frac{-(x - x_n)}{L_p}\right) \tag{2.92}$$

for the hole concentration derived for a pn junction with respect to x, where the 0 denotes the equilibrium value, the current:

$$J_p = \frac{qD_p p_0}{L_p}\left[\exp\left(\frac{qV}{k_BT}\right) - 1\right] \text{ for L} << \mathrm{L}_p \tag{2.93}$$

is obtained. For the low injection regime the hole injection ratio is:

$$\gamma_n = \frac{J_p}{J_p + J_n} \sim \frac{J_p}{J_n} = \frac{qn_i^2 D_p}{N_D L_p A^{**} T^2 \exp\left(\frac{-q\phi_b}{k_BT}\right)} \tag{2.94}$$

where the electron current (J_n) is that due to thermionic emission.

It can be seen that the injection ratio increases with increasing barrier height (ϕ_b) due to the reduction in the electron current. A reduction in γ_n occurs with increasing donor density (corresponding to low resistivity) because this causes a fall in the hole current and with smaller values of n_i (larger band gap). All particle detectors are made from high resistivity materials which will result in significant hole injection under forward bias. The reasonably high barrier heights in GaAs devices also contribute to a significant hole injection current.

At high bias, and thus high field in the neutral region, the drift component of the hole transport becomes significant. The high field limit of the injection ratio is proportional to the electron current and therefore $\gamma_n \propto J$ as $J \approx J_n$. The value of γ_n saturates at very high fields when the electron and hole densities in the neutral region become approximately equal.

2.6.5 Reverse bias characteristics

Under reverse bias the current characteristics are defined by the reverse of the first three processes discussed for the forward bias regime. Thermionic-emission theory states that the reverse current should saturate with a value of J_s given by equation (2.82), that is:

$$J_s = A^{**}T^2 \exp\left(\frac{-q\phi_b}{k_BT}\right) \tag{2.95}$$

However there are several reasons why this does not occur in practice.

Field dependence of the barrier height

It has been shown that the barrier height often depends upon the applied voltage which will cause the reverse current not to saturate. All mechanisms that affect the barrier height result in a lowering of the barrier with increasing electric field and therefore increasing applied reverse bias. An increase in current results.

Image force lowering of the barrier has been discussed in section 2.5.4 where it was shown that:

$$\Delta\phi_{bi} = \left[\frac{q^3 N_D}{8\pi^2{\epsilon_s}^3}\left(\phi_b - V - V_n - \frac{k_BT}{q}\right)\right]^{\frac{1}{4}} \tag{2.96}$$

Under reverse bias V is replaced by $-V_r$ that is $\Delta\phi_{bi}$ increases with V_r. For large values of reverse bias:

$$\Delta\phi_{bi} \propto V_r^{\frac{1}{4}} \tag{2.97}$$

A graph of $\ln J$ against $V_r^{\frac{1}{4}}$ will give a straight line which intercepts the $\ln J$ axis at $\ln J_0$. This effect is rarely sufficient to explain the increase in current.

The presence of an interfacial layer will also cause a lowering of the barrier height. In reverse bias the reduction in barrier height is:

$$\Delta\phi_{bi} = \alpha\mathcal{E}_{max} \tag{2.98}$$

where α is defined in equation (2.55) of section 2.5.3. Because of this reduction in the barrier the reverse current for a diode with a fairly thick interfacial layer may actually be greater than one with a very thin layer. The reason for this is that although the electrons must now tunnel through a thicker layer, which is still a very thin barrier, the reduction in the Schottky barrier over-compensates and allows a larger current to flow.

The presence of an interfacial layer is a common cause of 'soft' breakdown in the reverse current characteristics of a Schottky diode, especially if it has been made under poor vacuum or from a semiconductor with a contaminated surface.

The effect of tunnelling

The current due to tunnelling in a reverse bias junction may be observed at lower doping densities than generally required for the forward bias case as much larger reverse biases are applied. At moderately large reverse bias the potential barrier becomes thin and allows tunnelling of electrons from the metal into the semiconductor. Again either field or thermionic-field emission may take place. At a constant reverse bias, 3V for example, and temperature, the current will depart from pure thermionic emission with increasing doping density. For a silicon barrier departure occurs for $N_D > 1 \times 10^{17}$ cm^{-3} in reverse bias. At still higher doping concentrations field emission occurs. For silicon barriers room temperature field emission occurs when $N_D > 5 \times 10^{18}$ cm^{-3}. The tunnelling current is also a common cause of 'soft' breakdown in such diodes.

Edge effects are also important with respect to tunnelling currents. At the edge of the metal contact the field lines have a very high concentration which implies a high field strength. This causes the barrier width to be reduced thus increasing tunnelling. The image force lowering of the Schottky barrier is also increased. Edge effects may be reduced with careful fabrication techniques and with the addition of a guard ring around the diode the effect may be almost totally removed. The separation between the guard and the diode must be similar to or less than the thickness of the depletion region for this to be effective, and thus such a guard structure is limited to high resistivity materials which have a large depletion region. If edge effects are removed the breakdown is more likely to be that due to thermionic-field emission or impact ionisation, depending upon the doping density.

Generation in the depletion region

This effect is significant if the image force and the tunnelling currents are low (usually for low N_D and high barrier heights). Generation in the depletion region is the opposite process to the forward bias recombination of section 2.6.3. The current (J_g) is:

$$J_g = \frac{qn_i w}{2\tau_r} \tag{2.99}$$

where τ_r is the lifetime in the space charge region. Generation current is a function of applied bias due to the bias dependence of the depletion width, that is:

$$J_g \propto (V_{d0} + V_r)^{\frac{1}{2}} \tag{2.100}$$

where V_{d0} is the diffusion potential for zero external bias.

Due to the temperature dependence of n_i and τ_r, generation current has a temperature dependence of:

$$\begin{aligned} J_g &\propto \frac{n_i}{\tau_r} \\ &\propto v_{th}\sqrt{N_C N_V}\exp\left(-\frac{E_A}{k_B T}\right) \\ &\propto T^{\frac{2}{3}}T^{\frac{1}{2}}\exp\left(-\frac{E_A}{k_B T}\right) \end{aligned} \tag{2.101}$$

where E_A is the activation energy for the electron density which is $E_g/2$ for intrinsic material.

The effect is of greater significance for high ϕ_b and low lifetime materials, such a GaAs. At low temperatures generation current is more pronounced due to its lower activation energy than that of thermionic-emission. This effect is a common cause of the lack of reverse current saturation seen in many GaAs Schottky diodes[2].

2.7 The ohmic contact

An ohmic contact is defined as a metal-semiconductor contact which has a negligible contact resistance with respect to the bulk resistance of the semiconductor. The presence of the contact should not affect the device performance and should be able to provide the required current while the voltage drop across the junction is not significant relative to that across the active region of the device, the space charge region of a Schottky junction. The contact must also be non-injecting for minority carriers, that is to prohibit the passage of carriers so that the recombination current is negligible. The figure of merit for an ohmic contact is its specific contact resistance (R_c) which is defined as:

$$R_c = \left(\frac{\partial J}{\partial V}\right)^{-1}_{V=0} \tag{2.102}$$

for zero applied bias.

For semiconductors with low doping concentrations the current is dominated by thermionic emission, (of equation (2.82)). This implies that the specific contact resistance at V = 0 has the form:

$$R_c = \frac{k_B}{qA^{**}T} \exp\left(\frac{q\phi_b}{k_B T}\right) \tag{2.103}$$

and therefore R_c depends upon the barrier height. The lower the barrier height the lower the resistance. If the barrier height is given by equation (2.39) then an ohmic contact will be formed, on n-type material, if a metal with a lower work function than the semiconductor is used, as discussed in section 2.5.1. For most semiconductors there are few metals with this quality. If the metal work function is slightly larger than that of the semiconductor, however, then a rectifying contact with a low barrier height will be formed which may serve as an ohmic contact for most purposes.

If the semiconductor has a high doping concentration then the current is that of field emission due to tunnelling. Using equations (2.84) and (2.85) for the current gives a specific resistance at V = 0 of:

$$R_c \sim \exp\left(\frac{q\phi_b}{E_{00}}\right) = \exp\left[\frac{2\sqrt{\epsilon_s m^*}}{\hbar}\left(\frac{\phi_b}{\sqrt{N_D}}\right)\right] \tag{2.104}$$

Now the resistance decreases with increasing N_D and decreasing ϕ_b. Ohmic contacts may therefore be realised by depositing the metal onto a thin layer of heavily doped material on top of the semiconductor. This causes field emission to dominate and thus produce a low specific resistance. For n-type materials an n^+ layer is required which can be obtained either by diffusion or ion implantation into the semiconductor followed by the deposition of the metal or by metal deposition followed by heat treatment. The heat treatment of the deposited metal alloy causes a component of the alloy to dope the semiconductor. For GaAs germanium is used in the alloy to form an n^+ layer on n-type material. Chapter 3 describes the recipe used for Glasgow ohmic contacts.

2.8 Capacitance of a reverse biased Schottky barrier

Section 2.5.2 showed that a Schottky barrier has a differential capacitance per unit area which is related to the semiconductor donor density (equation (2.48)) and the barrier height, through the diffusion potential (equation (2.52)).

The situation with no interfacial layer will be considered for an n-type semiconductor under reverse bias V. If the reverse bias is increased by a small increment ΔV then the depletion region extends further into the bulk of the semiconductor by an amount Δw. The extension is caused by the recession of electrons into the bulk leaving uncompensated donors, a fixed charge which results in the junction having a capacitance. An equivalent circuit for the junction is therefore a capacitor in parallel with a resistor to represent the source of the reverse bias current.

For an ideal device the back contact is a good ohmic contact so that all the applied bias is dropped across the junction. The equivalent circuit for the device has a resistance to account for the bulk and ohmic contact resistances in series with the junction circuit. To make accurate barrier measurements the junction current or the series resistance must be low so that a negligible voltage is dropped across the bulk, that is so that the voltage across the junction equals the external bias.

Figure 2.12 shows a Schottky barrier under reverse bias. Listed below are the three sources of charge in the barrier:

- Q_D - positive - due to uncompensated donors.
- Q_h - positive - due to extra holes in the valence band at the junction.
- Q_m - negative - due to electrons on the metal surface.

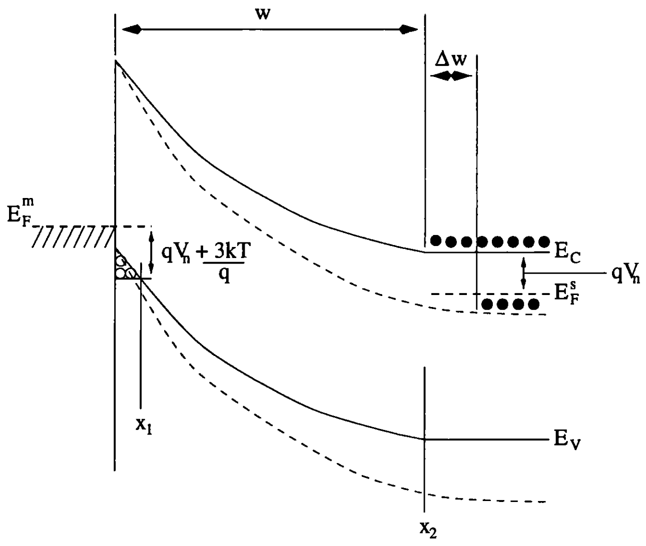

Figure 2.12: A Schottky barrier under reverse bias.

The extra holes in the valence band are present if the barrier is large. That is if the bands are bent to the extent that $E_F^m - E_V < qV_n + 3k_BT$. This in known as the inversion region as the material becomes p-type. Increasing the reverse bias will cause this hole charge to decrease.

For an increasing reverse bias there are three sources of current in the junction. The displacement current due to the increasing electric field in the depletion region ($J_d = \epsilon_s d\mathcal{E}/dt$) and a conduction current made up of two parts, that from the drift and diffusion of carriers injected over the barrier (J_1) and that due to the flow of carriers out of the space charge region as its width increases (J_2). J_d and J_2 give rise to the junction capacitance while J_1 results in a parallel resistance that represents the reverse current.

For depths in the junction between the inversion layer (x_1) and the edge of the depletion layer (x_2) the free carrier density is negligible and thus the charge density is that due to the donors. For an increase in reverse bias the depletion region extends but no electrons or holes enter or leave the region $\mathrm{x} = \mathrm{x}_1 \rightarrow \mathrm{x}_2$ due to the extension, so the current J_2 in this region must be zero. So the displacement current must equal the capacitance current, which may be expressed as:

$$J_{cap} = C\frac{dV}{dt} \tag{2.105}$$

So for an external bias (V) consisting of an DC component V_0 and an AC component

V_t:

$$J_d = J_{cap} \rightarrow \epsilon_s \frac{d\mathcal{E}}{dt} = C\frac{dV_t}{dt} \tag{2.106}$$

As the electric field is a function of the bias:

$$\frac{d\mathcal{E}}{dt} = \frac{d\mathcal{E}}{dV_t} \times \frac{dV_t}{dt} \tag{2.107}$$

the capacitance is:

$$C = \epsilon_s \frac{d\mathcal{E}}{dV_t} \tag{2.108}$$

To find the capacitance the electric field inside the depletion region must be found. Gauss's theorem applied over a closed surface which crosses the depletion region as two parallel planes situated between x_1 and x_2 and at $x >> x_2$, where there is no net charge, can be used to relate the change in electric field to the change in number of electrons at the edge of the depletion region due to a change in bias. As electron removal represents an increase in uncompensated donors then:

$$\epsilon_s \Delta\mathcal{E} = Q_D \quad \text{or} \quad \epsilon_s \frac{d\mathcal{E}}{dV_t} = \frac{dQ_d}{dV_t} \tag{2.109}$$

so that:

$$C = \frac{dQ_D}{dV_t} \tag{2.110}$$

The capacitance is therefore due only to the uncompensated donors.

If the positive charge at the metal-semiconductor interface is ignored, $x_1 = 0$, and the electric field at the interface is that due to the uncompensated donors only, then from equation (2.43), Q_D equals:

$$Q_D = \epsilon_s \mathcal{E}_{max} = \sqrt{2q\epsilon_s N_D}\left(V_d - \frac{k_B T}{q}\right)^{\frac{1}{2}} \tag{2.111}$$

with the diffusion potential for a reverse bias V equal to $V_d = V_{d0} + V$. From equation (2.110) the capacitance is therefore:

$$C = \left(\frac{q\epsilon_s N_D}{2}\right)^{\frac{1}{2}} \left(V_{d0} + V - \frac{k_B T}{q}\right)^{-\frac{1}{2}} \tag{2.112}$$

From the expression for the depletion width (equation (2.50)) the capacitance is simply equal to ϵ_s / w. It is evident that a plot of $1/C^2$ against V will give a straight line with a slope of magnitude $2/(q\epsilon_s N_D)$. From this the donor density can be found by measuring the capacitance of a metal-semiconductor junction.

If the effect of the holes at the metal surface can not be ignored ($\phi_b > E_g - V_n$) then the maximum electric field at the interface is due to the holes and the uncompensated donors and graphing $1/C^2$ against V no longer results in a straight line.

2.9 Extension to deep traps with reference to GaAs

An impurity present in a semiconductor may form either a shallow dopant, such as carbon in GaAs which can act as either a donor or an acceptor, be electrically inactive (for example boron), or give rise to a deep level. A deep level is one which is not readily ionised at room temperature and thus deep donors may contain an electron at room temperature and remain electrically neutral. Fermi-Dirac statistics still govern the fraction of ionised deep levels and therefore calculations of Fermi-level position may be performed, as discussed in section 2.2.2. The origin of the semi-insulating properties of GaAs will be explained with the use of these ideas in section 2.9.1.

As well as through the addition of impurities, deep levels may be created by lattice defects, an example of which is the EL2 level in GaAs. The exact origin of this defect has been the subject of extensive investigation over the last three decades since its existence was postulated in 1961[25]. Originally it was supposed that the EL2 level was due to oxygen present at the growth stage of the GaAs material. Studies have shown that this is not the case, however, and today the generally accepted view is that the mid-gap level is an arsenic atom on a gallium site (an arsenic antisite defect) with the possibility of an associated mobile arsenic atom between the normal lattice sites (an arsenic interstitial atom). The presence of deep levels in GaAs depends upon the purity of the original growth elements (gallium and arsenic), the growth process which can introduce dopants from the apparatus itself, and the relative ratio of gallium to arsenic in the growth mixture, as well as the addition of any intended dopants such as indium or chromium.

The concentration of EL2 depends upon the conditions under which the material

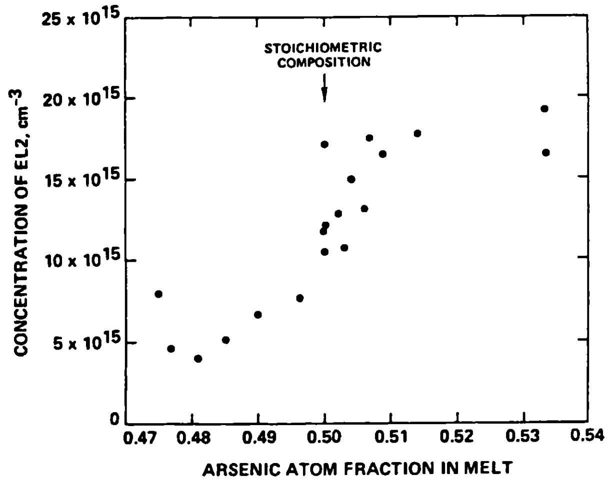

Figure 2.13: The concentration of EL2 as deduced from optical absorption measurement, versus the estimated arsenic atom fraction in an LEC melt[3].

was formed and some of the processes that the ingot undergoes after manufacture such as thermal annealing or an application of external stress. The EL2 concentration increases with increasing arsenic fraction in the starting melt. This is illustrated by Figure 2.13 which shows the dependence of the EL2 concentration on the arsenic atom fraction in a liquid encapsulated Czrochalski (LEC) melt (the most common method used to fabricate SI-U GaAs wafers). As an ingot is grown it has even been observed that the EL2 concentration falls along the ingot length from the seed end, a phenomenon explained by a reduction in the arsenic fraction in the melt. Therefore it is possible to regulate the concentration of the EL2 defect, which is the main deep defect in SI-U GaAs, via careful control of the ratio of gallium and arsenic atoms in the original melt.

2.9.1 Compensation in semi-insulating undoped GaAs

The semi-insulating nature of the GaAs material is obtained through the over-compensation of the shallow dopants in the material with deep EL2 levels. The shallow dopants in LEC material are carbon, which acts as an acceptor, and silicon, which behaves as a donor. The EL2 level is a deep donor, and in fact has the property of being a double donor which means that it has three charge states; neutral when it is occupied by electrons, plus one, and plus two when it has donated both its electrons. These three charge states give rise to two electrical energy levels of the

Impurity/ Defect	Energy above the valence band (eV)	Energy below the conduction band (eV)
Carbon	0.026	
Silicon		0.006
EL2(A)		0.75
EL2(B)	0.52	

Table 2.1: Ionisation energies of various levels in GaAs.

EL2 centre, one almost at mid-gap (EL2A) and one, (EL2B), 0.15 eV lower than this. The energy of these levels and those of the shallow dopants are given in table 2.1. Emission and capture rates of the EL2 defect under different conditions are discussed in section 2.9.3.

A high resistivity substrate is desirable for semiconductor detectors as discussed previously. Pure intrinsic GaAs will give a resistivity of 3.9×10^8 Ωcm which can be calculated using equation (2.21) and the value of n_i given in appendix A. Such a material can not be grown due to contamination from impurities and the presence of the EL2 level. Over-compensation by EL2 is the technique adopted to realise a very low free carrier concentration and thus very high values of resistivity, typically of order 10^8 Ωcm and above.

Over-compensation results in such a low carrier concentration by transferring all the free carriers that are present from the net shallow acceptors, (carbon dopants are usually present in excess to silicon), to deep levels where the probability of thermal excitation is low. The carrier concentration and position of the Fermi-level can be calculated for SI-U GaAs from the application of charge conservation, which gives:

$$n + N_{Car}^{-} = p + 2N_{EL2}^{++} + N_{EL2}^{+} + N_{Si}^{+} \tag{2.113}$$

where the subscripts Car and Si represent carbon and silicon respectively and the 2 is present due to the 2+ charge on the associated EL2 charge state.

The values for the free carrier concentrations follow from equations (2.10) and (2.11), while the concentrations of the ionised carbon and silicon atoms follow from equations (2.14) and (2.15). For a Fermi-level far from either the conduction or valence band the concentration of ionised dopants will be that of the atoms, that is full ionisation of the shallow dopants can be assumed. The additional charge due to the EL2 level when the single and double donor states are taken into account is quite complex and can be found in [26]. Simplification occurs due to the fact that the Fermi level in SI-U GaAs is close to the mid gap which implies that the concentration of N_{EL2}^{++} is small. The concentration of the single donor state is:

$$N_{EL2}^{+} = N_{EL2}\left[1 - \frac{1}{1 + \frac{1}{2}\exp\left(\frac{E_2 - E_F}{k_B T}\right)}\right] \tag{2.114}$$

where E_2 is the transition energy from the N_{EL2}^{0} to the N_{EL2}^{+} state.

From these equations the Fermi-level at a temperature of 300 K can be shown to equal 0.74 eV for typical dopant concentrations of $N_{EL2} = 10^{16}$ cm^{-3}, $N_{Car} = 2 \times 10^{15}$ cm^{-3} and $N_{Si} = 5 \times 10^{14}$ cm^{-3} and the free electron concentration with this Fermi-level is between 10^6 and 10^7 cm^{-3}. The semi-insulating nature of the material has thus been achieved and will be maintained as long as $N_{Si} < N_{Car} < N_{EL2}$. This is achieved by adjusting the amount of EL2 formed in the material via the control of the arsenic fraction as described above.

2.9.2 Trap occupation

The occupancy of a trap as determined by the relative position of the trap energy level and Fermi level are explored here.

Consider an n-type semiconductor with a single deep level with energy E_t. The trap is a donor and therefore neutral if occupied by a trapped electron and positive if empty; EL2 is such a trap. The assumption will be made that the trap is empty if E_t is above the Fermi level, and full if below. With an external bias applied to the system the Fermi level in the semiconductor splits into two quasi-Fermi levels, one for electrons (ζ_n) and one for holes (ζ_p). It can be assumed that under forward bias both the quasi-Fermi levels are horizontal and given by:

$$\begin{aligned} \zeta_n &= E_F^s \\ \zeta_p &= E_F^m \end{aligned} \tag{2.115}$$

where E_F^s and E_F^m are the Fermi-levels in the bulk of the semiconductor and the metal, respectively. For a reverse biased device the identities of equation (2.115) are approximately valid if the rising of the electron quasi-Fermi level at the barrier is ignored. The trap occupation is derived with Shockley-Reed-Hall statistics to give the probability of a trap being occupied by an electron (F_e) as:

$$F_e = \frac{\sigma_n n v_{th} + e_p}{\sigma_n n v_{th} + e_n + \sigma_p n v_{th} + e_p} \tag{2.116}$$

where $e_{n,p}$ is the trap electron/hole emission probability. The other terms are defined in section 2.4. The emission probabilities are related to the capture cross-sections by:

$$\begin{aligned} e_n &= \sigma_n v_{th} n_i \exp\left(\frac{E_t - E_i}{k_B T}\right) \\ e_p &= \sigma_p v_{th} n_i \exp\left(\frac{E_i - E_t}{k_B T}\right) \end{aligned} \tag{2.117}$$

where E_i is the intrinsic Fermi level; these equations are similar to equation (2.123).

It is convenient to introduce another energy level (E_1) given by:

$$E_1 = E_i + \frac{k_B T}{2q} \ln\left(\frac{\sigma_p}{\sigma_n}\right) \tag{2.118}$$

which has the property that if the trap energy is above this level then electron emission will dominate while if it is below hole emission is of greater significance. From the relative positions of the quasi-Fermi levels, E_i and E_1 the six inequalities listed below follow.

$$\begin{aligned} E_t > E_1 &\;\rightarrow\; e_n > e_p \\ E_t < \zeta_n &\;\rightarrow\; \sigma_n n v_{th} > e_n \\ E_t + \zeta_n > 2E_1 &\;\rightarrow\; \sigma_n n v_{th} > e_p \\ E_t > \zeta_p &\;\rightarrow\; \sigma_p p v_{th} > e_p \\ E_t + \zeta_p < 2E_1 &\;\rightarrow\; \sigma_p p v_{th} > e_n \\ \zeta_n + \zeta_p > 2E_1 &\;\rightarrow\; \sigma_n n > \sigma_p p \end{aligned} \tag{2.119}$$

It must be noted that, as the energies that define the emission rates and cross-sections appear in exponentials, a difference of more than $2k_BT/q$ in energy results in an order of magnitude difference in the two quantities. For example if $E_t = E_1 + 2k_BT/q$ then e_p is an order of magnitude less than e_n.

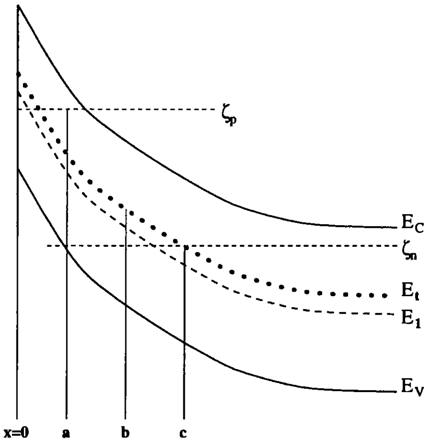

Figure 2.14: The band diagram of a Schottky junction under reverse bias with a deep trap where $E_t > E_1$.

Here we consider only the situation where $E_t > E_1$, as shown in figure 2.14 for a reverse bias V, thus $e_n > e_p$ throughout the depletion region.

At $x = a$, on the figure, the energy level E_1 lies half way between ζ_n and ζ_p and for $x > a$ the last inequality of (2.119) ($\sigma_n n > \sigma_p p$) applies. The capture of electrons by traps in this region is therefore more likely. At an x deeper into the material (x = b), E_1 is midway between E_t and ζ_n and so for:

$$x \geq c$$

$$E_t + \zeta_n > 2E_1 \quad \rightarrow \quad \sigma_n n v_{th} > e_p \tag{2.120}$$

The expression of equation (2.116) for the probability of a trap being occupied by an electron has simplified to:

$$F_e = \frac{\sigma_n n v_{th}}{\sigma_n n v_{th} + e_n} \tag{2.121}$$

which is the form of a Fermi-Dirac distribution function with a Fermi level at the electron quasi-Fermi level. That is to say the trap population is defined by the position of the electron quasi-Fermi level with respect to the level of the trap. When $E_t < \zeta_n$, which occurs for $x > c$, all the traps are full and thus have no charge. For values of x less than c the probability function falls to zero at $x = b$ because $E_t + \zeta_n > 2E_1$ is no longer true and therefore $\sigma_n n v_{th} < e_p$ so:

$$F_e \rightarrow \frac{e_p}{e_n} \sim 0 \tag{2.122}$$

2.9.3 Cross-sections and emission rates

A deep defect is characterised by its emission and capture cross-sections. Due to the nature of the EL2 trap the electron thermal-emission rate and capture cross-section are most important. The emission rate (e_n) has a temperature dependence given by[6]:

$$e_n = T^2 \alpha_n \sigma_{na} \exp\left(-\frac{E_{na}}{k_B T}\right) \tag{2.123}$$

where E_{na} ($= E_{i0} + E_b$) is the activation energy, E_{i0} is the extrapolation of the ionisation energy of the level to $T = 0$ K and E_b is the activation energy of the electron capture cross-section (σ_n). The constant σ_{na} is the emission section of the trap and depends upon the electron capture cross-section extrapolated to $T = \infty$ ($\sigma_{n\infty}$) and the rate of change of E_i with temperature. T is the temperature and α_n is a constant. Substituting the values given in table 2.2 gives a value of 0.045 s^{-1} for the emission constant at 300 K.

The electron capture cross-section has a temperature dependence given by[7]:

$$\sigma_n = \sigma_{n\infty} \exp\left(-\frac{E_{\sigma_n}}{k_B T}\right) + \sigma_{n0} \tag{2.124}$$

for temperatures between 50 K and 273 K. The term σ_{n0} is only significant for temperatures below 100 K. The constants are again given in table 2.2 and result in a value of 4.7×10^{-16} cm^2 for the capture cross-section at 300 K.

The hole capture cross-section of the EL2 trap has been determined and equals 2×10^{-18} cm^2 near room temperature.

The energy of ionisation for the trap E_T can be determined from the principle of detailed balance which states that in thermal equilibrium the carrier emission of a single state balances carrier capture. Given the emission rate and capture cross-section above and the fact the the free energy for ionisation is the difference between the thermal emission energy and the capture energy a value of $E_T = 0.760 \pm 0.010$ eV follows for the temperature range 300 K to 400 K.

The emission rate and capture cross-sections are also functions of electric field. The emission rate will increase with electric field strength according to the Poole-Frenkel effect[27]. This results from a lowering of a Coulomb potential barrier in a similar fashion to the image force lowering of the Schottky barrier ($\Delta\phi_S$), shown in

Term	Value
α_n	2.28×10^{20} cm^{-2}s^{-1}K^{-2}
σ_{na}	$1.5 \pm 0.5 \times 10^{-13}$ cm^2
E_{na}	0.825 ± 0.01 eV
$\sigma_{n\infty}$	0.6×10^{-14} cm^2
$E_{\sigma n}$	0.066 eV
σ_{n0}	5×10^{-19} cm^2

Table 2.2: Constants needed to determined the electron emission rate and capture cross-section for the EL2 level. The data is from [6] and [7].

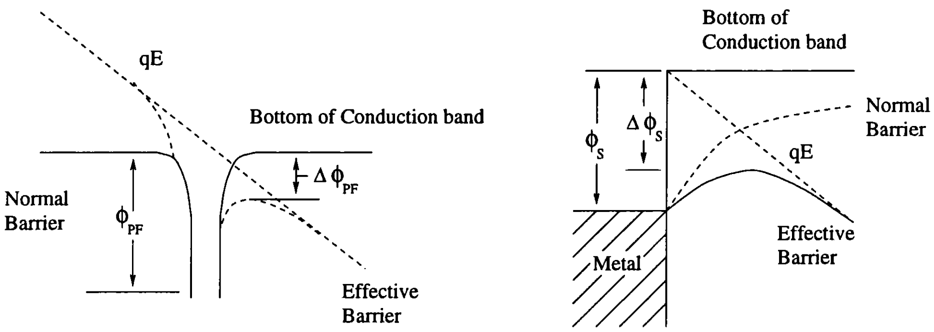

(a) Poole-Frenkel. (b) Schottky.

Figure 2.15: The Poole-Frenkel effect compared with the image-force lowering in a Schottky barrier.

figure 2.15. The image-force lowering in the Schottky barrier is due to the interaction of the electron and a mobile positive image charge, while for the Poole-Frenkel effect the positive charge is fixed and as a result the lowering for the trap ($\Delta\phi_{PF}$) is twice as great. For an electric field $\mathcal{E}$:

$$\begin{aligned} \Delta\phi_{PF} &= \left(\frac{q\mathcal{E}}{\pi\epsilon_s}\right)^{\frac{1}{2}} \\ \Delta\phi_S &= \left(\frac{q\mathcal{E}}{4\pi\epsilon_s}\right)^{\frac{1}{2}} \end{aligned} \tag{2.125}$$

where ϵ_s is the high-frequency dielectric constant.

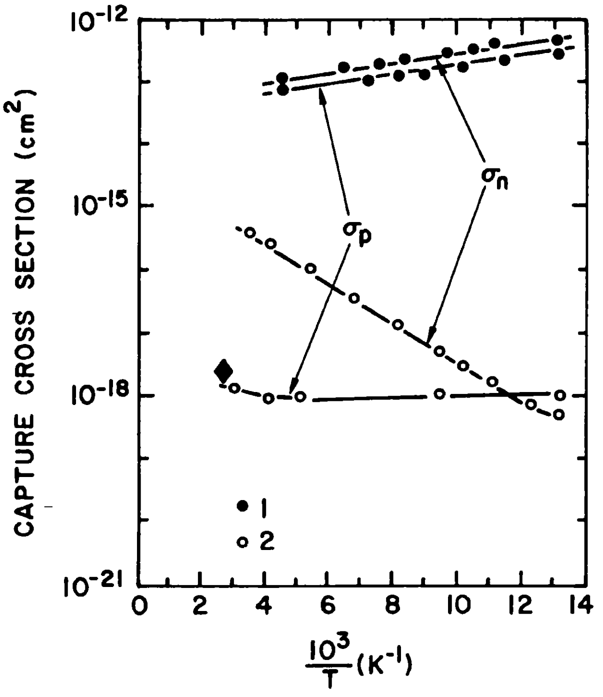

Figure 2.16: Experimental data from capture cross-section measurements of EL2 in (1) a strong electric field $E > 10^4$ Vcm^{-1} and (2) in zero electric field. The key is: σ_p - hole cross-section; σ_n - electron cross-section[4].

The current increases are of the form[27]:

$$\begin{aligned}
\text{Poole-Frenkel} \quad J_{PF} &= q\mu n\mathcal{E} \exp\left(-\frac{q(\phi_{PF} - \Delta\phi_{PF})}{rk_BT}\right) \\
\text{Schottky} \quad J_S &= A^*T \exp\left(-\frac{q(\phi_S - \Delta\phi_S)}{k_BT}\right)
\end{aligned} \qquad (2.126)$$

where thermionic emissions has been assumed. The value of r lies between 1 and 2 depending upon the position of the Fermi level, μ is the electron mobility and n is the electron density. This effect only occurs for very high fields and it has been shown that for GaAs the electron emission rate does not increase for fields below 1×10^5 Vcm^{-1}[28].

The capture cross-section for both carriers has been observed to increase with field. The electron and hole capture cross-sections for high and low field as a function of temperature are shown in figure 2.16. The hole capture cross-section for temperatures of order 300 K shows an increase of over 5 orders of magnitude while the electron cross-section increases to a value a few times that of the holes.

The changes in capture cross-sections and emission rates have been shown to have dramatic effects on the field distribution of a reverse biased junction. The field for a reverse biased n$^+$-ν gold-doped silicon junction has been measured to be flat in the depletion region[29], implying zero net space charge. The high field region, which remained at a constant value of 2.9×10^4 Vcm^{-1}, was shown to increase in length with a linear dependence on bias. This effect was explained by considering the relative emission and capture rates of the deep gold acceptor under low and high field conditions. The concentration of ionised gold atoms is:

$$N_{Au^-} = \frac{N_{Au\text{total}}}{1+\frac{e_n}{e_p}} \tag{2.127}$$

where $N_{Au\text{total}}$ is the total concentration of gold acceptors, and e_n and e_p are the emission rates for electrons and holes respectively. The total charge in the space charge region is:

$$\begin{aligned} \rho &= q(N_D^+ + N_{Au^-}) \\ &= qN_D\left(1 - \frac{N_{Au\text{total}}}{N_D(1+\frac{e_n}{e_p})}\right) \end{aligned} \tag{2.128}$$

where N_D is the net shallow donor density. To obtain zero charge density, and thus a flat field distribution, the condition

$$\frac{N_{Au\text{total}}}{N_D} = 1 + \frac{e_n}{e_p} \tag{2.129}$$

follows from equation 2.128. The number of gold atoms greatly exceeds the net shallow donor density and therefore the fraction $\frac{e_n}{e_p}$ must become large. As the field is increased, by applying a greater external bias, the ratio of emission rates does increase and the condition is met.

If the double donor nature of EL2 is ignored, then the concentration of ionised EL2 in GaAs is simply the concentration of EL2 levels that are not occupied by an electron. Therefore from equation 2.121:

$$\begin{aligned} N_{EL2^+} &= N_{EL2\text{total}}(1-F_e) \\ & \frac{N_{EL2\text{total}}}{1+\frac{nc_n}{e_n}} \end{aligned} \tag{2.130}$$

where c_n is the electron capture coefficient of the level ($= \sigma_n v_{th}$) and $N_{EL2\text{total}}$ is the total concentration of EL2 defects. Therefore the ratio of the capture and emission

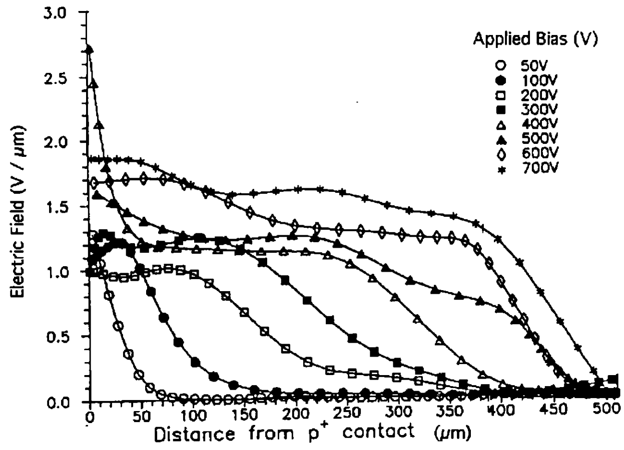

Figure 2.17: The measured electric field distribution inside the bulk of a SI-U GaAs diode for various values of reverse bias. The key is shown on the figure[5].

rates are of importance. The capture cross-section has been shown to increase with field and the current is also expected to increase and thus the carrier concentration will increase. For fields up to 1×10^5 Vcm^{-1} the emission rate will remain constant and thus the ratio $\frac{nc_n}{e_n}$ will increase with electric field. This will result in a fall in EL2$^+$ concentration in the space charge region with increasing fields. At a critical field strength the net charge in this region will be zero, similar to what occurred in the $n^+ - \nu$ gold-doped silicon junction. A constant field distribution, similar to that found in the gold doped silicon diode, may therefore occur. The magnitude will be dependent upon the field-dependent increase in the electron capture coefficient.

The electric field in an SI-U GaAs diode has been measured with a contact probe technique at UMIST[5] the results of which are shown in figure 2.17. The results revealed a field profile, at a bias in excess of 50 V on a 500 μm thick device, with a constant magnitude over a region of the bulk extending from the reverse biased contact, in agreement with the discussion above. The magnitude of the electric field was $1 - 1.8 \times 10^4$ Vcm^{-1} over the applied bias range. At high bias the electric field distribution therefore divides the device into two regions; the high, constant field region and the low field region extending from the edge of high field region to the back contact of the diode.

2.9.4 Capacitance measurements in the presence of deep traps

Following the discussion in section 2.8 of the capacitance of a Schottky barrier with shallow traps, this section considers the details for a device with deep traps.

The difference between the capacitance of a barrier with and without deep traps arises due to the fact that the occupation of the deep level changes as the bands are bent, and therefore the charge state is altered. This results in a change in the charge of the depletion region and thus the C-V characteristics are different. Therefore the C-V characteristics can be explained with reference to section 2.9.2

For $E_t > E_1$ the trap time constant is:

$$\tau_t = \frac{1}{e_n + \sigma_n v_{th} n} \qquad (2.131)$$

As only the traps close to the quasi-Fermi level will change charge state under the application of a small voltage change, only these are of importance. For such traps the emission and capture rates are approximately equal and therefore:

$$\tau_t = \frac{1}{2e_n} \qquad (2.132)$$

The effect that the traps have on the capacitance will depend upon the relative values of the trap time constant, the frequency of the small A.C signal used to determined the capacitance (ω_s) and the rate of change of the applied reverse bias (ω_b). Three situations arise:

1. $\tau_t^{-1} > \omega_s > \omega_b$
2. $\omega_s > \tau_t^{-1} > \omega_b$
3. $\omega_s > \omega_b > \tau_t^{-1}$

Only the first case will be examined further.

$\tau_t^{-1} > \omega_s > \omega_b$

Here the traps can follow the test signal and be filled before the small A.C signal goes through a quarter cycle. The energy bands and the charge density for such a situation are shown in figure 2.18 for an n-type semiconductor with donor traps.

As the traps are donors, those beyond $x = y$ are occupied and therefore neutral while those in the region from the metal to $x = y$ are empty and positively charged.

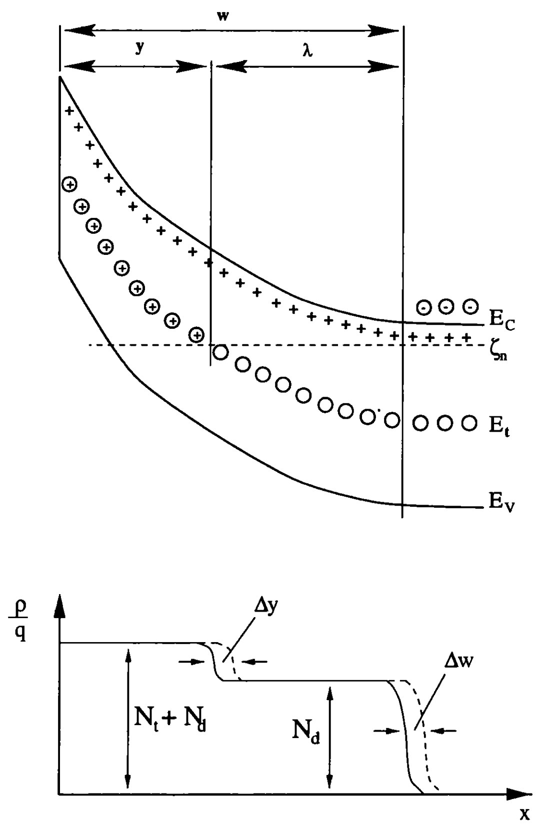

Figure 2.18: The energy bands and charge density for a reverse biased Schottky junction with a deep trap.

The shallow donors are uncompensated in the depletion region of width w. In the region up to $x = y$ the total charge in the space charge region is $N_D + N_t$ due to the extra contribution from the traps. Beyond this, up to the edge of the depletion region the charge is due to the shallow donors and equals N_D, as before.

An increase in the reverse bias by ΔV causes the depletion region to increase by Δw and the charged trap region to increase by Δy, shown in the figure. The extra charge contributions from the the donors (ΔQ_D) and the traps (ΔQ_t) are simply:

$$\begin{aligned} \Delta Q_D &= qN_D\Delta w \\ \Delta Q_t &= qN_t\Delta y \end{aligned} \tag{2.133}$$

The value of the field in the space charge region changes due to the increase in fixed charge in a similar fashion to that discussed in section 2.8. Referring to

Gauss's theorem the electric field increases by:

$$\begin{aligned} \Delta E = &\ \tfrac{q}{\epsilon_s}(N_D\Delta w + N_t\Delta y) && \text{for } 0 < x < y \\ \Delta E = &\ \tfrac{q}{\epsilon_s}(N_D\Delta w) && \text{for } y < x < w \end{aligned} \tag{2.134}$$

The corresponding increase in potential across the depletion region is:

$$\Delta V = \frac{q}{\epsilon_s}(N_D w\Delta w + N_t y\Delta y) \tag{2.135}$$

Resulting in a capacitance of:

$$C = \frac{dQ}{dV} = \frac{\epsilon_s(N_D\Delta w + N_t\Delta y)}{N_D w\Delta w + N_t y\Delta y} \tag{2.136}$$

In deriving this capacitance both the donor and trap densities were presumed to be uniform. If this is not true then the expression for the capacitance is still valid but with N_D and N_t replaced by N_D(w) and N_t(y) respectively.

The difference in x and y can be expressed in terms of the trap density and the energy levels by replacing x by y in equation (2.45) of the depletion approximation (see section 2.5.2) and by noting that this region was so defined that the change in the energy bands equals ζ_n - E_t which is $(E_F - E_t)_{bulk}$. Therefore:

$$w - y = \left[\frac{2\epsilon_s}{qN_D}(E_F - E_t)_{bulk}\right]^{\frac{1}{2}} = \lambda \tag{2.137}$$

where λ is a constant. As $w - y$ is a constant it implies that $\Delta w = \Delta y$ and thus:

$$C = \frac{\epsilon_s(N_D + N_t)}{N_D w + N_t y} \tag{2.138}$$

From equation (2.135) with $\Delta y = \Delta w$ the expression for $1/C^2$ can now be found:

$$\frac{d1/C^2}{dV} = \frac{2}{\epsilon_s q(N_D + N_t)} \tag{2.139}$$

where N_t is the density at $x = y$ and not at the edge of the depletion region.

Chapter 3

Detector Fabrication and Characterisation

3.1 GaAs detector fabrication

The work reported in this thesis includes work performed with GaAs devices fabricated at Glasgow University's III-V semiconductor laboratory in the Electrical Engineering Department. The process stages involved in the fabrication of these devices are described below.

3.1.1 Material and contact choice

To fabricate a GaAs detector two choices have to be made, namely the substrate material and the contacts used.

The GaAs used almost universally was semi-insulating undoped (SI-U) Liquid Encapsulated Czochralski (LEC) industrial substrate material, available from various manufacturers world-wide. Semi-insulating indium doped (SI-In doped) LEC GaAs material has been tested in Glasgow and LEC material with a low carbon concentration [30] has also been tested by other groups to investigate its radiation hardness properties.

Other types of substrate are also available. Chromium and iron in-diffused material, supplied by SITP, Tomsk [22] has been tested at Glasgow (results of which are, however, not included in this thesis) and in Russia as an alternative to LEC material with improved radiation hardness properties.

Detectors fabricated with material grown by the Horizontal Bridgman technique [31] have been tested by other groups and have given generally poorer results in comparison with the LEC material [32].

Liquid Phase Epitaxial (LPE) and Vapour Phase Epitaxial (VPE) materials, which are also available, are more expensive options. Epitaxial materials, grown on an LEC substrate, can approach a thickness of 200 μm for some techniques. Low dopant concentrations ($\approx 10^{13}$cm^{-3}) are possible, with little trapping present, enabling good detectors to be fabricated. The price of this material has however prevented it from being considered for the ATLAS experiment. Low pressure VPE material[33], which is less expensive than conventional VPE material, has been investigated at Glasgow University for X-ray imaging[34] and radiation hardness (section 5.7.2). Detectors were fabricated from this material by the same processes used for the LEC material.

The detector may be fabricated either with a p-i-n structure [21] by doping the substrate material, or with a p-π-ν-n junction created by in-diffusion of chromium or iron to produce a dopant concentration gradient [22], or with a Schottky and an ohmic contact realized by metal deposition. The latter option is preferred due to its simplicity in processing and as no advantages have been demonstrated by the p-i-n structures over the Schottky detectors. While p-π-ν-n structures have shown better radiation hardness than the conventional detectors they still remain to be proved completely satisfactory.

Detectors fabricated commercially by Alenia SpA, Rome with SI-U LEC substrates have also been tested.

3.1.2 Initial wafer treatment

Most of the detectors described were fabricated at Glasgow University using SI-U LEC substrates supplied by MCP[35]. The substrates arrived as 2 inch diameter, 500μm thick wafers. The first processing stage was to thin (lap) and polish the wafer to the desired thickness. Detectors were usually processed with the 200μm thickness chosen by ATLAS for the GaAs forward wheels (see section 1.3.3), however detectors of various thicknesses were also used to investigate material properties.

A Logitech PM4 lapping and polishing machine was used to lap and polish the wafers. The wafer was wax bonded to a glass substrate which was attached by vacuum to the PP6 Polishing jig of the PM4 machine and polished with an RO (reverse osmosis) water, ammonia and hydrogen peroxide mixture with a pH fixed at 7.9. This process reduced the thickness of the wafer by between 20 μm and 30 μm or until all surface defects were removed. The wafer was removed from the glass substrate, de-waxed, turned over and re-wax bonded to expose the unpolished side. A suspension of 3 μm alumina particles in RO water was used to lap the wafer to within 30 μm of the desired final thickness. Chemical polishing, as described above, removed the final 30 μm. Finally the wafer was de-waxed and cleaned with Opticlear, acetone, methanol, and RO water in that order and dried under compressed nitrogen.

Fabrication of the desired contacts on the substrate followed.

3.1.3 Contact fabrication

The process of contact fabrication is outlined in figure 3.1. The first stage of the process was the mask design which defines the position of the structures that were fabricated, for example the metal contacts. The design was made using the PC based design software Wavemaker. The patterned side for pixel and strip detectors was usually the Schottky side which implies that the collection of holes dominated the signal from these devices (see section 6.3). The detectors had a passivation encapsulation which protected the device from scratches. To allow connectivity of the device to external electronics, holes were required in the passivation; these were defined by a separate mask. The device designs ranged in complexity from a simple circular pad detector, described in section 3.1.4, to an AC coupled strip detector with air bridges and a punch-through DC path to ground (see section 6.2).

The masks once designed were transferred to an electron beam writer which wrote a set of chromium master masks. From the masters negative ferric copies, to be used in the device fabrication, were made by photo-lithography techniques.

Photo-lithography

Photo-lithography was used to realise the mask design on the wafer.

S1400 resist liquid was applied to the surface of the wafer which was spun at

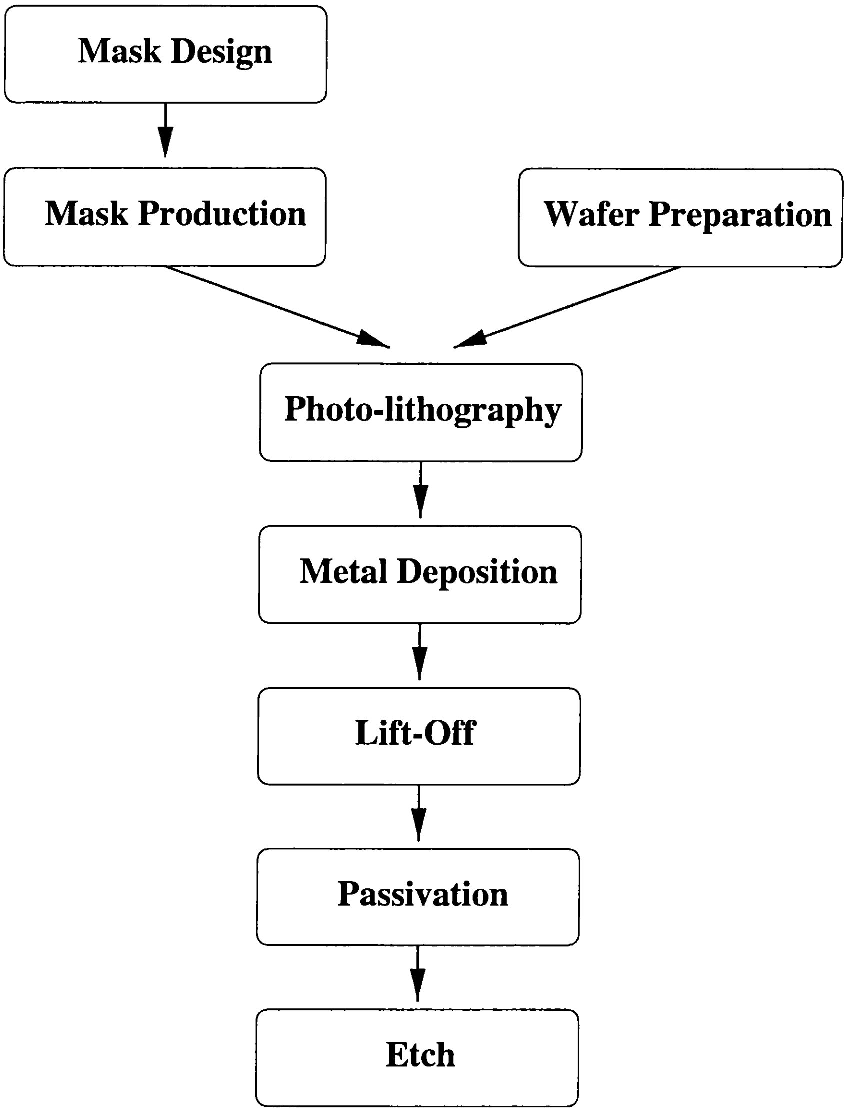

Figure 3.1: The fabrication process.

4000 r.p.m. for 60 s to spread the resist uniformly over the surface of the wafer. To harden the resist it was baked for 30 minutes at 90°C. Improved edge quality can be obtained at the lift-off stage if the wafer is soaked in chlorobenzene for about 10 s to harden further the surface of the resist. This process was only necessary in devices that had very fine structure definitions such as strip detectors. The resist-covered wafer was placed in close contact with the Schottky metallisation mask using an infra-red mask aligner. Ultra-violet light illuminated the wafer through the mask, destroying the bonds of the resist in the areas that were not masked out. The exposed resist was removed by placing the wafer for 75 s in a solvent (Microposit

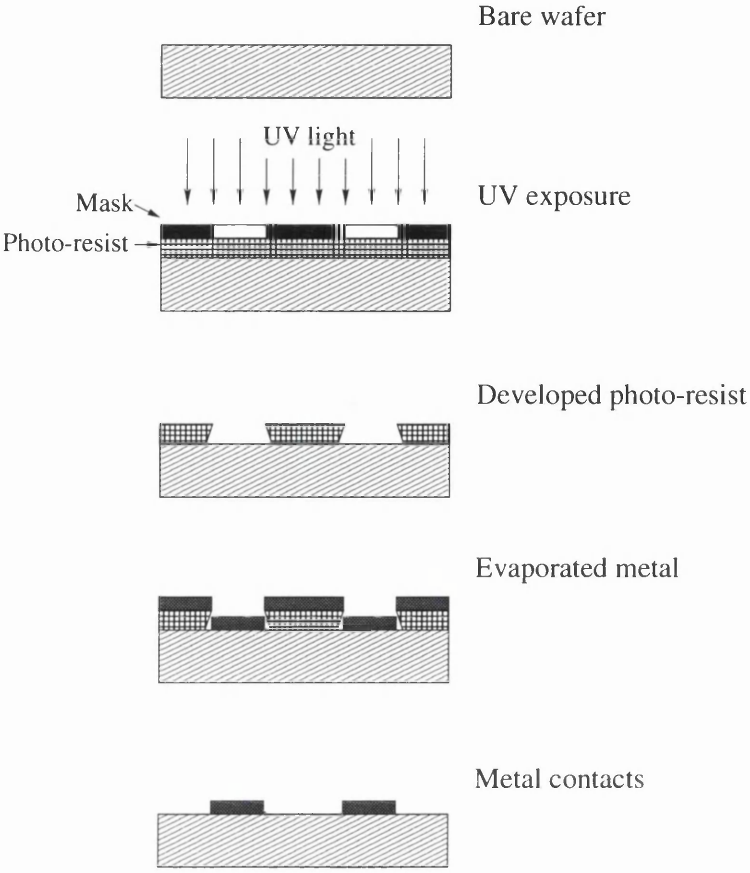

Figure 3.2: Photo-lithography, metal evaporation and lift-off.

1400-31 developer) that preferentially dissolved the weakened resist, then washed with RO water and dried with compressed nitrogen. On the wafer the resist formed a negative of the desired metallisation pattern, as shown in figure 3.2.

Figure 3.1 shows that metal deposition is the next stage of the process, however the alignment of the rear contacts will first be explained. Once the front contacts had been processed to completion rear contacts had to be fabricated. In a few cases this contact was a uniform ohmic contact that covered the entire wafer, but more frequently the contact had a defined pattern and had to be aligned to the front contact with a precision better than $5\mu m$ required by the fine detail of the patterns. This was possible because GaAs is optically transparent to infra-red light. The wafer was placed in the mask aligner, as before, with the rear covered with resist and in contact with the appropriate mask. Infra-red light illuminated the wafer from behind and passed through the wafer but was absorbed by the metal contacts. All the masks had alignment marks, thus, front metallized marks could be aligned to those on the mask for the rear contact. Ultra-violet illumination and resist development followed as before.

Metal evaporation

Before metal deposition the wafer was de-oxidised for 60 s in a 1 to 4 solution of hydrochloric acid and RO water which removed any natural oxide that had grown on the surface of the wafer since the polishing stage.

Deposition of the metal contact was performed with a Plassys Evaporator (model MB430). The sample was placed into an air lock, which was evacuated to a pressure of 10^{-6} bar, and then transferred under vacuum to the main chamber. The sample was cleaned further with an RF plasma cleaning cycle to ensure removal of all contaminants. Both the Schottky and the ohmic contacts were made of multiple metal layers, which are discussed below. The desired metal was evaporated onto the wafer in the Plassys by focusing an electron beam onto a crucible of the metal in the chamber. The metal was accelerated towards the sample and deposited.

At Glasgow the metal layers used for the contacts are 33 nm titanium, 30 nm palladium, 150 nm gold for the Schottky contact and for the ohmic contact 40 nm palladium and 100 nm germanium [36]. Gold diffuses very rapidly into GaAs and the palladium layer prevents this so that a rectifying junction is formed. Titanium is used to improve the metal adhesion to the GaAs. Annealing of the second multi-metal layer, during the passivation stage described below, forms the ohmic contact. The palladium transforms into a palladium-germanium compound and the excess germanium diffuses through this into the GaAs, resulting in a smooth contact which has uniform diffusion into the GaAs. The ohmic behaviour is obtained because germanium is a group IV element and acts as a donor in GaAs by occupation of gallium antisites. Diffused germanium thus forms a highly doped n-region which leads to the desired non-rectifying nature.

Once the metal contact had been deposited the wafer was removed from the evaporator and placed in a bath of acetone. The acetone dissolved the photo-resist which was under some of the deposited metal, a process know as lift-off, to leave only the desired metallized regions, shown in figure 3.2. Warming of the acetone in a water bath or ultra-sonic agitation can be employed to ensure the removal of all the photo-resist. Before withdrawing the sample from the acetone bath it was checked optically to ensure that the lift-off was complete. Care was taken to make sure that no metal particles redeposited themselves onto the surface by washing the wafer as it was taken out of the acetone bath with fresh acetone, isopropanol and then RO water. The sample was dried with compressed nitrogen.

Passivation and etch

The next stage of processing was the passivation of the front side. For most detector designs this represents the last stage of processing for this side. In the fabrication of AC coupled strip detectors the passivation layer is the dielectric of the decoupling capacitance for the strips and several more steps are required after this stage.

Silicon nitride passivation of typically between 200 nm and 400 nm was deposited on the wafer by heating the sample to approximately 300°C for one minute per 12 nm of passivation in an atmosphere of the nitride at high pressure.

To realise holes in the passivation, photo-lithography was used with an appropriate mask that defined the position of the required aperture. The photo-resist was developed as before, and the unprotected passivation was removed with a C_2F_6 plasma etch at a rate of 50 nm per minute.

Further metallisation of the front side could then be performed and the rear side of the wafer processed in a similar fashion.

3.1.4 Devices

The main types of device that were fabricated were simple pad detectors, which were used to investigate material properties, strip detectors and pixel detectors. This section will explain the geometry of the simple pad detector while microstrip detectors are discussed in chapter 6.

The front contact of the simple pad detector is a circular Schottky contact, 2 mm or 3 mm in diameter, surrounded by a 200 μm or 500 μm wide Schottky guard ring, separated from the pad by 10 μm. Edge effects were discussed in section 2.6.5 as a source of increased current and therefore the guard ring was introduced to remove this effect. The ohmic contact is aligned with and is geometrically identical to the Schottky contact. As the ohmic contact was usually held at ground potential, both

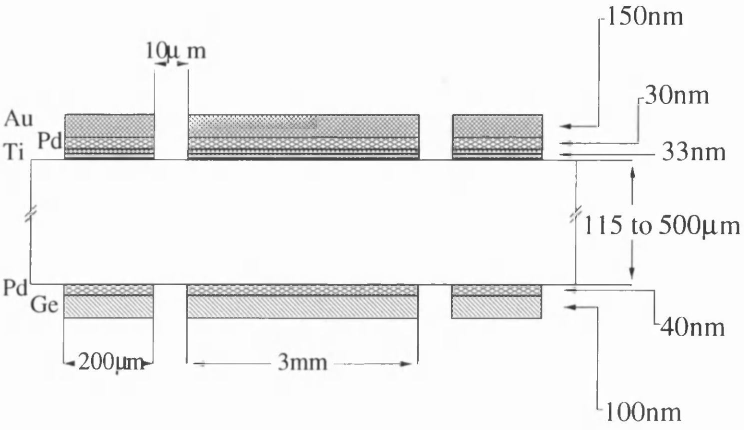

Figure 3.3: The cross-section of a simple pad GaAs detector.

the pad and guard ring were often shorted together. Figure 3.3 shows a cross-section of a simple pad detector.

3.2 Characterisation methods

The electrical and charge collection characteristics of a diode are fundamental in obtaining an understanding of that given diode. The experimental procedures needed for the characterisations are described below.

3.2.1 Current-voltage characteristics

The dependence of the current through the diode on applied bias was investigated with the use of a Keithley-237 source measurement unit. A LabView[37] program was written to control the Keithley and enable the results to be output to a spread sheet. The diode under test was placed in a metal box for electrical screening and to keep it dark, due to the light sensitivity of the current. As the current characteristics are also temperature dependent the diode was placed in an environmental chamber which allowed the temperature to be controlled to within an accuracy of 0.2°C between -40°C and 160°C. The current of interest was that which flowed through the device and thus surface currents had to be reduced. For measurements on the circular pad detectors this was achieved by the use of the guard ring arrangement described above. During the measurement the guard ring was held at the same potential as its pad, via the Keithley guard, which resulted in the surface current being collected by

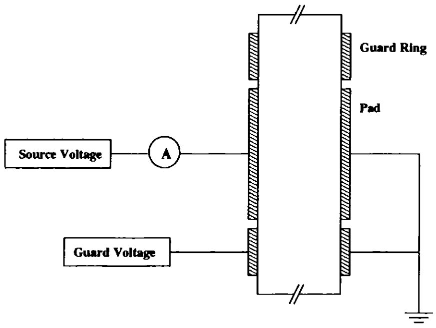

Figure 3.4: Apparatus for current voltage measurements.

the guard ring and not the pad. The circuit for such a measurement is shown in figure 3.4. Measurements were made with both forward and reverse bias, with respect to the front Schottky contact. All measurements were made from zero initial bias. A voltage step was applied and the current was measured after a given time interval which was necessary to allow the diode to reach equilibrium. In GaAs diodes time constants of order 1 s were measured at low bias and thus a minimum delay of 10 s was imposed. The voltage step between zero and the final bias could be either linear or logarithmic. A 'compliance' was set that defined a maximum current through the device, to avoid damage to the diode or the measurement equipment.

The current characteristics of strip detectors were also measured and the results are reported in chapter 6.

3.2.2 Capacitance measurements

In chapter 2 the existence of space charge and its implications for a detector's capacitance were discussed. Here the experimental details of how the capacitance was measured are outlined.

The capacitance measurements used a Hewlett Packard 4274A multi-frequency LCR meter and a Keithley-237 bias supply. Both instruments were controlled by a LabView program.

The detector under measurement was housed in a metal, light-tight box with temperature control as in the current-voltage measurement. The pad and guard on the Schottky side of the detector were connected to the high outputs (H_{POT} and H_{CUR}) of the LCR meter while the ohmic pad and guard were shorted together and connected to the meter's low outputs (L_{POT} and L_{CUR}). DC bias was supplied from the Keithley-237 via the high output of the LCR instrument, to deplete the detector. A milli-volt A.C signal from the LCR machine was used to determine the reactance of the device and hence the capacitance. It is assumed that the capacitance is the only element in the circuit so that when a small signal bias is applied the current that flows is phase shifted by 90^o. It is this current that is measured by the LCR machine. The current and applied voltage are related by:

$$I = \frac{V}{Z} = j\omega VC \tag{3.1}$$

where Z is the capacitor impedance and V is the small A.C signal of angular frequency ω. Therefore from the current measurement the capacitance is determined. Capacitance measurements were performed at 11 A.C. signal frequencies ranging from 100Hz to 100kHz at zero bias. A bias step was applied to the device and, after a time delay of 10 s to allow equilibrium to be re-established, the capacitances were measured again. This procedure was repeated until the maximum desired bias was reached.

Measurements of capacitance characteristics of strip detectors were also performed. These are reported in chapter 6.

3.2.3 Alpha particle tests

The alpha source test allows the electron and hole charge collection of the detectors to be investigated individually.

The detector was reverse biased by the application of a negative bias to the front contact via an EG&G Ortec (type 142) charge pre-amplifier. The back contact was held at either ground or a positive potential to increase the total bias applied to the detector. For electrical screening the detector was placed inside a metal box which had only two small holes in it, one above the front and one below the back contact. An Americium-241 source placed, in turn, above each hole irradiated either the front or back side of the detector with 5.45 MeV alpha particles, as shown in figure 3.5.

Due to the limited range of alpha particles in air the apparatus was placed inside an evacuated metal container at a pressure between 20 and 30 mbar. The signal was read out using the Ortec pre-amplifier connected to a post amplifier with a 500 ns shaping time, and processed by a PC-based multichannel analyser to obtain

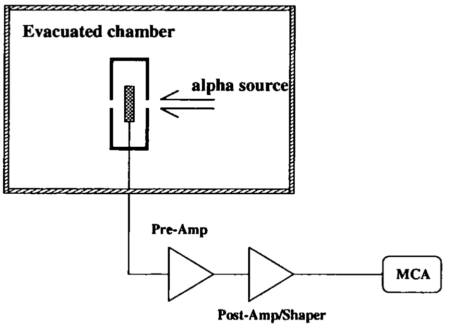

Figure 3.5: Alpha measurement apparatus.

a pulse height spectrum. Alpha particles in GaAs deposit energy according to the Bragg ionisation curve [38] which results in most of the alpha particle energy being deposited at a depth of 20 μm in the detector. Ramo's theorem[39] states that the signal collected is due to the motion of the charge carriers, therefore the charge carrier that travelled only 20 μm will produce a small signal with respect to the carrier that travelled (almost) the total thickness of the detector, assuming that all the detectors were significantly thicker than 40 μm, which they were. The signal from either electrons or holes could be observed depending upon the side from which the alphas were incident.

As the energy to create an electron-hole pair in GaAs is 4.2 eV, for the 5.45 MeV alpha source used a charge of 0.21 pC (equivalent to 1.3×10^6 electrons) was deposited in the detector. From this value and the peak positions in the spectra the charge collected for electrons and holes was found for many GaAs detectors. A charge collection efficiency, (*cce*), was defined as the amount of charge collected divided by the amount deposited.

The system was calibrated with the use of a voltage pulse applied to a 1.8 pF capacitor at the front of the pre-amplifier. This calibration was verified with the use of an alpha signal from a 100% efficient, over-depleted silicon detector which gave a 1.5×10^6 electron signal.

The GaAs material used in the fabrication of the detectors contained both electron and hole traps. The charge carriers will therefore not be able to cross the total thickness of the detector without being trapped, leading to the carriers having a mean free absorption length less than the physical thickness of the detector. Ramo's theorem states that the charge collected, Q_{col}, on the electrodes of a detector by the motion of a charge carrier is given by

$$Q_{col} = q\frac{\lambda}{W} \tag{3.2}$$

where λ is the mean free absorption distance travelled by the carrier and W is the separation of the detector electrodes. As the carriers are trapped the reduction in the number of free carriers with distance of detector traversed (x) may be assumed to decrease according to the exponential relationship:

$$n_x = n_0 \exp[-\frac{x}{\lambda}] \tag{3.3}$$

where n_0 is the original number of carriers produced.

The charge collection efficiency, is therefore

$$cce = \frac{\lambda}{W}(1 - \exp[-\frac{W}{\lambda}]) \tag{3.4}$$

To take into account the signal from both carriers, equation (3.4) must be extended to:

$$cce_\alpha = \frac{\lambda_e}{W}\left(1 - \exp[-\frac{(W - x_0)}{\lambda_e}]\right) + \frac{\lambda_h}{W}\left(1 - \exp[-\frac{x_0}{\lambda_h}]\right) \tag{3.5}$$

where x_0 is the position at which the carriers were created (20 μm for 5.45 MeV alpha particles in GaAs). The charge collection efficiency given in equation (3.5) is for front illumination, that is an electron signal, where λ_e and λ_h are the mean free absorption lengths for electrons and holes, respectively. Mean free absorption lengths for both carriers may therefore be obtained from the alpha data.

3.2.4 Charge collection from minimum ionising particles

Measurements were made with minimum ionising particles (mips) which allow the charge collection of both carriers across the entire bulk of the detector to be investigated, using a strontium-90 source which emits beta particles with an end point energy of 2.283MeV.

The GaAs detector under test was placed in front of the beta source, while several layers of aluminium foil and a silicon detector were positioned behind the GaAs detector as shown in figure 3.6. The aluminium foil stopped the low energy beta particles, produced by the source, from reaching the silicon detector. The

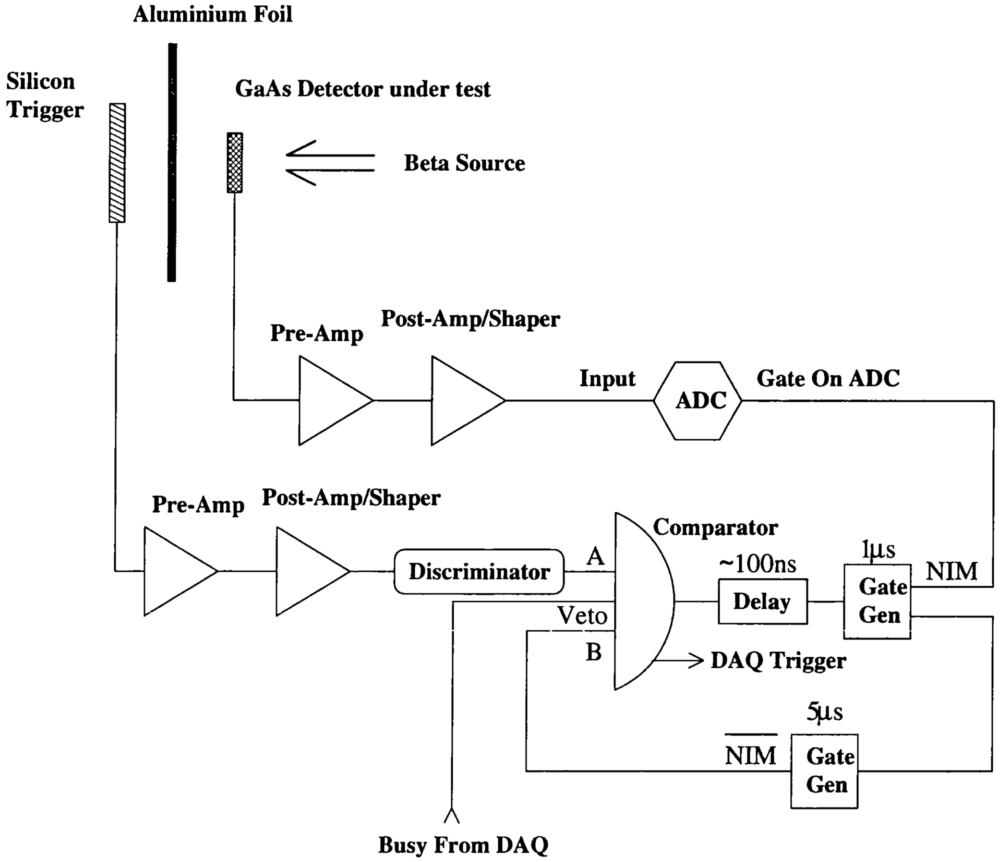

Figure 3.6: The apparatus used to obtain beta spectra.

signal from the beta particle in the silicon detector triggered a NIM module to create a 1 μs pulse that was used as a gate for an ADC. The signal from the GaAs detector that occurred in coincidence with the silicon trigger was sent to the ADC and recorded. The detectors and ^{90}Sr source were placed inside a metal box for electrical shielding and in an environmental chamber for temperature control as described previously. When an electron passes through a material it loses energy. The energy loss per unit length of material traversed is described by the Bethe-Bloch formula[38]. Electrons with an energy above a few MeV are relativistic and are said to be minimum ionising particles (mip). A mip deposits a given amount of energy for a given substance per unit length traversed. The energy deposited for lower energy electrons, however, is a function of energy and is large for electrons with a momentum below 1 MeV/c. Rejection of low energy electrons from creating a gate for the ADC was thus necessary to ensure that the electrons that traversed the GaAs detector were sufficiently high in energy to be regarded as mips. For GaAs a mip deposits 56 keV/100μm, resulting in the creation of 13300 electron-hole pairs per 100 μm traversed.

The read-out system was calibrated with the use of a voltage pulse onto a known capacitor to give an injected charge into the pre-amplifier. This calibration was checked with the use of an X-ray source and a silicon detector with a 100% charge collection efficiency.

The actual charge collected from a GaAs detector was measured and the charge collection efficiency for a mip calculated (cce_{mip}). The signal is due to both electrons and holes as the charge is deposited across the entire thickness of the detector. Integration of equation (3.5) with respect to x, where x varies from zero to W, gives:

$$cce_{mip} = \frac{1}{W}\left[(\lambda_e + \lambda_h) - \frac{\lambda_e^2}{W}\left(1 - \exp[-\frac{W}{\lambda_e}]\right) - \frac{\lambda_h^2}{W}\left(1 - \exp[-\frac{W}{\lambda_h}]\right)\right] \tag{3.6}$$

for the charge collection efficiency of mips. Electron and hole mean free absorption lengths found from the alpha data can thus be used to predict the mip charge collection efficiency.

3.2.5 Pulser noise measurements

The read-out apparatus described above was also used to determine the noise of the detector.

A pulse generator was used to supply both a voltage pulse to the back of a GaAs detector under test and the trigger for the gate of the ADC. The detector was biased via the Ortec pre-amp and read out as before. The detector was electrically shielded and temperature controlled as above. The spectrum obtained was Gaussian in shape with a mean pulse height related to the size of the voltage pulse applied to the detector and a FWHM determined by the noise of the detector and electronics ($\sigma_{tot}(V)$). A Gaussian function ($f(x)$) is described by:

$$f(x) = \frac{1}{\sigma\sqrt{2\pi}}\exp\left(-\frac{(x-\mu)^2}{2\sigma^2}\right) \tag{3.7}$$

where μ is the average value of the variable x and the variance is σ^2. The full width at half maximum (FWHM) of the function is:

$$FWHM = \sqrt{2\ln 2}\sigma = 1.18\sigma \tag{3.8}$$

With zero bias applied the noise was that due to the electronics and the detector capacitance (σ_0). The current dependent noise of the detector at a given bias is therefore given by:

$$\sigma_{Idet}(V) = \sigma_{tot}(V) - \sigma_0 \tag{3.9}$$

if σ_0 is assumed constant with bias. This value will change due to the reduction in the capacitance of the diode as the device is depleted, however for the diodes tested the capacitance noise contribution to the over all noise is small and can be neglected.

Spectral noise measurements were also performed on two detectors prior to irradiation with the method and results reported in section 4.2.

Chapter 4

Characteristics of GaAs Detectors

To obtain the best detector performance the signal-to-noise ratio of the detector must be maximised and thus a high charge collection and low reverse current are required. Therefore both the electrical and charge collection characteristics of the simple pad diodes were investigated. The results for unirradiated GaAs detectors are contained within this chapter.

4.1 Electrical characteristics

The electrical characteristics of the LEC SI-U diodes were investigated under both forward and reverse bias. Current measurements revealed two distinct sections in the reverse characteristic, shown in figure 4.1. The low voltage characteristic was that of a Schottky barrier which demonstrated non-ideal behaviour at a few tenths of a volt. The second part of the characteristic was a plateau in the reverse current for a reverse bias above a few tens of volts. The two regions, termed the low and high voltage characteristics, respectively, will be discussed separately.

4.1.1 Low voltage characteristics

A simple pad diode with a guard ring was characterised using standard Schottky theory, however due to the nature of the material some careful considerations were necessary.

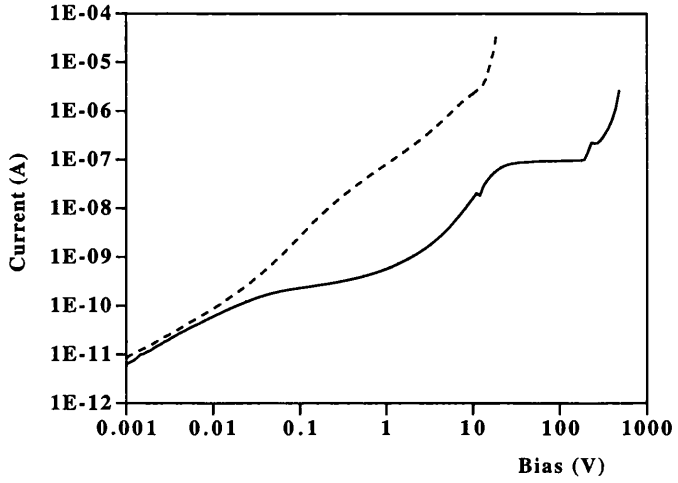

Figure 4.1: The current characteristics of an SI-U GaAs diode with a guard ring measured at 20°C. The key is: solid line - reverse bias; dashed line - forward bias.

A correction had to be made to the data due to the experimental apparatus used. The measurements were made as described in section 3.2.1 with a Keithley-237. For very low applied voltage the magnitude of the reverse current should equal the forward current, but as the above figure illustrates, this was not the case. A measured IV characteristic of a 10 MΩ resistor showed that the actual bias applied was offset from that shown on the Keithley by an amount dependent upon the sign of the bias. The resistor IV implied that to obtain the actual bias applied it was necessary to add 2.4×10^{-4} V to the forward and 8×10^{-5} V to the reverse bias value shown on the Keithley. At low bias the current expression of equation (2.71) for a diode simplifies to:

$$J_{\pm} = J_0 \frac{\pm qV}{k_B T} \tag{4.1}$$

where ± is positive for forward and negative for reverse bias. The current characteristics are therefore a straight line. Measurements were made over a wide range of temperature, for the analysis explained below, and, at each temperature, a separate fit was performed to the forward and reverse IV curves between 0.0001 V and 0.002 V from which the voltage offsets were calculated. The offset voltages showed no temperature dependence and equalled $2.4 \pm 4.0 \times 10^{-4}$ V and $8.0 \pm 2.0 \times 10^{-5}$ V for forward and reverse bias respectively.

Due to the high resistivity of the bulk material the equivalent circuit of the diode is the junction resistance (R_ϕ) in series with the bulk resistance (R_{bulk}). The diode current (I) will pass through both resistors and thus, for an applied bias V, only $V - IR_{bulk}$ will be dropped across the junction. The voltage dropped across the bulk material therefore must be accounted for when fitting theoretical current characteristics to the data.

From the linear low voltage curves the effective resistance (R_{eff}) of the junction and bulk in series was found with Ohm's law. To determine the contribution of R_ϕ and R_{bulk} to the effective resistance the diode was assumed to obey the ideal diode equation up to a bias of $k_BT/2$. The data points, corrected for the measured offset bias, were fitted with the equation:

$$J = P(1)\left[\exp\left(\frac{V - IR_{bulk}}{P(2)}\right) - 1\right] \tag{4.2}$$

where $P(1)$ and $P(2)$ are free parameters. The value of R_{bulk} was altered until the fitted curve and the ideal Schottky theory differed by less than $1 \times 10^{-3}\%$ at a bias of $k_BT/3$. From the effective and the bulk resistances the junction resistance was found. Figure 4.2 shows the corrected data points fitted as described.

To determine the activation energies of the bulk and contact resistances the measurements were performed over a large temperature range from 10°C to 147°C. Seven measurements were made between 10°C and 40°C in 5 degree steps, this was the low temperature region. Between 115°C and 147°C, the high temperature region, eight measurements were performed. The high temperature range was chosen because this was the region of interest for the capacitance measurements reported in section 4.3.2. Measurements at three temperatures between the two regions were also carried out. The results obtained for the three resistances for each measurement temperature are listed in table 4.1. The largest source of error to the value of R_{bulk} was due to the offset voltages used to correct the bias data. The $R_{bulk-min}$ and $R_{bulk-max}$ values shown in the table were obtained with the 'one sigma' variation in the experimentally obtained offset voltages. The value of the bulk resistivity (ρ_{bulk}) was determined from R_{bulk} and the geometry of the diode.

The quality of the Schottky contact was investigated by performing the fit for higher values of applied bias. The bulk resistance was kept constant and the function:

$$J = J_0 \exp\left(\frac{q(V - IR_{bulk})}{P(3)k_BT}\right)\left[1 - \exp\left(\frac{-q(V - IR_{bulk})}{k_BT}\right)\right] \tag{4.3}$$

Temperature		R_{eff}	R_{bulk}	$R_{bulk-max}$	$R_{bulk-min}$	R_{ϕ}	ρ_{bulk}
(C)	(K)	MΩ	MΩ	MΩ	MΩ	MΩ	MΩcm
10	283	515.0	61.94	68.99	55.06	453.1	239.3
15	288	262.0	17.38	20.90	13.94	244.6	67.13
20	293	138.6	16.60	18.56	14.68	122.0	64.12
25	298	74.67	15.26	16.59	13.98	59.41	58.94
30	303	41.59	6.263	6.910	5.634	35.33	24.19
35	308	23.29	3.907	4.278	3.547	19.38	15.09
40	313	13.35	2.258	2.471	2.051	11.09	8.722
		kΩ	kΩ	kΩ	kΩ	kΩ	kΩcm
60	333	1674.	399.0	432.5	377.7	1275.	1541.
80	353	294.5	80.00	86.15	76.08	214.5	309.0
100	373	65.68	16.71	17.81	15.99	48.97	64.54
115	388	20.05	6.464	6.887	6.194	13.59	24.97
120	393	14.10	4.740	5.050	4.542	9.36	18.31
125	398	10.35	3.674	3.894	3.533	6.68	14.19
130	403	7.841	2.794	2.939	2.702	5.047	10.79
135	408	5.694	2.150	2.260	2.080	3.544	8.305
140	413	4.081	1.559	1.641	1.507	2.522	6.022
145	418	2.963	1.358	1.428	1.315	1.605	5.245
147	420	2.702	1.136	1.195	1.099	1.566	4.388

Table 4.1: The measured diode resistances as a function of temperature.

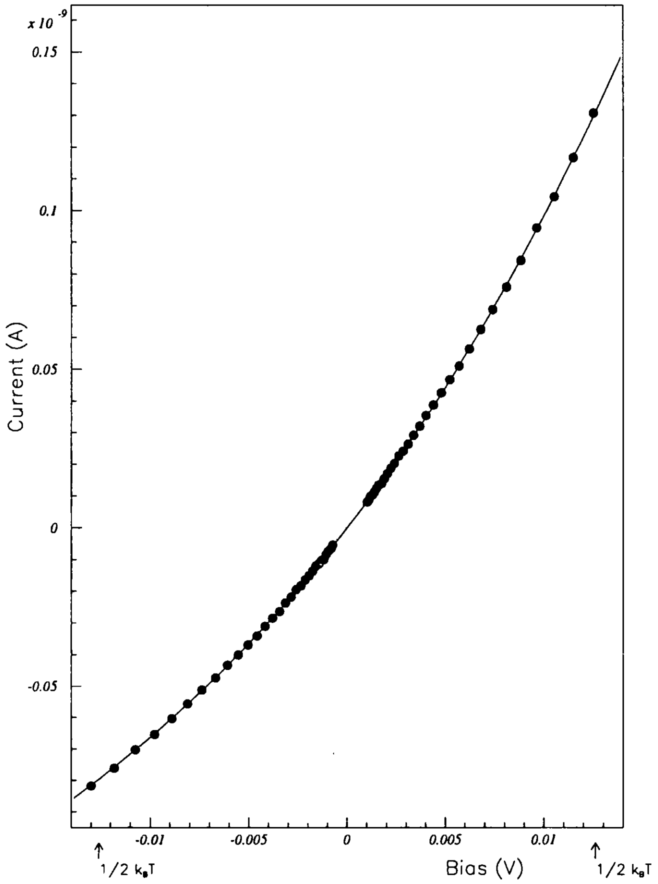

Figure 4.2: The current characteristic at 20°C of a guarded SI-U GaAs diode and the fit obtained with equation 4.2. The free parameters were $P(1) = 2.017 \times 10^{-10}$ Acm^{-2}, $P(2) = 2.524 \times 10^{-2}\ V$ and $R_{bulk} = 1.660 \times 10^{6}\ \Omega$.

where $P(3)$ is the free parameter known as the ideality factor (n) (see equation (2.78) section 2.6.1), was fitted to the data.

As the bias increased the forward current increased and there was therefore an increase in the electron density in the material which caused a change in the bulk resistivity of the diode. For this reason the fit could not be applied to high forward bias voltages. The fit was therefore performed over the reverse bias section of the curve and for a forward bias up to $k_BT/2$. The value of n obtained for fits from $1k_BT$ to $10k_BT$ ranged from 1.03 to 1.04. This demonstrated the quality of the Schottky contact. Figure 4.3 shows the corrected data measured at 20°C and the result of the fit performed up to $10k_BT$. The ideality factor is 1.04.

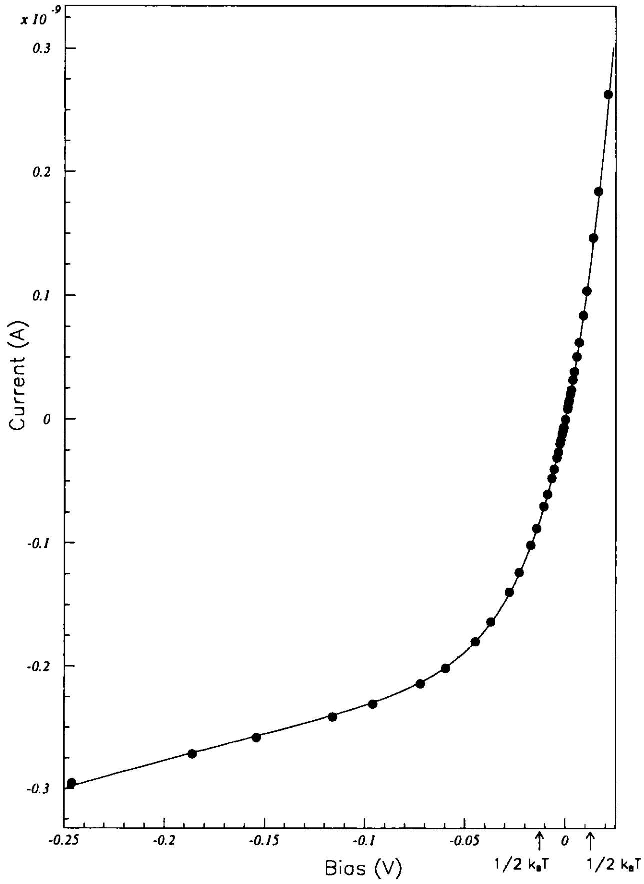

Figure 4.3: The current characteristic at 20°C of a guarded SI-U GaAs diode and the fit obtained with equation 4.3 up to $10k_BT$. The value of the ideality factor is 1.04.

From the temperature dependence of the contact resistance the barrier height was found. As discussed above the low bias diode current is proportional to the applied voltage, therefore from Ohm's law:

$$\frac{1}{R_\phi} = \frac{JS_e}{V} = \frac{qS_eJ_0}{k_BT} \tag{4.4}$$

where S_e is the electrically active area of the diode. Substitution for J_0 from equation (2.71) of section 2.6.1 gives:

$$\ln\left(\frac{1}{R_\phi S_e T}\right) = \ln\left(\frac{\sigma_{contact}}{T}\right) = \ln\left(\frac{qA^*}{k_B}\right) - \frac{q\phi_b}{k_B}\frac{1}{T} \tag{4.5}$$

where $\sigma_{contact}$ is the contact conductivity. A graph of $\ln(\frac{\sigma_{contact}}{T})$ against 1/T will give a straight line with a gradient of magnitude $q\phi_b/k_B$ if A^* (defined in equation

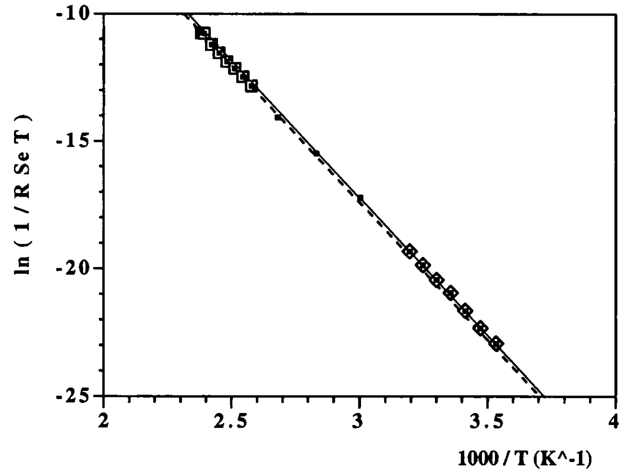

Figure 4.4: The activation plot to determine the barrier height of an LEC SI-U GaAs diode from the contact conductivity. The units used are: R - Ω; S_e - cm^2; T - K .The key is: small squares - all data; large squares - high temperature range; large diamonds - low range; dashed line - high temperature fit; solid line - low range fit.

2.72) and ϕ_b remain constant. Separate curves were fitted to the high and the low temperature regions shown in figure 4.4, where, over each limited temperature range, the assumption of constant A^* and ϕ_b values is valid.

The barrier height found for the low temperature range was 0.92 ± 0.02 V and for the high temperature range was 0.91 ± 0.02 V. The quoted error is that derived from the variation in the bulk resistance. The Schottky contact was made from titanium which has been reported to form a barrier height of 0.83 V[23] on n-type material.

Barrier heights can also be determined by utilising the dependence of the forward current upon the measurement temperature. If the current density of equation (2.82) is multiplied by the electrically active area (S_e) then the dependence, for forward bias, is given by:

$$\ln\left(\frac{I}{T^2}\right) = \ln A^{**}S_e - \frac{q}{k_B T}(\phi_b - V) \tag{4.6}$$

A plot of $\ln(I/T^2)$ against $1/T$ therefore gives a straight line with a gradient equal to $q/k_B(\phi_b - V)$. Here V is the corrected bias that was actually applied across the contact. Such a graph is shown in figure 4.5 for the LEC diode under a forward bias of 0.01V. The barrier heights found were 0.87 ± 0.03 V and 0.91 ± 0.03 V for the low and high temperature ranges respectively.

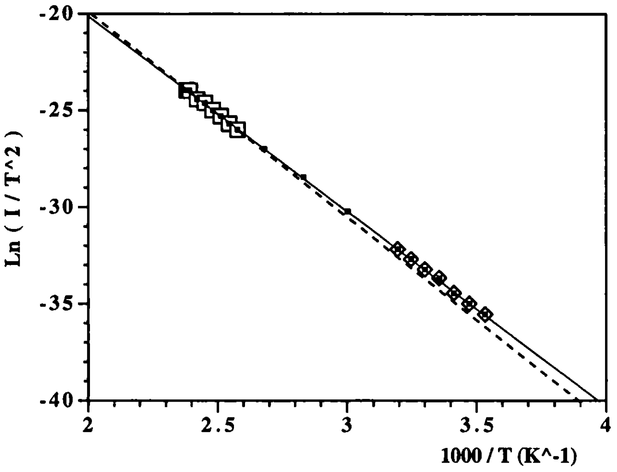

Figure 4.5: The activation energy plot for determination of the barrier height for the LEC diode under a forward bias of 0.01V. The units used are: I - A; T - K. The key is: small squares - all data; large squares - high temperature range; large diamonds - low range; dashed line - high temperature fit; solid line - low range fit.

The quoted error was determined from the variation in the current due to the error in the value of the bulk resistance and thus V. Both barrier heights were equal within their errors, and equal to the results from the conductivity measurement.

The activation energy of the bulk conductivity (E_A) can be found from the bulk conductivity (σ_{bulk}), given by:

$$\sigma_{bulk} = \frac{1}{\rho_{bulk}} = \frac{t}{R_{bulk}S_e} = qn\mu_n \tag{4.7}$$

where t is the thickness of the substrate, n is the electron density in the conduction band and μ_n is the electron mobility. The activation energy of the conductivity therefore corresponds to the activation energy of the electron density given in equation (2.5) of section 2.2.2. The temperature dependence of the conductivity is defined by the dependencies of the electron density and the mobility. From equation (2.5) the electron density is proportional to N_C and thus has a $T^{\frac{3}{2}}$ dependency while the variation of the mobility with temperature has been measured to depend upon the magnitude of the temperature[40]. For temperatures of order room temperature $\mu_n \propto T^{-\frac{1}{2}}$, while at higher temperatures the mobility is inversely proportional to the temperature. Therefore:

$$\sigma_{bulk} \propto T^{\frac{3}{2}}T^{-\frac{1}{2}} = T^1 \quad \text{Low temperature range}$$

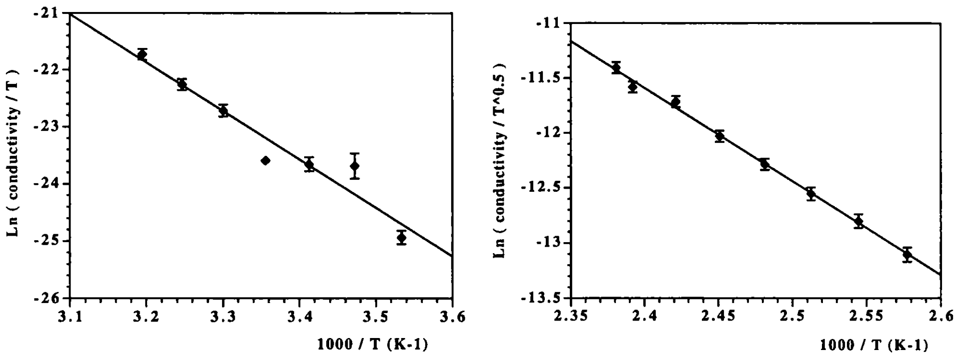

(a) Low temperature range.

(b) High temperature range.

Figure 4.6: Bulk conductivity activation plots.

$$\sigma_{bulk} \propto T^{\frac{3}{2}}T^{-1} = T^{\frac{1}{2}} \quad \text{High temperature range} \qquad (4.8)$$

So for the low temperature range a plot of $\ln(\sigma/T)$ against $1/T$ will have a gradient equal to $-\frac{E_A}{k_B}$ and for the high temperature range the same gradient will result from a graph of $\ln(\sigma/T^{\frac{1}{2}})$ against $1/T$. Figure 4.6 shows the results obtained. The gradients were 9.26 and 8.46 which gave the activation energies 0.78 ± 0.04 eV and 0.73 ± 0.02 eV for the low and high temperature ranges respectively. The errors were obtained from the variation in R_{bulk}. The two activation energies are equal within the errors of the experiment.

The values obtained for the activation of the bulk conductivity and thus the electron density are dependent upon the temperature dependence of the mobility. If the low temperature range mobility dependence was in fact the same as that given for the high temperature range an activation energy of 0.74 eV is obtained, which is within the errors of the above value.

The actual electron density can be derived from the conductivity with the use of equation (4.7). The value of the mobility depends upon the material used and the measurement temperature, as discussed above. The mobility value used was obtained from Hall measurements made on Hitachi material[40] , and equalled 7710 $\text{cm}^2\text{V}^{-1}\text{s}^{-1}$ at 305 K with a $T^{-\frac{1}{2}}$ temperature dependence and 6140 $\text{cm}^2\text{V}^{-1}\text{s}^{-1}$ at 400 K with a T^{-1} dependence. The mobility in the low temperature region was found using the former relationship and the latter was used for the high temperature

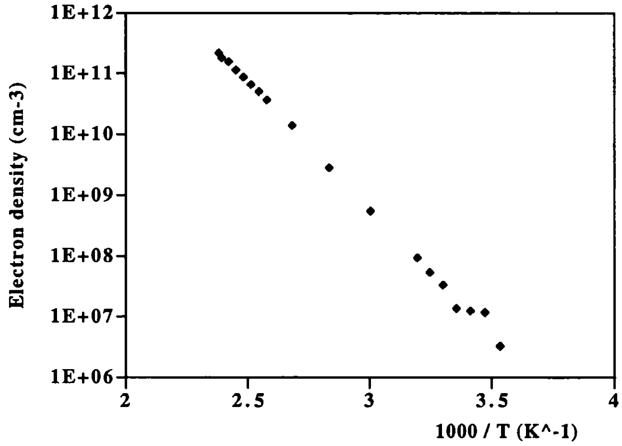

Figure 4.7: The electron density, found from the bulk conductivity, as a function of inverse temperature.

region. The number of electrons in the conduction band against inverse temperature is shown in figure 4.7.

The value obtained for the activation energy of the conductivity is between the values $(E_C - E_V)/2 = E_g/2$ and $E_C - E_{EL2}$, where E_g is the band gap energy and E_{EL2} is the energy level of EL2, the dominant donor. The activation energy will approach half the band gap energy as the temperature increases because the electron density at very high temperatures is defined by the intrinsic electron density given by equation (2.12)[26]. For LEC SI-U GaAs the dominant level is the EL2 donor, (discussed in the theory chapter), with an energy level of $E_C - E_{EL2} = 0.75$ eV. The band gap in GaAs is given by[1]:

$$E_g(T) = 1.519 - \frac{5.405 \times 10^{-4} T^2}{T + 204} \tag{4.9}$$

and therefore equals 1.43eV at 20°C. It is clear that $E_g/2$ is close to $E_C - E_{EL2}$ at this temperature. It is unlikely that at this temperature the electron excitation from the valence to conduction band has become the dominant process. Therefore it is concluded that the electron density for the temperature range examined is governed by the EL2 level in the material.

From the measured number of free carriers in the material the Fermi level (E_F), with respect to the valence band, can be found with the use of:

$$E_F = E_g - k_B T \ln\left(\frac{n}{N_C}\right) \tag{4.10}$$

At 20°C the Fermi level was found to equal 0.81 eV which is consistent with the compensation model of Look[26].

4.1.2 High voltage characteristics

The low voltage characteristics of the diodes fabricated upon the high resistivity material have been shown to obey standard theory when the effect of the substrate resistivity is removed. However, as the reverse bias was increased still further the current characteristic changed dramatically. The leakage current no longer increased with bias but reached a plateau value. This is termed the high voltage characteristic and was found to be the region under which charge collection experiments could be performed, results of which are detailed later in this chapter. That is, the magnitude and extension of the electric field in this region was sufficient to cause separation and transportation of the charge carriers without excessive loss due to trapping processes.

The typical high voltage IV of a 200 μm thick LEC SI-U GaAs diode, measured at 20°C, is shown in figure 4.8. The metal contacts were those described in section 3.1.3. A second characteristic is shown in the figure for the same diode but measured with the guard ring connected to the pad. The increase in current is due to an increase in surface currents and/or an increase in the lateral spreading of the depletion region. The latter will only be of importance if the excess current at these high voltages is due to generation processes in the bulk material rather than emission over the barrier.

The current at -10 V was assumed to be generation current and therefore from equation (2.101) has a temperature dependence given by:

$$J_{gen} \propto T^2 \exp\left(-\frac{E_A}{k_B T}\right) \tag{4.11}$$

therefore a plot of $\ln(I/T^2)$ against $1/T$ gives a straight line with a gradient equal to the activation energy. The result, shown in figure 4.9(a), gave an activation energy of 0.76 ± 0.02 eV which corresponds to $E_A = 0.75 \pm 0.02$ eV for generation involving the EL2 trap[41].

Generation current is not expected to plateau with increasing bias, contrary to observation. The plateau in reverse current has been suggested to be due to

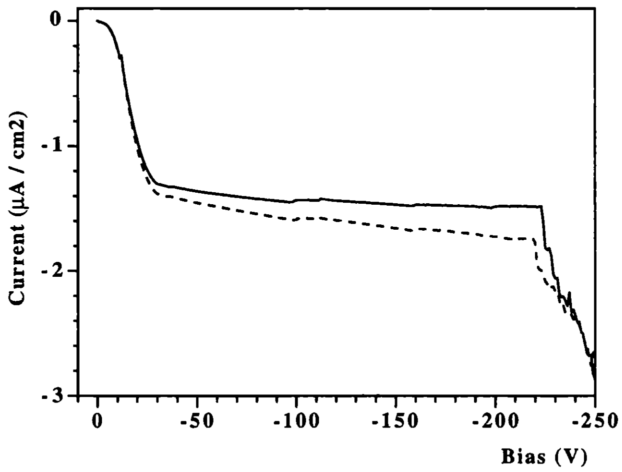

Figure 4.8: The high voltage reverse bias current characteristic of a 200 μm thick LEC SI-U GaAs diode, measured at 20°C. The key is: solid line - guarded; dashed line - unguarded measurement.

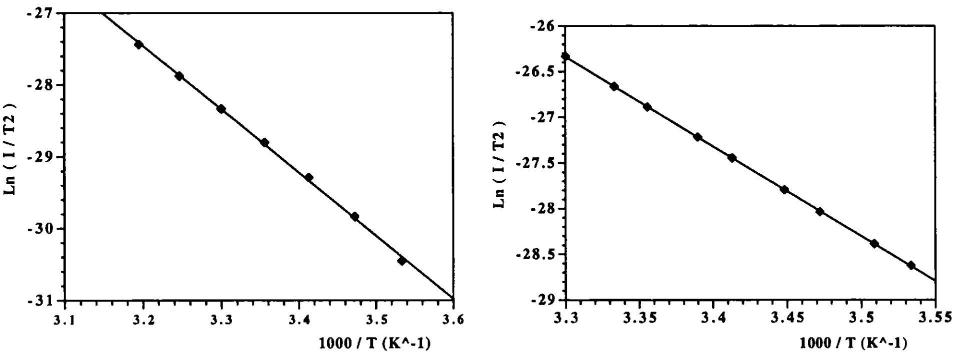

(a) Measured at a bias of -10 V.

(b) Measured at a bias of -100 V.

Figure 4.9: Activation plots for the high voltage reverse current of an LEC SI-U GaAs diode.

space charge limiting effects involving the enhanced electron capture cross-section of the EL2 defect[42]. The plateau current at a reverse bias of 100 V was measured as a function of temperature, the results of which are shown in figure 4.9(b). If the temperature dependence follows that of generation current then the activation energy of the reverse current is 0.85 ± 0.01 eV. Such an activation energy is consistent with the activation energy of the EL2 electron emission rate of 0.83 ± 0.01 eV (see section 2.9.3). Therefore it is suggested that the current does not increase with bias above 50V due to limiting effects involving the EL2 defect. Such a model has successfully predicted the presence of a quasi-neutral region behind the reverse biased contact and the resultant electric field distribution as shown in the section 2.9.3.

Furthermore the activation energy did not change if the diode was unguarded, which implies that the reverse current was a bulk effect and not surface generation. The increase in the reverse current for the unguarded measurement therefore was due to the lateral spreading of the high field region in the bulk material.

The magnitude of the leakage current is very flat from a few tens of volts up to a voltage where the current increases dramatically. For reasons which will become apparent later this bias is referred to as the full depletion voltage (V_{fd}) of the diode. Figure 4.10 shows that V_{fd} scales with the substrate thickness of the diode. The curve fitted to the diodes with a substrate thickness of less than 300 μm gave a V_{fd} equal to 0.9 ± 0.1 V/μm of diode thickness. The thickest substrates ($\sim$ 500 μm) did not undergo the same surface treatment before metallisation, resulting in a reduction in surface quality which could alter V_{fd}. However, if the 500 μm thick devices are included in the fit then $V_{fd} = 1.2 \pm 0.2$ V/μm which is consistent with the above value.

While the full depletion voltage scaled with detector thickness the magnitude of the reverse bias plateau current remained constant up to V_{fd}, illustrated by figure 4.11 for a 115 μm and a 500 μm thick diode.

Figure 4.12 shows the high voltage reverse current characteristic for three diodes, all with Schottky front contacts. Diodes A and B were fabricated from MCP material as described in section 3.1 of chapter 3. Diode A underwent a 16.5 minute and diode B a 33 minute anneal. The third diode (C) was fabricated by the company Alenia SpA with LEC SI-U GaAs from the manufacturer Sumitomo. The ohmic contact

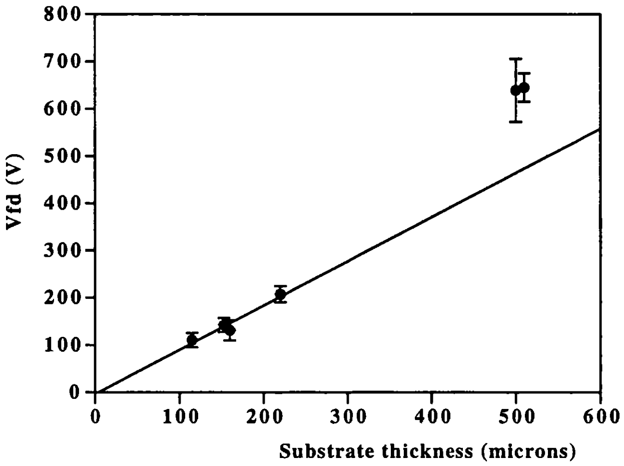

Figure 4.10: The full depletion voltage as a function of detector thickness measured at 20°C.

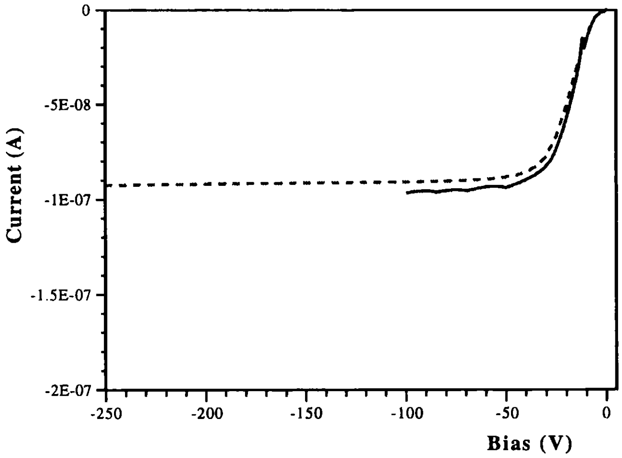

Figure 4.11: Reverse current of two SI-U diodes of different thickness measured at 20°C. The key is: solid line - 115 μm; dashed line - 500 μm thick.

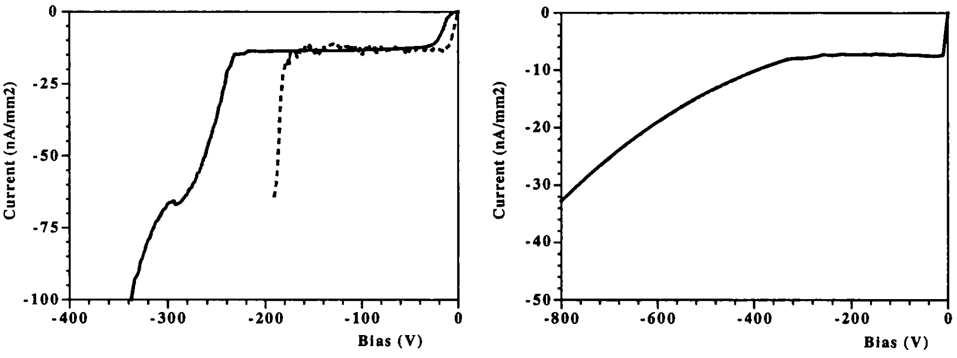

(a) MCP diodes. The key is: dashed line - diode A; solid line - diode B.

(b) Alenia diode C.

Figure 4.12: The reverse bias current characteristics of three diodes measured at 20°C.

was again realised through metallisation but via a different process to that used at Glasgow University. The figure clearly shows for all three detectors that, while the magnitude of the leakage current did not alter significantly, the post-V_{fd} current characteristics varied greatly. The MCP diode B had a leakage current density of 13.7 nA/mm^{-2} at -200 V compared to 7.3 nA/mm^{-2} for the Alenia detector. Diode B showed a slower rise in the post-V_{fd} current with respect to A while the Alenia diode had the best high voltage characteristic. The value of V_{fd} increased from approximately 180 V to 240 V for the MCP diodes and was close to 300 V for the Alenia diode.

The linear dependence on the diode thickness found for V_{fd} and the increase in reverse current for voltages in excess of this bias leads to the conclusion that V_{fd} corresponds to the high field region, commented on in section 4.1.2, reaching the back contact of the device. The penetration rate of the high field region has been measured to equal $0.7 - 1.0\mu$m/V[43] which corresponds to the rate of increase in V_{fd} with substrate thickness. The ohmic contact fabricated with the longer anneal time will have a larger n^+ layer and thus a greater bias is required before the depletion region crosses the doped region. Therefore the reduction in leakage current for the MCP diode B in the post-V_{fd} region is due to a better n^+ layer and thus a reduction in charge injection.

The Alenia diode demonstrated the ability to withstand very high voltages without a dramatic increase in current, due to the very good, non-injecting back contact. The current increase for high applied bias, and thus high fields, could be due to the Poole-Frenkel effect. In section 2.9.3 the current dependence for this effect was given in terms of the electric field. Before full depletion the electric field has been measured to remain reasonably constant with applied bias. After full depletion the electric field is expected to increase with applied bias. The field was modelled in [44] and a linear dependence between the field and applied bias was obtained after full depletion. If Poole-Frenkel emission is the cause of the extra current at high voltage then the extra current should increase, according to equation (2.126), as:

$$J \propto V \exp\left(C\sqrt{V}\right) \tag{4.12}$$

where C is a constant.

Figure 4.13 shows the current characteristic of the Alenia diode fitted for voltages above 500 V with the function:

$$I = P(1) \times V \exp\left(P(2)V^{\frac{1}{2}}\right) \tag{4.13}$$

where $P(1)$ and $P(2)$ were free parameters. Values of 4.4×10^{-11} and 0.067 were obtained for P(1) and P(2), respectively. The good agreement between the fit and the data leads to the suggestion that the extra current is indeed due to the Poole-Frenkel effect.

4.2 Spectral noise measurements

The signal-to-noise ratio of a semiconductor detector is very important and leads to limiting effects on the spatial resolution of microstrip devices (see chapter 6). Therefore the noise spectrum of a simple pad detector was investigated.

This section is divided into three subsections: a brief introduction to noise sources in a semiconductor device, (a detailed discussion of noise theory can be found in [45, 46]), the experimental procedure used to perform noise spectral measurements, and the results obtained for SI-U GaAs diodes.

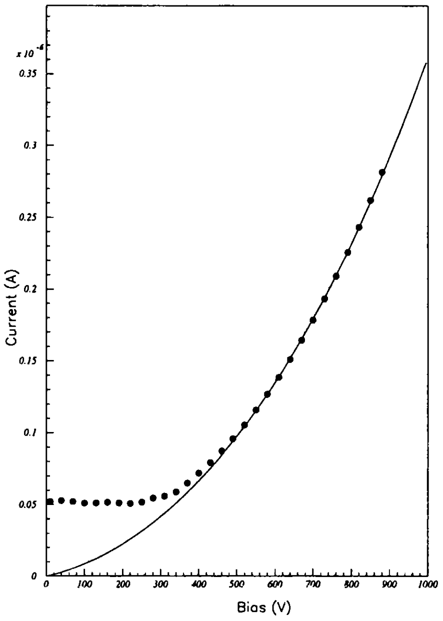

Figure 4.13: The high voltage reverse bias current characteristic of an Alenia diode and the fit of equation (4.13).

4.2.1 Noise sources

The electrical noise or fluctuations in a semiconductor can be described as a series of pulses that are generated by the movement of electrons between scattering or generation-recombination events. This is manifested as spontaneous fluctuations in the current passing through, or the voltage dropped across, a device.

Any quantity $X(t)$ that shows noise can be expressed as:

$$X(t) = < X > + \Delta X(t) \tag{4.14}$$

where $\Delta X(t)$ is the deviation of $X(t)$ from its time average value ($< X >$) at a given time t. $< X >$ is obtained for the fluctuating variable $X(t)$ if the quantity is measured over a sufficiently long time interval. For a stationary function the deviation $\Delta X(t)$ may be written as the Fourier series:

$$\Delta X(t) = \sum_i a_i \exp(i2\pi f_i t) + a_i^* \exp(-i2\pi f_i t) \tag{4.15}$$

where the coefficients a_i are fluctuating amplitudes with an associated frequency f_i.

For a noise component measured at a given frequency f_i:

$$< \Delta X_i(t) >= 0 \tag{4.16}$$

and

$$< (\Delta X_i(t))^2 >= 2 < a_i a_i^* > \tag{4.17}$$

For measurements in a given bandwidth Δf the components of the Fourier series add quadratically to give the total fluctuation. The noise within a unit bandwidth is known as the spectral density, $(S_X(f))$, or power spectral density as it may be considered to be related to the total energy of the system in a unit bandwidth per second. The definition of $S_X(f)$ is:

$$S_X(f) = \lim_{T \to \infty} \overline{\frac{2|\mathcal{X}(f)|^2}{T}} \tag{4.18}$$

where $\mathcal{X}(f)$ is the Fourier transform of $X(t)$ and $\overline{|\mathcal{X}(f)|}$ is the average over many identical events (the ensemble average), rather than over a time duration.

In the simplest case where the transitions that cause the noise are described by:

$$\frac{-d\Delta X}{dt} = \frac{\Delta X}{\tau} \tag{4.19}$$

where τ is the lifetime of the fluctuation causing interaction, the spectral density is Lorentzian and equals:

$$S_X(f) = \frac{< (\Delta X)^2 > 4\tau}{(1 + (2\pi f \tau)^2)} \tag{4.20}$$

From simple statistical considerations $< (\Delta X)^2 >$ can usually be found, for example in the case of number fluctuations it is given by Poisson statistics.

This equation is very general with only the condition of independent electron interactions being imposed. For small fluctuations this is indeed true and thus the Lorentzian spectrum appears often. At low frequencies $(f\tau \ll 1)$ the spectrum is white, that is independent of frequency, while at high frequencies $(f\tau \gg 1)$ it varies as $1/f^2$, and its half power point is at $f = \frac{1}{2\pi\tau}$.

There are four noise source classifications in semiconductors: thermal, shot, generation-recombination, and modulation or $1/f$ noise.

Thermal noise is a white noise source which, for a semiconductor of resistance R, has a mean squared current noise (the spectral current noise density S_i) and a mean squared voltage noise (the spectral voltage noise density S_v):

$$S_i = \frac{4k_BT}{R} \quad ; \quad S_v = 4k_BTR \tag{4.21}$$

Shot noise in a diode is related to the statistical nature of the injection of charge carriers over the Schottky barrier into the semiconductor[45]. For a diode with reverse current I equal to $q < n >$, where n is the spontaneously fluctuating number of electrons that cross the barrier per second, the spectral density is:

$$S_i(f) = 2\alpha q^2 < n >= 2\alpha qI \tag{4.22}$$

where $\alpha = 1$ for full shot noise. In fact as long as the current generating process is related to a time-dependent random variable, which consists of a large number of independent, random, identical events described by Poisson statistics, then the spectral current density will have the same form.

Shot noise is therefore linearly dependent on the frequency of the electrons crossing the barrier and quadratically dependent on the charge of the pulse that the electron creates in the external measuring circuit. The spectrum is white because of the very short transit time of the carriers across the barrier, where the barrier includes the space charge region. For the barrier to show full shot noise at all frequencies two conditions must be met. When charge carriers are injected into the material space-charge neutrality must be re-established in a very short time, given by the material dielectric relaxation time $\epsilon\rho$ [1], where ρ is the resistivity and ϵ the permittivity of the material. For SI-U GaAs this is of the order of 10^{-5} s. The second condition is that each current pulse should be able to displace a charge equivalent to that of one electron in the external circuit, therefore a low probability of trapping is required in the space charge region. If the second condition is not met then α is not equal to one.

For a semiconductor with a significant trap density a third noise source is introduced (generation-recombination noise) due to the continuous trapping and detrapping of the charge carriers. This causes a fluctuation in the number of carriers in the conduction and valence bands. The transitions are described by equation (4.19) and therefore the spectral density is Lorentzian, with a corner frequency given by the lifetime of the electrons in the conduction band (τ_n). The current noise density was calculated by van Vliet[47] to equal:

$$S_n(f) = \frac{< (\Delta n)^2 > 4\tau_n}{(1 + (2\pi f \tau_n)^2)} \tag{4.23}$$

where $< (\Delta n)^2 > \propto I^2$. Measured spectra usually have a dispersed corner frequency which implies a wide distribution of lifetimes. If the diode current is due to generation processes then the expression for the noise will be given by equation (4.23) rather than the shot noise expression of equation (4.22). However, in most Schottky junction devices the applied voltage will increase the injection rate and the noise will show a very close resemblance to shot noise.

At low frequencies an excess noise spectral density with a 1/f amplitude dependence, known as modulation noise, is observed in semiconductors. The magnitude of this noise source is dependent upon the device, material and processing techniques.

A diode may be represented by an equivalent current generator $\sqrt{S_{Idiode}(f)}$ in parallel with a noise-less device through the definition of an equivalent noise current (I_{eq}), or as a voltage source $\sqrt{S_{Vdiode}(f)}$ with an equivalent noise resistance (R_n), by:

$$S_{Idiode}(f) = 2qI_{eq} \quad ; \quad S_{Vdiode}(f) = 4k_BTR_n \tag{4.24}$$

4.2.2 Experimental

The noise spectral densities were measured for two simple pad diodes fabricated from 200 μm thick SI-U MCP material. Both diode contacts were Schottky in nature, the front circular contact had a 200 μm wide guard ring while the rear covered the entire area of the substrate. The reverse (relative to the guarded front contact) saturation current density of both diodes, in the high bias plateau region, was 25nA/mm^2.

The diode was D.C coupled to the input of a low-noise wide-band feedback transimpedance amplifier from the Politecnico di Milano[48]. A feedback transimpedance amplifier is realized by connecting an impedance between the output and the inverting input of a high-gain voltage amplifier. The equivalent circuit is given in figure 4.14, where the labels are explained in the caption. The spectral

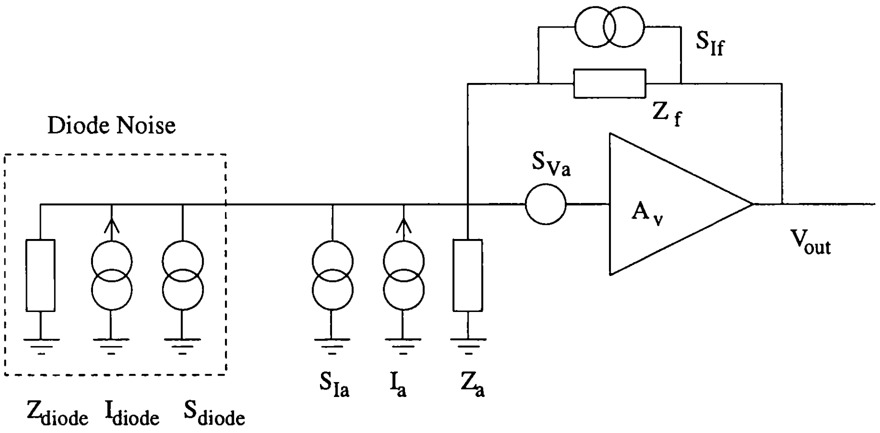

Figure 4.14: The equivalent circuit of the diode connected to the transimpedance amplifier. The diode is represented by its impedance Z_{diode}, reverse bias current I_{diode}, and current noise spectrum, S_{diode}. The feedback impedance is represented by the impedance Z_f and noise spectrum S_{If}. The transimpedance amplifier, with open loop gain A_V, is represented by an open loop input impedance Z_a, and input leakage current I_a with a noise spectrum S_{Ia}. S_{Va} is the spectral density of the input voltage noise of the amplifier.

noise density of the output voltage $S_{V_{out}}(f)$ is given by:

$$S_{V_{out}}(f) = (S_{Idiode}(f) + S_{Iamp}(f))\,|Z_f(f)|^2 \qquad (4.25)$$

where $S_{Iamp}(f)$ is the total equivalent input noise current spectrum of the amplifier and $Z_f(f)$ is the frequency dependent feedback impedance. As long as $Z_f(f)$ is known and $S_{Iamp}(f)$ is small, the current noise spectrum of the diode can be obtained. The output of the amplifier was connected, via a low-noise voltage amplifier, to a signal analyser.

The feedback impedance was realised by a resistor (R_f) and capacitor (C_f) in parallel. The resistor value was large to maximise the gain of the amplifier and minimise the resistor thermal noise, which was the dominant contribution to $S_{Iamp}(f)$. However, the maximum value was limited by the magnitude of the diode leakage current because an excessive voltage drop across the amplifier resulted in saturation. The feedback capacitor was incorporated to increase the high frequency gain. Values of 33 MΩ and 1 pC were used for the feedback circuit. The theoretical background current noise was therefore $2.2 \times 10^{-14}\mathrm{A}/\sqrt{Hz}$ at 300 K. The measured input-referred background noise of the amplifier chain was white over the total frequency range (10 Hz to 100 kHz) with a magnitude of $1.7 \pm 0.5 \times 10^{-14}\mathrm{A}/\sqrt{Hz}$

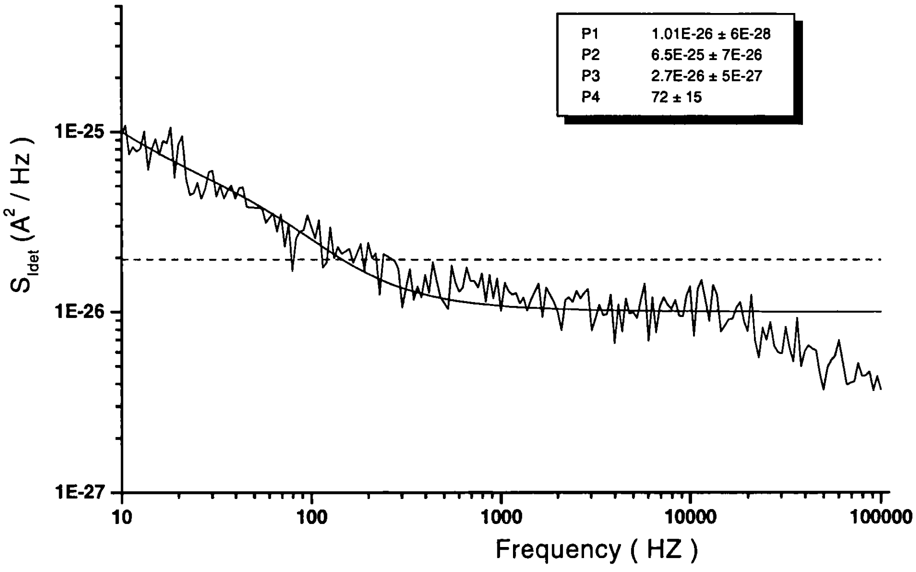

Figure 4.15: Typical noise spectrum of a SI-U GaAs diode in reverse bias measured at 20°C. The key is: solid line - measurement; dashed line - theoretical shot noise; smooth curve - fit of equation (4.26).

at 300 K, which is within the theoretical prediction.

4.2.3 Results and discussion

At zero bias the measured noise was the thermal noise of the feedback impedance and test diode in parallel. From equation (4.24) the equivalent noise resistances of the diodes were found. From the dimensions of the two diodes the material resistivity of $1.5 \pm 0.3 \times 10^7 \Omega$cm was found, which is the same as the bulk resistivity found for a similar diode in section 4.1.1.

Figure 4.15 shows a typical noise spectrum. The spectra were white at frequencies above the corner frequency of the excess noise, however the value of the current noise density was less that that expected from equation (4.22). At a frequency of 10 kHz the noise over the measured leakage current range was between 1.7 and 2.3 times less than the simple shot noise prediction and therefore α equalled 0.5 ± 0.1.

If the leakage current was due to the thermionic emission of carriers over the Schottky barrier, or any other Poisson statistical process, then the noise should be shot noise. A simple model can be devised to explain the shot noise spectra obtained,

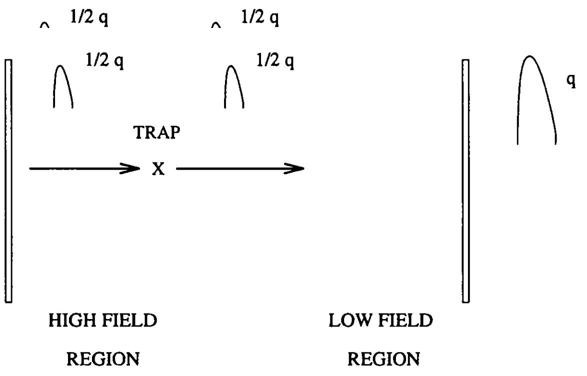

Figure 4.16: Simple model for shot noise.

with reference to equation (4.22) and figure 4.16. One can say that if an electron is trapped in the space charge region, and at a later instant released, then this electron will produce two pulses of charge whose sum is equal to q. If the electron is captured after producing a charge pulse equal to $\frac{1}{2}q$ in the external circuit and then released, on average the frequency of charge pulses produced by the emitted electrons is doubled while the charge is halved. The shot noise spectral density is thus reduced by a factor of two. This process is possible due to the high EL2 trap concentration in SI-U GaAs.

Shot noise should be white due to the fast transit time of the electrons across the high field region behind the reversed biased Schottky junction, however this was not observed. At a frequency between 20 kHz and 30 kHz there was a corner in the noise spectrum. This is explained with reference to the condition imposed on shot noise that charge neutrality is obtained in a time given by the dielectric relaxation time (section 4.2.1). Assuming that the noise source is Lorentzian, the corner frequency corresponds to the reciprocal of this time constant and implies a lifetime of the order 10^{-5} s, comparable with the dielectric relaxation time for SI-U GaAs.

The activation energy plot for the current at -10 V implied that the current, at this bias, was due to generation processes while the plateau in the reverse current at higher voltages was assumed to be due to the enhanced electron capture of the EL2 trap in the high electric field. Therefore, a generation noise spectrum was also expected. An iterative fit of the form:

$$S_{Idet} = P(1)f + \frac{P(2)}{f} + \frac{P(3)}{1 + (f/P(4))^2} \tag{4.26}$$

was performed to the noise spectral density obtained for a reverse bias of 30V at

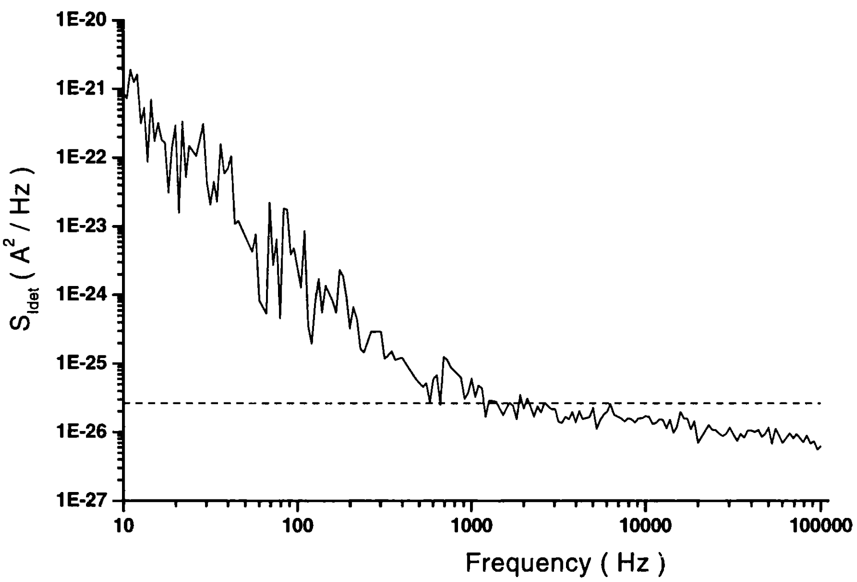

Figure 4.17: Noise spectrum for a bias of 230 V and a leakage current of 82 nA, measured at 20°C. The key is: solid line - measurement; dashed line - theoretical shot noise.

20°C, where P(1) to P(4) were free parameters. The fit and the obtained parameters are shown in figure 4.15. The generation component was significant only at low frequency. The lifetime of the process obtained from the fitted corner frequency of 70 ± 15 Hz was 2.3 ± 0.6 ms.

The final part of the diode noise spectrum was the low frequency excess noise. This was observed for both diodes for currents up to 70 nA (75 V bias) with a frequency dependence of approximately $1/f^{\alpha}$, with $\alpha = 1$. The total excess noise equalled the white noise at a critical frequency of order 500 Hz. At high bias the excess noise and the critical frequency both increased. For a bias close to V_{fd} (230 V for this diode) the critical frequency was greater than 1kHz, see figure 4.17. The shot noise, however, remained less than the theoretical value predicted from the leakage current.

Pulser noise measurements, described in section 3.2.5, were also performed on a simple SI-U GaAs pad diode with a guarded Schottky front and a guarded rear ohmic contact. The substrate was 200 μm thick MCP material.

A 3 μs shaping time (τ) was used for the amplifier to ensure that the measured noise was dominated by the white leakage current noise[49]. The noise was measured

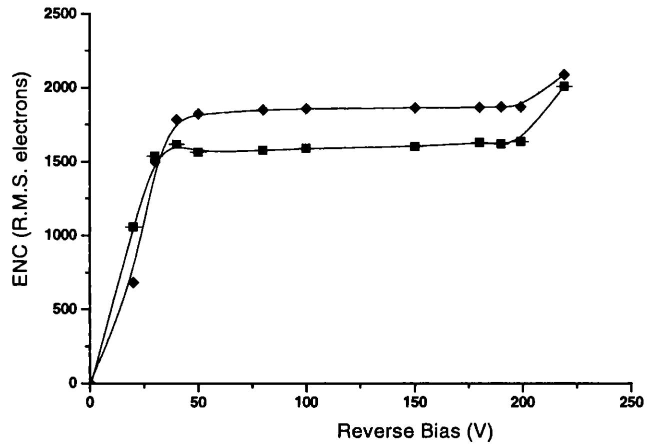

Figure 4.18: Reverse current noise of a SI-U GaAs diode in units of equivalent electrons measured at 20°C. The key is: squares - measured; diamonds - predicted from the measured reverse current.

to increase with shaping time which implies that the measured noise was dominated by current rather than capacitance noise. This was expected for peaking times ~ 1μs due to the high value of the reverse current of the diode and the low input capacitance noise of the amplifier diode combination.

The zero bias FWHM of the Gaussian noise due to the readout electronics and the diode capacitive load was 490 electrons. The Gaussian noise was measured over the high voltage reverse bias characteristic of the diode and the additional leakage current noise was calculated with equation 3.9, and plotted as a function of bias, shown in figure 4.18. The theoretical shot noise (ENC_{shot}), in equivalent electrons, due to the reverse current of the diode (I_{det}) was calculated with:

$$ENC_{shot} = \frac{e}{q}\sqrt{\left(\frac{q\tau I_{det}}{4}\right)} \tag{4.27}$$

where e is the base of natural logarithms, and q the electron charge. The reverse current shot noise is shown in figure 4.18. The figure demonstrates that the Gaussian noise is dependent upon the leakage current, however the magnitude is less than that expected from simple theory. The ratio of the measured to theoretical shot noise at a bias of 100 V was 0.85 which implies $\alpha = 0.7$, to be compared to $\alpha = 0.5 \pm 0.1$ from the earlier spectral noise measurements.

In summary, the current spectral noise of SI-U GaAs diodes has been measured and shown to have a white noise spectrum with a magnitude close to half that expected from the leakage current. A simple model was proposed that assumed charge carrier trapping was responsible for the reduction. A noise component due to generation-recombination noise was observed and the low frequency excess noise was measured to be negligible at the readout frequency of the charge collection experiments (~2 MHz), due to the low value of the critical frequency. Only for bias values approaching V_{fd} was the excess noise significant for frequencies above 1 kHz.

4.3 Capacitance characteristics

This section reports the results obtained using capacitance measurement techniques. The theory of the capacitance of a reverse biased metal-semiconductor contact is contained in section 2.8 for a material without deep levels and extended in section 2.9.4 to include such levels. The implications of the relative magnitude of the trap emission, the test signal voltage and the bias voltage frequencies to the measured capacitance when such levels are present were discussed.

It was shown that both the extension of the depletion region (the sensitive depth of a detector) and the effective doping concentration can be found with the use of capacitance measurements under the correct measurement conditions.

4.3.1 Room temperature measurements

Capacitance measurements of a guarded simple pad SI-U GaAs diode were performed as described in section 3.2.2 at a temperature of 300 K. Results obtained for a diode 4mm in diameter and 183 μm thick, with a test signal of amplitude 0.05 V, are shown in figure 4.19

The figure shows a significant variation in measured capacitance with the test signal frequency, with the lower the frequency the higher the measured capacitance. At the maximum frequency of 100 kHz the measured capacitance was independent of the applied bias. There are two reasons for such an effect: the high resistivity of the substrate material and the low emission rate of the deep traps, of which EL2 is the lowest in GaAs.

Section 3.2.2 explained that the capacitance is determined from the measurement

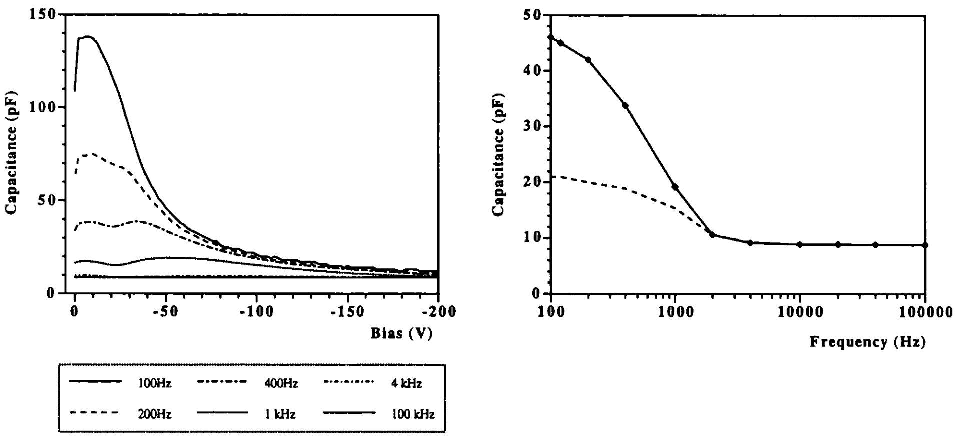

(a) Capacitance as a function of reverse bias for different test signal frequencies. The key is shown on the figure.

(b) Capacitance as a function of test signal frequency at two values of reverse bias. The key is: solid line - 50 V; dashed - 100 V.

Figure 4.19: The capacitance characteristics of a reverse biased SI-U GaAs diode with an area of 0.13 cm^2, measured at 300 K. The capacitance at -10V measured with a test signal of 100 Hz is 1100 pF/cm^{-2}.

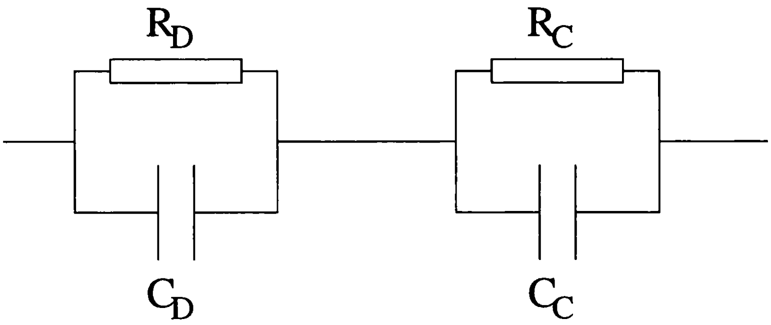

Figure 4.20: The equivalent circuit for a SI-U GaAs diode.

of an A.C. current 90^o out of phase with to the A.C. test voltage. The presence of the large series resistance implies that the phase shift will not be 90^o and thus the measured capacitance was affected.

Capacitance measurements on semi-insulating material can be understood with reference to the equivalent circuit of figure 4.20. The circuit has a substrate capacitance (C_S) and resistance (R_S) in parallel with each other and in series with the depletion region of capacitance C_D and resistance R_D. The impedance (Z) of the circuit is:

$$Z = \frac{R_D}{1 + j\omega R_D C_D} + \frac{R_S}{1 + j\omega R_S C_S} \tag{4.28}$$

If the series resistivity (ρ_S) is very high ($\rho_{\text{SI-U GaAs}} > 10^7$ Ωcm) it will approach that of the depleted region ($\rho_D \approx \rho_S$) and therefore for a diode of length $L + w$ with a depletion region of width w:

$$\begin{aligned} R_D &= \frac{\rho w}{S_e} \\ R_S &= \frac{\rho L}{S_e} \\ C_D &= \frac{S_e \epsilon_s}{w} \\ C_S &= \frac{S_e \epsilon_s}{L} \end{aligned} \tag{4.29}$$

where S_e is the area of the contact, and ρ is the common resistivity. Equation (4.28) now simplifies to:

$$Z = \frac{\rho(w + L)}{S_e(1 + j\omega\rho\epsilon_s)} \tag{4.30}$$

From Ohm's law the current through the device is:

$$\begin{aligned} I &= V\left[\frac{S_e(1 + j\omega\rho\epsilon_s)}{\rho(w + L)}\right] \\ &= V\left[\frac{S_e}{\rho(w + L)} + \frac{S_e j\omega\rho\epsilon_s}{\rho(w + L)}\right] \\ &= V\left[\frac{1}{R_D + R_S} + j\omega C_T\right] \end{aligned} \tag{4.31}$$

where C_T is the total geometric capacitance of the diode. The phase shifted current is therefore equal to ωVC_T which is constant regardless of the depth of the depletion region.

The capacitance obtained at 100kHz was indeed constant with reverse bias at a value of 8.77 ± 0.03 pF; this should be compared to the theoretical geometric capacitance for this diode of 8.04 pF. This 10% difference could result from an inaccuracy in the area of the diode. The diode was not guarded and thus effects due to lateral spreading of the high field region were not taken into account. This would increase the effective area of the diode and thus the value of the measured capacitance.

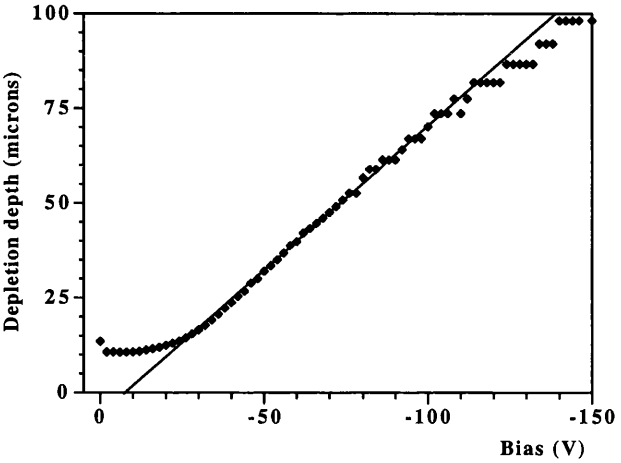

Figure 4.21: The calculated depletion depth (space charge region) as a function of reverse bias for a SI-U GaAs diode measured with a test signal of 100 Hz at 300 K. The fit was performed between -50 V and -100 V.

If the measurement frequency is reduced the electrons released at the edge of the depletion region can short the substrate region and the active region is now, in effect, only in series with the resistance R_S. The measured capacitance will therefore vary as a function of bias, illustrated in figure 4.19(b). The series resistance at room temperature, however, is still very large and the A.C. current and voltage will not be 90^o out of phase.

With equation (2.48) the extension of the space charge region of the diode as a function of reverse bias was found from the capacitance-voltage (C-V) measurement performed with a test signal of 100 Hz and amplitude of 0.05 V; shown in figure 4.21. At a reverse bias greater than 100 V the accuracy of the measurement was limited by the equipment which explains the scatter in the calculated values of w at large reverse bias. The extension of the depletion region measured with the capacitance did not show the standard theoretical dependence of $w \propto V^{\frac{1}{2}}$. Above approximately 30 V reverse bias the extension of the depletion region was proportional to the applied bias. A linear fit performed to the data for a reverse bias between 50 V and 100 V gave the dependence $w = 0.8 \pm 0.1$ V which is consistent with that found in section 4.1.2 and that given in [43].

4.3.2 High temperature measurements

To obtain the trap density of a semiconductor from a capacitance measurement the emission frequency of the trap must be greater than the test voltage frequency, as discussed in section 2.9.4, the bulk resistivity must not be excessive, otherwise the phase difference between the current and voltage is affected, and the leakage current must not be too large or a significant voltage will be dropped across the bulk.

For GaAs the emission rate of the EL2 trap as a function of temperature is given by equation (2.123). At 300 K the emission rate is 0.045 s^{-1} which implies that the trap time constant (τ_t) is 11s (see equation (2.131) of section 2.9.4). For the capacitance technique to be sensitive to this deep level the frequency of the test signal (ω_s) must be less than the reciprocal of this time constant. That is, a frequency of less than 0.09 Hz is required. The minimum test frequency of the Hewlett Packard LCR meter used, however, was 100 Hz and therefore from equation (2.123) a temperature above 410 K was required. The measurements were performed at 420 K with a test signal frequency of 120 Hz to ensure that the EL2 trap was measured.

To overcome the problem of the high resistance of the substrate, (the series resistance), and the voltage drop across the back contact boundary conditions must be imposed upon the measurement procedure. The influence of the forward biased back contact may be ignored for applied voltages considerably greater than the diffusion voltage, due to the very small resistivity of the forward biased contact above this voltage. The effect of the high bulk resistance has been considered by Berman[50] who showed that the perturbation is small and sensible interpretations can be made, from the C-V data, as long as the condition:

$$\omega_s \tau_M \left(\frac{C_B}{C_S} \right)^{\frac{1}{2}} \ll 1 \tag{4.32}$$

is satisfied; where ω_s is the angular frequency of the test signal, $\tau_M = \mathrm{C}_S \times \mathrm{R}_S$, where C_S and R_S are the capacitance and resistance of the substrate, and C_B is the capacitance of the barrier.

The value of τ_M simplifies to $\epsilon_s \rho$ ($= \epsilon_{\mathrm{vacuum}} \epsilon_r \rho$) which has a temperature dependence. The dielectric constant (ϵ_r) has a temperature dependence given by[51]:

$$\epsilon_r(T) = \epsilon(0)(1 + \lambda T) \tag{4.33}$$

where $\epsilon_r(0) = 12.4$ is the dielectric constant at 0K and $\lambda = 2.0 \times 10^{-4}\ K^{-1}$. The value at 410 K is therefore 13.4. The bulk resistance was found in section 4.1.1 to be of order 1 kΩ at this temperature. The ratio of the barrier and substrate capacitance is equal to the ratio of the lengths of the substrate and space charge region. For a low bias the depletion depth is small (~1 μm) and this ratio is approximately equal to the thickness of the diode, (=183μm/1μm for this experiment), due to the low extension of the depletion region. Therefore the Berman condition states that at 410K:

$$\begin{aligned} \omega &\ll (\frac{w}{L})^{\frac{1}{2}} \frac{1}{\epsilon \rho} \\ &\ll (\frac{1}{183})^{\frac{1}{2}} \frac{1}{1.2 \times 10^{-9}} = 6 \times 10^7 \end{aligned} \tag{4.34}$$

and the condition is satisfied for a frequency of 100 Hz.

The reduction in barrier resistivity due to hole injection, tunnelling and image force lowering was not taken into account by Berman. It has been shown[52], however, that as long as the resistance of the barrier is greater than the bulk resistance capacitance measurements on the diode will give the barrier capacitance. If the applied voltage is too high the barrier resistance will fall and the measurement accuracy will be affected. The leakage current will also increase, causing an excessive voltage drop across the bulk.

The reverse current-voltage characteristic of a SI-U GaAs diode was measured at 420 K. The current remained reasonably saturated up to a bias of -10V, as illustrated in figure 4.22. Therefore the voltage dropped across the bulk was small and at -7.5 V equalled:

$$V_S = I_r \frac{\rho L}{S_e} \sim 0.2V \tag{4.35}$$

From the capacitance measurements the doping concentration of the diode was determined. The compensation in SI-U GaAs was discussed in section 2.9.1. The major deep donor is EL2 with a concentration of N_{EL2}. This is partially ionised

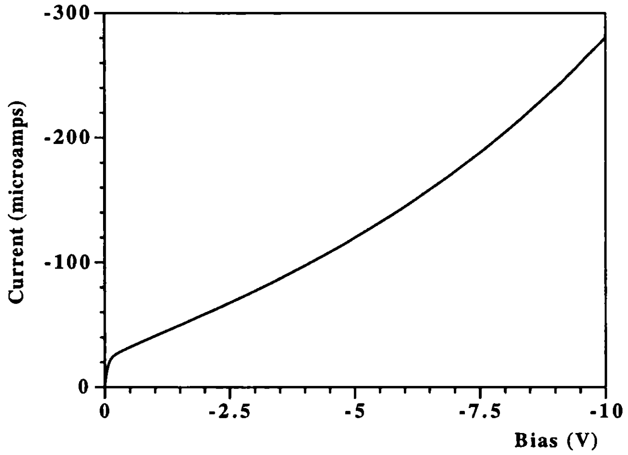

Figure 4.22: The reverse bias current characteristics of a SI-U GaAs diode measured at 420K.

(N^+_{EL2}) and compensates the net shallow acceptors $(N_{net} = N_A - N_D)$, where the shallow dopants are assumed to be fully ionised. In section 2.9.4 N_D and N_t of equation (2.133) must therefore be replaced by $N^+_{EL2} - N_{net}$ and $N_{EL2} - N^+_{EL2}$, respectively. The negative sign is present in the acceptor term due to the negative charge on ionised acceptors.

Satisfying all the above considerations allows the effective trap density $(N_{eff} = N_D + N_t = N_{EL2} - N_{net})$ to be calculated with:

$$N_{eff} = \frac{2}{q\epsilon_s S_e^2}\left(\frac{d1/C^2}{dV}\right)^{-1} \tag{4.36}$$

which is derived from equation (2.139). The temperature dependence of the dielectric constant must be included.

The capacitance measured at -5V with a test signal of 120 Hz is shown as a function of temperature in figure 4.23(a). The value of the capacitance increased from 0.35 nFcm^{-2} at 300 K to 20.7 nFcmn^{-2}pF at 420 K. The increase was due to the contribution of the stored charge in the deep levels because of the increase in electron emission rate with increasing temperature.

The variation of the capacitance with bias voltage is shown in figure 4.23(b). Compared to the measurement at 420 K the capacitance at the lowest temperature hardly changed with bias, illustrating clearly the effect of the low trap electron emission rate and a large bulk resistivity. As the temperature was increased the low

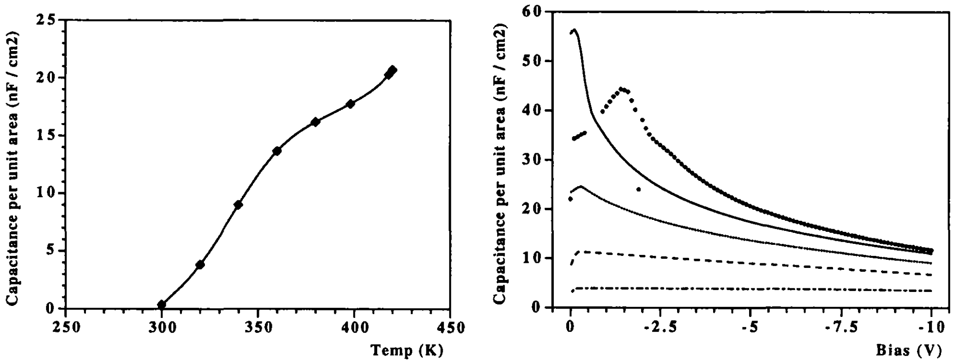

(a) Capacitance at -5 V as a function of temperature. The curve is an interpolation between the measured points.

(b) Capacitance as a function of bias for five temperatures. The key is: dot-dashed line - 320 K; dashed - 340 K; dotted - 360 K; solid - 380 K; circles - 420 K.

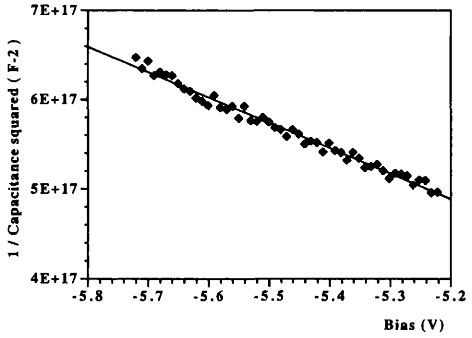

(c) Calculated dependence of $1/C^2$ as a function of voltage across the barrier for a SI-U GaAs Schottky barrier at 420 K.

Figure 4.23: The capacitance characteristics of a reverse biased SI-U GaAs diode, measured with a 0.05 V test signal of frequency 120 Hz.

bias capacitance increased as expected. At 420 K the effective doping concentration was obtained from equation (4.36). It should be noted that for low bias, at the highest temperatures measured, there was a large increase in capacitance with temperature and at a given temperature a steep fall in capacitance with increasing reverse bias. This is clearly visible in figure 4.23(b) for an applied bias below 0.75 V in the C-V measurement performed at 380 K. The 'extra' capacitance could be due to an extra source of charge but the reason for this is not understood at present.

Figure 4.23(b) shows that for the measurement performed at 420 K the change in the gradient of the C-V curve occurred at a larger reverse bias ($\approx -3\ V$). Therefore, reliable measurements could not be performed at this temperature for a reverse bias less than 3 V.

The doping concentration calculation was performed with data above a reverse bias of 5 V to be sure that the contribution from this 'extra' capacitance did not affect the result. The value of the reverse bias could not be increased arbitrarily because it will give rise to an unacceptable flow of free carriers across the barrier and at still higher voltages the barrier will break down. At 420 K a voltage drop across the bulk occurred which required a correction to be made to the voltage actually across the barrier.

The effective doping concentration was found for the limited applied voltage range of -5.25 V to -5.75 V to ensure that the effects of excessive voltage and reverse current did not occur. From the plot of 1/C^2 against bias shown in figure 4.23(c) N_{eff} was found to equal 7.4 $\times$ 10^{15} cm^{-2}. The largest variation in this value occurs due to the exact bias voltage chosen for the 1/C^2 fit. A change of 20% occurs in N_{eff} if the fit is performed at -10V where the reverse current flow is larger. The value, however, is comparable to that given in the literature[52] for Schottky barriers on LEC SI-U GaAs material.

4.4 Charge collection

The SI-U GaAs diodes having been measured and characterised with respect to their electrical properties, their ability to function as working particle detectors must be established. The discussion of signal formation in a particle detector and that relevant to alpha and minimum ionising particle (mip) detection has already been covered in previous chapters (Experimental methods are described in chapter 3). This section therefore contains only the results of charge collection experiments and the inferences that can be made.

The charge signal from a GaAs detector consists of two components, a fast pulse which is mainly determined by the drift time of the carriers and a slow component due to detrapping effects inside the material[23]. The slow component contribution to the total signal is both material- and bias-dependent. The quality of the material determines the amount of trapped charge, while the electric field, determined by the applied bias, defines the drift velocity of the carriers and the extension of the high field region (the active region for charge collection) of the device. The slow component is of the order of several micro-seconds which leads to a dependence of the charge signal on the peaking time of the amplifier. For all the charge collection experiments a peaking time of 500 ns was used. A longer time constant would lead to an increased signal but would also give rise to an increase in the electrical noise due to the high reverse current of the device.

4.4.1 Alpha results

All detectors tested were fabricated with a Schottky front and an ohmic back contact. The signal collected from a reverse-biased detector illuminated with alpha particles from the front side is due to the motion of electrons. The pulse size allows the electron mean free absorption length (λ_n) to be found. Similarly, the illumination of the back side allows the determination of the hole mean free absorption length (λ_p) (see section 3.2.3). The charge collected (Q_{col}) is a fraction of the total deposited by the 5.45 MeV alpha particle ($Q_{dep} = 0.21$ pC). The ratio is the charge collection efficiency (cce). Front illumination will therefore give the electron cce of the detector while back illumination implies the hole cce.

Figure 4.24 shows the electron cce dependence upon applied bias for three detectors of different thickness. The detectors were all made from MCP material (ingots M5/224/UN and M2/295/UN) and were 160 μm, 205 μm and 500 μm thick.

The charge collection increased with decreasing detector thickness but was less

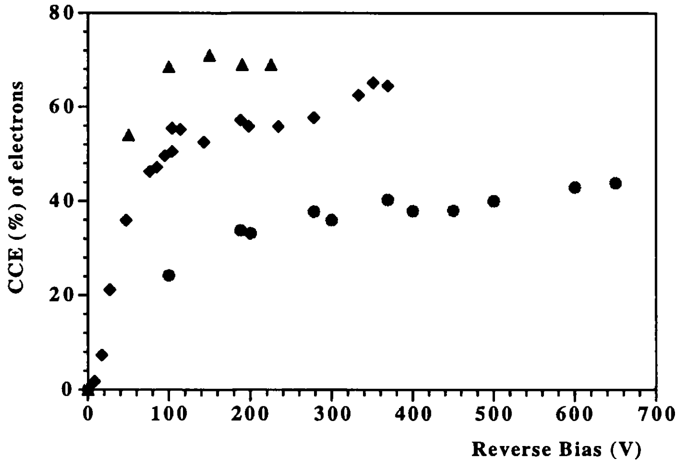

Figure 4.24: Alpha charge collection efficiency as a function of bias for GaAs detectors fabricated from MCP material of three thicknesses. The key is: triangles - 160 μm (M5/224/UN); diamonds - 205 μm (M2/295/UN); circles - 500 μm (M5/224/UN).

than 100% even for the 160 μm thick detector. The electron charge collection increased with bias and plateaued for each detector at approximately the same bias voltage of order 100 V.

The collection of holes will only start to occur when a sufficiently high electric field (and thus the active region of the device) extends to within 20 μm of the back contact. It has been shown for most diodes that at a voltage close to 1 V/μm of detector thickness (V_{fd}) the leakage current increases dramatically due to minority carrier injection, and device operation at a higher bias is prevented. Hole collection, from alpha particles incident on the back contact, has only been observed for an applied bias in excess of this value. Figure 4.25, which shows both electron and hole charge collection efficiencies, was obtained for detector G178. This was a 205 μm thick detector with improved back contact, (diode B of section 4.1.2), which allowed a bias of 400 V to be applied before excessive current prevented detector operation. It must therefore be concluded that the electric field reached the back contact when the applied bias, measured in volts, equalled the detector thickness, measured in microns. Therefore V_{fd} is indeed the full depletion voltage.

For this particular detector the hole charge collection efficiency (= 78.5%) was greater than the electron collection efficiency, which plateaued at 57.7%. Therefore the mean free absorption distance for holes is greater than that for electrons.

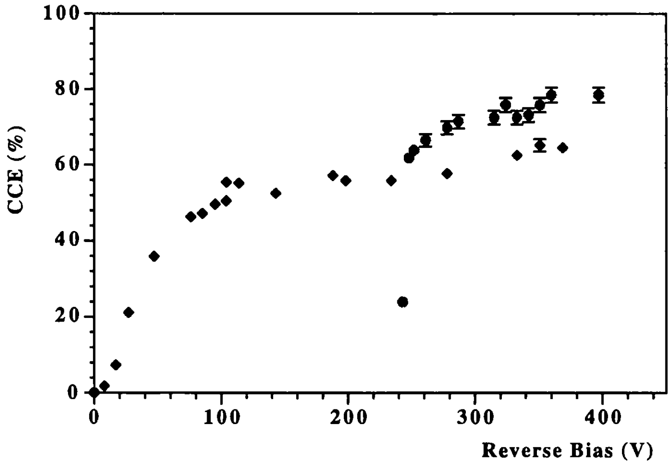

Figure 4.25: Alpha charge collection efficiency for electrons and holes obtained for a 205 μm thick GaAs detector made from MCP material (M2/295/UN). The key is: diamonds - electrons; circles - holes.

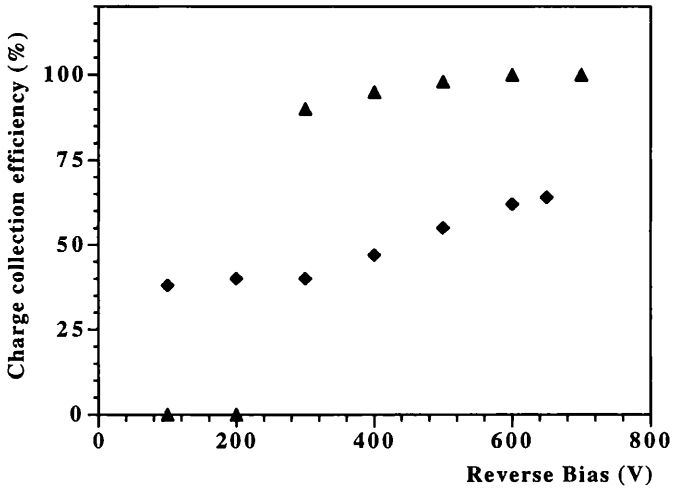

Figure 4.26: Alpha charge collection efficiency as a function of bias for the 200 μm thick Alenia detector AL-W3-8. The key is: diamonds - electrons; triangles - holes.

Due to the nature of the Alenia detectors' back contact (section 4.1.2) they were able to withstand very high voltages before excessive current flowed. The substrate material was supplied by a different manufacturer and therefore the carrier mean absorption distances and charge collection could differ significantly from the MCP material. Figure 4.26 shows the electron and hole cce as a function of bias for a 200 μm thick detector. Again the holes are only detected at a bias in excess of

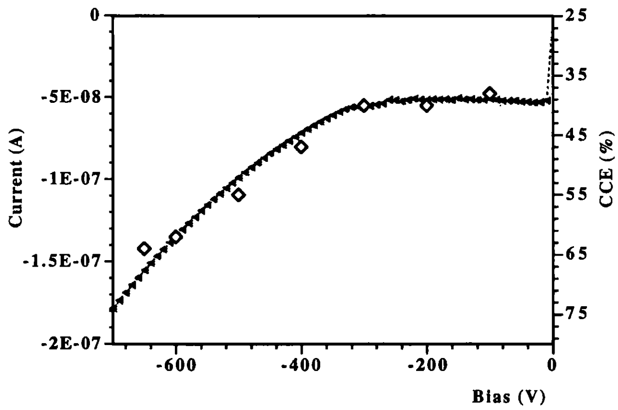

Figure 4.27: The electron charge collection efficiency (diamonds) and the reverse leakage current (triangles) of a 200 μm thick Alenia GaAs detector as a function of bias at very high bias. Both measured at 20°C.

V_{fd} and the cce increased slightly with bias above the minimum bias required for detection to a plateau at 100%. The electron charge collection plateaued at 37% for an applied bias between 100 V and 300 V. At a bias greater than 300 V the electron charge collection increased.

The observed increase in the charge collection of the electrons at very high bias could be due to field-enhanced detrapping of electrons from the EL2 trap. It was suggested in section 4.1.2 that the increase in leakage current at very high voltages was due to the Poole-Frenkel effect. A correlation would therefore be expected between the field-enhanced increase in the current and the increase in electron charge collection. Figure 4.27 shows such a correlation when the plateau region of the electron cce has been normalised to the plateau in the current characteristic. Electron detrapping is therefore very likely to be the cause of both effects.

The mean carrier absorption distances for detectors from both MCP ingots and the Alenia detectors were calculated using equation (3.5) of section 3.2.3. The plateau charge collection efficiency for both carriers must be used, that is the electron cce before the onset of field-enhanced emission. The values of λ_n and λ_p were found through an iterative process where their values were changed by a small amount until agreement occurred between the measured values and those predicted by the equations. From these values the corresponding mip charge collection efficiencies were obtained with the use of equation (3.6). Table 4.2 reports the results.

Detector Material	Absorption distance (μm) Electron	Hole	Predicted Mip CCE (%)
MCP (M5/224/UN)	200.6	704.7	82.4
MCP (M2/295/UN)	130.5	337.2	73.3
Alenia	64	9870	72

Table 4.2: The mean carrier absorption distances measured for GaAs ingots and the predicted mip charge collection efficiencies for 200 μm thick detectors.

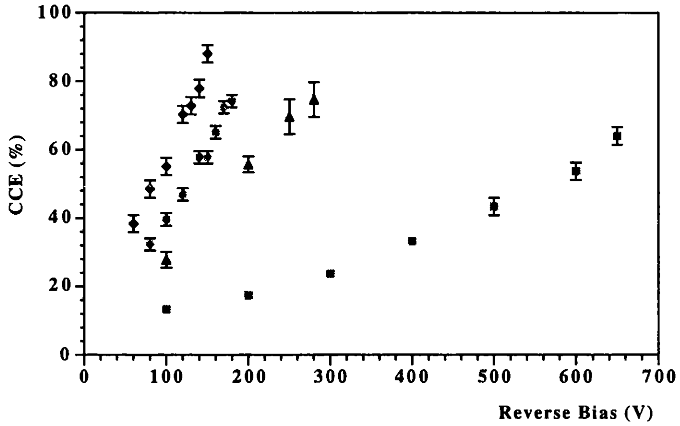

Figure 4.28: The mip charge collection efficiencies as a function of bias for GaAs detectors of four thicknesses fabricated from MCP material. The key is: diamonds - 115 μm (M5/224/UN); circles - 160 μm (M5/224/UN); triangles - 205 μm (M2/295/UN); squares - 500 μm (M5/224/UN).

The calculation of the hole absorption distance in the Alenia material reached the upper bound allowed by the calculation code. The hole absorption distance will approach infinity for the complete charge collection observed. The predicted mip charge collection efficiencies of these detectors are compared to the measured values in the next section.

4.4.2 Minimum ionising particle results

Figure 4.28 shows the mip charge collection efficiencies obtained for MCP detectors of four thicknesses. The detectors were the three of figure 4.24 and a fourth, fabricated in an identical fashion to the others, which was only 115 μm thick. Again the cce of the detectors increased with decreasing detector thickness, as the physical thickness of the detector approached the mean absorption lengths of the carriers.

The actual charge deposited, however, has a linear dependence upon detector thickness (equal to 56 keV/100 μm). Therefore even though the cce of the thickest device is only 64% at a bias of 650 V the charge collected is equivalent to 42560 electrons. While the 115 μm thick detector has a cce of 88% at 150 V, (equivalent to 13460 electrons), the signal is only a third of the magnitude of the 500 μm thick detector. At these operating voltages the leakage current of GaAs detectors was shown to be independent of detector thickness and thus a factor of three is gained in the signal-to-noise ratio for the thicker detector. A thickness of 200 μm is proposed for the GaAs detectors in the ATLAS experiment due to the necessity to keep the amount of material in the inner detector to a minimum (see section 1.3.3). Therefore the increased signal-to-noise ratio of the thickest detector will not be utilised.

The mip cce as a function of bias shows a linear increase with bias which was expected due to the linear increase in the active region of the detector[43]. When the active region extends across the entire detector the increase in charge collection should stop. This is not seen in the figure because of detector breakdown at high bias.

Below full depletion Alenia detectors again showed similar charge collection characteristics to those obtained for Glasgow MCP detectors. Figure 4.29 shows a typical Alenia mip charge collection efficiency as a function of bias. The charge collection plateaued at 350V, which was close to the bias required for a significant alpha hole signal (300V). Therefore the high electric field had extended across the entire bulk of the detector and the device was fully active. The charge collection efficiency, however, did not remain constant for ever increasing values of bias. The reason for this is again the high field detrapping of electrons.

Mip cce's calculated from the alpha data can be compared to those obtained from experiment at a bias value which must be chosen carefully. A low bias will give a low charge collection, due to the low extension of the active region, while a very high bias implies detrapping of electrons. The comparison is made in table 4.3. The cce calculations for the detectors that were not ~200 μm thick were made using the mean carrier absorption lengths calculated for the ~200 μm thick detectors

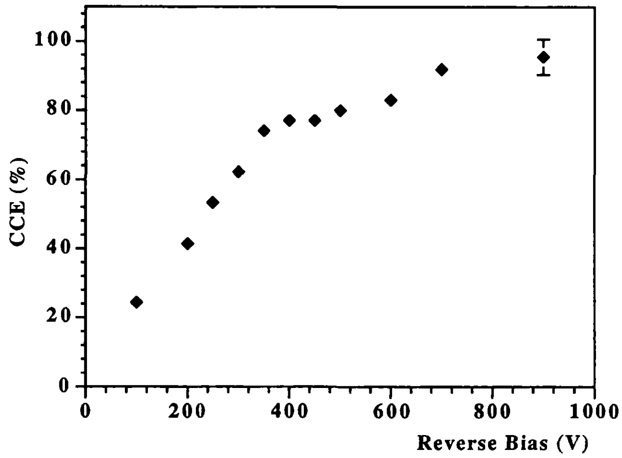

Figure 4.29: The mip charge collection efficiency as a function of bias for a 200 μm thick Alenia detector.

Detector Material	Thickness (μm)	Calculated Mip CCE (%)	Measured Mip CCE (%)
MCP (M5/224/UN)	115	89	88±2.5
MCP (M5/224/UN)	160	85	74±1.8
MCP (M5/224/UN)	220	81	78±2.5
MCP (M2/295/UN)	204	73	75±5.0
MCP (M5/224/UN)	500	65	64±1.8
Alenia	200	72	74±3

Table 4.3: The measured and calculated MIP charge collection efficiencies for GaAs detectors.

fabricated from the same ingot. This process was necessary due to the lack of hole cce data, which could not be obtained because of early detector breakdown.

The quoted error for the measured cce is the experimental error due to the uncertainty in the measurement of the peak in the Landau distribution. During the calculation of the mean absorption distance of the carriers it was assumed that all the charge from the alpha particle was deposited at a depth of 20 μm, which is clearly not the case, that the velocity of the carriers across the detector was constant and the detector was fully active. An error is therefore present in the calculated cce due to the uncertainty of the absorption distances. However the agreement was

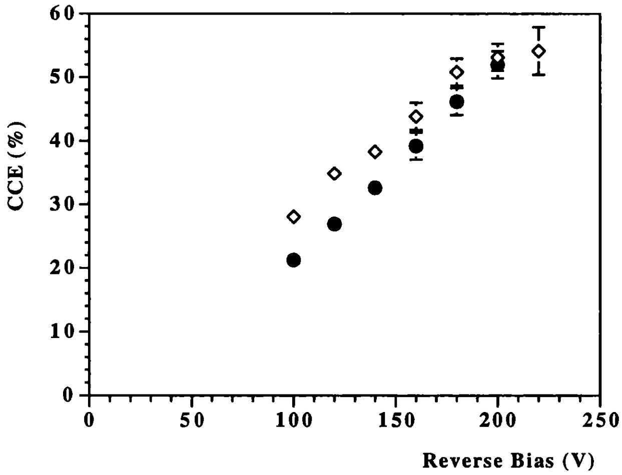

Figure 4.30: The mip charge collection efficiency as a function of bias for a 205 μm thick MCP detector (M2/295/UN) measured at 20°C and -10°C. The key is: open diamonds - 20°C; filled circles - -10°C.

satisfactory which demonstrated the accuracy of the calculated absorption lengths.

The difference between the measured and calculated mip cce for the 160 μm thick detector was because the detector became noisy at high bias and therefore sufficient bias could not be applied to reach the plateau in the cce. The good agreement for the other MCP detectors implies that the detectors either reached, or were very close to, their mip cce plateau.

The agreement between the calculated and measured cce of the Alenia detector is very good. This was expected as the charge collections were seen to reach a constant value for both alpha and mip experiments.

The ATLAS inner detector will be operated at -10°C, however, all the charge collection measurements discussed so far have been carried out at 20°C. Investigation of the effect that the lower temperature has on the charge collection was therefore performed. It was not possible to perform the alpha experiments at -10°C because the equipment was too large to fit in the environmental chamber used for temperature control. Therefore only mip charge collections were obtained. Figure 4.30 shows the mip cce for a 205 μm thick detector measured at both temperatures. A fall in charge collection efficiency at the lower temperature was observed for all bias voltages below that required for a fully active detector.

The reason for the reduced charge was a reduction in the emission rate of the EL2 trap. It was shown in the theory chapter that the emission rate has a temperature dependence given by:

$$e_n = T^2 \alpha_n \sigma_{na} \exp\left(-\frac{E_{na}}{k_B T}\right) \tag{4.37}$$

The emission rate equals 0.02Hz and 0.0004Hz for temperatures of 20°C and -10°C respectively. The low field electron capture cross-section, however, only falls by 25% over the same temperature range, while the high field cross-section in fact shows a very slight increase (see figure 2.16 in section 2.9.3). Because the charge signal is due to the movement of free carriers a reduction in the emission rate of the EL2 trap implies that a signal reduction will occur due to the loss of free carriers. For a bias of 180 V the two cce differed by 10% for the 205 μm thick detector. The majority of the signal has been shown to be due to a fast pulse (25ns) caused by the movement of the carriers before trapping[23] which is the reason why a greater reduction in cce was not observed.

4.5 Other substrate materials

GaAs may be grown by a variety of methods (chapter 3 section 3.1.1) and can be doped with either indium or chromium to form a semi-insulating substrate. Very pure epitaxial layers can also be grown on top of such substrates via many methods. Two of these many material options were investigated from a detector perspective.

4.5.1 Semi-insulating Indium doped GaAs

The high resistivity of SI-U GaAs is obtained through the over-compensation of the net shallow acceptors by the deep EL2 trap (see section 2.9.1). Compensation may also involve other deep traps. Chromium and indium form deep traps in GaAs and are used by industry to produce semi-insulating substrates.

Diodes were fabricated from a 500 μm thick semi-insulating indium doped GaAs wafer so that the electrical and charge collection properties could be obtained. Initial wafer surface preparation and contact metallisation were performed in a similar fashion to the fabrication of the semi-insulating detectors (section 3.1). The only difference in processing between the indium and the SI-U detector was that the longer anneal (described in section 4.1.2), and thus improved back contact, was

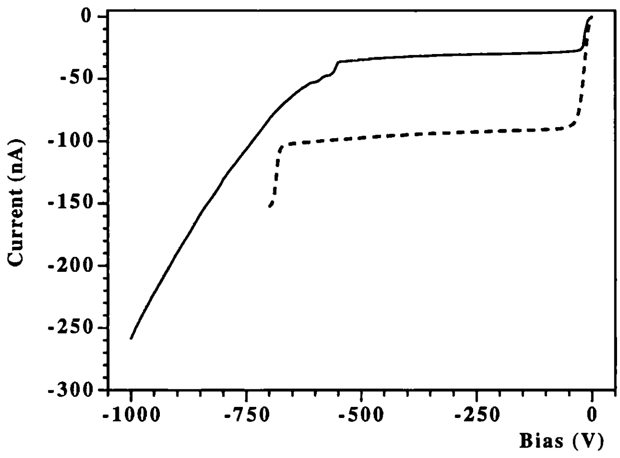

Figure 4.31: The reverse current characteristic of two 500 μm thick GaAs detectors measured at 20°C. The key is: solid curve - indium doped; dashed curve - SI-U.

applied to the indium doped wafer. The radiation hardness of these detectors was tested together with the SI-U devices: the results are reported in chapter 5.

Figure 4.31 compares the current characteristics, at 20°C, of two 500 μm thick detectors fabricated from the indium doped wafer and a SI-U wafer.

The leakage current of the indium doped detector showed a similar characteristic to the undoped device but with a plateau current of only 4.88 nA/mm^2 compared to 13.77 nA/mm^2. The current increased at a voltage comparable to that observed in previous detectors and must therefore be due to the high field region reaching the back contact. The diode did not break down as fast at higher voltages; an effect likely to be due to the annealed back contact rather than the change in substrate material. The similarity in the operational current characteristics of the two devices leads to the assumption that a similar field profile inside the two devices may also be present and thus a zero space charge region could exist. Investigations of the low voltage characteristics were not performed and no studies concerning the mapping of the electric field have been performed on such devices. The motivation of this particular study was to determine whether these diodes would work as detectors, and if so, were they more radiation hard than SI-U GaAs detectors.

Their performance as particle detectors was verified with the use of both mip and alpha experiments. The results are given in figure 4.32. Figure 4.32(b) compares the mip cce to that from a 500 μm thick SI-U detector.

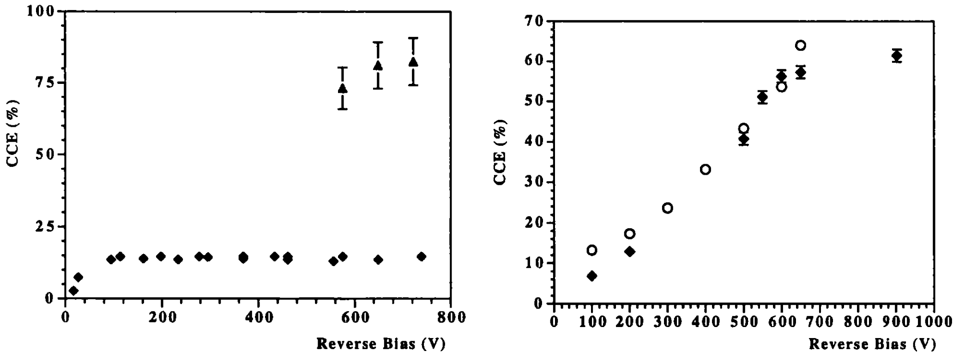

(a) Alpha particles. The key is: diamond - electron; triangle - hole.

(b) Mips. The key is: empty circle - SI-U; solid diamond - SI-indium doped.

Figure 4.32: The charge collection efficiency of indium doped GaAs detectors for electrons and holes, determined from alpha particle and mip experiments.

It is clear that both detectors behaved similarly with respect to the collection of charge deposited by minimum ionising particles. The charge collection efficiency showed the same bias dependence, observed for all the SI-U detectors, with a linear rise which plateaued when the detector was fully active. The plateau was not observed for this undoped detector due to the nature of the back contact, but it is expected that the charge collection would not have increased significantly with bias, until field-enhanced detrapping occurred at a very high applied bias. The linear rise in cce again implies an increasing active region width with applied bias.

The results obtained from the alpha experiments showed that the high field region approached the back contact only for a bias in excess of 500V, in agreement with the IV curve and the SI-U detectors. The hole charge collection is again greater than the electron cce. The mean absorption distances obtained from these results are $\lambda_n = 53\ \mu$m and $\lambda_p = 1204\ \mu$m. The hole charge collection efficiency might have increased slightly if a higher bias could have been applied to the device and therefore the hole absorption distance is a lower limit. The electron absorption distance is significantly lower than that measured for the MCP material, but the collection of holes was much better, which is the reason why similar mip cces were obtained. For this detector the predicted charge collection efficiency for mips is 53% which is less than the 60% observed experimentally. The difference may be due to an underestimation of the hole absorption distance.

The electrical behaviour of the semi-insulating indium doped GaAs detectors was similar to the SI-U devices. The charge collection showed that the mean carrier absorption distances differed between the SI-U and the indium doped material but for each material the hole absorption distance was the greater. However, the charge collection for mips as a function of bias was very similar in both dependency and magnitude. Indium doped GaAs detectors therefore work and the predicted mip cce for a 200 μm thick detector is 67%.

4.5.2 VPE material

Thick epitaxial layers of GaAs have been grown using low pressure vapour phase epitaxy techniques [33]. Such wafers have been processed at Glasgow University to investigate their possible application as X-ray detectors [34]. The results reported here include the electrical characterisation and the detector performance determined as for the semi-insulating material.

The epitaxial layer was grown on top of a 450 μm thick, heavily doped LEC substrate. The substrate, doped with silicon at a concentration of order 10^{18} cm^{-3}, produced an n$^+$ back contact to the epitaxial layer. The epitaxial layer had a non-uniform thickness with a definite gradient across the wafer. A maximum thickness of 239 μm which reduced to 125 μm was measured. Due to the non-uniform profile of the layer, mechanical lapping (chapter 3 section 3.1.2) was not utilised and only the chemical polishing stage was performed to remove surface defects. Before polishing the original surface quality was very poor. The chemical polishing removed 30 μm of the epitaxial surface and left an improved surface quality, however the gradient in epitaxial layer thickness was still present.

Contact fabrication was performed in exactly the same fashion as that used for the SI-U diodes to produce simple pad diodes. However, due to the large thickness gradient the mask was unable to make a perfect contact with the upper surface and caused the pad and guard ring on the Schottky side to short together.

The reverse current characteristics of an epitaxial diode and a 200 μm thick SI-U LEC diode are shown in figure 4.33. While the epitaxial diode did not have a plateau in the current characteristic, the leakage current of this diode was

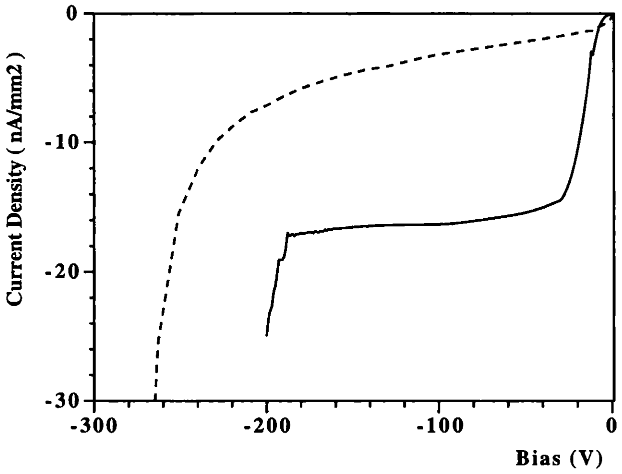

Figure 4.33: The reverse current characteristics of a VPE GaAs diode and a 200 μm thick SI-U LEC GaAs diode measured at 20°C. The key is: solid curve - SI-U LEC; dashed curve - VPE.

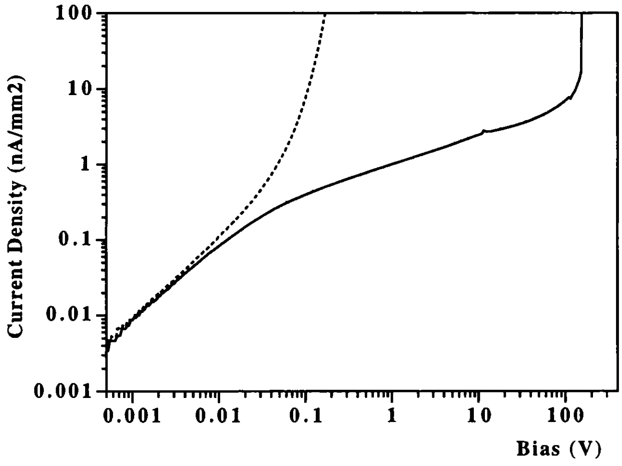

Figure 4.34: The forward and reverse current characteristics of the VPE diode epi-8 measured at 300K. The key is: solid curve - reverse; dashed curve - forward.

less than the typical SI-U LEC GaAs diode. At a bias of 100V the current was 3.1 nA/mm^2 compared to 16.33 nA/mm^2 for the SI-U device. At 160V the currents were 4.96 nA/mm^2 and 16.65 nA/mm^2 for the VPE and LEC diodes respectively.

The current-voltage characteristic of the VPE diode was investigated further using the ideas developed in the theory chapter. The forward and reverse current characteristics, after correcting for the offset voltages as discussed in section 4.1.1, are shown in figure 4.34 for the diode epi-8.

The barrier height for this device can be found from the current dependence by a number of methods.

The first was to examine the very low voltage section of the dependence. If thermionic-emission is assumed, the expression for forward and reverse characteristics simplifies to equation (4.1). The gradient (m) of the forward and reverse bias dependences should therefore be equal and the I-V curve should pass through the origin. Substituting for the saturation current of equation (2.82) gives:

$$\phi_b = -\frac{k_B T}{q} \ln \left[\frac{k_B T}{q} \frac{1}{A^{**}T^2} \frac{m}{S_e} \right] \tag{4.38}$$

which allows the barrier height to be determined. The active area of the diode (S_e) was $\pi\times$ 0.201^2 cm^2. The gradients of the forward and reverse bias curves, for a voltage from 0.00014 to 0.001V, and the calculated barrier heights, for the diode epi-8, were:

$$\begin{aligned} \text{Forward: m } &= 1.2246 \times 10^{-7}\ A/V \rightarrow \phi_b = 0.805\ V \\ \text{Reverse: m } &= 1.2143 \times 10^{-7}\ A/V \rightarrow \phi_b = 0.805\ V \end{aligned} \tag{4.39}$$

The dependence upon the value of A^{**} chosen is not critical, with a factor of 10 increase in A^{**} altering the barrier height by only 7%. The barrier height determined from both the forward and reverse sections of the curve were equal.

The second method used to determine the barrier height involves the forward bias current dependency shown in figure 4.35. With reference to equation (2.82), the extrapolation of the log of the current density at zero voltage is the saturation current J_s and the barrier height is:

$$\phi_b = \frac{k_B T}{q} \ln \left(\frac{A^{**}T^2}{J_s} \right) \tag{4.40}$$

From the dependency shown, the extrapolated value of the current was 2.373 nA, or 1.870 $\times$ 10^{-8} Acm^{-2}. From this value of J_s at 300K a barrier height of 0.81 V was found. Again the value is insensitive to the exact value of A** used.

These two methods are similar and have relied on the value of the active area of the diode. This can be different from the actual area of the metallized region. For a poorly cleaned or incompletely reacted surface the electrically active area may

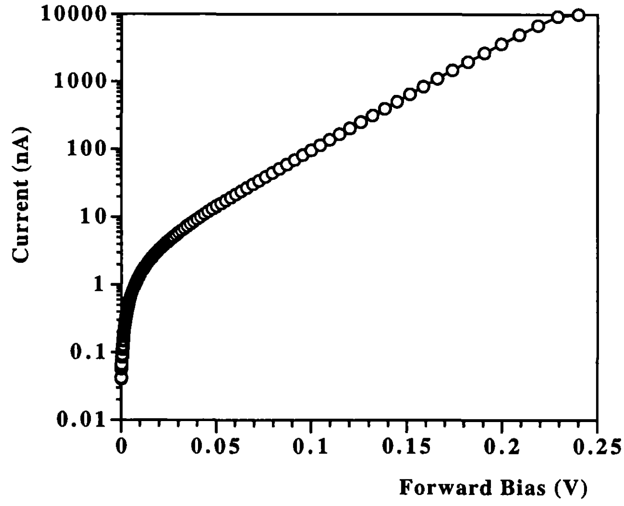

Figure 4.35: The forward current characteristic of a VPE GaAs diode measured at a temperature of 300K.

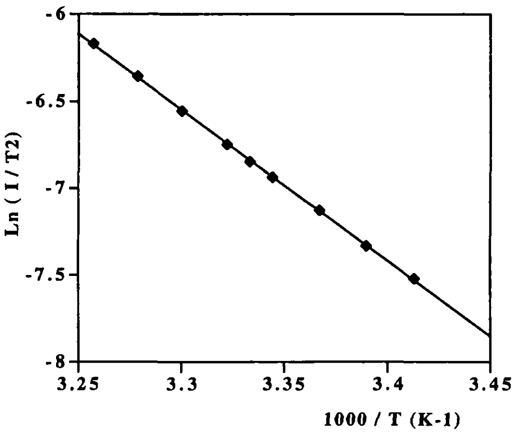

Figure 4.36: The activation energy plot for determination of the barrier height for the VPE diode epi-8 under a forward bias of 0.1V.

only be a small fraction of the geometrical area, whereas for a strong metallurgical reaction the active area may be larger than the apparent area. The active area is therefore not known precisely.

Barrier heights may be found by utilising the dependence of the forward leakage current on the measurement temperature as shown in section 4.1.1 for the LEC SI-U diode. An activation energy plot is shown in figure 4.36 for the VPE diode epi-8 under a forward bias of 0.1V. The gradient equals -8.69 ± 0.06, from which a barrier height of 0.848 ± 0.005 V was determined. From the intercept of the curve with the

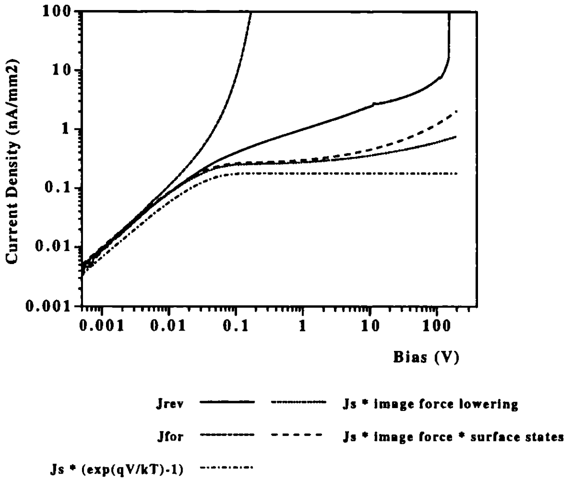

Figure 4.37: The current characteristics of the VPE diode epi-8 measured at 300K and theoretical predictions of the reverse current. The key is shown on the figure.

y-axis the product of the Richardson constant and the electrically active area can be found. A value of 1.02 AK^{-2} was obtained for this diode.

This product was required for the barrier height determination for the first two methods. Substituting this value into equation (4.38) gave for the first method a barrier height of 0.803V while a new barrier height of 0.810V was obtained from method two. The difference between the barrier height found from the activation method and the average of those found from the IV characteristics was only 5.5%.

Figure 4.34 illustrates that the reverse current of this diode did not saturate. Section 2.6.5 discussed several reasons why such an non-ideal behaviour may occur. The current characteristics are plotted again in figure 4.37 with the expected ideal reverse characteristic and the theoretical predictions for two sources of barrier lowering, for a barrier height of 0.81V.

The ideal reverse characteristic is denoted as $J_s(\exp(qV/kT)-1)$ in the key and shows no increase with bias for voltages above $3k_BT/q$, contrary to observation.

Barrier lowering can occur due to image force lowering (see section 2.5.4) which results in an increase in current with reverse bias. The barrier is lowered through this process by:

$$\Delta\phi_{bi} = \left[\frac{q^3 N_D}{8\pi^2 {\epsilon_s}^3}\left(\phi_b - V - V_n - \frac{k_B T}{q}\right)\right]^{\frac{1}{4}} \tag{4.41}$$

and therefore to calculate this effect the net donor density of the material must be known. The free carrier density of a Schottky junction can be found from the capacitance as a function of reverse bias (see section 2.8). Such a method was employed and is discussed after the current characteristics. A value for the free carrier density was found to be 2.8 $\pm 0.2 \times 10^{14}$ cm^{-3} and assumed to equal the net donor density of the material. The donor density is also required to determine V_n with equation (2.38). The image force lowering for this barrier of 0.81 eV at a temperature of 300K was therefore:

$$\Delta\phi_{bi} = \left[9.34 \times 10^{-9}(0.59 + V_r)\right]^{\frac{1}{4}} \tag{4.42}$$

where V_r is the absolute value of the reverse bias. The increase in the reverse current through this process is insufficient to account for the observed current (see figure 4.37).

A second process that reduces the barrier height, discussed in section 2.6.5, is that due to the effect of an interfacial layer. The barrier lowering is proportional to the maximum electric field at the barrier which has a dependence upon the applied bias. Barrier lowering due to this process is:

$$\Delta\phi_{bi} = \alpha\left(\frac{2qN_D}{\epsilon_s}\right)^{\frac{1}{2}}\left(\phi_b - V_n - \frac{k_BT}{q} + V_r\right)^{\frac{1}{2}} = \alpha \times 8800 \times (0.59 + V_r)^{\frac{1}{2}} \tag{4.43}$$

where α is usually of the order 10Å. Included in figure 4.37 is the calculated current due to this effect, labelled as an additional effect due to surface states. Again the measured current is greater than theory. The barrier lowering by the two above processes did not correctly reproduce the shape of the measured current characteristic.

A third source of leakage current discussed in chapter 2 is due to generation processes (see section 2.6.5 equation (2.99)). Generation current will only become significant for diodes with high barriers, such as that found for this diode. The shape of the IV curve is also significantly different, with a current dependency given by:

$$J_{gen} = \frac{qn_iw}{2\tau_r} \propto (V_{d0} + V_r)^{\frac{1}{2}} \tag{4.44}$$

The ideal thermionic current and the best fit found for the generation current with the thermionic current added in series (labelled as Jgen + $J_s(\exp(qV/kT) - 1)$) are shown in figure 4.38 up to a reverse bias of 10V. The fit was performed between 0 and

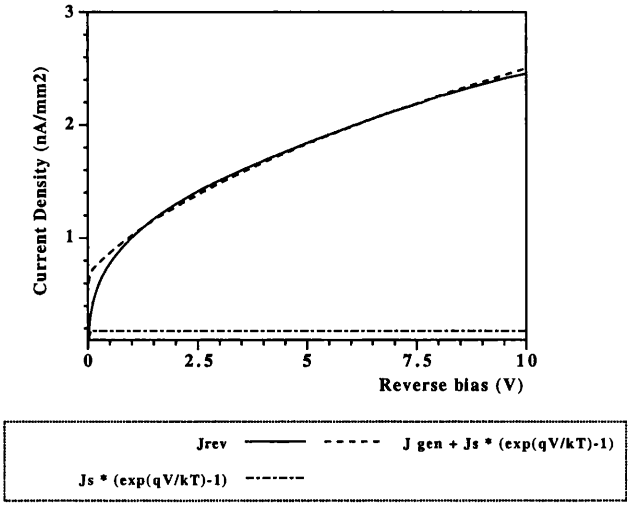

Figure 4.38: Current fits to the reverse current characteristic of the VPE diode epi-8 fitted for an applied bias between 9.5×10^{-2} and 9.5 V.

10V with the value of V_{d0} fixed to that obtained from experiment while the power and the constant of proportionality were free parameters. Values of 0.53 ± 0.02 and 0.66 ± 0.02 were obtained for the power and the constant respectively, consistent with the assumption of generation current.

The activation energy of this section of the reverse bias IV characteristics was found by measuring the current (I) as a function of temperature (T) with an applied reverse bias of 10 V. The current was assumed to be generation current and thus a plot of $\ln(I/T^2)$ against 1/T gives a straight line with the gradient equal to the activation energy (E_A). The result is shown in figure 4.39 and a value of $E_A = 0.73 \pm 0.02$ eV was obtained. This is equal, within errors, to the expected value of $E_g/2 = 0.71$ eV for generation current in pure GaAs.

For a reverse bias greater than 11 V the shape of the current characteristic changed for reasons not fully understood. The pad diode did not have a guard ring and excess current due to edge effects is expected. Such edge currents are described as the dominant effect by Sze[1] for most practical devices without guard structures. Devices with guard rings and/or different diode diameters were not available and therefore systematic studies of this effect could not be made.

In contrast to the LEC SI-U material, the epitaxial layer was grown in an environment designed to minimise the production of the EL2 defect. Therefore the

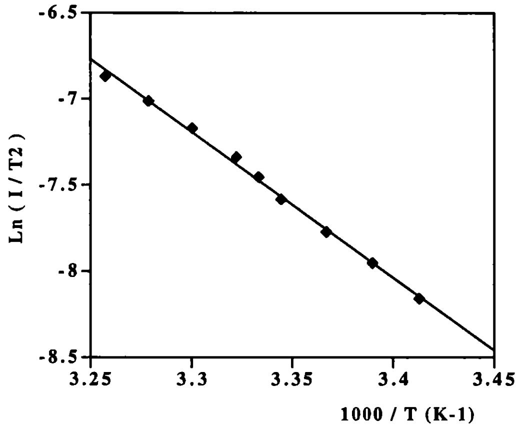

Figure 4.39: Activation energy plot for the VPE diode epi-8 performed for a reverse bias of 10V.

capacitance characteristic can be understood from simple theory. Two capacitance measurements were performed, one with a test signal of 100Hz and the other with a signal of 100kHz. The results obtained from the two test signals showed only a slight difference in the capacitance as a function of bias confirming the assumption of a low concentration of deep levels. From the CV curve the free carrier density in the material was found, which is equal to the donor density if the dopants are shallow (see section 2.8).

The graph of $1/C^2$ against V for voltages below 20V had a gradient of 2.4×10^{-6} $pF^{-2}V^{-1}$ at 100kHz which gave an effective doping density of 2.8×10^{14} cm^{-3} for the diode geometry used. Capacitance measurements should be performed on diodes which have a reverse current of only a few nA/mm^{-2} to prevent a significant voltage drop across the bulk of the diode. Figure 4.40(a) shows the calculated doping density and the reverse current as a function of bias. The variation in the doping density with reverse bias is only of the order 10% and is not thought to be significant. The accuracy of the measurement depends upon the electrically active area (S_e) of the device because:

$$N_D = \frac{2}{q\epsilon S_e^2}\left(\frac{d1/C^2}{dV}\right)^{-1} \tag{4.45}$$

This area is not known to the accuracy of the physical measurement of the device due to the effects mentioned above and an error of at least 10% can be expected in the measurement of N_D.

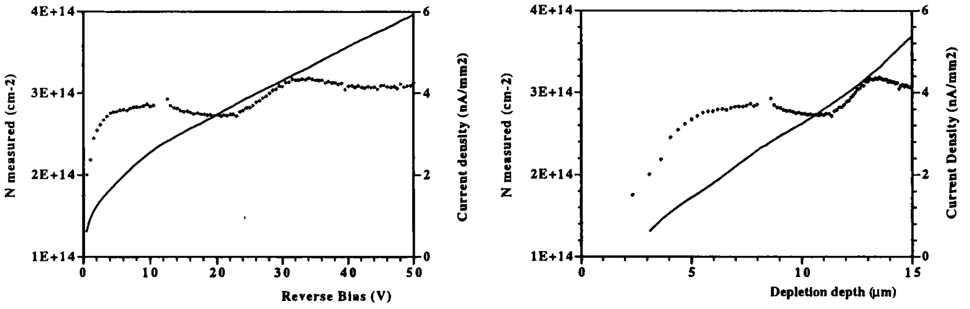

(a) Applied bias. (b) Depletion depth.

Figure 4.40: Results obtained from CV measurements on a VPE GaAs Ti/Pd/Au barrier as a function of applied bias and depletion depth. The key is: dots - doping density; curve - current density.

From the expression for the capacitance of a reverse-biased Schottky barrier the depletion depth of the barrier can be found (equation (2.48), section 2.5.2). The calculated doping density and the measured reverse current are shown as a function of the calculated depletion depth in figure 4.40(b). The current shows a linear increase with depletion depth up to 8 μm (corresponding to a bias less than 10V) which again suggests that it is due to generation rather than thermionic processes.

The depletion depth of the barrier as a function of bias is shown up to the break down bias of 180 V for the VPE diode epi-8 in figure 4.41. The detector was only depleted by 22.3 μm at 100V and 27.4 μm at 150V due to the high value of the free carrier density. It should be noted that no correction has been applied to the data to account for any voltage drop across the diode bulk due to the significant current at these high voltages. The small extension of the depletion width with bias has implications for the use of such devices as particle detectors.

If the detectors demonstrated a charge collection efficiency of 100% then a signal of 3644 electrons would be detected at a bias of 150 V from the passage of a mip. The leakage current (I_{det}) at this bias was 200 nA. If the detector was read out by an amplifier with CR-RC shaping, with equal differentiation and integration time constants, and a peaking time (τ) of 500 ns, an equivalent noise charge (Q_l), due to the leakage current of:

$$Q_l = \frac{1}{q}\sqrt{2 \times 0.924 q \times I_{det}\tau} \tag{4.46}$$

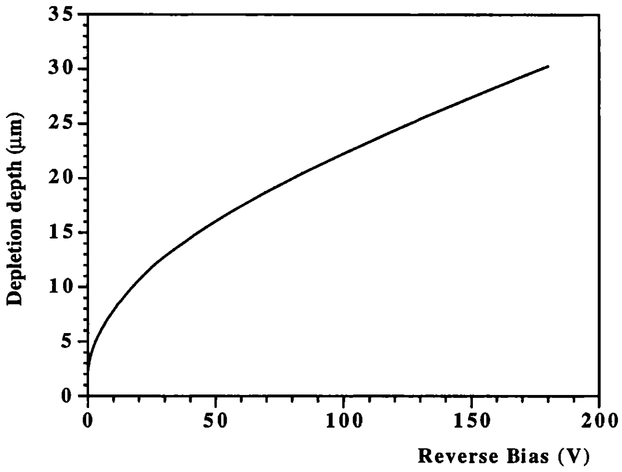

Figure 4.41: The dependence of the depletion width on applied bias.

is expected. Therefore the signal-to-noise ratio for a mip will equal 3.4. The experimental noise was also increased by the addition of pre-amplifier and load capacitance noise and a distinguishable signal was not obtainable.

The charge collection from an alpha particle was also affected. No hole signal could be obtained due to the 450 μm thick substrate. The ^{241}Am alpha source used had a thin absorption layer in front of the source which reduced the average energy of the alpha particles. The energy was measured with an over depleted silicon detector to be 4.1 MeV. These deposit their energy, according to the Bragg equation, within the first 13 μm of the GaAs material. However, due to the small extension of the depletion width it is no longer true to say that the signal from this detector is mainly due to the motion of one carrier. Also as the energy deposition is non-uniform, with a larger fraction occurring at the end of the alpha particle path, the alpha signal is not equally dependent upon both carriers.

The charge collection efficiencies obtained for alpha particles incident upon the front of two VPE detectors are shown in figure 4.42(a) as a function of bias and in figure 4.42(b) as a function of depletion width. The measured charge collection efficiency was very high, even at a bias of 20V. The charge collection showed the expected increase due to the increase in depletion width. For the diode epi-5 a cce of 100% was obtained for a depletion width between 10 μm and 15 μm as expected from the alpha particle range in GaAs. However, at zero applied bias the depletion

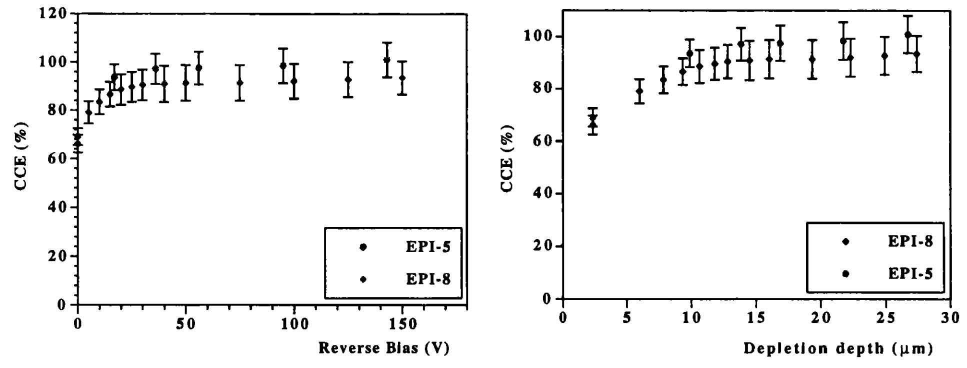

(a) As a function of applied bias.

(b) As a function of depletion width.

Figure 4.42: The charge collection efficiency obtained from alpha particles incident upon the front contact of a VPE GaAs Schottky detector.

width was only 2 μm but a signal of 65% was obtained. Therefore diffusion or drift of charge into the depletion region must occur.

The charge collection efficiency from the absorption of a gamma photon was also obtained. The experimental apparatus was the same as that for the alpha experiments except that the measurement was not performed under vacuum. An encapsulated ^{241}Am source, which produces 60keV γ photons that interact in the material to give a 60keV photo peak, was used. The charge collection from such a source does not depend upon detector thickness as long as the liberated electron does not escape from the depletion region. For the diode epi-5 a cce of 93±17% was obtained at a bias of -50 V increasing to 97±17% at -200 V. The large error arose due to the large leakage current of the diode. Noise limitations prevented results from the diode epi-8 being obtained.

The VPE material tested behaved according to simple theory, that is without the presence of a significant concentration of deep traps. The donor concentration was obtained via CV analysis of the material to be 2.8 $\pm 0.2 \times 10^{14}$ cm^{-3}. This high value prevented the extension of the depletion region beyond 30 μm before breakdown occurred, due to the high bias required (>200 V). Charge collection experiments were limited due to the small depletion region. However, the charge collection efficiencies obtained from alpha particles and 60keV gammas were close to 100%. The material could be very promising for detector development if the free carrier concentration can be reduced. Radiation tests were performed on four samples with the results reported in the next section.

Chapter 5

Radiation Studies

The primary motivation for the development of GaAs position sensitive detectors for the ATLAS project is the requirement for radiation hard devices. The radiation environment at the experiment has been discussed in chapter 1 where it was stated that, at full luminosity ($10^{34}/\text{cm}^2/\text{s}$), the major particular radiation fluxes in the ATLAS detector at the proposed GaAs positions in the forward tracker are expected to be: pions $\sim 3 \times 10^{13}$ /cm^2/year, neutrons with a flux between $0.5 - 1.0 \times 10^{13}$ /cm^2/year and protons and kaons both $\sim 0.3 \times 10^{13}$ /cm^2/year.

GaAs detector performance was therefore studied after high fluences of neutron, proton and pion radiation. This chapter discusses the theory of radiation damage, the experimental procedure used to perform the irradiations, and the post-irradiation detector characteristics.

5.1 Theory

The effect that radiation has on the operation of a particular device depends upon the energy and type of the radiation, the material from which the device is made and the semiconductor characteristics upon which the device depends for successful operation. The interactions of the incident radiation in the material usually produce four types of effect:

- **Transient ionisation effects**

  When a high energy particle passes through matter it will create electron-hole pairs. These are used to detect the passage of such particles and are therefore necessary for position sensitive detectors.

- **Long-term ionisation effects**

  Where the mobilities of the charge carriers differ greatly, the production of ionisation can cause long term effects. This effect will occur more predominantly at semiconductor-insulator interfaces due to the large difference between the carrier mobilities of the materials. The mobile carriers in the semiconductor will be removed, resulting in a fixed charge in the insulator of the device (usually an oxide). The charge will increase with fluence, leading to changes in the electrical characteristics of the device. This is the cause of the radiation sensitivity of MOS devices due to their semiconductor-oxide interface.

- **Nuclear transmutations**

  For some semiconductors the incident radiation will cause nuclear reactions in the material which can result in significant isotope doping of the device. These dopant isotopes may form both shallow and deep levels in the material.

- **Displacement effects**

  The displacement of atoms from their normal lattice sites, via interatomic collisions, produces a less ordered crystal structure and long-lived changes to the device.

For GaAs detectors the first effect, used as the source of signal production, is non-damaging. The second is insignificant because the detection process is dependent upon bulk properties, rather than processes at the surface and, while the increase in surface charge can reduce the interstrip capacitance of microstrip detectors[53], understanding this effect was not the aim of this work. It is the latter two that cause significant radiation-induced effects in bulk semiconductor detectors.

The production of a room temperature thermally stable displacement effect can be divided into four stages:

1. The first is the primary interaction between the irradiating particle and a lattice atom. If the incoming particle has sufficient energy the lattice atom will be knocked out of its normal lattice position, creating the primary knock-on atom (PKA). The energy required to remove an atom from its lattice site, the

Wigner energy, is of order 10 eV for GaAs[54]. The maximum non-relativistic energy transfer (E_{T-max}) between the energetic particle, of mass m and energy E, and the lattice atom (mass m_l) is:

$$E_{T-max} = 4\frac{mm_l}{(m+m_l)^2}E \tag{5.1}$$

Therefore for GaAs an electron requires an energy $\sim$ 300 keV to displace a lattice atom, while a neutron only needs an energy of order 200 eV. That is, the higher the mass of the energetic particle the lower the kinetic energy required to cause lattice displacements. Below the Wigner energy the energetic particle only causes lattice excitations and ionisation.

For very high energy interactions the lattice atom can fragment and the PKAs are made up of several smaller particles which now have lower mass.

2. If the fragments of the target atom have sufficient energy they move through the lattice and displace additional atoms. A cascade results. As the PKA interacts it loses energy and its mean free path is reduced, resulting in a higher density of lattice defects at the end of the path. When the mean free path of a recoil atom is less than the range of the lattice distortion then a terminal cluster is formed. Here strong mutual interactions occur among the large number of displacement defects. The structure of a cascade of displaced atoms due to an initial PKA can be calculated[55]. The important aspects are illustrated in figure 5.1.

   The number of primary displaced lattice atoms is proportional to the non-ionising energy loss (NIEL) of the incident particle. The NIEL of a particle depends on both the incident particle and the target material.

3. Due to the thermal motion of defects they can anneal even at room temperature. The amount of annealing depends on the defect type and thus can depend on impurities present prior to irradiation, as well as the type and energy of the incident particle and the irradiated material. In silicon, room temperature annealing reduces the number of electrically active defects to 2% of the theoretically calculated unannealed displacements[56]. Similar effects are expected in GaAs.

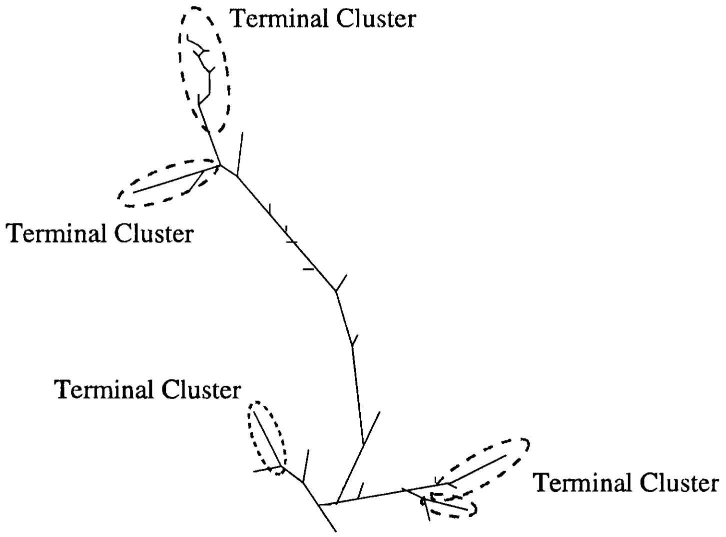

Figure 5.1: An illustration of a typical recoil-atom track produced in a semiconductor device.

4. The thermally stable defects influence the properties of the material and thus the device operation. A defect formed from a displaced atom situated between lattice sites is an interstitial defect and the space created in the lattice is known as a vacancy. Most defects will be electrically active and form generation-recombination centres.

Thermally stable radiation-induced generation centres degrade the performance of semiconductor detectors. An increase in the generation current of the reverse-biased detector leads to an increase in electrical noise and power dissipation which, for high currents, causes detector heating. Leakage current increase is one of the most serious radiation effects for silicon detectors[57, 58].

For an operational detector the defects act as trapping centres and reduce the free carrier absorption length. If the de-trapping time of the defect is greater than the collection time of the read-out electronics, signal reduction will occur and the charge collection efficiency of the detector falls.

An increase in the output pulse width may occur[59] due to de-trapping within the amplifier shaping time, or due to a reduction in the mobility because of an increase in carrier scattering or change in electric field distribution in the detector.

The compensation in the detector will also be altered. The defects created in the terminal clusters are close together and cause a significant space charge region, which will alter the electric field inside a device. A large percentage of all the defects will carry charge and therefore change the effective doping of the material. For a fluence ~ 10^{13} (1MeV) n/cm^2 silicon undergoes type inversion[60] and the rectifying junction in a p-n detector changes side: $p^+nn^+ \rightarrow p^+pn^+$. This has important consequences with respect to the fabrication of microstrip detectors.

Another important effect of radiation damage on the operation of a silicon detector follows from the increase in doping concentration with fluence and thus irradiation time. The higher the doping concentration the higher the bias required to deplete the device fully. After a large dose, this could become unacceptable for operation in the ATLAS inner detector. If the detector is not fully depleted signal loss will occur due to incomplete carrier collection. This is therefore a major concern for successful operation of silicon detectors at ATLAS.

The number of displaced atoms, which depends upon the type of incident particle and its energy, can be calculated. Limited calculations have been performed for GaAs. However, predictions of the macroscopic changes to device parameters from the microscopic deformations are not well understood and experimentation is therefore required. Scaling rules have been developed so that the macroscopic effect of one type of irradiation of a known energy and fluence on a given material can be compared with other energies and fluences for that and other particle types. For electronic components made from GaAs the observed radiation damage has been shown to be proportional to the NIEL[61]. The NIEL of a particle is given by the Lindhard curve[62], shown in figure 5.2 for a PKA in silicon and GaAs. It can be seen that the higher the kinetic energy of the incident particle the lower the probability of energy loss through NIEL. Due to the higher effective mass of the 'GaAs' ion the Lindhard curve for GaAs is shifted to higher energies and therefore a PKA of the same kinetic energy will undergo more NIEL.

The NIEL stopping power is dependent upon the Lindhard curve and the differential cross-section to produce a recoil fragment with a given energy and atomic weight. Calculations of this cross-section are very complex and detailed modelling requires a detailed understanding of the nuclear physics of the entire interaction process. Detailed theoretical calculations have been performed for silicon[63, 64, 65, 66]. For GaAs, however, only neutron[63, 64] interactions up to 10 MeV and proton[61]

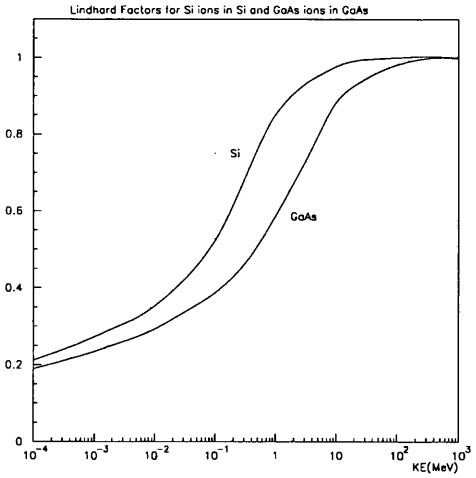

Figure 5.2: Total fraction of energy appearing as ionisation energy, due to interactions with atomic electrons, for 'GaAs' ions in GaAs and Si ions in Si, calculated according to the Lindhard formulae. The curves are labelled on the figure.

interactions with an energy less than 1 GeV have been calculated. Extrapolations from the silicon and GaAs NIEL curves were performed[67] to estimate the NIEL in GaAs for protons and pions up to an energy of 30 GeV. This allowed a correlation to be made between the measured macroscopic detector effects, (cce and reverse leakage current), and the incident radiation damage. Figure 5.3(a) shows two NIEL calculations for neutrons in silicon and GaAs. The difference between the two GaAs calculations for a 1MeV neutron is 14%. Figure 5.3(b) compares the results of the extrapolations for GaAs and the calculations of the NIEL stopping power in silicon as a function of kinetic energy for both protons and pions. It should be noted that earlier correlations of NIEL with degradation in device performance have been shown only for electronic components where a very limited fraction of the bulk is required for device operation. Therefore it is not necessarily true that for GaAs detectors, where the total substrate thickness is of importance, the same device correlations will be obtained.

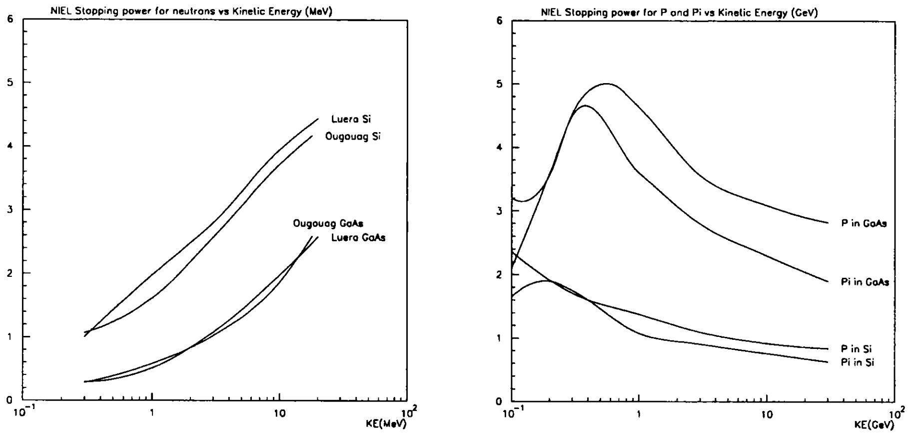

(a) Neutrons in Si and GaAs as a function of kinetic energy (smoothed through nuclear resonances)

(b) Protons and pions in Si and GaAs as a function of kinetic energy.

Figure 5.3: Calculations of the NIEL stopping power. The y-axis is the NIEL stopping power in units of keVgm^{-1}cm^2.

5.2 Experimental procedure

The detectors have been exposed to three types of radiation. The neutrons used, from the ISIS machine at R.A.L.[68] had an energy spectrum, shown in figure 5.4, with a high energy section centred at approximately 1MeV. Those with an energy below 10keV are low energy, background neutrons and are non-damaging. Protons with a momentum of 24 GeV/c, from the PS beam at C.E.R.N.[69] and pions with a momentum of 300 MeV/c, from the PSI beam, Villigen[70], were used to irradiate the detectors with high energy charged hadrons.

The ISIS neutrons were produced by the collision of the 800 MeV proton beam with a graphite/copper collector. The neutron flux followed a 1/R^2 law which allowed the dose rate to be varied by altering the distance of the samples from the collector. For the charged hadron irradiations the samples were placed in the most intense part of the hadron beam. A typical proton beam profile, shown in figure 5.5, was obtained by exposing a large pure aluminium foil, for a short period of time, to the beam. The foil was placed on top of a gamma sensitive film whose

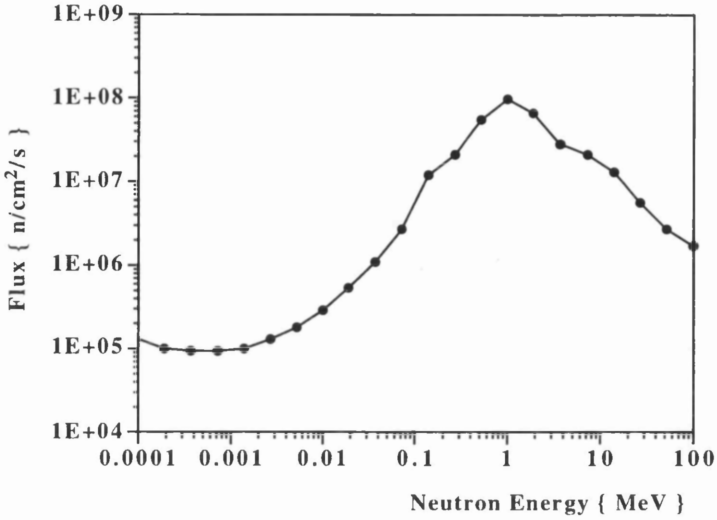

Figure 5.4: The ISIS neutron spectrum.

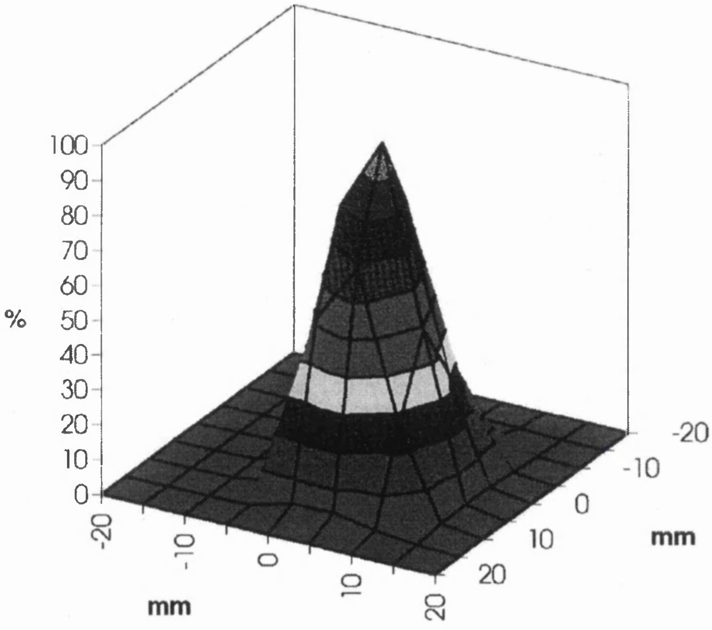

Figure 5.5: A typical proton beam profile, measured as a relative intensity.

exposure correlated to the initial beam intensity. The beam profiles actually used for the irradiations varied greatly and were not under the control of the user.

The detectors used throughout were the simple circular pad diodes with double sided guard rings, described in previous chapters. The diodes were mounted on and bonded to PCB mounts for ease. These were held between two layers

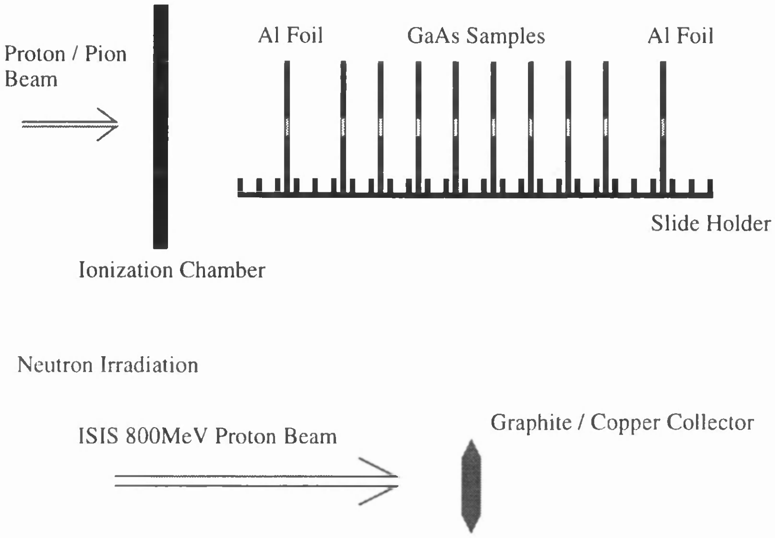

Figure 5.6: The experimental arrangement used for the irradiations.

of card and placed in a standard slide holder, which was positioned above the graphite/copper collector in the neutron irradiation and along the beam line for the hadron experiments, illustrated in figure 5.6.

The foil activation technique[71] was used to calculate the dose. The foils were cut to the size of the active area of the detectors and positioned in the slide holder directly in front of and behind the detectors. In the pion beam, foils were interleaved with the samples due to the divergence of the beam along the length of the slide holder. Cobalt-59 and indium-115 foils were used for the neutron irradiations. Cobalt was chosen since it has four useful reactions with long half-life products that have energy thresholds covering the interesting part of the neutron spectrum, while the indium reaction covered the 1MeV to 10MeV neutron energy range. The reaction cross-sections for cobalt and indium are shown in figure 5.7. High purity aluminium foils were used for the hadron irradiations.

The activity of a foil was measured with a Ge(Li) gamma spectrometer. The acquisition was stopped when a 2σ error of less than 6% was achieved. The measured activity, A_m, was determined from the number of counts in the peak (N_c) in a counting time t_c with:

$$A_m = \frac{N_c}{t_c \eta \epsilon} \tag{5.2}$$

where η is the emission probability of the gamma from the daughter isotope with a detection efficiency of ϵ in the spectrometer.

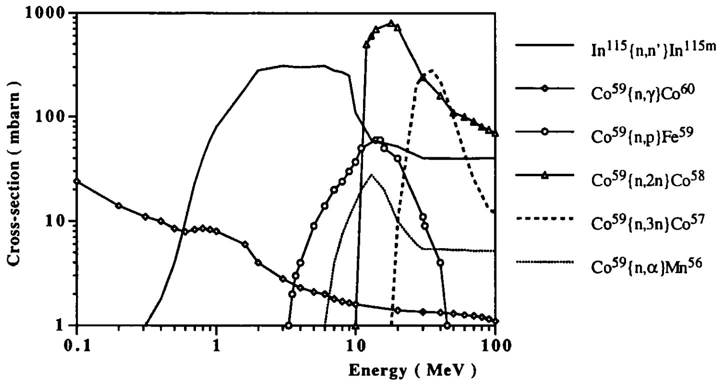

Figure 5.7: The neutron cross-sections for the cobalt and indium reactions. The key is shown on the figure.

The fluence on the foils, and thus the detectors, was then determined. The activity of the irradiated foil is given by:

$$A = A_\infty \left[1 - \exp\left(-\lambda t_i\right)\right] \tag{5.3}$$

$$A_\infty = \phi \sigma N_0 \tag{5.4}$$

where A_∞ is the saturation activity, ϕ the particle flux, σ the activation cross-section and $N_0 = N_A PM/W$ is the number of atoms in the foil. N_A is Avogadro's constant, P the isotopic abundance ($\approx$100%), M the mass of the foil and W the atomic mass of the target atom. The exponential factor corrects for decays of the daughter atom during the irradiation time t_i, where $\lambda = \ln 2/t_{\frac{1}{2}}$ and $t_{\frac{1}{2}}$ is the half-life of the daughter atom. As the activity was measured an elapsed time (t_e) after the irradiation period for a counting time t_c the corrections (5.5) and (5.6) were required to account for the decays in the two periods respectively.

$$\exp\left(-\lambda t_e\right) \tag{5.5}$$

$$A_m \lambda t_c \left[1 - \exp\left(-\lambda t_c\right)\right] \tag{5.6}$$

The saturation activity is therefore:

$$A_\infty = A_m \lambda t_c \frac{\exp\left(\lambda t_e\right)}{\{[1 - \exp\left(-\lambda t_c\right)]\left[1 - \exp\left(-\lambda t_i\right)\right]\}} \tag{5.7}$$

which leads to an expression for the flux of:

$$\phi = \frac{W}{N_A P M \sigma} A_m \lambda t_c \frac{\exp(\lambda t_e)}{[1 - \exp(-\lambda t_c)]\,[1 - \exp(-\lambda t_i)]} \tag{5.8}$$

The fluence (Φ) is simply:

$$\Phi = \phi t_i \tag{5.9}$$

The irradiation time does not take into account periods when the beam was off. However, in practice, these were short in comparison to the total irradiation time and the half-life of the daughter products and therefore no corrections were made.

Figure 5.6 shows an extended ionisation chamber in front of the detectors for the proton/pion irradiations. The chamber was calibrated to the fluence measured on an aluminium foil to provide a real-time estimate of the flux actually on the detectors.

Most of the irradiations were performed at room temperature ($\approx 27^oC$) except for one set of proton irradiations which were situated in a constant flow of cold dry nitrogen gas inside a thermally insulated box. The atmospheric temperature inside the box was maintained at -6 ± 4^oC throughout the irradiation period except during the period when the nitrogen supply was replaced. This took up to one hour during which the air temperature rose to a maximum of 10 ± 10^oC for a short period of time. After the irradiation the detectors were transfered to a refrigerator at -5^oC for storage and testing. The detectors remained at room temperature for a period of two hours during the process of removal from the beam area and transportation into storage. Irradiations were carried out at -10^oC because it is proposed to operate the inner detector of the ATLAS experiment at this temperature to prevent detrimental room temperature annealing effects in the silicon detectors, and therefore the effects of low temperature irradiations on GaAs detectors were required.

For the room temperature pion and proton irradiations the leakage current and charge collection efficiency of a given detector were obtained as a function of fluence. This was achieved by removing the detector during the irradiation period, testing, and replacing it. This was repeated at several fluences for several detectors.

Most of the irradiated detectors were Glasgow devices fabricated from MCP LEC SI-U GaAs. A few SI-U Alenia detectors were also tested. Two detectors fabricated from semi-insulating indium-doped, (SI-In doped), LEC material and four from the VPE wafer were exposed to a proton fluence.

The radiation effects were analysed with respect to the reverse current and charge collection characteristics of the detectors. The results, for all three radiation types are contained in the next two sections while section 5.5 compares the characteristics of the detectors irradiated at room temperature and at -6°C. The effects of room temperature and elevated temperature annealing of the devices were investigated with respect to the macroscopic detector characteristics; these results are reported in section 5.6. The chapter closes with the results of limited irradiation tests performed on detectors fabricated from the other substrate materials discussed in section 4.5.

5.3 Current characteristics

The changes in the current characteristics were observed to depend on the radiation type. However, the low voltage analysis of section 4.1.1 was only performed for three fluences of 24 GeV/c proton radiation. The operational high voltage characteristic sub-section compares the results of irradiation by all three particle types.

5.3.1 Low voltage characteristics

The current characteristics of three SI-U GaAs diodes fabricated from the same wafer, after proton fluences of 0.0, 4.5×10^{13} and 13.5×10^{13} /cm^2, are shown in figure 5.8. All the low voltage (< 0.1 V) characteristics had a similar shape and therefore the contact and bulk characterisation technique of section 4.1.1 was applied. Measurements were made for each diode over the low temperature region (10 → 40°C) and the effective resistances of the barrier (R_{eff}) and bulk (R_{bulk}) were found. From these values the contact resistance (R_ϕ) and the bulk resistivity (ρ_{bulk}) were determined. Table 5.1 reports the results obtained for the three diodes at 20°C. The quoted errors in R_{bulk} were determined, as before, from the 'one sigma' variation in the experimentally determined offset voltages. The accuracy of the fits performed to the I-V characteristics of the irradiated detector decreased with increasing fluence, which implied a reduced accuracy in the Schottky theory to describe the diode.

The bulk resistivity of the detector increased with fluence, as illustrated in figure 5.9. The resistivity of the material at 20°C was found to increase from $64 \pm 7 \times 10^6$ Ωcm for the pre-irradiated device to $97 \pm 4 \times 10^6$ Ωcm at the maximum

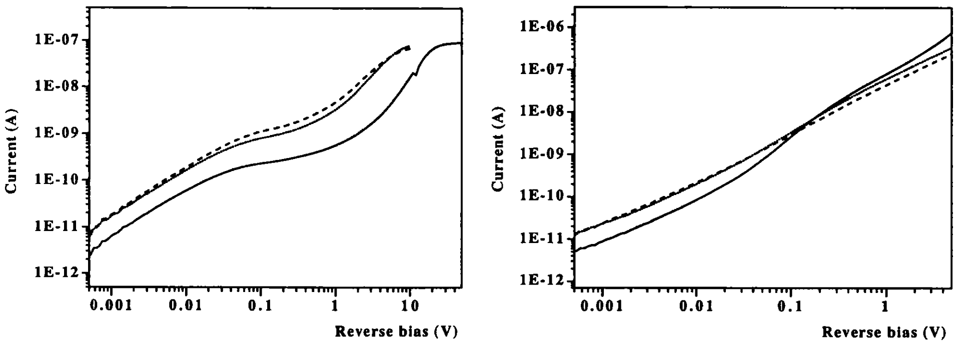

(a) Reverse bias. (b) Forward bias.

Figure 5.8: The current characteristics of SI-U GaAs diodes as a function of 24 GeV/c proton fluence, measured at 20°C. The key is: solid - 0.0 cm^{-2}; dashed - 4.5 × 10^{13} cm^{-2}; dotted line - 13.5 × 10^{13} cm^{-2}.

Fluence $10^{13}\mathrm{cm}^{-2}$	R_{eff} MΩ	R_{bulk} MΩ	$R_{bulk-max}$ MΩ	$R_{bulk-min}$ MΩ	R_{ϕ} MΩ	ρ_{bulk} MΩcm
0.0	138.6	16.60	18.56	14.68	122.0	64.1
4.5	55.5	20.0	21.4	19.2	35.5	77.3
13.5	48.9	25.2	26.9	24.1	23.7	97.3

Table 5.1: The measured diode resistances at 20°C as a function of 24 GeV/c proton fluence.

fluence. The increase in resisitivity implies an decrease in the conductivity. The bulk conductivity of a material is proportional to the product of the number density of free carriers and their mobility; therefore the free electron density of the material was reduced with fluence. The mobility will also be reduced due to the increase in scattering centres introduced by the irradiation. A reduction in the free carrier concentration occurs due to the radiation-induced increase in the number of deep level defects which act as electron traps in the material.

The activation energy (E_A) of the bulk conductivity was determined from the measured values of R_{bulk}. Again the mobility temperature dependence of $\mu_n \propto T^{-\frac{1}{2}}$ was assumed for the experimental temperature range. A plot of $\ln(\sigma/T)$ against $1/T$ will therefore have a gradient equal to $-\frac{E_A}{k_B}$. Table 5.2 lists the activation

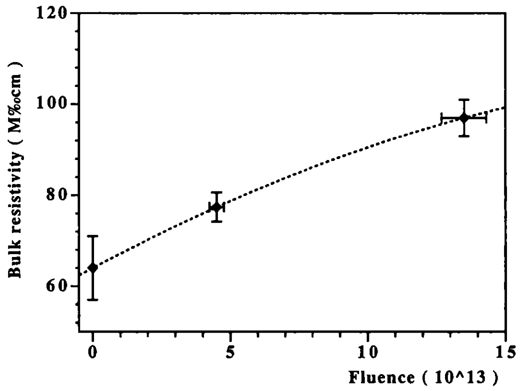

Figure 5.9: The variation of the bulk resistivity of a SI-U GaAs diode as a function of 24 GeV/c proton fluence, measured at 20°C. The curve is just to guide the eye.

Fluence 10^{13}cm^{-2}	E_A (eV)	ϕ_b (V)
0.0	0.78 ± 0.04	0.92 ± 0.02
4.5	0.79 ± 0.01	0.83 ± 0.02
13.5	0.747 ± 0.005	0.78 ± 0.01

Table 5.2: The measured bulk activation energies and barrier heights at 20°C as a function of 24 GeV/c proton fluence.

energies found at 20°C for each fluence. The value of E_A changed slightly with increasing fluence and approached the energy of the EL2 defect level of 0.75 ± 0.1 eV. The radiation-induced defects are therefore deep, as expected from the reduction in free carrier density, and close in energy to the EL2 defect. Radiation-induced production of an arsenic antisite defect has been reported[72, 73] and it is suggested that this defect was also created by exposure to the high energy protons. The arsenic antisite defect forms the core of the EL2 defect, see section 2.9, and therefore similar activation energies were found.

The contact resistance was reduced with fluence from $122 \pm 2 \times 10^6$ Ω to $24 \pm 2 \times 10^6$ Ω, at 20°C. From the temperature variation of the contact resistance the barrier height (ϕ_b) was found, see section 4.1.1 for details. The activation plots for the three diodes are shown in figure 5.10 and table 5.2 reports the determined barrier heights. The dramatic reduction in the barrier height, and thus the low voltage effective

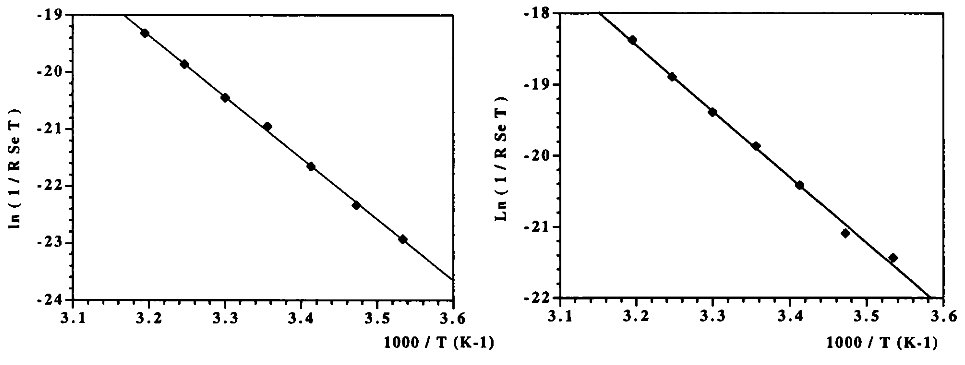

(a) 0.0 $\times 10^{13}$

(b) 4.5 $\times 10^{13}$

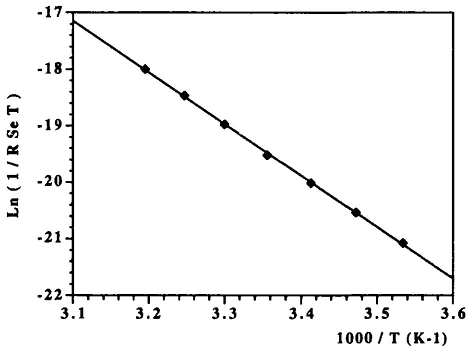

(c) 13.5 $\times 10^{13}$

Figure 5.10: The activation plots to determine the barrier heights of LEC SI-U GaAs diodes from the contact conductivity for three 24 GeV/c proton fluences.

resistance of the device, explains the large increase in current with fluence.

The reduction in the barrier height is proposed to be due to an increase in the ohmic nature of the barrier. Standard LEC SI-U GaAs has been shown to be far from a perfect crystal. The surface dislocation density of typical LEC material has been measured to be $\sim 1 \times 10^5$ cm^{-2}[74]. The dislocations at the surface are suggested to be part of a bulk dislocation network[75]. Such a model suggests that the material consists of many ordered micro-volumes surrounded by dislocation paths. Therefore the surface of the wafer can be visualised as ordered crystal zones with dislocations between them. It has been suggested that the dislocations may be thought of as having increased hole conductivity, that is behave as less n-type material. Where the metal covers the dislocations it will therefore not form a good Schottky contact and thus the measured or effective barrier height of the whole diode is reduced from that expected for a homogeneous material. Radiation will increase the number of dislocations in the material and thus increase the percentage of the surface that is relatively 'p-type', resulting in a reduction in the effective barrier height with increasing fluence.

If the reduction in the barrier height is due to a degradation in the Schottky barrier then the ideality factor of the barrier should increase with fluence. The ideality factor was found for each diode from the current characteristics, following the fitting procedure developed in section 4.1.1, up to a reverse bias of $10k_BT$. The value of the saturation current and thus zero bias barrier height were determined from each data set. An increase in the ideality factor was obtained but it was slight. For the pre-irradiated diode a value of 1.04 was obtained, which increased to 1.06 after a fluence of 13.5×10^{13} cm^{-2}. Figure 5.11 shows the results of the fits performed for the three fluences. Although the ideality factor did not degrade significantly, it must be noted that the quality of the fit was reduced, with the chi-squared doubling at the highest fluence.

The bulk resistivity of the material has been shown to increase with radiation while the Schottky barrier height has fallen. The resistivity increase was assumed to be due to carrier removal via an increased trap concentration. Increased dislocations in the material, and thus p-type zones, have been suggested as an explanation of the reduction in the barrier height.

5.3.2 High voltage characteristics

The effect of all three types of irradiation on the high voltage reverse current characteristics of the GaAs detectors was small. Figure 5.12 shows reverse current characteristics for four increasing proton fluences for a 210μm thick detector measured at 20°C. The plateau current after a fluence of 8.9×10^{13} p/cm^2 is only 2.2 times larger than the pre-irradiated value. Before irradiation the reverse current increased dramatically at a bias of 250V corresponding to the full depletion voltage of the detector (V_{fd}). After only 1.56×10^{13} p/cm^2 a knee in the current characteristic was observed at 160V. The 'knee voltage' fell only slightly with higher fluence, as shown in figure 5.13 for a 200μm thick GaAs device. For an applied bias greater

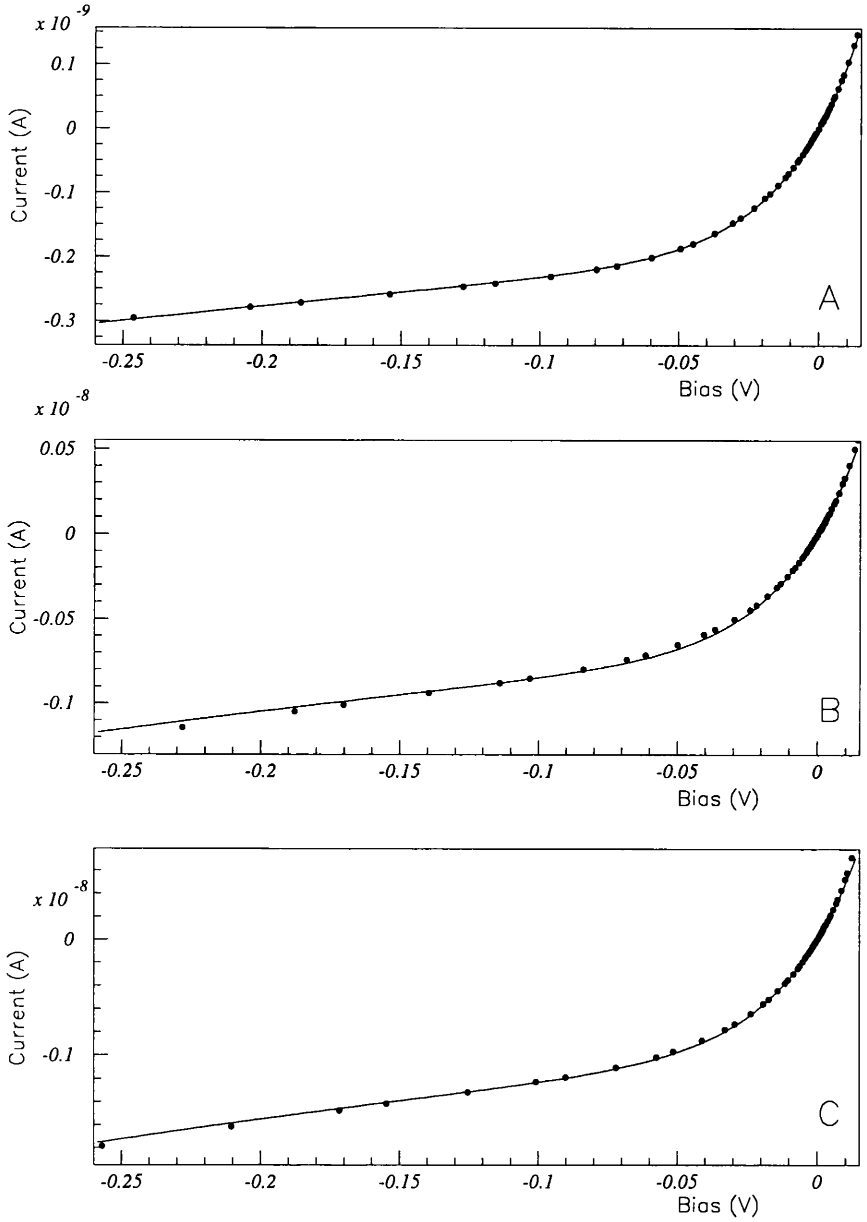

Figure 5.11: The current characteristics at three 24 GeV/c proton fluences, measured at 20°C, for a guarded SI-U GaAs diode and the fit obtained with equation (4.3) up to $10k_BT$. The key is: A - 0.0 cm^{-2}; B - 4.5×10^{13} cm^{-2}; C - 13.5×10^{13} cm^{-2}.

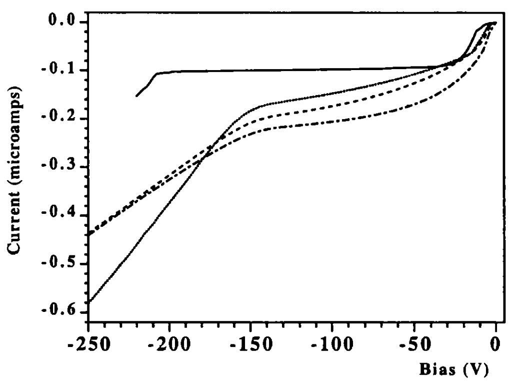

Figure 5.12: The reverse current characteristics of a 210μm thick GaAs detector with increasing 24GeV/c proton fluence, measured at 20°C. The key is: solid line - 0.0 cm^{-2}; dotted - 1.6 × 10^{13} cm^{-2} ; dashed - 3.9 × 10^{13} cm^{-2}; dot-dashed - 8.9 × 10^{13} cm^{-2}.

than this knee voltage the signal created by irradiating the ohmic contact with an alpha source (the hole signal) was non-zero, which verified that the detector was fully active and that the knee in the current characteristic corresponded to V_{fd}. As the value of V_{fd} was reduced with fluence the high field region in the detector must have been altered with irradiation. V_{fd} was observed to diminish for all three radiation types and fell to between 2/3 and 1/2 the pre-radiation value, regardless of the substrate thickness, within the first few 10^{13} particles/cm^2.

The Alenia detectors that showed very good pre-radiation high voltage characteristics due to the nature of the back contact had identical post-radiation high voltage characteristics to the Glasgow MCP diodes after 1 × 10^{13} p/cm^2.

For silicon diodes the value of V_{fd} increases with fluence, after type inversion, due to the increase in the doping concentration. This was not observed in GaAs diodes, but it must be stated that the reverse current characteristic and high field extension at these voltages is not described by simple semiconductor theory as in silicon.

Figure 5.14 shows the plateau current of 200μm thick guarded diodes as a function of fluence for the three particle types. The dependence on fluence was very similar for the pion and proton irradiations, with the data points overlapping on the figure. The current increase with neutron fluence was significantly less at a given fluence than for charged hadrons. The majority of the current increase occurred before a charged hadron fluence of 4 × 10^{13} /cm^2, with the observed current above

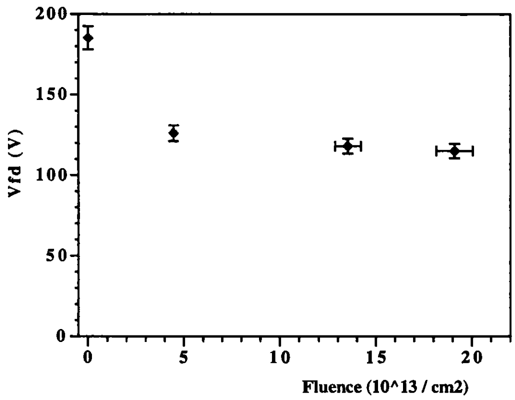

Figure 5.13: V_{fd} as a function of 24 GeV/c proton fluence, measured at 20°C, for a 200μm thick SI-U GaAs detector.

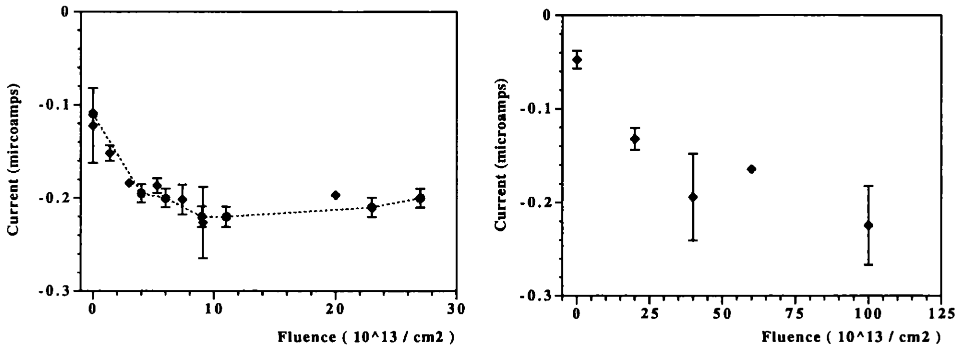

(a) 300 MeV/c pions and 24 GeV/c protons. The key is: diamonds - pions; circles - protons.

(b) 1 MeV neutrons.

Figure 5.14: The plateau current as a function of fluence, measured at a reverse bias of 100V.

1×10^{14} p/cm^2 remaining approximately constant.

The value of the reverse current for voltages in excess of V_{fd} was reduced with increased fluence and the reverse current characteristic became more resistive in nature, due to the increase in substrate resistivity.

Reverse current characteristics of two detectors of different thickness, 160μm and 500μm, both irradiated to 6×10^{13} p/cm^2 are shown in figure 5.15. It can be seen that the value of the leakage current up to V_{fd} is independent of the detector thickness. This is not the case in silicon where the leakage current (I_r) has a dependence on

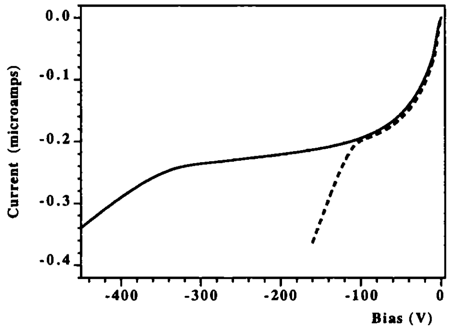

Figure 5.15: The reverse current characteristics of two GaAs detectors after a fluence of 6×10^{13} 24 GeV/c protons/cm^2. The key is: dashed line - 160 μm thick; solid - 500 μm.

fluence (Φ) given by:[76]

$$\frac{\Delta I_r}{Vol} = \alpha\Phi \tag{5.10}$$

where α is the reverse current damage constant and Vol is the active volume of the detector. The pre-irradiation current characteristics showed no substrate thickness dependence and it is suggested that the observed post-radiation operational current is a trap-limited generation current. However, the trap concentration and type have been altered, resulting in the observed change in high field penetration rate and plateau current. No variations in the reverse current were observed for detectors that were biased during the irradiation period.

The high voltage forward current characteristics also changed with increasing fluence. The effect is illustrated in figure 5.16 where the forward characteristic of a 160μm thick detector is shown as a function of proton fluence. A plateau appeared that extended to higher bias values with increasing fluence while the magnitude of the plateau current fell. If this is due to a space charge limiting effect then a high field region may be formed which could allow device operation under forward bias.

5.3.3 Pulser noise measurements

Pulser noise measurements were performed on four detectors so that the equivalent noise charge as a function of 24 GeV/c proton fluence could be obtained. Figure 5.17 reports the results for the measured noise charge and that predicted from the reverse current with simple shot noise theory. The figures show the noise measured at both a fixed bias of 150 V, which is close to the operational voltage of a 200μm

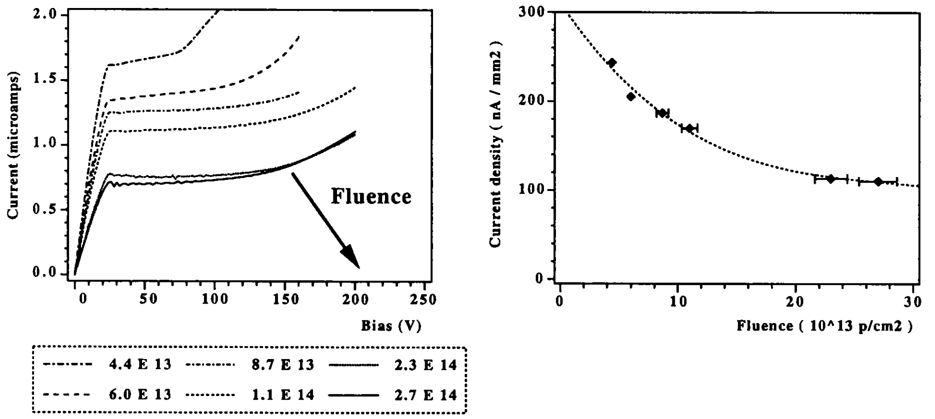

(a) Forward IV. The key is shown in the figure.

(b) The forward plateau current as a function of fluence.

Figure 5.16: The forward current characteristics of a 160μm thick GaAs detector with increasing 24 GeV/c proton fluence measured at 20°C. The curve of figure 5.16(b) is just to guide the eye.

thick device, and at a fixed current of 100 nA. Due to an increase in reverse current the theoretical shot noise at a fixed bias increased, however the measured noise in fact fell. The second figure shows that, while the theoretical shot noise at the fixed current was constant at 1860 electrons, the measured noise charge fell with fluence. The value of α in the shot noise expression (4.22) is only 0.03 at the maximum fluence.

It is again suggested that the reduction in measured noise charge is related to the increase in electron traps. A high trapping probability would be required which must lead to a large reduction in the response to charge deposition due to traversing charged particles.

The leakage current of a GaAs detector increased slightly with particular radiation but the noise current was in fact reduced. This noise source is therefore not expected to be a problem for successful operation of GaAs detectors at the ATLAS experiment.

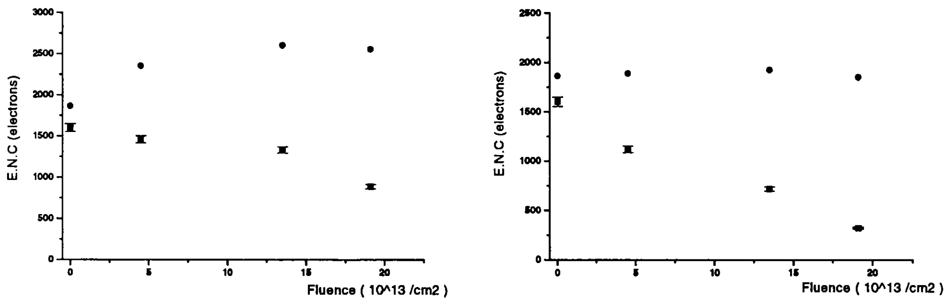

(a) Measured at a constant bias of 150 V.

(b) Measured at a constant current of 100 nA.

Figure 5.17: The measured and theoretical shot noise of a guarded 200μm thick simple pad SI-U GaAs detector as a function of 24 GeV/c proton fluence, measured at 20°C. The key is: circles - theory; squares - measurement.

5.4 Charge collection characteristics

The irradiated detectors were characterised using the alpha and mip charge collection experiments of chapter 3.

5.4.1 Reverse biased operation

Figure 5.18 illustrates typical post-irradiation electron and hole charge collection as a function of reverse bias for a 200μm thick device, determined from the alpha experiments. A significant hole cce was observed above 100 V which corresponds to the value of V_{fd} deduced from the change in slope of the current characteristic. The hole charge collection efficiency was reduced to less than that observed for electrons and increased only slightly with increasing bias after its initial steep rise at V_{fd}. The electron cce was flat, at $6 \pm 1\%$, up to approximately 200 V, after this fluence, and increased at higher bias. The increase in electron signal could be due to field-enhanced electron detrapping, as suggested in section 4.4.1 to explain the rise in electron signal at very high bias in the Alenia detectors.

Mean absorption distances of the charge carriers were found from the experimental electron and hole charge collection efficiencies as a function of 24 GeV/c proton fluence, shown in figure 5.19. Before irradiation the hole signal, and therefore mean

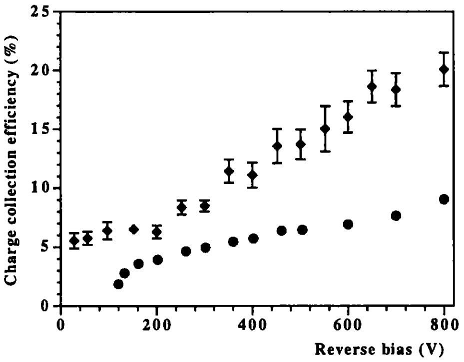

Figure 5.18: Electron and hole charge collection efficiencies as a function of bias for a 200μm thick SI-U GaAs detector after a 1.9 × 10^{14} 24 GeV/c proton fluence, measured at 20°C. The key is: diamond - electrons; circles - holes.

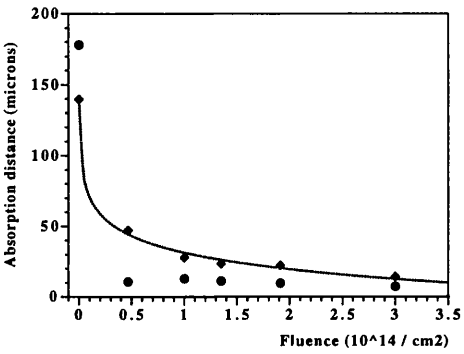

Figure 5.19: The electron and hole absorption distances as a function of 24 GeV/c proton fluence. The key is: diamond - electrons; circles - holes.

carrier absorption distance, was greater than that of the electrons, which implied that the electrons were trapped more than the holes. The hole signal, however, fell at a faster rate with fluence than that due to the electrons and therefore both electron and hole traps were introduced with irradiation but electron trapping was less important after irradiation, contrary to what was observed for unirradiated detectors. It was found that the neutron irradiation reduced the carrier absorption distance at a lower rate than the high energy protons. Therefore, the introduction rate of active defects, hole and electron traps, by the 1 MeV neutrons was lower than for the charged hadrons.

The reduction in carrier absorption distances with fluence reduced the mip charge collection efficiency of the detectors. At a given bias the magnitude of the mip cce

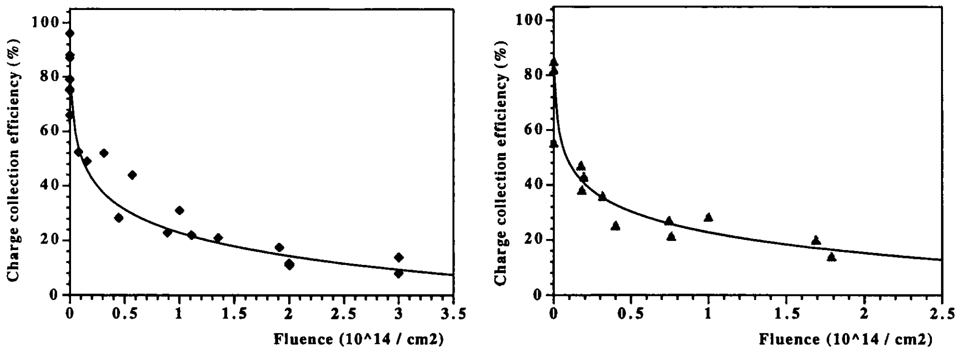

(a) 24 GeV/c protons.

(b) 300 MeV/c pions.

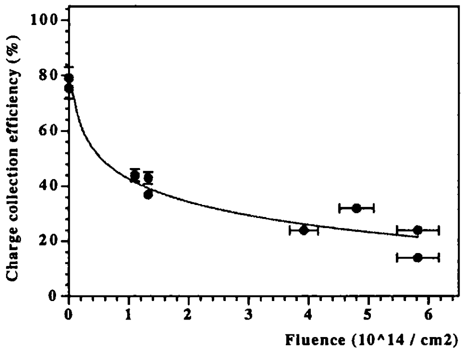

(c) 1 MeV/c neutrons.

Figure 5.20: The mip charge collection efficiency as a function of fluence. Measured with an applied bias of 200V on 200μm thick SI-U GaAs detectors at 20°C.

was dependent upon the type of irradiation as well as the fluence. The mip cce measured with an applied bias of 200V on 200μm thick detectors at 20°C is shown for all three radiation types in figure 5.20. The reduction in cce with fluence occurred at a greater rate for pions and protons than for neutrons as was expected from the alpha data. A 10000 electron signal response to the ^{90}Sr source, ($\approx$ 40% cce), was obtained after 1.4×10^{14} n/cm^2, 6.0×10^{13} p/cm^2, and only 3.0×10^{13} π/cm^2. The cce fell rapidly initially and then at a slower rate for higher fluences with the position of the change in gradient depending upon the particle type.

Irradiated detectors biased in excess of V_{fd} demonstrated an increase in mip cce. For example the signal from a 160μm thick detector irradiated to a fluence of 1.0×10^{14} p/cm^2 increased from 8500 electrons at 200V to 12000 electrons at 400V.

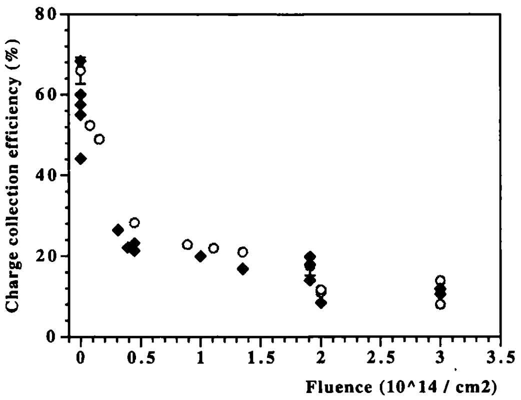

Figure 5.21: The measured and calculated mip charge collection efficiency as a function of 24 GeV/c protons for a 200 V bias on 200 μm thick SI-U LEC GaAs detectors. The key is: open circles - measured; closed diamonds - calculated. Each calculated point represents data from a separate diode.

The reason for the increase was the increased electron signal observed in the alpha charge collection data.

From the mean absorption distances, calculated from the electron and hole charge collection data, the mip charge collection efficiency at V_{fd} as a function of bias was predicted. Measured and calculated values of the mip cce are compared as a function of 24 GeV/c proton fluence in figure 5.21. The predicted values are well within the scatter of those found from direct measurement.

The dependence of charge collection degradation with particle type has been explained in terms of the different non-ionising energy loss (NIEL) of the particles in the detector material[67]. The correlation is shown in figure 5.22, where total NIEL is the product of the NIEL stopping power and the radiation fluence. The NIEL stopping powers calculated for the 1 MeV ISIS neutrons and for the charged hadrons are given in table 5.3.

At the ATLAS experiment each particle type will have a characteristic energy spectrum and thus if the total NIEL is found for the expected energy spectra a prediction of the mip cce of a GaAs detector can be made. Such a prediction was made in [67] where the pion fluence was considered the most damaging. The results reported in [67] were based on the measurements reported here. A detector with an average pre-irradiation charge collection efficiency of 84% (22300 electron signal)

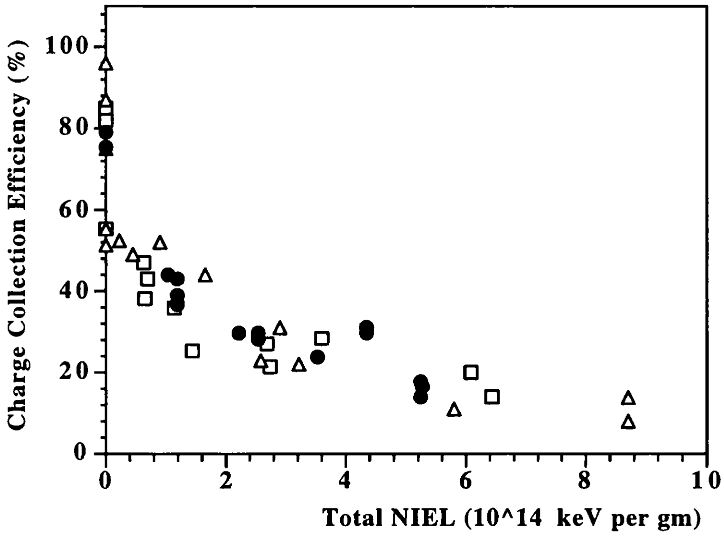

Figure 5.22: The mip charge collection efficiency as a function of total NIEL for ISIS neutrons, 300 MeV/c pions and 24 GeV/c protons for 200μm thick SI-U LEC GaAs detectors. The key is: closed circles - neutrons; open triangles - protons; open squares - pions.

Irradiation type	NIEL stopping power (keVgm^{-1}cm2)
ISIS neutrons (nominally 1 MeV)	0.9
24 GeV/c protons	2.9
300 MeV/c pions	3.6

Table 5.3: Calculated values of the NIEL stopping power in GaAs.

was calculated to degrade in the radiation flux of the ATLAS inner detector to give a signal of 11700 electrons (44% cce) after two years of operation. The rate of decrease in cce will slow down with increasing fluence. Therefore after four years of operation a cce of 35% is expected. At the end of the proposed operational lifetime of the ATLAS experiment (10 years) the signal would be 7400 electrons (only 29% cce). A charge signal of at least 10000 electrons is required to give a signal-to-noise of 10:1 with the expected read-out electronics at the ATLAS experiment[9].

It has been shown that the SI-U GaAs detectors used in these studies would not give the required signal throughout the operational lifetime of the experiment and therefore the reduction in charge collection efficiency is expected to be a problem for successful operation of GaAs detectors at the ATLAS experiment.

5.4.2 Forward biased operation

The plateau in the forward current characteristic motivated an investigation of forward biased detector operation. Alpha and mip charge collection experiments were performed as before. However, when the diode was forward biased the signal from the alpha experiment gave the electron cce when the diode was illuminated from the rear (ohmic) contact rather than the front (Schottky) side. Figures 5.23(a) and 5.23(b) show the results obtained from the alpha and mip experiments after a fluence of 3×10^{13} π/cm^2. The measurements had to be made cold so that the noise due to the forward current of the diode did not swamp the signal. The alpha experiments were performed by cooling the detector in an environmental chamber to 0°C. The diode was placed in the vacuum chamber which was surrounded by ice to keep the temperature close to 0°C. The experiment could not be carried out in the environmental chamber due to size limitations of the equipment, which was discussed in section 4.4.2. The mip charge collection experiments were perform at -10°C in the environmental chamber.

The fact that charge collection was possible at all implied that there was a space charge region inside the diode over which a significant electric field was present. The electron signal was observed at very low voltages which implied the active region of the device extended as far as the reverse-biased back (ohmic) contact of the device. The hole charge collection was observed only after an applied bias of 75 V, slightly

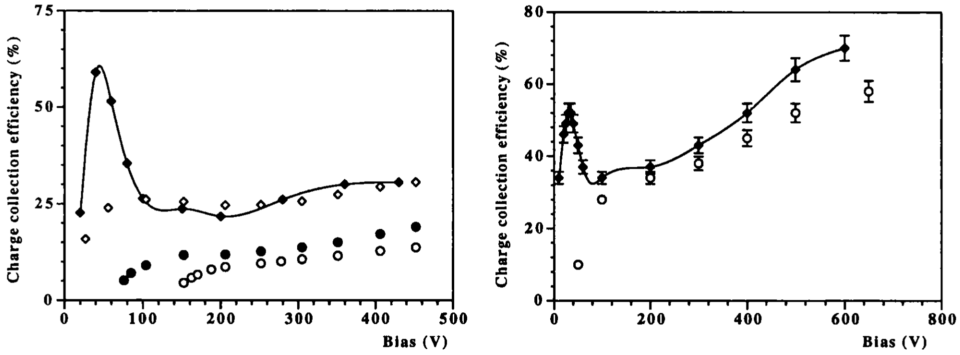

(a) Electron and hole charge collection efficiencies. The key is: closed diamonds - forward biased electrons; open diamonds - reverse biased electrons; closed circles - forward biased holes; open circles - reverse biased holes.

(b) Mip charge collection efficiency. The key is: closed diamonds - forward bias; open circles - reverse bias.

Figure 5.23: Charge collection efficiencies measured in forward and reverse bias as a function of bias after a fluence of 3×10^{13} π/cm^2. The alpha experiment was performed at 0°C and the mip experiment at -10°C. The curves are just to guide the eye.

less than the voltage required to obtained the reverse biased hole signal. Therefore the active region extended across the entire substrate at a slightly lower voltage under forward bias than with reverse bias. This voltage also corresponded to the knee in the forward current characteristics which was similar to that observed under reverse bias.

After 3.0×10^{13} π/cm^2 the electron cce was $59 \pm 3\%$ at a bias of 40 V, which was over twice as large as the reverse bias electron charge collection efficiency. However, the forward biased cce fell with higher applied bias to a value less than the reverse biased charge collection at a bias of 200 V. With still higher bias the forward biased charge collection rose to be slightly greater than that obtained under reverse bias, shown in figure 5.23(a). The forward hole cce was greater than that obtained under reverse bias, and was $17.2 \pm 3\%$ at a bias of 400 V compared to $12.8 \pm 1\%$ obtained in reverse bias. As a result of the enhanced electron lifetime the mip charge collection efficiency was increased at low bias, illustrated in figure 5.23(b). For a forward bias above that required for the low bias cce peak, the mip cce increased with bias

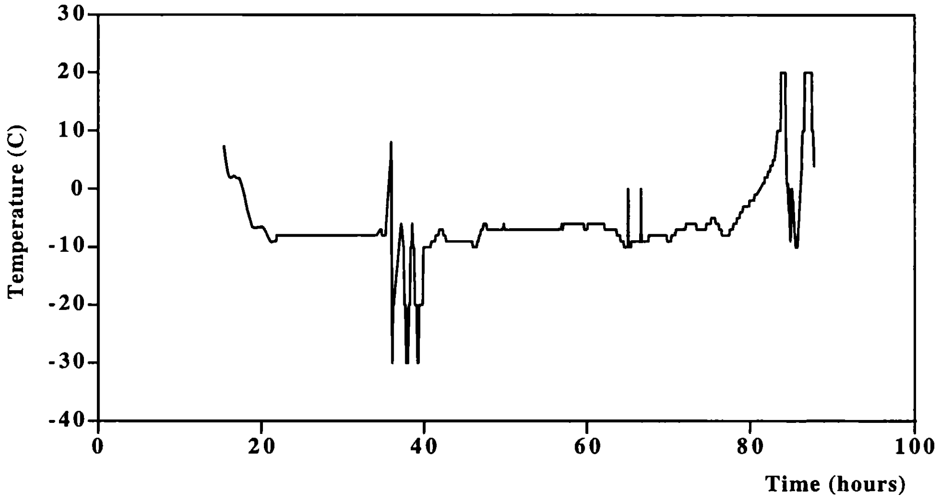

Figure 5.24: The atmospheric temperature of the cold box for the second proton irradiation run of 70 hours.

and remained above the value obtained under reverse bias. Above a fluence of $\approx 1.5 \times 10^{14}$ p(π)/cm^2 the detector was symmetrical, within experimental errors, with respect to mip charge collection above the initial peak. The magnitude of the peak also fell with increasing fluence.

The increased electron charge collection in forward bias may be due to the presence of the larger forward current. It is suggested that the current fills the electron traps and therefore increases the life-time of the ionisation induced carriers due to the reduction in ionised deep levels. It is not understood, however, why such an active region should be present inside the device under forward bias.

5.5 Low temperature irradiations

Twenty-five 200μm thick detectors were irradiated by 24 GeV/c protons at a temperature of -6 ± 4°C. The detectors were divided into three sets and exposed to fluences of 1.9 ± 0.2, 3.0 ± 0.3 and $19 \pm 2.0 \times 10^{13}$ p/cm^2. The temperature variation for the second irradiation run of 70 hour duration is shown in figure 5.24. The large peaks were due to the refilling of the nitrogen supply.

Two of the detectors were connected in parallel and reverse biased to 180 V during the second irradiation run. The guard ring and pad of the two detectors were connected together and the reverse current was recorded. The current,

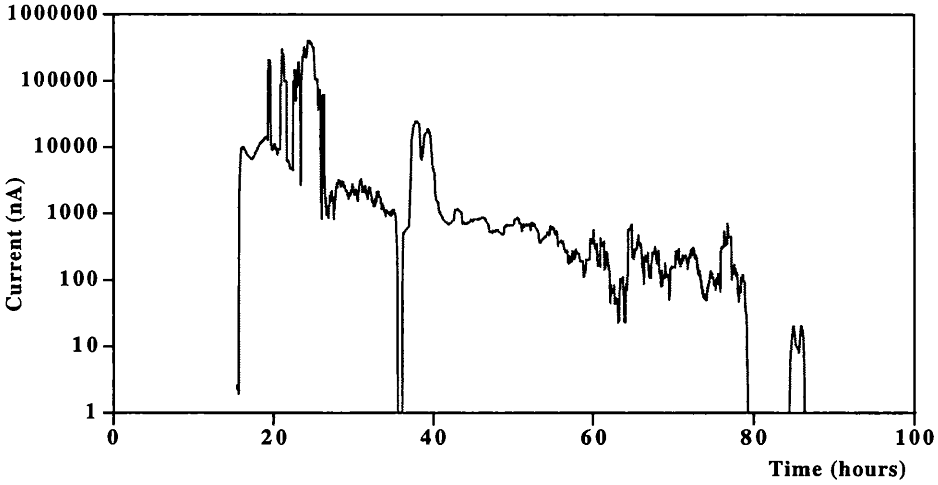

Figure 5.25: The variation in reverse current for two diodes in parallel as a function of time. The measurement temperature is that shown in figure 5.24.

after smoothing with a 9 point moving average function to remove small thermal variations, is shown in figure 5.25. The large peaks in the recorded current are either due to the peaks in temperature, caused by the refilling of the nitrogen supply, or the coincidence of the current measurement and the proton beam hitting the detectors. The leakage current showed a dramatic increase from 3 nA to over 10000 nA at the start of the irradiation run. This very large increase in current was not expected from measurements made at room temperature, where the leakage current increases have been at the factor of two level for all fluences. The leakage current fell with increasing fluence and was of order 100 nA at the end of the run after $7.5 \pm 1.0 \times 10^{13}$ p/cm^2.

Mip charge collection efficiency experiments were performed at a reverse bias of 200 V at -5^{o}C; the results are shown in figure 5.26. A slight decrease ($\approx$8%) in charge collection efficiency was observed with respect to detectors measured at -10^{o}C after room temperature irradiation, as illustrated in figure 5.26(b). However, the reduction may be due to the lower pre-irradiation cce of the detectors used for the cold irradiation.

The two detectors that were biased at 180 V during the irradiation period (the circles in figure 5.26(a)) had a better post-irradiation response with respect to those that were not biased. Two other detectors were reverse-biased at 180 V after the irradiation period and kept at room temperature for ten hours to observe if there

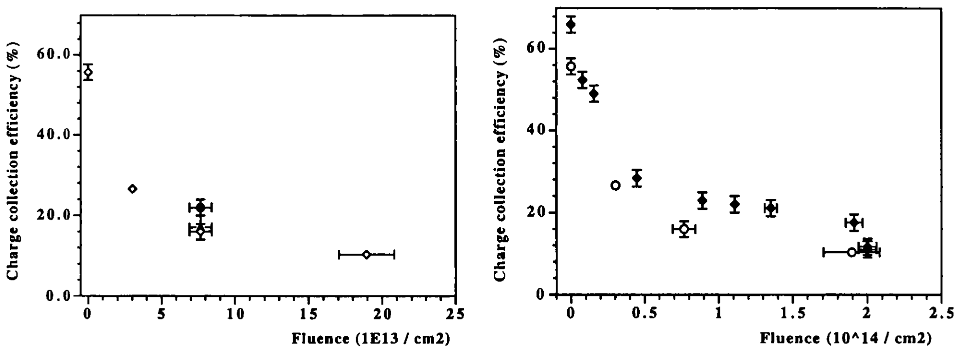

(a) Cold irradiation. The key is: open diamonds - no bias no annealing; circle - biased during irradiation; triangle - biased during anneal. (The triangle is partially obscured by the open circle)

(b) Comparison of cold and room temperature irradiations. The key is: open circles - cold; closed diamonds - room temperature irradiation.

Figure 5.26: The mip charge collection efficiency as a function of 24 GeV/c proton fluence, irradiated at -6 ± 4^oC and measured at -5°C. Figure 5.26(b) compares the results with those obtained from room temperature irradiations measured at -10°C.

were any room temperature annealing effects. No change in their charge collection efficiency was measured, see figure 5.26(a).

The thermal annealing of radiation-induced defects was therefore not significantly altered by the reduced irradiation temperature and/or the subsequent room temperature anneal. However, significant annealing of traps occurred for the two detectors biased during the irradiation period. Current assisted annealing of radiation-induced defects has been suggested in the literature[77] and it is thus suggested that such a process occurred in these two diodes. More experimentation is required to understand the improved charge collection and the high reverse current that was measured.

5.6 Annealing studies

The change in the reverse current of a detector irradiated to 1.0×10^{14} p/cm^2 has been measured over a period of time greater than 1 year. The sample was stored at room temperature which varied throughout the year between 17°C and 25°C. All the current measurements were carried out at 20°C with the same Keithley-237 voltage source measurement unit. The first current measurement was performed 20 days after the irradiation period because the initial activity of the sample and holder prevented earlier handling. The value of the reverse current (I_r) at V_{fd} reduced with time (t), measured in hours from the first measurement, with a logarithmic dependence given by

$$I_r \times 10^7 = -0.06ln(t) + 2.4 \tag{5.11}$$

The value of V_{fd} remained constant over this period. Some samples have shown an increase in cce over a similar period of annealing, however this represented at most an improvement of 8% of the initial cce and has not been observed consistently over all the detectors.

The constant value of V_{fd} is very different to that observed in silicon detectors where it increases due to room temperature annealing[78]. At room temperature the thermal motion allows displaced atoms to move through the lattice and form stable complex defects with each other and native impurity atoms. It is these stable defects that degrade the silicon detector, but no such effects have been observed in GaAs devices.

Elevated temperature annealing, for periods ranging from 15 minutes to 33 hours, were performed in an oven at 210°C in air without bias on six irradiated detectors. The reverse current and charge collection efficiency variations for a 180μm thick detector annealed after a proton fluence of 1.0×10^{14} /cm^2 are shown in figure 5.27. The reverse current, measured at 20°C, decreased with increasing duration of anneal from 0.22 μA to 0.14 μA after 33 hours, (corresponding to currents densities of 30nA/mm^2 and 20nA/mm^2). The pre-irradiation current was 0.10μA (14nA/mm^2). The full depletion voltage remained unaffected by the annealing.

For an applied bias of 100V the cce increased from 23% to 30% for annealing times up to 5 hours. However, for the annealed detectors the rate of increase in cce was less for applied voltages in excess of V_{fd}. After the 33 hour anneal the cce was reduced to only 15% at 100V. Irradiation-induced defects in n-type material have been shown to anneal at three stages[79]: stage I at $\sim 230K$, stage II around 280K and stage three around 500K. A 'set of defects' responsible in part for the increase in the leakage current and, to a lesser extent, the reduction of the charge collection

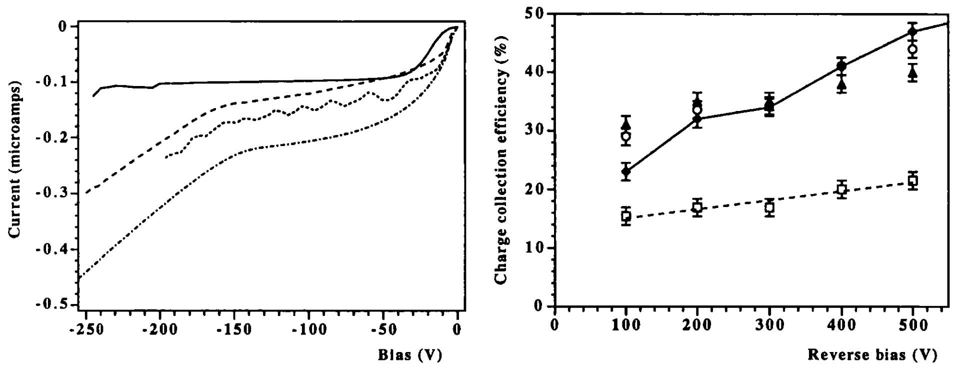

(a) The reverse current characteristics. The key is: solid line - pre-; dot-dashed - post-irradiation; dotted - 5 hour; dashed - 33 hour anneal.

(b) The charge collection efficiency. The key is: filled diamonds - post irradiation; open circles - 15 minute; filled triangles - 5 hour; open squares - 33 hour anneal.

Figure 5.27: Detector characteristics of a 180μm thick GaAs detector irradiated by 24 GeV/c protons to a fluence of 1.0×10^{14} /cm^2 and then thermally annealed at 210°C. All measurements were performed at 20°C.

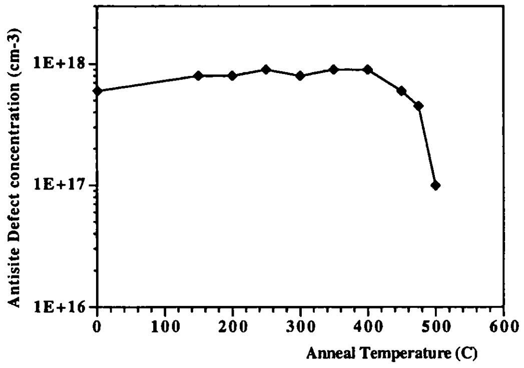

Figure 5.28: Annealing of neutron induced Arsenic antisites.

efficiency have been shown to anneal at 210°C and are therefore in stage III. The charge carrier reduction could be directly due to the trapping effects of this 'set of defects' or result from the perturbation of the electric field that these defects caused which resulted in enhanced trapping cross-sections of other deep defects. Further annealing studies are required combined with DLTS measurements to examine the exact effect of the anneals on these defects.

The arsenic antisite defect in GaAs is known to anneal at temperatures in excess of 450°C[73], illustrated in figure 5.28. As the irradiation is expected to produce such antisite defects the effect of annealing at 450°C was also investigated. A flash-lamp anneal was used to illuminate the detectors between 30 and 120 seconds. The effect was shown to be independent of which side of the detector was illuminated, demonstrating that the whole bulk was heated. Figure 5.29(a) illustrates that the plateau reverse current and the value of V_{fd} were both reduced with the anneal. The gradient in the IV characteristic above V_{fd} was increased which prevented the operation of the detector at the high voltages used before annealing.

The mip cce of the detector was increased for an applied bias less than V_{fd}, illustrated by figure 5.29(b) for an irradiated detector which was annealed at 450°C for 90 s. The increase in mip cce was due to an increase in electron signal (figure 5.29(c)) which increased with anneal time, however, the hole signal was not affected.

5.7 Other substrate materials

Irradiation tests were performed with GaAs diodes fabricated from SI-indium doped and VPE substrates.

5.7.1 SI-indium doped material

Two detectors fabricated from 500μm thick, SI indium-doped, (SI-In doped), GaAs substrates (see section 4.5.1) were exposed to a 24GeV/c proton fluence of 1.4×10^{14} /cm^2.

The reverse current characteristic of an indium- and an un-doped diode are shown in figure 5.30(a). After the irradiation the value of V_{fd} for the SI-In doped diode was reduced to only 220V compared to 340V for the undoped device and to the pre-irradiation value of 550V. The reverse current, which was less than the SI-U diode before irradiation, was almost twice that of the undoped sample after irradiation at approximately 400nA at V_{fd} (the knee in the current-voltage characteristic).

The charge collection efficiency for the indium-doped sample was comparable to the undoped samples before irradiation (figure 5.30(b)). After the irradiation, however, the cce fell to $10 \pm 1.5\%$ (6700 electrons) compared to $18 \pm 1.5\%$ (12300

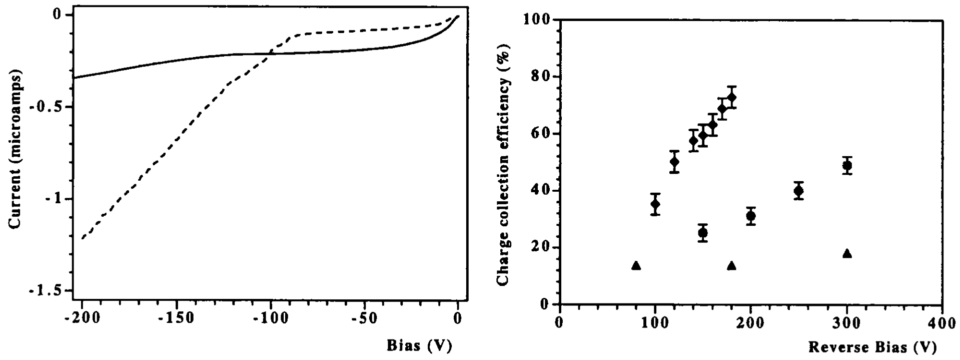

(a) Leakage current characteristic at 20°C. The key is: solid line - post irradiation; dashed - 90 s anneal.

(b) Mip charge collection efficiency. The key is: diamonds - pre-; triangles - post-irradiation; circles - 120 s anneal.

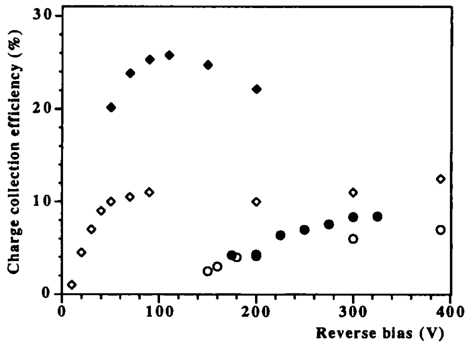

(c) Electron and hole charge collection. The key is: open diamonds - electrons post-irradiation; closed diamonds - electrons after 90 s anneal; open circles - holes post-irradiation; closed circles - holes after anneal.

Figure 5.29: The current and charge collection characteristics of SI-U GaAs detectors after a 24 GeV/c proton fluence of 1×10^{14} /cm^2 and a rapid thermal anneal at 450°C.

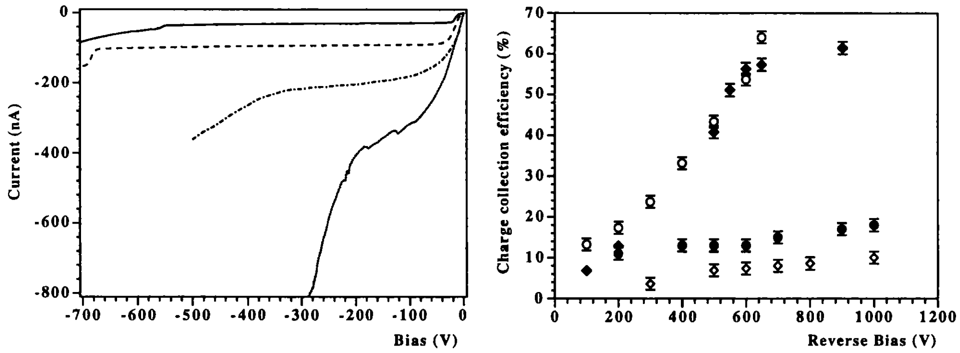

(a) Current characteristic. The key is: solid line - SI-In doped pre-; dashed line - SI-U pre; dotted - SI-In doped post; dot-dashed - SI-U post-irradiation.

(b) Mip charge collection. The key is: closed diamonds - SI-In doped pre-; open circles - SI-U pre-; open diamonds - SI-In doped post-; closed circles - SI-U post-irradiation.

Figure 5.30: Comparison of the current and charge collection characteristics of a 500μm thick SI-indium doped and a SI-U GaAs detector after a 24 GeV/c proton fluence of 1×10^{14} /cm^2, measured at 20^{o}C.

electrons) for a SI-U detector at an applied bias of 1000V.

The SI-indium doped samples tested were therefore less radiation hard than the SI-U detectors.

5.7.2 VPE material

Four of the VPE diodes described in section 4.5.2 were irradiated with 24 GeV/c protons/cm^2 to a fluence of 1.25×10^{14} /cm^2. The current- and capacitance-voltage characteristics are shown in figure 5.31. The current increased dramatically from the pre-irradiation value of 90 nA to 1500 nA for an applied bias of 200V. This represents an increase of more than an order of magnitude.

The activation energy of the reverse bias current was determined from the temperature dependence of the current at an applied bias of 10V. The current was assumed to be generation current and thus a plot of ln(I/T^2) against 1/T gives a straight line with the gradient equal to the activation energy (E_A). The result, shown in figure 5.31(b), gave a value of $E_A = 0.57 \pm 0.01$ eV. An electron trap introduced by electron irradiation has been reported with an energy level of 0.5eV[80]. This trap represented at most 5% of the electron trap concentration formed after electron irradiation, however, such irradiation will cause a majority of point-like defects. Proton irradiation will create a higher concentrations of complex defects, which this level represents, and therefore it is not unreasonable to expect a higher concentration of such levels in the VPE sample. DLTS experiments are required to obtain a better understanding of the traps created. If the level is created in LEC SI-U GaAs it might not change the activation energy due to the large concentration of the native EL2 defect.

The capacitance as a function of voltage showed a marked dependence upon the frequency of the test signal used, as was observed for the LEC SI-U material where deep levels are present. The measured capacitance at a given bias fell and was only 40 pF compared to 300 pF at -5 V. As the measured capacitance depends upon the density of free carriers and the number in traps which have emission rates greater than the frequency of the A.C test voltage, the reduction in the measured capacitance implies that the density of these carriers was reduced. Therefore a significant concentration of deep levels was created in the material due to the proton fluence. These were responsible for the increase in the generation current and the change in the diode capacitance.

The introduction of deep levels with a long electron emission time will affect the charge collection efficiency of the detectors. A spectrum from the 60keV ^{241}Am gamma source could not be obtained because the signal response was less than the noise. The charge collection efficiency of electrons from the Am^{241} alpha source used for the pre-irradiation measurements (section 4.5.2) was obtained, and is shown as a function of bias in figure 5.32. The charge collection was reduced to 55 ± 5% at the maximum applied bias, which represented a reduction of 45% with respect to a similar diode before irradiation.

After a 24GeV/c proton fluence of 1.3×10^{14} /cm^2 a SI-U GaAs device at 20^{o}C had a reverse current density of 2.8×10^{-6} A/cm^2 compared to 5.3×10^{-6} A/cm^2 for the VPE diode measured at 100V reverse bias. It must be noted, however, that the VPE diode was not guarded and therefore guarded diodes could demonstrate lower currents due to a reduction in surface currents. Charge collection from a SI-

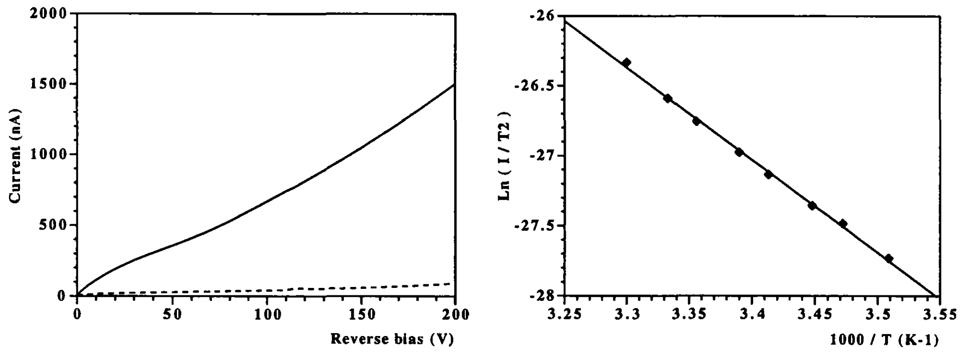

(a) Current characteristic measured at 20°C. The key is: solid line - post-; dashed - pre-irradiation.

(b) The activation plot for the irradiation VPE diode measured at -100V.

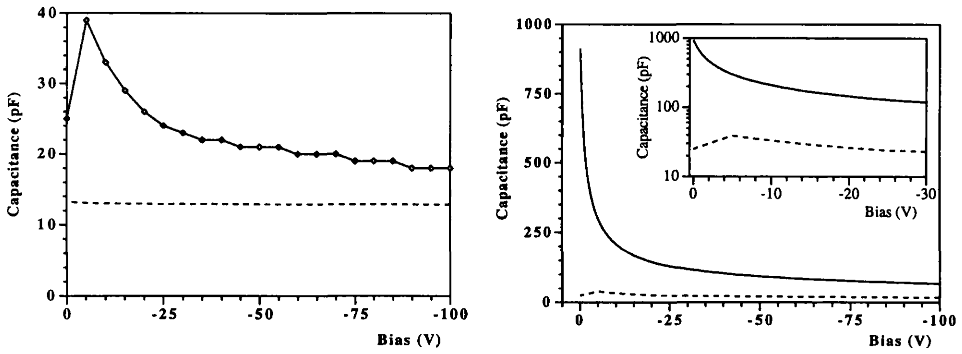

(c) Capacitance characteristic, measured at 20°C with two test signals. The key is: solid line - 100Hz ; dashed - 100kHz.

(d) Pre- and post-irradiation capacitance-voltage characteristics measured at 20°C with a test signal of 100Hz. The key is: solid line - pre; dashed - post.

Figure 5.31: The current- and capacitance-voltage characteristics of a VPE diode before and after a 24 GeV/c proton fluence of 1.25×10^{14} /cm^2.

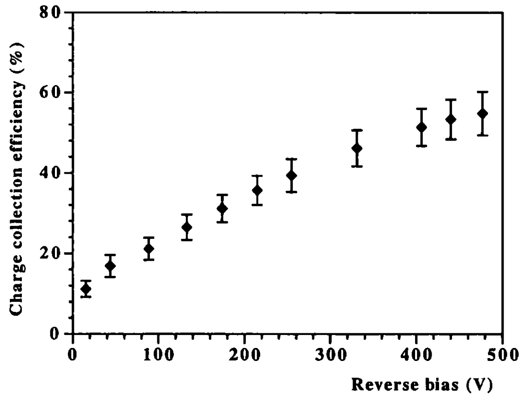

Figure 5.32: The electron charge collection efficiency as a function of reverse bias for a VPE diode after a 24 GeV/c proton fluence of 1.25 x 10^{14} /cm^2.

U detector was considerably worse than in the VPE device both before and after the radiation fluence. The electron cce for a typical SI-U device measured at 200V fell from 62 ± 5% to 11 ± 3%, after this proton fluence, a reduction of 82%. By comparison, the VPE diode had an electron cce at -200 V bias of 100% before irradiation which fell by 68% to 32 ± 5% after the proton fluence of 1.3 × 10^{14} /cm^2.

In summary the VPE material had a much better post-radiation charge collection efficiency than the SI-U material, however the reverse current was significantly worse.

Chapter 6

Microstrips

Useful Vocabulary : *test beam - a practice smile*

6.1 Introduction

GaAs detectors proposed for the ATLAS experiment are not simple pad detectors, as described in the previous chapters, but are microstrip detectors. To ascertain the quality of GaAs microstrip detectors three were fabricated and tested in a 70 GeV/c π beam from the SPS in the X1 area at CERN, during the summer of 1995. The detectors were tested in the laboratory before being coupled to Viking read-out electronics[81]. After testing with the read-out electronics they were placed in the beam where the read-out chain consisted of the Viking front-end amplifier, a repeater card, followed by a VME Sirocco ADC[82] and finally by data recording on tape so that off-line analysis could be performed on the data. The figures of merit for a strip detector - the signal-to-noise ratio, spatial resolution and detection efficiency - were obtained for each GaAs microstrip detector. This chapter discusses the stages from detector design and laboratory testing through to the final off-line analysis of test beam data from the strip detectors.

6.2 The microstrip detectors used

The detectors tested in 1995 were all parallel strip, constant pitch devices with 384 strips per detector. Three strip detectors were tested in the X1 beam, one fabricated

Detector	Pitch (μm)	Aspect ratio	Strip length (mm)	Number of strips	Strip contact
G114	50	40:10	18.5	128	Rectifying
G114	50	25:25	18.5	128	Rectifying
G114	50	10:40	18.5	128	Rectifying
AL-W3-6	50	30:20	25	384	Rectifying
AL-W3-8	50	30:20	56.5	384	Ohmic

Detector	Thickness (μm)	Bias resistance	Decoupling capacitance
G114	500	Reach through	External
G114	500	Reach through	External
G114	500	Reach through	External
AL-W3-6	200	Reach through	Integrated
AL-W3-8	200	Substrate resistivity	External

Table 6.1: The GaAs microstrip detectors used in the 1995 test beam.

at Glasgow University (G114) and two from Alenia SpA of Rome, Italy (Al-W3-6 and AL-W3-8). The design of the microstrip detectors is summarised in table 6.1.

All the devices had a strip pitch of 50 μm which matched the input pitch of the read-out electronics. Device G114 was fabricated upon a 500 μm thick SI-U GaAs substrate from MCP with the rectifying contact segmented to form 384 strips 1.85 cm in length. These strips were divided into three groups with different strip width to gap ratios (aspect ratios) of 10:40, 25:25 and 40:10, so that the dependence of charge sharing and thus ultimately spatial resolution could be obtained as a function of aspect ratio. The resolution of a strip detector improves if the signal charge is shared between two strips, as will be shown in section 6.3. More charge sharing will occur if the applied voltage is low so that the charge carriers have a low drift velocity and thus have time to diffuse laterally. It was feared that charge sharing in GaAs detectors might be small because they have to be operated at high bias voltages to obtain full charge collection, resulting in high drift velocities. The problem is compounded by the high electron mobility of the material. The question of a possible region of low charge collection between the strips could also be investigated.

The two Alenia detectors, both with strip aspect ratios of 30:20, were fabricated on 200 μm thick SI-U GaAs substrates from the manufacture Sumitomo. Detector AL-W3-8 had strips of length 5.65 cm, close to the intended length of the final ATLAS detector modules, formed from segmentation of the ohmic side of the device. The back side of this device was the rectifying contact. Section 6.3 will discuss the process of signal formation in strip detectors which will explain the importance of this alteration in metallisation. The other Alenia detector, AL-W3-6, had rectifying strips of only 2.5 cm in length.

Two possible particle detector read-out methods are available, schematics of which are shown in figure 6.1. The first is where the strip is directly coupled to the amplifier (D.C read-out) while the second schematic is for an A.C coupled detector. The advantage of a D.C read-out scheme is that the input capacitance at the pre-amp is minimised, an important consideration with respect to the noise of the device. Disadvantages of this method are that detector leakage current shifts, due to thermal changes, can cause baseline shifts in the electronics resulting in signal loss. The fact that the detector is grounded through the amplifier is also not ideal. Some amplifiers can only sink a small amount of current, which rules out D.C coupling if the detector current exceeds this maximum.

The A.C coupled detector overcomes these difficulties at the expense of new problems. An increase in input capacitance from the decoupling capacitor occurs, obviously. If the decoupling capacitor on its own is added to the D.C circuit, there is no path to ground for the detector current and so a bias resistor must be incorporated. This resistance must be high in order to keep the extra noise from this component to a minimum and to ensure that the A.C signal sees a much higher impedance from this than from the decoupling capacitor, so that no signal loss occurs. Noise considerations for signals from charge-sensitive read-out electronics are discussed later with reference to the Viking pre-amplifier (see section 6.4.1).

For all three devices the bias resistors were realised on the GaAs detectors themselves, while detector AL-W3-6 also had integrated decoupling capacitors. These were fabricated as a layer of silicon nitride on top of the 30 μm wide diode

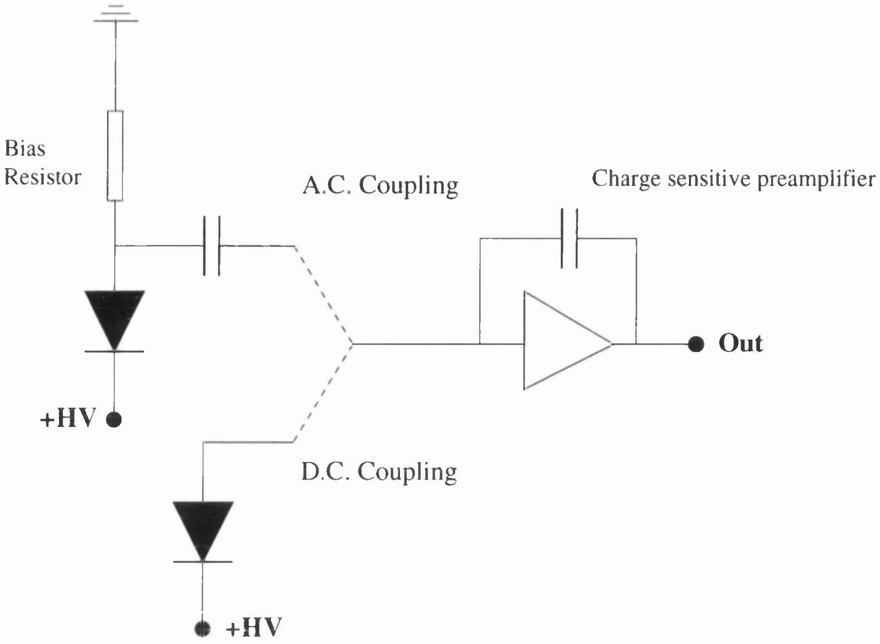

Figure 6.1: An A.C. and a D.C. coupled read-out scheme for a strip detector.

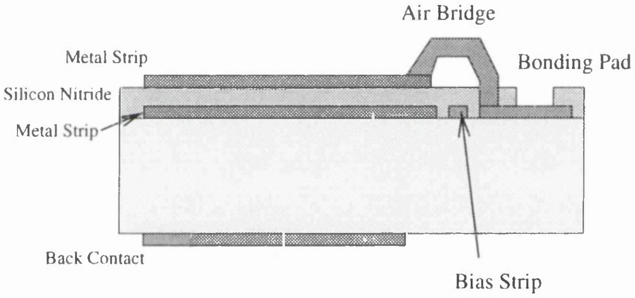

Figure 6.2: Cross-section of the AL-W3-6 detector with integrated capacitors.

strips, the upper layer of which was metallized with a 20μm wide read-out strip, shown in cross-section in figure 6.2. External capacitor chips fabricated on a quartz substrate with a capacitance of 150 pF per strip were used to decouple the two other detectors. These devices had back-to-back diode protection at the input so that, if a strip was floating at a significant voltage ($>$ 7 V) above ground, the detector strip would be shorted to ground and thus prevent damage to the capacitor chip and ultimately the front end electronics.

The required DC path to ground was realised for detectors G114 and AL-W3-6 via a reach-through biasing scheme. The ohmic strip detector had a similar metallisation, but due to the non-rectifying nature of the strips the bias resistance was simply that due to the resistivity of the SI GaAs substrate. Figure 6.3 shows the

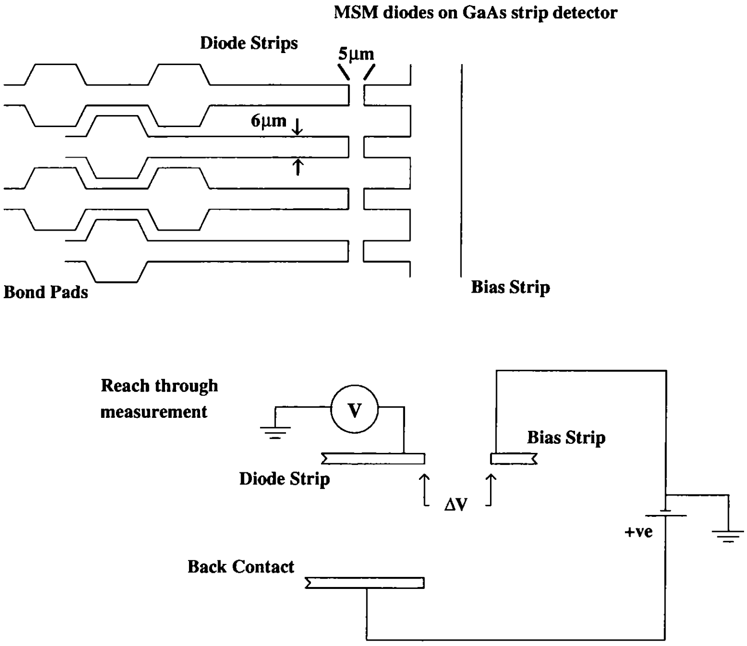

Figure 6.3: The MSM bias structure on a GaAs microstrip detector and the measurement schematics for the reach-through potential.

metallisation of the bias strip with fingers that extend towards the read-out strips. The gap between the fingers of the biasing rail and the detector strip was 5 μm long and 6 μm wide. The bond pads at the end of the read-out strip allow connectivity to the read-out electronics. Each strip has four such pads with two at either end. The structure of the reach-through biasing scheme is a metal-semiconductor-metal (MSM) diode shown in figure 6.4. At zero applied bias (A in figure 6.4) a depletion region is present under both strips due to the built in potential of the barrier. On application of a potential across the two junctions the depletion region extends from the reverse-biased barrier into the material. During normal operation it is the bias rail that is held at a negative potential. The reach-through potential (V_{rt}) is obtained (B in figure 6.4) when the depletion regions from the bias strip and the read-out strip join.

For n-type silicon with p-type contacts the reach-through potential is given by[83]

$$V_{rt} \simeq \frac{qN_d}{2\epsilon_s}L^2 - L\left(\frac{2qN_dV_{bi}}{\epsilon_s}\right)^{\frac{1}{2}} \tag{6.1}$$

where L is the length of the gap between the finger and the read-out strip. Typically, for a silicon detector with a donor density of 5×10^{12} cm^{-3}, this occurs at a bias of 7.6 V for $L = 5\mu$m. Expression (6.1) results from equating the depletion lengths for

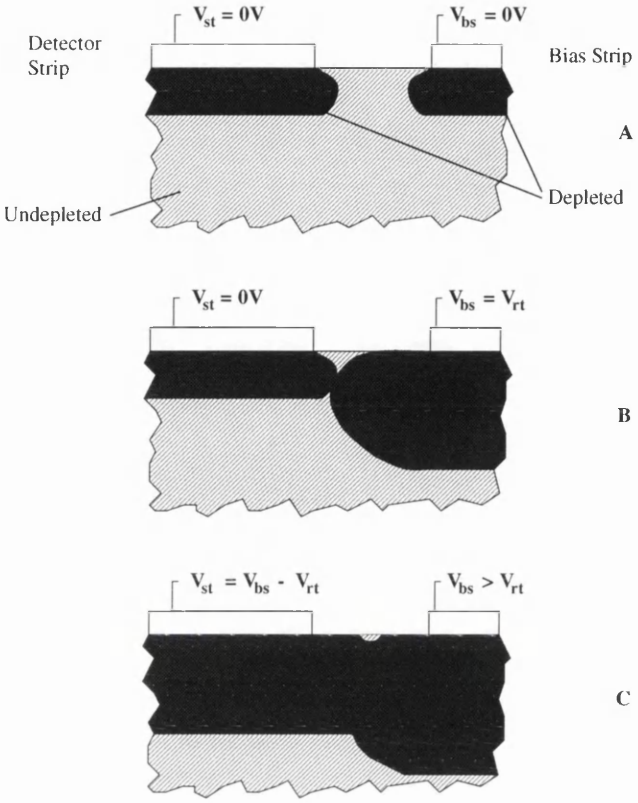

Figure 6.4: A schematic of the reach-through structure.

a back-to-back silicon diode. In SI-U GaAs, however, the extension of the depletion region is not given by simple theory, as discussed in previous chapters, and therefore a different potential is required for reach-through.

For an applied bias greater than V_{rt} (C in figure 6.4) the current that flows through the diode is that due to the forward biased junction, which is limited by that of the strip current, I_{st}, in series with the MSM structure. The biasing structure has a dynamic resistance, R_{bs}, given by the differential of the current with respect to the voltage. The current that flows through this resistance thus causes a voltage drop and it is this voltage drop that must be found for correct detector operation.

The experimental apparatus used to measure this voltage is shown in figure 6.3. The bias rail was held at ground and a positive bias was applied to the back contact of the detector. The strip voltage (V_{st}) was measured as a function of the applied bias (V_{bk}). Figure 6.5 shows the result of such as measurement made on detector G114 at room temperature for a 10 μm and a 40 μm wide strip. The value of V_{st} follows the applied voltage until the reach through voltage is applied. From such a

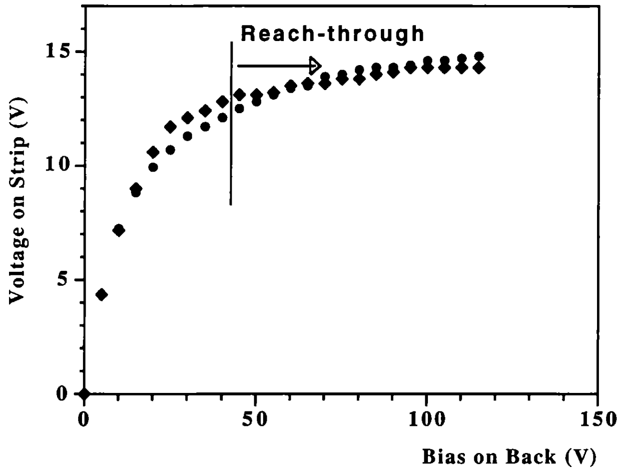

Figure 6.5: The voltage on the detector strip versus back contact voltage for the G114 detector with the bias rail held at ground. The key is: circles - 10 μm; diamonds - 40 μm wide strips.

plot the reach-through voltage is thus obtained. It is also apparent that the strip voltage does not increase significantly on application of higher voltages. During the operation of a microstrip detector the bias rail is held at a negative voltage sufficient to keep the read-out strips close to zero volts. This ensures that the DC current flows through the biasing network. To prevent an excessive voltage being applied across the bulk of the detector between the bias strip at a negative bias and the forward biased back contact the rear metallisation extends only up to the end of the read-out strips and does not overlap the bond pads and bias strip.

The V-V characteristic can be explained by considering a floating read-out strip where the voltage on the strip is:

$$V_{st} = V_{bs} - \Delta V \tag{6.2}$$

where

$$\Delta V = I_{bf} R_{bs} \quad = \quad I_{st} R_{bs} \quad \text{for} \quad V_{bs} > V_{rt} \tag{6.3}$$

and I_{bf} is the current of the forward biased bias strip. Therefore, if the voltage on the strip is measured for an applied voltage on the back contact of the detector with the bias rail held at ground, when the voltage V_{rt} is reached the strip voltage will equal V_{rt} (=ΔV) and follow ΔV. However, ΔV is limited by the constant strip current I_{st} and is therefore constant at the value given in equation (6.3). The reach-through voltage of approximately 40 V for detector G114 is typical of MSM bias structures formed on SI GaAs. The extension of the high field region has been seen to be roughly 1 μm/V which would imply that 5 V would be required for the reach-through condition to be satisfied for a separation of only 5 μm. The greater bias required must be due to the necessity for the depletion region to extend laterally rather than perpendicularly to the metal contacts. Lower values of V_{rt} have been recorded with SI GaAs MSM structures fabricated with diffused strips where the contacts formed are deeper in the material [84].

The Al-W3-8 detector has ohmic strips and thus the reach-through bias structure will not work. The required resistance is obtained from the semi-insulating substrate itself. The resistance (R_{bs}), measured by applying a D.C bias between the bias rail and a strip, was temperature dependent with a value of 14 MΩ at 26^{0}C. During the operation of this strip detector the bias rail must be held to ground and not the negative voltage required for the reach-through system.

Figure 6.6(a) shows the total leakage current of each set of 128 strips for each aspect ratio in the G114 detector. Figure 6.6(b) is that for the 384 strips of detector AL-W3-6; both were measured at 20^{0}C. The measurements were performed by biasing the detector through the bias strip, holding the back contact to ground and allowing the read-out strips to float. The leakage current is independent of the width of metallisation in the rectifying contact and is proportional to the area of the back contact. The leakage current per unit area of all three devices, calculated from the measurement of the total leakage current, is given in table 6.2.

The knee in the AL-W3-6 current characteristic at 50 V is due to the reach-through process connecting the strips to the bias rail. The current below this voltage is small and due to the leakage current of the bias rail only. The lack of a low bias plateau in detector G114 is probably due to a fabrication error which resulted in some of the strips becoming shorted to the bias rail. Thus reach-through did not need to occur before some strips contributed to the leakage current.

The single strip current voltage characteristics of detectors G114 and Al-W3-6 are shown in figure 6.7. These were obtained by applying a bias to one read-out strip and measuring the current while the strips on either side were kept at the

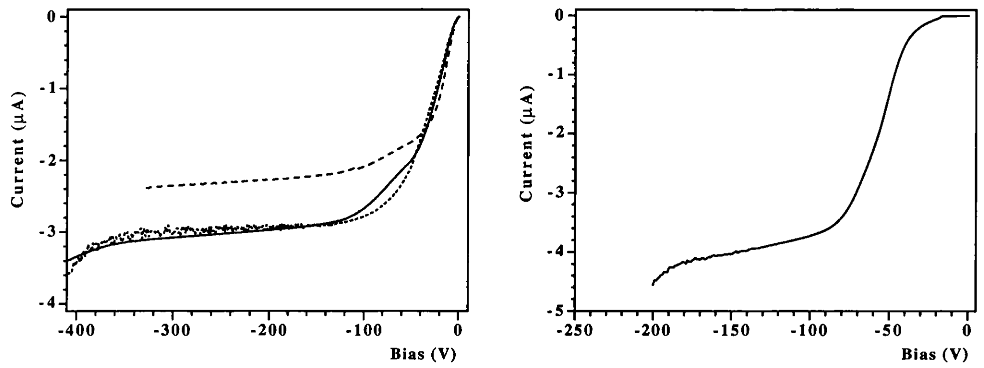

(a) The leakage current of 128 strips measured for each aspect ratio of detector G114. The key is: dashed line - 40 μm wide strips; solid - 25 μm; dotted - 10 μm.

(b) Total leakage current of detector AL-W3-6

Figure 6.6: Total detector leakage currents for detectors G114 and AL-W3-6 measured at 20^0C.

Detector	Strip widthμm	Current per unit area (nA/mm^2)	
		From total IV	From single strip IV
G114	10	29	25
G114	25	32	25
G114	40	17	20
AL-W3-6	30	8	9
AL-W3-8	30	9	8.5

Table 6.2: The leakage currents of the three strip detectors measured at 20^oC.

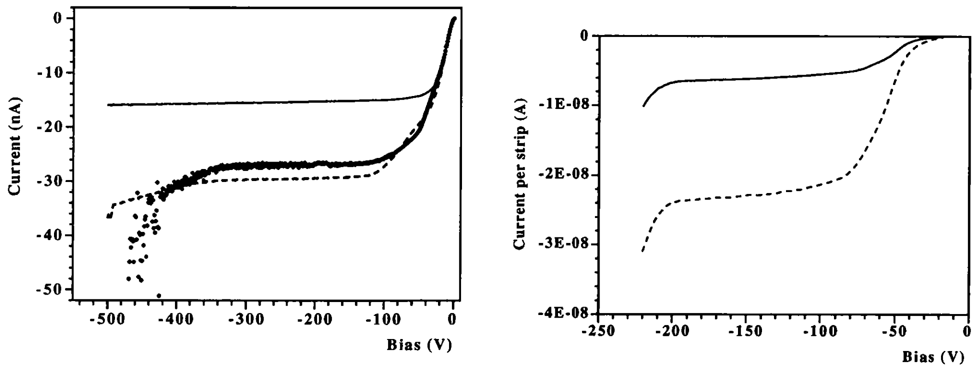

(a) Detector G114 at 20^{0}C for the three aspect ratios. The key is: solid line - 40 μm wide; dashed - 25 μm; dots - 10 μm.

(b) Detector AL-W3-6 measured at two temperatures. The key is: solid line - 17^{0}C; dashed - 27^{0}C.

Figure 6.7: The signal strip current voltage characteristics of two microstrip detectors.

same bias to act as a guard ring around the strip under investigation. The back of the device was grounded. The detectors all operated correctly with a plateau in the current characteristics as seen with simple pad devices. The leakage current through the device is that due to the active region under the strip with a width defined by the strip pitch and the lateral spreading of the field. In general the magnitude of the leakage current is reasonably independent of strip width with a value equal to the total current that was measured above divided by the number of strips in the detector. The leakage current per unit area calculated from the single strip characteristics are given in table 6.2.

The breakdown voltage of the 10 μm strip has been consistently measured over a large number of strip detectors to be slightly lower that that measured for the other strips. This might be due to a region of high field at the edge of the narrow strips which causes early breakdown.

From figure 6.7(b) the importance of operating the detectors at a low temperature to reduce leakage current noise is obvious. The proposed operating temperature of the ATLAS SCT is -10^{0}C which is advantageous from current considerations. For the test beam the temperature was kept within the range of 13^{0}C to 18^{0}C using a portable air conditioning unit.

Capacitance measurements were carried out on the strip detectors to find the inter-strip capacitance. The inter-strip capacitance is the dominant capacitance term at the input of the amplifier. From signal processing arguments, this capacitance should be kept to a minimum to reduce the noise associated with the amplified signal. Capacitance measurements were performed on test structures similar in design to the complete strip detector. These consisted of strips of three different lengths grouped in sets of only six strips per aspect ratio. The other difference in design was that the strips only had bond pads at one end. Capacitance measurements were performed with zero applied bias on the structures. Since the capacitance will fall with increasing bias as the depletion region grows, these measurements give an upper limit to the value experienced in the test beam. Ideally, measurements should be performed at a frequency which corresponds to the shaping time of the readout electronics to be used. For the Viking electronics this implies a frequency of $\sim$ 2 MHz. The LCR machine used in Glasgow, however, has a maximum frequency of 100 kHz, so this was used for the measurements. The variation of inter-strip capacitance with strip length for the three aspect ratios of detector G114 are shown in figure 6.8 to depend linearly on the strip length. The plot also shows the measured values of inter-strip capacitance for a 1.85 cm long strip detector. The difference between the predicted value and that measured is due to the presence of the extra bond pads on the full strip detector.

The variation of interstrip capacitance as a function of the width of the non-metallized region between the strips does not follow a simple 1/r relationship, as expected for parallel plate capacitors, but the capacitance does decrease with separation distance, as shown in figure 6.9.

According to these measurements the interstrip capacitance of the Al-W3-8 strip detector, which is the largest of all the three detectors tested, is approximately 4 pF. Therefore the decoupling capacitance of 150 pF will not add significantly to the input capacitance of the detector and can be ignored for noise considerations.

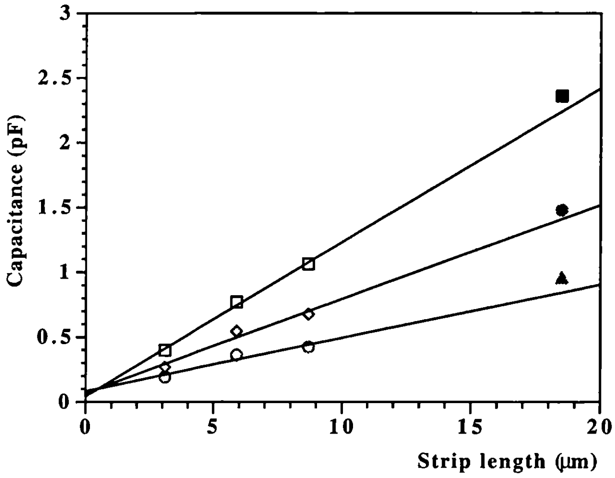

Figure 6.8: The variation of the interstrip capacitance with strip length for three aspect ratios: The key is: square - 10 μm gap; triangle - 25 μm gap; circle - 40 μm gap, the open points are from a test structure while the solid ones correspond to an actual detector.

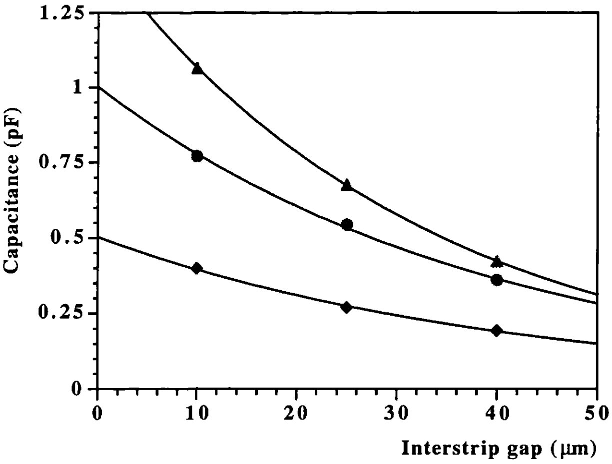

Figure 6.9: The variation of interstrip capacitance with interstrip gap for three strip lengths: diamond - 3.1 mm; circle - 5.9 mm; triangle - 8.7 mm.

6.3 Signal generation

The signal observed in a detector is induced by the motion of carriers around an electrode. The electrode geometry may be a simple parallel plate arrangement or the more complex situation of the microstrip detector, where one or both of the electrode plates are divided into many parallel strips. The induced current on the sense electrode (i_1) due to a charge (q_m) moving with velocity v, as a function of position of the moving charge, is given by Ramo's theorem[85] as:

$$i_1 = -q_m . E_w v \tag{6.4}$$

where E_w is the weighting field, and the presence of the negative sign is because the induced charge has been assumed positive. The weighting field results from an electrostatic analysis of the problem using Green's theorem and is a measure of the electrostatic coupling between the moving charge and the sense electrode. The sense electrode for a microstrip detector is the particular strip that is under investigation. The weighting field is calculated by setting all the potentials of the system to zero except for the sense electrode which is held at one volt. It should be clear that the weighting and the operating fields of a detector are quite different.

An associated weighting potential (V_w) may also be defined from the weighting field as:

$$E_w = -\mathrm{grad}(V_w) \tag{6.5}$$

To obtain the current as a function of time, that is the waveform of the induced signal, the weighting field must first be found. Second, the velocity of the charge as a function of position must be determined from the operating field of the detector and the properties of the material. From this the induced current as a function of position follows. Finally, the equations of motion that govern the charge must be solved to obtain $x(t)$, $y(t)$ and $z(t)$ which are substituted back into $i_1(x, y, t)$ to give $i_1(t)$.

If only the total induced charge (Q_1) is required then:

$$Q_1 = \int i_1 dt = -\int_{m_1}^{m_2} E_w dl = q_m [V_w(m_1) - V_w(m_2)] \tag{6.6}$$

where the velocity has been replaced by $\frac{dl}{dt}$, dl being a small change in distance. The induced charge is therefore the difference in the weighting potentials between any two positions (from m_1 to m_2) of the moving charge inside the device.

The magnitude of the weighting field, calculated for the detector geometry shown in figure 6.10(a), is shown in figure 6.10(b). The curves represent the modulus of the field calculated at 25 μm steps in depth into the device. It can be seen that the field is much higher just under the sense strip and falls rapidly with distance into the bulk of the detector and across to the neighbouring strips. The operational field in such a detector is uniform throughout the bulk and perpendicular to the strip planes. According to equation (6.4), the majority of the induced current will be created in the vicinity of the sense strip. This has important consequences with respect to the fabrication of a detector with ohmic strips.

Figure 6.11 illustrates the difference between a strip detector with rectifying strips and one with ohmic strips. The electric field shown, with a high field plateau region and low field region, is that which has been observed in SI-U GaAs devices. Charge carriers in the low field region have a negligible velocity and therefore induce no signal on the sense strip. For the situation with rectifying strips, most of the signal is due to the motion of holes as they approach the strip and the detector can be thought of as collecting holes. The high field region extends from the strips and the induced current from the holes will be significant even if the detector is not fully depleted. Ohmic strips are illustrated in the second part of figure 6.11. Here the operating field will reach the strips only when the detector is fully depleted and thus the induced charge will be small until this occurs.

The second implication of the non-uniform weighting field concerns the current induced on neighbouring strips. To illustrate this the weighting field must be represented as lines of equipotential, as shown in figure 6.12(a)

When a positive charge passes along a path directly under and perpendicular to the sense strip (path A) and traverses the full detector towards the sense strip the observed charge is:

$$Q_1 = q_m \tag{6.7}$$

The current increases with distance as the carrier approaches the electrode because the electrostatic coupling increases, that is V_w increases. The resultant wave form is that shown in figure 6.12(b)

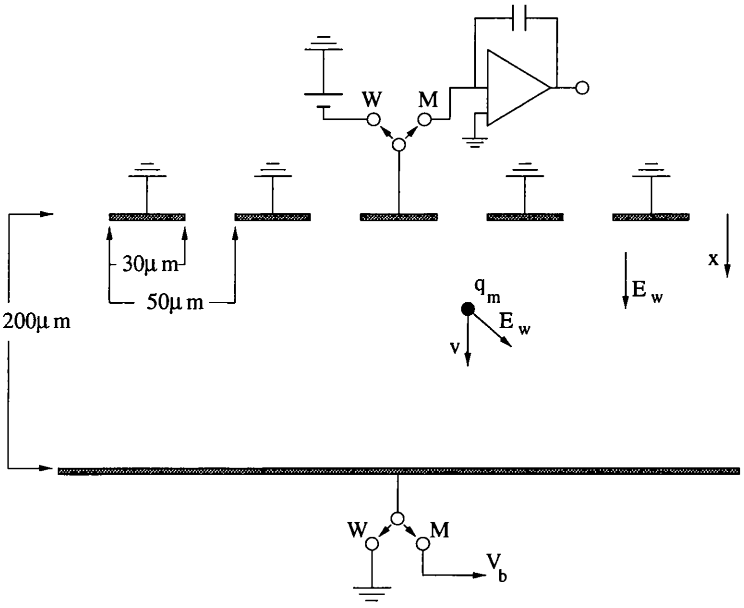

(a) The microstrip detector, 200μm thick with a 50 μm strip pitch and 30 μm width. The weighting field is found with the switches at position W and the operating field is that obtained for position M, where the sense strip is connected to an amplifier and the back is biased to V_b.

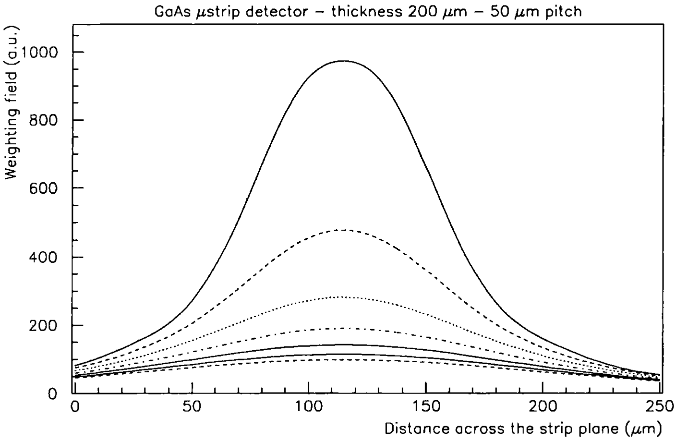

(b) Modulus of the weighting field for the strip detector with the sense strip centered at 115 μm. The different curves refer to distances from the strip plane differing by 25 μm.

Figure 6.10: The weighting field concept for a microstrip detector.

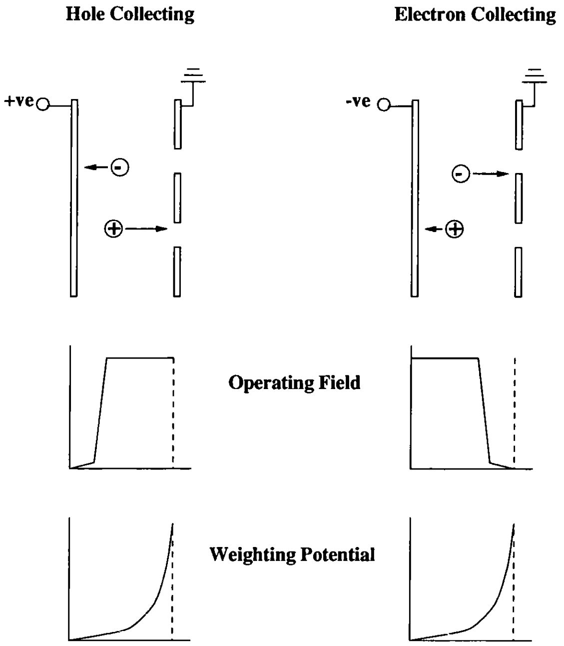

Figure 6.11: Microstrip detectors with rectifying or ohmic strips.

For a charge that follows path B in figure 6.12 the size of the induced charge depends upon the collection time, that is the shaping time, of the amplifier. If the collection time is greater than the charge transit time of the detector the total charge is zero. However, for a shorter collection time an induced charge is observed. This arises because the current waveform is bipolar (see figure 6.12(c)) due to the change in weighting field direction along the path, as shown.

Due to charge trapping in GaAs detectors a net charge will be induced on the neighbouring strip. The magnitude of the net charge depends upon the time at which the bipolar signal swaps sign and the proportion of carrier trapping. The position along the path of the charge at which the signal swaps sign depends upon the position at which the weighting field direction becomes perpendicular to the direction of motion. This is dependent upon the strip geometry and is closer to the strips for small interstrip separation. That is, a longer positive signal occurs for smaller interstrip gap, which is balanced by a short negative signal. Incomplete charge cancellation, due to carrier trapping, will be more significant for small strip separation as the total negative current is produced over a smaller distance.

Charge sharing will also occur in a strip detector through carrier diffusion so that the deposited charge cloud spreads over more than one strip. The carriers created

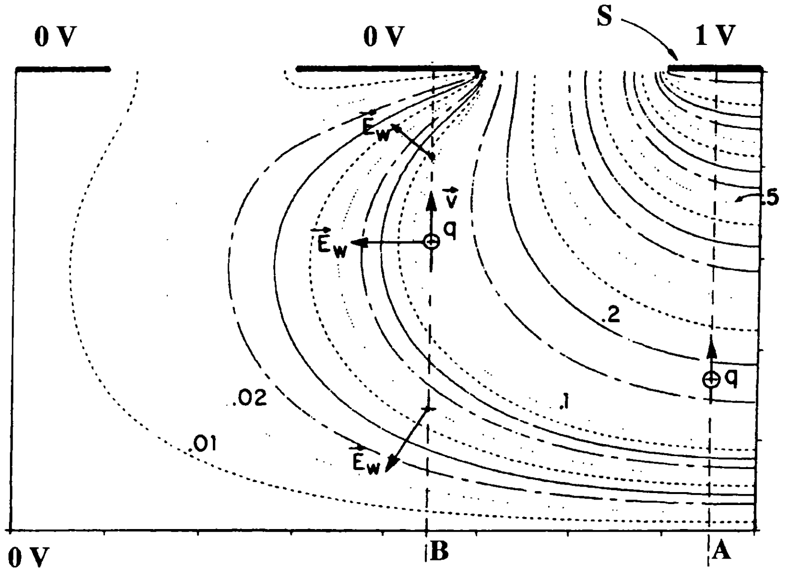

(a) A sketch of the weighting field shown as a plot of equipotential lines for the left hand side of a sense strip, S.

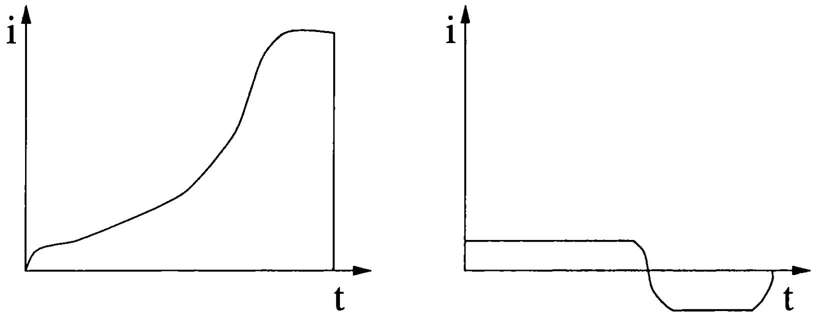

(b) Waveform of the induced charge on the sense strip for a charge that follows path A

(c) Waveform of the induced charge on the sense strip for a charge that follows path B

Figure 6.12: Signal formation on neighbouring strips.

diffuse as they drift towards the electrodes in the drift time t_d and create a Gaussian distribution with a standard deviation, sigma, given by:

$$\sigma = \sqrt{2Dt_d} \tag{6.8}$$

where D is the diffusion constant, which is proportional to the carrier mobility[12]. The spread, however, is independent of the mobility due to the drift time being inversely proportional to it. If the low field relationships for D and t_d are assumed (although this is not correct as the GaAs detector are operated at high voltages) then:

$$\sigma = \sqrt{\frac{2k_BTd}{qE}} \tag{6.9}$$

where d is the thickness of the detector, and E is the applied electric field in the detector. For a 200 μm thick detector biased at 200 V and operated at 300K, the spread due to diffusion is only 3.2 μm. The amount of charge sharing depends on the relative magnitude of this distribution and the strip pitch. Strip detectors are never fabricated with a strip pitch of less than 20 μm and the detectors tested in the test beam all had read-out pitches of 50 μm. The strip width for two detectors was 30 μm with a 20 μm non-metallized region. Charge sharing due to diffusion will take place for only 3.2 μm of this about the centre of the gap. That is, only 6% of the signals will appear on two strips and a cluster size of 1.06 results.

Charge sharing can also take place via capacitative coupling effects between the strips due to the interstrip capacitance (C_{is}) [13]. The fraction (K) of the charge that arrives at one strip that appears on the neighbouring strip due to this effect is

$$K \approx \frac{C_{is}}{C_D} \tag{6.10}$$

where C_D is the decoupling capacitance. For the test beam typical values of C_{is} and C_D were 2 pF and 150 pF, respectively. The fraction of charge sharing due to this effect is therefore only 1.3%, corresponding to a mean cluster size of 1.013.

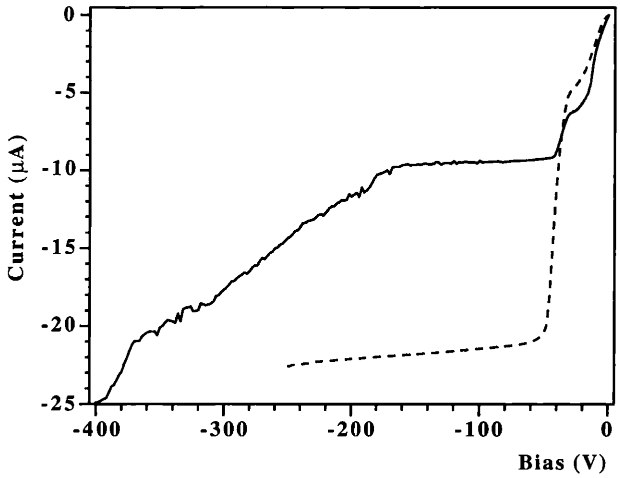

Figure 6.13: The current-voltage characteristics of detector AL-W3-8 before and after bonding to the read-out electronics. The temperature was 26.0^0C for the former and 21.5^0C for the latter measurement. The key is: dashed - before bonding; solid - after.

6.4 The test beam

6.4.1 Read-Out electronics

All three detectors were wire bonded to VA2 read-out electronics, one of the next generation of Viking amplifier chips [81]. The VA2 amplifier is described here after a short section discussing the bonding process and heat dissipation.

The detectors were ultrasonically wire bonded to the electronics. This proved to be problematic for the Glasgow detector and the long Alenia detector. The top metallisation layer of detector G114 was evaporated gold which has a very smooth surface. This led to the bond head sliding on the surface and therefore a high power setting was required to form a bond. Such a situation is undesirable due to the damage that the extra force causes to the GaAs under the bond pads. Bonding problems were also experienced with detector AL-W3-8. As a result, the current-voltage characteristic after bonding showed a premature increase in current, as seen in figure 6.13. The leakage current in the plateau region of this characteristic is the same for both curves when the temperature variation is taken into account, and was therefore not affected by the bonding process. The other Alenia detector, AL-W3-6, had a thick sputtered gold contact on the bond pads which improved the 'bond-ability' of the device to the extent that no bonding problems occurred with

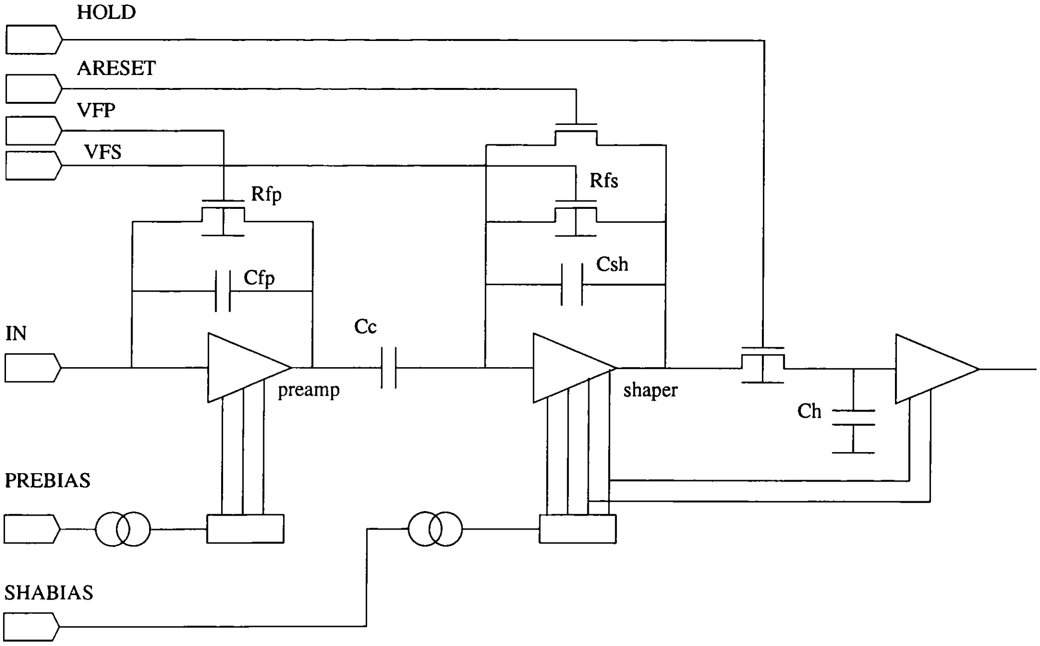

Figure 6.14: Schematic diagram of one channel of the Viking amplifier.

this detector.

As GaAs has a lower thermal conductivity and specific heat capacity than silicon (see appendix A), the problem of detector heating from the electronics must be considered. The leakage current has been shown to be a strongly dependent function of temperature and thus every precaution must be taken to minimise the heating of the device. The VA2 chip bonded to the AL-W3-6 detector was mounted directly on an aluminium heat sink to dissipate any heat from the electronics. The other detectors were separated from the electronics by the quartz capacitor chips which should minimise detector heating. During the beam test the air around the detectors was cooled using the air-conditioning unit mentioned previously.

The VA2 chip contains 128 low power (1.5 mW/channel) charge sensitive per-amplifiers followed by CR-RC shapers and sample-and-hold circuitry, shown in figure 6.14. The capacitor Ch is the charge storage device. The stored charge of each channel is read out sequentially via an analogue multiplexer to a single output buffer and sent to an external differential amplifier and finally to an ADC. The amplifier feedback resistors R_{fp} and R_{fs} are non-linear MOS elements controlled by external bias voltages VFP and VFS, respectively. The pre-amplifier, shaper and buffer operation are controlled by externally defined biasing currents.

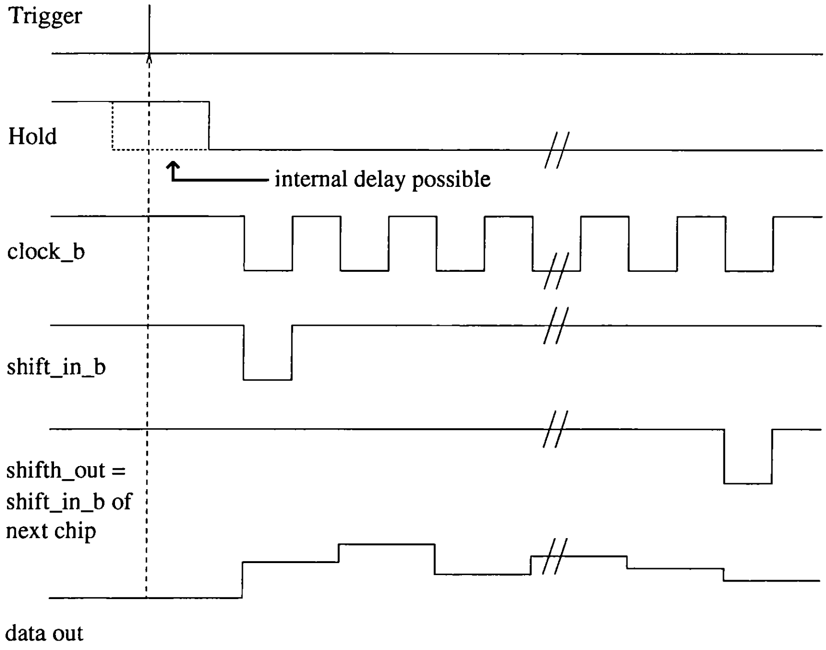

Figure 6.15: The timing diagram for the Viking amplifier chip.

The chip allows an external trigger to clock out a single channel, enabling the optimisation of signal shape for each detector, before test beam installation, through the adjustment of the aforementioned voltages and currents. The peaking time of the VA2 circuit is adjustable from a minimum of approximately 300 ns to over 2 μs; the range 1.5 μs $\rightarrow$ 2 μs is most commonly used.

The timing diagram of the Viking chip is shown in figure 6.15. Once the external trigger is applied to the chip the amplified charge is sampled after the time defined by the hold signal and stored on the capacitor Ch. The hold time should correspond to the peaking time chosen for the signal so that the peak of the signal is sampled and stored. The shift_in and clock signals read-out each channel sequentially.

Noise considerations

One of the most important features of an amplifier is its noise slope. This relates the noise, referred to the input of the amplifier, to the load capacitance. The noise is measured as an equivalent noise charge in units of electrons. The detector will also contribute additional noise due to the leakage current shot noise and thermal noise from the biasing resistor at the input.

The pre-amplifier noise for a CMOS input transistor with CR-RC shaping is[86]:

$$Q_{na}^2 = \frac{1}{q^2}\left(e_n^2\frac{F_v}{\tau} + 4A_f\right)(C_{det} + C_i)^2 \tag{6.11}$$

where q is the electron charge and e_n is the spectral density of the equivalent input noise voltage. F_v is a form factor associated with the shaping and has a value of 0.924 for CR-RC shaping with equal differentiation (τ_{diff}) and integration (τ_{int}) time constants ($\tau_{diff} = \tau_{int} = \tau$), which is the case for the Viking amplifier[87] used throughout this study. The term A_f expresses the intensity of the 1/f noise which is independent of the shaping time used. C_{det} and C_i are the detector and amplifier input capacitances, respectively. The equivalent input noise voltage is related to the transconductance (g_m) of the input FET by:

$$e_n^2 = 4k_BT_0\frac{\gamma}{g_m} \tag{6.12}$$

where $T_0 = 300$K, and γ is an empirical constant which depends upon the device type, geometry and operating conditions. The gain of an FET is proportional to the transconductance and thus a high gain input stage should be used to keep the amplifier noise contribution to a minimum. The pre-amplifier noise contribution will increase with decreasing peaking time and increasing input capacitance. The amplifier input capacitance is determined by the chip designer while the detector capacitance is a function of the desired strip length. The Viking has the following experimentally determined dependence upon the detector capacitance for 1.5 μs and 2 μs peaking times:

$$\begin{aligned} Q_{na} &= 125e^- + 14.4e^-C_{det} \quad \tau = 1.5\mu s \\ Q_{na} &= 136e^- + 12.3e^-C_{det} \quad \tau = 2.0\mu s \end{aligned} \tag{6.13}$$

where C_{det} is measured in pico-Farads. From equation (6.11) the first term corresponds to:

$$\frac{1}{q^2}\left(e_n^2\frac{F_v}{\tau} + 4A_f\right)^{\frac{1}{2}} C_i \tag{6.14}$$

This should therefore increase with decreasing peaking time, contrary to observation.

The second term, which shows the required increase in noise with decreasing peaking time, is similar to equation (6.14) but with the detector capacitance

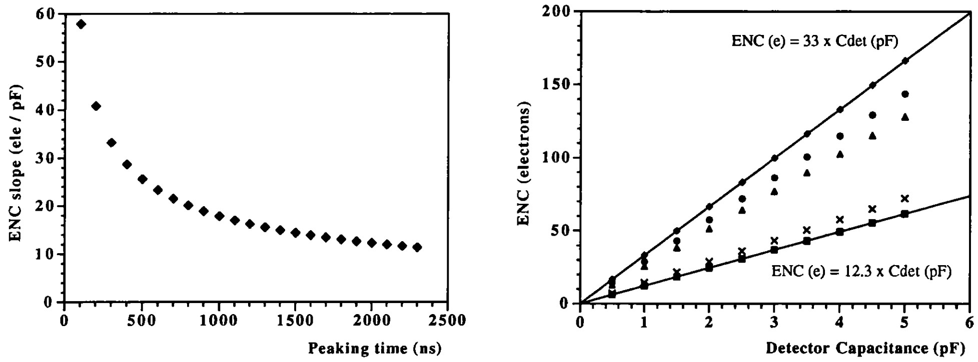

(a) Second term of noise slope for a $C_{det} = 1$ pF.

(b) ENC as a function of detector capacitance for five peaking times. The key is: square - 2000ns; cross - 1500ns; triangle - 500ns; circle - 400ns; diamond - 300ns

Figure 6.16: The dependence of Viking amplifier noise charge on peaking time.

replacing C_i. From the two measured noise slopes the variation of this second term can be deduced as a function of peaking time. This term is shown in figure 6.16(a) for a 1 pF detector capacitance while figure 6.16(b) shows the change in slope as a function of this capacitance for 5 peaking times.

The shot noise due to the leakage current I_{det} is:

$$Q_{ni}^2 = \frac{1}{q} 2 I_{det} F_v \tau \tag{6.15}$$

The noise charge therefore has a $\tau^{\frac{1}{2}}$ dependence. The actual magnitude of this noise source in GaAs diodes was shown in section 4.2 to be approximately half that predicted by theory.

The input resistor will also contribute thermal noise current with a corresponding noise charge given by:

$$Q_{nr}^2 = \frac{1}{q^2}\left(\frac{4k_BT}{R}F_v\tau\right) \tag{6.16}$$

where T is the temperature of the resistor and is equal to the temperature of the detector for most applications.

The total noise charge (Q_{tot}) is given by adding each term in quadrature:

$$Q_{tot} = \sqrt{Q_{na}^2 + Q_{ni}^2 + Q_{nr}^2} \tag{6.17}$$

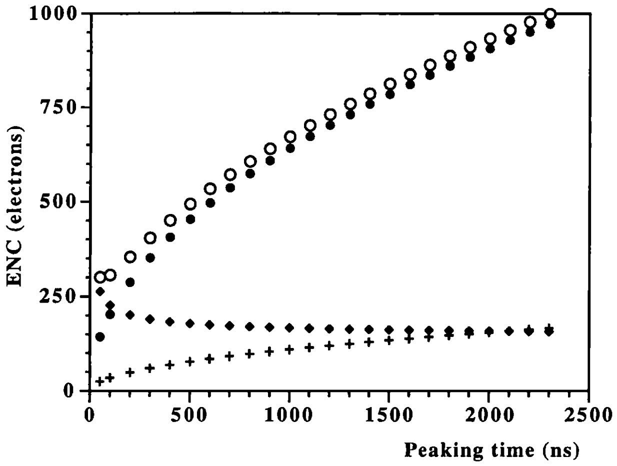

Figure 6.17: The individual and total equivalent noise charge for a Viking amplifier as a function of peaking time for a detector with a reverse current of 30nA, interstrip capacitance of 1.5pF and a biasing resistor of 50MΩ. The key is: closed circles - current; diamond - amplifier; cross - resistor; open circles - total noise.

Figure 6.17 shows the three individual components and the total equivalent noise charge for a Viking amplifier as a function of peaking time for a detector with a leakage current of 30 nA per strip, an interstrip capacitance of 1.5 pF and a bias resistor of 50 MΩ. Similar values apply for the detectors used in the test beam. The first term in the amplifier noise slope was kept constant at 140 electrons. It can be seen that at peaking times of 500 ns an equivalent noise charge of 500 electrons is expected. Even at this peaking time the total noise is still dominated by leakage current noise and only when the current falls to below 13 nA per strip will the current noise be less than 50% of the total noise. For GaAs detectors the lowest noise occurs for short peaking times due to the large reverse currents and therefore the peaking time was minimised for each detector used.

The single channel read-out option allowed the noise of each channel to be measured and optimised in the laboratory before the detector was placed in the test beam. The noise in mV RMS for each strip of the AL-W3-6 detector is shown in figure 6.18 for a VA2 peaking time of 300ns. The measurements were made at a temperature of 25^0C with a bias of 151 V on the back contact and -40 V on the bias strip. A total current of 16 μA flowed, corresponding to 42nA per strip.

The channels marked 'bad' are those that showed excessive noise. This was

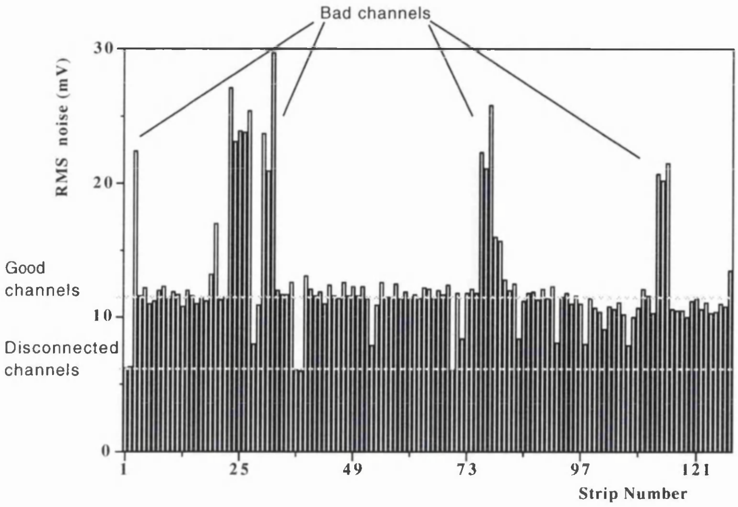

Figure 6.18: Noise plot of Al-W3-6 with 150 V depletion bias, 40 V punch-through bias and a total reverse current of 15.7 μA for 128 strips, measured at 23.9^{0}C.

thought to be due to the VA2 chip, as the excessive noise was present when the detector was not biased. The first two channels were not bonded to the detector and their noise was due to the electronics only. It can be seen that, for these conditions, the noise due to the amplifier without the detector capacitance term was half the total noise of a good strip for this detector. The average noise was 11.5 mV for good channels.

The noise in the test beam area is always more than that found in a laboratory due to the amount of extra electrical pick-up and ground loops that are present. At the X1 beam, however, the detectors were cooled to a temperature below 18^{0}C to reduce the leakage current noise and therefore this measured noise should be a good upper limit.

The AL-W3-6 detector response to electrons from a Sr^{90} beta source was investigated. Due to the lack of an adequate trigger, low energy betas could not be rejected and therefore the signal was not that of a mip. However, the signal measured across the detector was reasonably uniform at a value of 126±3 mV for the good strips.

The VA2 chip was calibrated using a 1.8 pF capacitor connected to the test input. The calibration remained constant across the chip, with a value of 48±4 V/pC for the AL-W3-6 detector and 35±1.5 V/pC for the AL-W3-8 detector. (The calibration of detector G114 could not be performed because there was no test capacitor present on this VA2 hybrid.) The noise of the AL-W3-6 detector measured above therefore corresponds to 1500 electrons and the signal from the source was 16400 electrons. From mip charge collection measurements performed on simple pad detectors, a cce of 50% was expected for a bias of 150 V. Therefore a mip signal would be 13000 electrons or 100 mV. The signal-to-noise ratio expected from this detector biased at 150 V is then 8.7. A higher bias would increase the signal-to-noise ratio through improved charge collection.

The noise for the channel without the detector bonded to it was 780 electrons. This implies that the noise due to the detector is 1280 electrons, greater than the 470 electrons expected for this detector with the given peaking time and leakage current. The reason for this is not clear. It should be noted, however, that the amplifier noise was 5.5 times more than expected from the noise slope quoted above, although the increase in the slope with a reduction in peaking time has not been included. The reach-through bias structure has been cited as a likely source of the extra noise in GaAs detectors [88].

During the beam test the gain and the peaking time of the Al-W3-6 detector were altered. The gain was reduced to 40±2 V/pC to prevent saturation of the ADC.

6.4.2 Test beam set-up

The GaAs detectors under test were placed inside a silicon telescope, shown in figure 6.19. This consisted of eight silicon microstrip detectors arranged into four sets with two sets in front of the test detectors and two further downstream. The two detectors per set were orthogonal to each other to define x- and y-coordinates. Five trigger scintillators were also present. The telescope system defines the point of interaction of the pion beam with the test detectors to a precision of order 1 μm.

For an event to be written to tape the trigger conditions that must be met are that the event must occur in the beam extraction time, the DAQ must not be busy and that a coincidence occurred in the scintillators.

The silicon detectors were read-out with Viking pre-amplifiers with a 2 μs peaking time. The large difference in peaking times between the silicon telescope

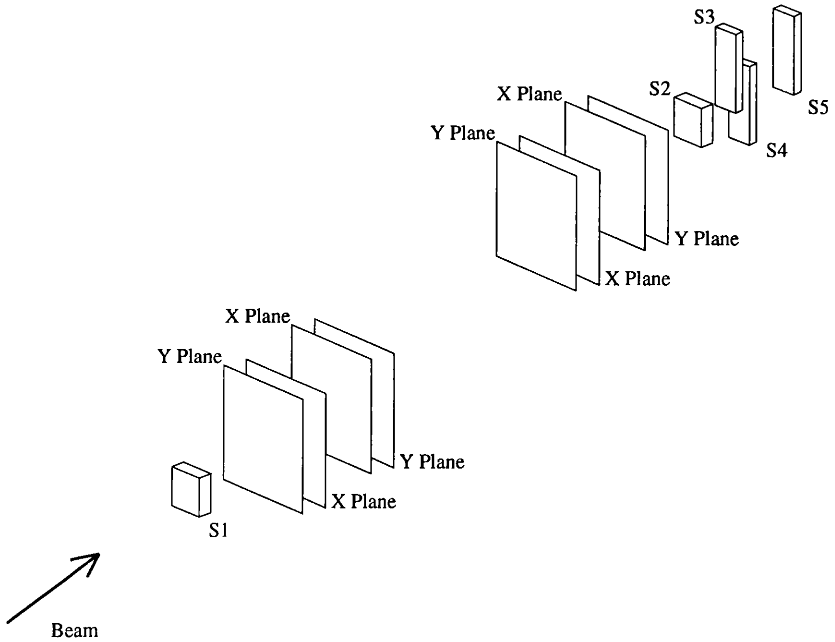

Figure 6.19: The Strasbourg telescope. S1 to S5 are scintillators used to define the beam and trigger the DAQ. The four x- and four y-planes are silicon microstrip detectors with 384 channels each.

and the GaAs detectors required that the hold delay be generated separately for the two sets of detectors. The initial trigger for an event comes from the coincidence of the scintillators. The trigger signal is taken via cables from the telescope to the control room where a VME Viking driver unit generates another trigger signal (Trigger$_{out}$) to send back to the Viking chips in the experimental area if the other 'valid event' conditions are met. After the Trigger$_{out}$, the driver generates the hold signal, the delay between the two being defined by the user. A final delay results between the generation of the 'hold' signal and its arrival at the Viking card due to the long cable between the control room and the experimental area. The timing diagram for the 'hold' signal generation, shown in figure 6.20, gives the minimum possible delays at the test beam.

The total delay was 286 ns, close to the required delay of 300 ns for the GaAs detectors. The silicon detectors, however, required a delay of 2 μs otherwise the performance of the telescope would have been degraded. This problem was overcome by using the Trigger$_{out}$ from the VME driver to start a set of timing units that generated a separate 'hold' signal for the GaAs devices. The signal was carried into the experimental area via its own cable to minimise the extra delays and allowed

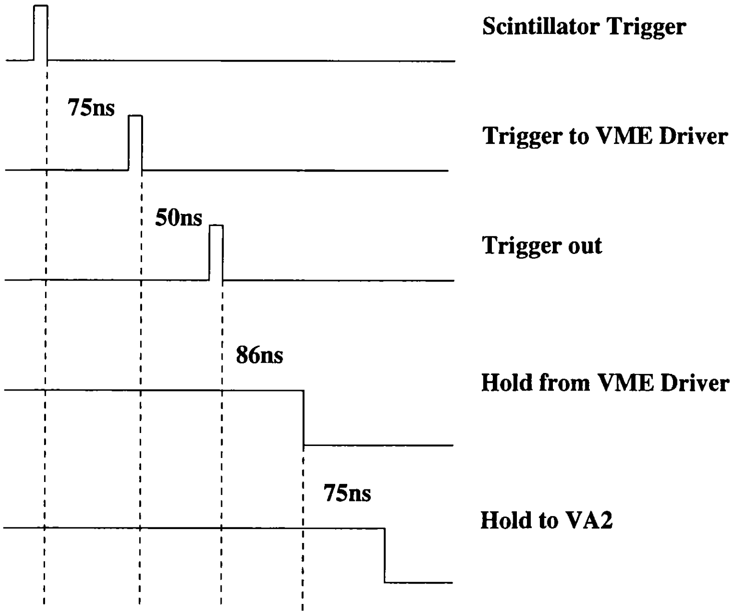

Figure 6.20: The generation of the 'hold' signal.

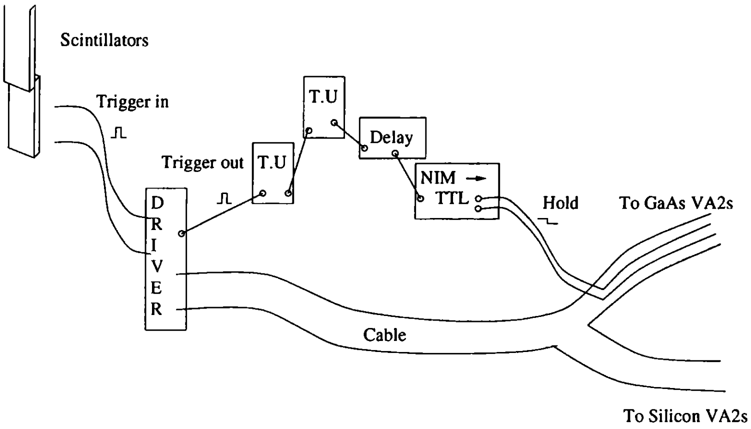

Figure 6.21: Schematic for the generation of the GaAs hold signal.

the delay for the telescope to be set to the desired 2 μs. Additional 'hold' delay was supplied for the GaAs VA2's through a delay box, the setting of which was altered during the running of the test-beam to obtain the best signal-to-noise for the detectors. It was found that extra delay was not required. The schematic of the 'hold' generation is shown in figure 6.21. The rest of the timing signals were generated for the GaAs devices in the same fashion as those for the silicon telescope.

6.4.3 Data Analysis

The off-line data analysis was performed in two distinct sections. The first found hits in the GaAs test detectors while the second used the telescope to define tracks through the detector and determine the position resolution of the device.

Before the analysis was started the bad channels measured previously in the laboratory were masked out in the software so that they did not interfere with the final results obtained. Bad channels were defined as those that had an RMS noise greater than 5 standard deviations from the average noise or those that were disconnected.

The electronic channels of the VA2 all float at an indeterminate voltage level, known as the 'pedestal' of the channel. The first 100 events of each run were used to determine the average ADC value (P_{ave}) for each channel individually. The next 100 events were used to determined the noise of each channel given as the RMS in the ADC value after pedestal subtraction (N_{ave}). The outputs of all the channels of a chip can shift coherently in what is know as 'common mode shift' (CMS). This was also observed and subtracted from the data. The signal on a channel is defined as the ADC value of the channel after pedestal subtraction.

The average pedestal and noise values of each individual channel were updated continuously throughout the run for each channel which did not contain a signal (that is an ADC value above the signal-to-noise cut). This was performed by taking a weighted mean, given in equation (6.18) for pedestal calculations, where the value X determines the relative importance of the new event. High values of X reduce the effect of signals from actual events that are below the signal-to-noise cut.

$$P_{ave\_new} = \frac{P_{ave} \times X + P_{new}}{X + 1} \tag{6.18}$$

The program then performed cluster searches. Three signal-to-noise cuts were defined: $(S/N)_1$, $(S/N)_2$ and $(S/N)_3$. The first, which was higher than the second, was used to find the largest signal in the detector for each event. The second determined the presence of hits on neighbouring strips. Once the signal had been found, the signal-to-noise ratio for strips on either side of the signal strip was compared to $(S/N)_2$ and the signals were added to the cluster if they were above this cut. Table 6.3 gives the signal-to-noise cuts used for the telescope and test detectors

Cut Type	Si	GaAs
Centre Strip (S/N)$_1$	4	3
Neighbour (S/N)$_2$	2	1.5
Whole Cluster (S/N)$_3$	4	3

Table 6.3: The signal-to-noise cuts applied on the telescope and test detectors.

throughout the analysis of the data. The cluster signal size (S_C) is defined as:

$$S_C = \sum_{cluster} S \tag{6.19}$$

and the associated noise of the cluster (N_C) is:

$$N_C = \sqrt{\frac{\sum_{cluster} N^2}{\text{Number of strips}}} \tag{6.20}$$

where S and N are the signal size and associated noise for a given channel in the cluster. Finally a cut (S/N)$_3$ was applied to the signal-to-noise of the total cluster.

The position at which the pion passed through the detector can be determined from the two largest signals in a cluster with the use of charge sharing. These signals will be from adjacent strips and thus one can be assigned as the left (S_L) and the other the right (S_R) signal of the pair. The charge sharing between them is non-linear and the algorithm used for position determination utilises the 'eta' function, defined as:

$$\eta = \frac{S_L}{S_L + S_R} \tag{6.21}$$

The eta function is shown in figure 6.22(a) for a typical AL-W3-6 detector run. When the signal passes through the centre of the strip it will have all its charge collected by that one strip and the eta should equal zero or one. These events have been removed from the plot.

Since the hits are uniformly distributed over the test detector the position of the track (X) from a cluster with respect to the left hand strip is given by:

$$X = P\frac{\int_0^{\eta_X} \frac{dN}{d\eta} d\eta}{\int_0^1 \frac{dN}{d\eta} d\eta} \tag{6.22}$$

where P is the strip pitch, N is the number of hits at a given eta and η_X is the measured eta value for the hit.

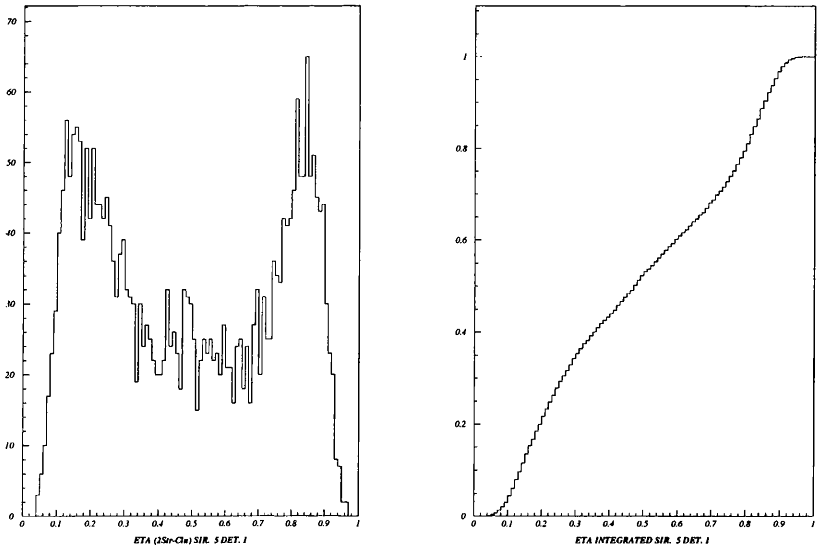

(a) Typical eta distribution.

(b) Integrated eta distribution.

Figure 6.22: Eta distributions for detector AL-W3-6.

The first program, used in the analysis of 1995 test beam data, wrote out a file which contained the cluster data for every event in the silicon telescope and the GaAs test detectors. The channels that were read out were in fact the maximum signal and the five channels on either side of this, regardless of their signal-to-noise ratio.

A second program read this file and used it to determine the position of the tracks through the telescope and thus through the detectors under test. This information was used to determine the residual of each detector, defined as the difference in the pion position determined by the test detector signals and the actual position defined by the silicon telescope.

The telescope was aligned by the software relative to an origin at the centre of the first silicon plane. Once the reference plane was known the alignment of the test detector to this plane was performed. First the residual plot was centered about zero. The possibility of the detector not being orthogonal was corrected for by plotting the residual against position along the strip. A linear fit was made to this residual distribution and the hits were rotated to align the strip with the reference frame.

Detector	Aspect Ratio	Signal to noise	Cluster size	Res (μm)	Cluster Res (μm)	Detection efficiency (%)
AL-W3-6	30:20	14.77	1.66	12.75	10.83	94
AL-W3-8	30:20	6.9	1.81	12.6	11.8	93.5
G114	10:40					
G114	25:25	18.99	1.78	14.15	14.1	>99
G114	40:10	23.88	1.79	14.8	14.33	>99

Table 6.4: The best results obtained from the three GaAs microstrip detectors. The cluster size is the mean cluster size in units of strips.

The position of the detector along the beam direction (z) was only known to within a cm from measurements in the experimental area. The software found the correct position by adjusting the z position until the residual distribution width was minimised. Rotation of the strip detector about the y-axis was determined by rotating the detector about the central strip through small angles until the width of the residual was minimised. The standard deviation of the resulting residual distribution was the position resolution of the detector.

The detection efficiency of the detector was determined by counting the number of hits that were found in the detector and dividing this total by the number of tracks that the telescope predicted to have passed through the detector (neglecting tracks through masked strips).

6.4.4 Results

The best results obtained for the two Alenia detectors and the three aspect ratios of detector G114 are given in table 6.4 for the conditions given in table 6.5.

Results from detector G114 will be discussed first followed by those from detector AL-W3-6, which gave the best cluster residual, and finally the results of AL-W3-8.

Detector G114 had a serious fabrication problem which was not apparent until a few days before the test beam started. Photo-lithography was employed to obtain the 5 μm gap between the bias strip and the read-out strip. The resolution of this process at the University of Glasgow facility is close to the desired structure

Detector	Aspect Ratio	Back bias (V)	Bias strip (V)	Strip current (nA)	Peaking time (ns)	Hold Delay (ns)
AL-W3-6	30:20	185	30	6	300	280
AL-W3-8	30:20	300	0	30	330	280
G114	10:40	370	6	14	360	118
G114	25:25	370	6	35	360	118
G114	40:10	370	6	30	360	118

Table 6.5: The operating conditions for the three GaAs microstrip detectors.

dimensions and complications might therefore have been expected. In effect, some of the bias strip fingers and the read-out strips were shorted together, via resistances ranging from zero to 100kΩ, by debris left in the gap as a result of the lift-off process. These strips were therefore held at or close to the potential of the bias rail, which should have been -40V to obtain successful reach-through. At such a voltage the diode protection of the capacitor chip would have shorted these strips, and thus the bias rail, to ground, causing an unacceptable current to flow. These strips were therefore disconnected from the read-out. Another problem became apparent, namely that the strip detector now had a negative bias applied to the front of the device, via some of the read-out strips, which would affect the operational field of the device. The bias strip was therefore held at only -6 V.

The section of the detector with the aspect ratio 10:40, that is the thinnest strips, was so badly affected by this fabrication problem that it could not be operated as a functional detector.

For the two other aspect ratios, results were obtained but only for small sections of the device and only when the low bias was applied to the bias strip. The signal-to-noise ratio was very high due to the large signal that was obtained from the 500μm thick detector biased at 370 V. From simple test pads fabricated upon the same wafer a charge of 24700 electrons was collected at this bias. With the bias strip held below the punch-through voltage, the resistance of the D.C. path to ground was that due to the intrinsic resistance of the material, as it is in an ohmic strip detector. The resolution of the detectors was poor, however, with a value comparable to that

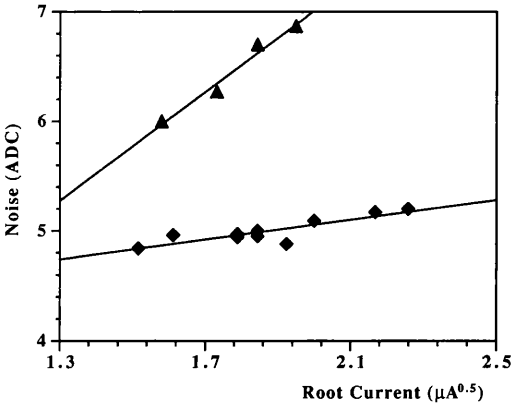

Figure 6.23: The dependence of the noise upon the detector reverse current. The key represents two peaking times: squares - 380ns; diamonds - 300ns.

from binary read-out of $\frac{\text{pitch}}{\sqrt{12}}$. This was not expected with the very good signal-to-noise ratio and large cluster size (an average of 1.78 strips wide). Due to the poor resolution obtained, the variation in the residual distribution width as a function of aspect ratio could not be deduced. It has been shown elsewhere that for GaAs strip detectors a smaller interstrip gap results in a larger cluster size and thus a better resolution[21]. This is expected for a strip detector with trapping (see section 6.3).

The results from the AL-W3-6 detector were more encouraging. Figure 6.23 shows the increase in the noise recorded for the detector as a function of the square root of the detector reverse current. A linear dependence was found as expected. It can be seen that the magnitude of the noise was less for the shorter peaking time as expected from theory.

During the test beam run, the best 'hold' delay was found by observing the dependence of the signal-to-noise ratio as a function of the difference between the 'hold' delay and the peaking time. The dependence, given in figure 6.24(a), indicates that the largest signal was obtained for a 'hold' delay slightly less that the measured signal peaking time. Extra, unaccounted for hardware delays in the 'hold' signal explain why a delay slightly less than the peaking time gave the largest signal. The results obtained with this delay are given in table 6.4. The signal-to-noise ratio increases with reverse bias due to the increase in the depth of the active region and thus signal size (figure 6.24(b)). The signal-to-noise ratio approached a plateau for a bias of 200V and therefore higher potentials were not applied. An example of the

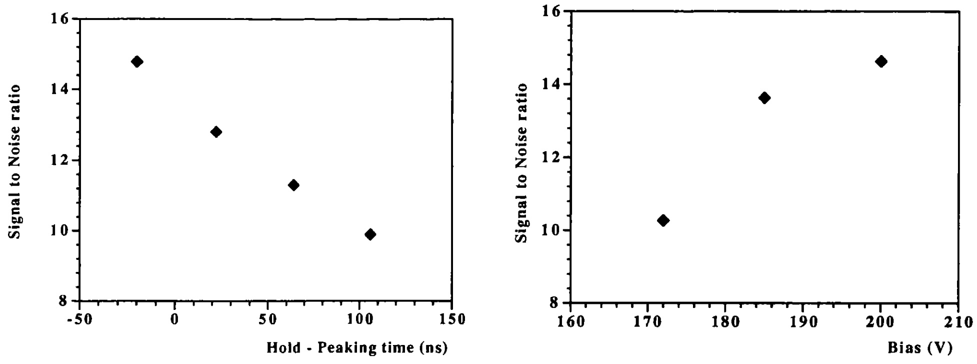

(a) Dependence upon the hold delay. (b) Dependence upon the detector bias.

Figure 6.24: The variation of the signal-to-noise ratio for detector AL-W3-6.

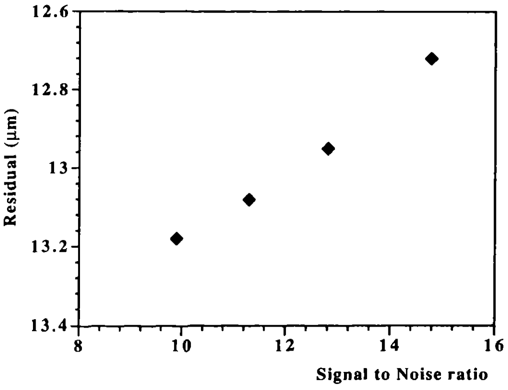

Figure 6.25: The dependence of the residual on the signal-to-noise ratio.

signal-to-noise plot obtained for this detector is given in figure 6.26(a).

The increase in the signal-to-noise ratio produced the expected increase in the precision of the position measurement, as shown in figure 6.25.

The cluster size of the signal also affects the resolution, with larger clusters implying more sharing and thus a greater number of tracks determined with the eta function. The best resolution of the detector, (the cluster resolution), shown in figure 6.26(b), using only clusters of two or more strips was 10.83μm. This was not obtained with the detector bias at 200V but at 185V, even though the signal-to-noise ratio and the cluster size were larger at 200V. This is inconsistent with the theory. When the detector was operated at 200V the potential on the bias strip was reduced to -9V. The current that flowed through the bias strip was equal to

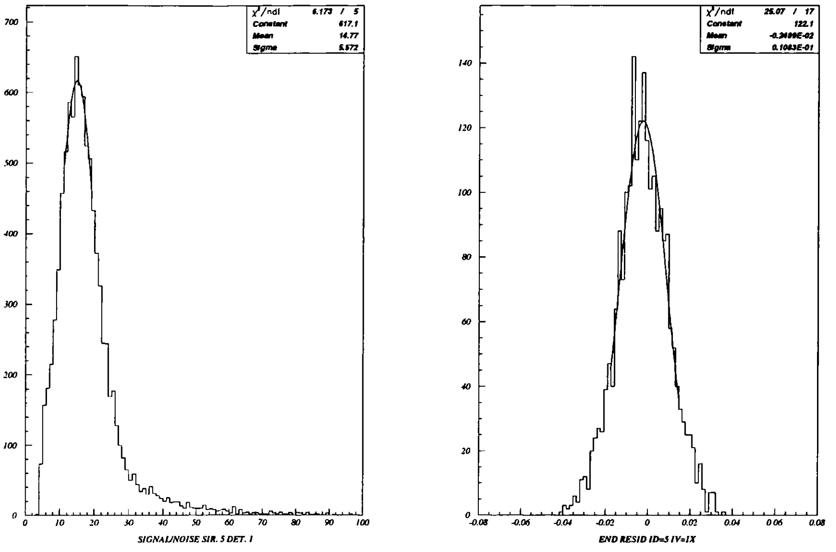

(a) The signal-to-noise.

(b) The residual obtained for clusters two or more strips wide.

Figure 6.26: The results obtained with detector AL-W3-6.

that which was measured by the reverse bias supply, demonstrating that the bias strip still functioned as the D.C path to ground. The read-out strips continued to be held close to the ground potential because no strips were shorted to ground, via the protection diodes on the capacitor chip, due to their potential exceeding 7V. It appears that the reduced potential on the bias strip adversely affects the resolution of the detector but the mechanism is not yet understood.

The detection efficiency was slightly less than the 100% expected for this detector. The low detection efficiency could be due to a loss of some signals because the signal-to-noise cut was too high. Reducing the cut however, led to the inclusion of too many fake signals due to noise and the residual distribution was adversely affected. The detection efficiency of the G114 detector was better than 99%, as would be expected with such a high signal-to-noise ratio.

The best results obtained with the Al-W3-8 detector are also given in table 6.4. The signal-to-noise cuts applied to this detector were the same as those of detector Al-W3-6. The peaking time of the VA2 electronics was 330 ns and the hold delay was set at 280 ns.

The ohmic strip detector (Al-W3-8) was operated at a bias of 300V. The high bias ensured full depletion and removed the potential problem of a non-depleted layer of low charge collection under the strips. The resolution obtained was 12.6μm, which improved to 11.8μm if only clusters of two or more strips were analysed. The expected binary read-out resolution for this detector with a pitch of 50μm is 14.4μm.

The detector signal-to-noise was not as high as that obtained for the Al-W3-6 detector due to an increase in noise with respect to AL-W3-6. The noise was greater for two reasons: firstly the detector interstrip capacitance was larger due to the longer strips and secondly, and more significantly, the reverse current was higher due to the damage suffered during bonding and because of the larger detector area.

The signal size for the total cluster was approximately the same for both detectors. A slightly larger signal might have been expected from the AL-W3-8 detector due to the higher applied bias and thus larger charge collection efficiency. As a significant increase was not observed it must be concluded that some of the signal was lost in the larger clusters observed in the AL-W3-8 detector. A proportion of the signals at the edge of a cluster will be lost as they do not pass the first signal-to-noise cut and thus a larger cluster will result in more signal loss as the signal is spread over a larger number of strips.

The mean cluster size in this detector was in fact 10% larger than that of Al-W3-6, see figure 6.27. The explanation for this is that the electron absorption distance in SI-U GaAs detectors is less than that for holes. Thus more carrier trapping occurs in this detector which ‘collects’ electrons. This causes a greater induced signal on the neighbouring strips through incomplete charge cancellation in the bipolar signal, as explained in section 6.3. The increased cluster size and therefore charge sharing lead to a better resolution than expected from the signal-to-noise ratio, with respect to the results of AL-W3-6. The detection efficiency was 93.6%.

After operating the detector at a bias of 300V for over four-and-a-half hours, problems started to occur. The cluster size increased, as shown in figure 6.28, and the strip detector stopped working correctly. This degradation was probably due to a build-up of surface charge between the strips. This problem has been found for double-sided silicon detectors, where an electron accumulation layer at the Si-

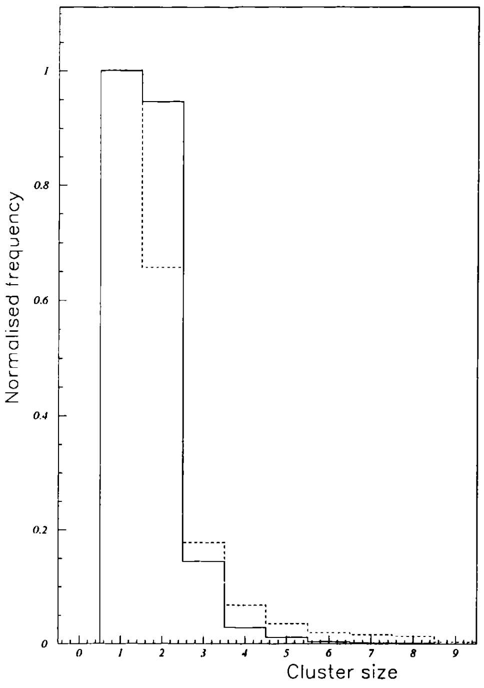

Figure 6.27: The normalised cluster size for detectors AL-W3-6 (solid line) and AL-W3-8 (dashed line).

SiO_2 interfaces is present due to the positive fixed charge in the SiO_2. The positive voltage on the strips causes the electron layer to spread between the strips, forming a conducting channel with a resistance of typically a few kΩ. A similar situation could be present in the GaAs detector with the silicon nitride passivation.

6.5 Conclusions

Three GaAs microstrip detectors were tested in a high energy particle beam.

Due to a fabrication problem the variable aspect ratio detector (G114) gave unsatisfactory results and the desired variation in resolution as a function of aspect ratio could not be measured.

The two other detectors performed much better, with resolutions better than $\frac{\text{Pitch}}{\sqrt{12}}$. One detector (AL-W3-6) consisted of rectifying strips with integrated reach-through biasing and integrated silicon nitride capacitors. The second detector (AL-W3-8) utilised ohmic strips, integrated biasing and external decoupling capacitors.

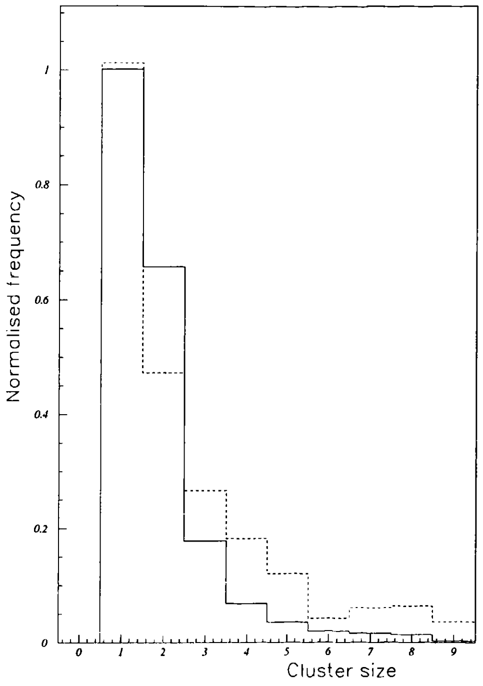

Figure 6.28: The normalised increase in cluster size for detector AL-W3-8 after operation for 4.5 hours. The solid line is after 2 hours operation and the dashed line after 6.5 hours

The signal-to-noise ratio of the AL-W3-6 detector was 14.8 while that of the ohmic detector was only 6.9. The lower signal-to-noise ratio for the ohmic detector was believed to be due to poorer charge carrier collection. The detection efficiency of all the detectors was over 90%. The lower than 100% detection efficiency resulted from a loss of signal due to the signal-to-noise cuts applied.

Chapter 7

Summary and Conclusions

The thesis is divided into three sections: the characterisation of simple pad detectors, the investigation of the effects of high energy neutron, proton and pion irradiation, and position measurements with microstrip detectors in a 70 GeV/c π test beam.

Three substrate materials were used for the first two sets of investigations. These were SI-U LEC bulk GaAs, which was examined in greatest detail, SI-indium doped GaAs and low pressure vapour phase epitaxial GaAs.

Electrical characterisation of the SI-U diode revealed two distinct regions in the current-voltage characteristic; the low and high voltage regions. The low voltage region behaved as a standard Schottky diode in series with a large resistance due to the semi-insulating nature of the bulk material. From the current-voltage characteristic the resistivity of the bulk at 20°C was found to equal 6.4×10^7 Ωcm. The barrier height determined from the temperature dependence of the barrier conductivity, measured for voltages below 0.002 V, was found to be 0.92 ± 0.02 V for temperatures between 10°C and 40°C and to equal 0.91 ± 0.02 V between 115°C and 147°C. The barrier height was also determined from the temperature dependence of the forward current. Values of 0.87 ± 0.03 and 0.91 ± 0.03 V were measured for the low and high temperature regions, respectively. These were equal, within errors, to the values found from the barrier resistance. From the variation of the bulk resistivity with temperature the bulk activation energy was determined for the two temperature ranges. Values of 0.78 ± 0.04 V and 0.73 ± 0.02 V were found for the low and high temperature ranges, respectively. Therefore it was concluded that the electron density of the material was due to the deep level defect EL2. The Fermi level of the material was found from the electron number density derived from the bulk resistivity of the material. At 20°C a value of 0.81 eV was obtained, which is consistent with compensation models.

The quality of the Schottky barrier was assessed by fitting theoretical expressions for the thermionic current to the data. The measured ideality factor was 1.04 for a fit performed between a forward bias of $k_BT/2$ and a reverse bias of $10k_BT$. The fit could not be extended to higher voltages because the correction required to account for the voltage drop across the bulk could not be accurately determined.

At a bias of -10 V the current was assumed to be generation current and an activation energy for the diode of 0.76 ± 0.02 eV was measured. This implied that the current was due to a mid-gap defect which was assumed to be the EL2 trap. At higher reverse bias the current characteristic changed. This was termed the high voltage region.

The current characteristic started to plateau between -30 V and -50 V and remained flat until a bias was reached corresponding to 1 V/μm of detector thickness, (V_{fd}). The current density at 20°C was of order 1.5 μA/cm^2. The current increased slightly for a diode that was not guarded due to the lateral spreading of the active region in the bulk under the contact. The activation energy of the current for an applied bias of -100 V was 0.85 ± 0.01 eV and was insensitive to whether the diode was guarded or not. This activation energy was noted to be close to the activation energy of the electron thermal-emission rate of the EL2 trap. The increase in current for voltages above that required for a high field extension across the entire diode, (V_{fd}), was shown to be affected by the nature of the back contact. Diodes fabricated by Alenia had very good high voltage characteristics. An expression for Poole-Frenkel emission with an electric field strength proportional to the applied bias described the high bias data well.

Spectral noise measurements were performed on two diodes at room temperature. The measured shot noise was half of that expected from the reverse current. A simple model of carrier capture in the high field region of the diode was proposed to account for the observed effect. The low frequency excess noise had a corner frequency of order 1 kHz or less for a bias up to 230 V, close to V_{fd}, and therefore the excess noise is not a concern for detector operation.

Capacitance measurements made on the diodes illustrated that to obtain the doping concentration of the deepest traps the measurement temperature must be in excess of 400 K for a small A.C. signal with a frequency of 100 Hz. A value for N_{eff} of $7.4 \times 10^{15}/\mathrm{cm}^3$ was obtained, which is close to that given in the literature.

For the semi-insulating material it was found that the electrical characteristics at an applied bias greater than a few volts were dominated by the effects of deep traps, of which the EL2 trap has the highest concentration.

Charge collection experiments were used to determine the mean free absorption lengths of the carriers in the material and the charge collection efficiency of the detector for minimum ionising particles as a function of applied bias. Three ingots were tested, two from MCP and one from Sumitomo which had been processed by Alenia. For all three the hole charge collection was better than that for electrons. The Alenia diode had a 100% hole cce, at a bias greater than 600 V, but a cce of only 40% for electrons, in the plateau region (200 - 300 V). The MCP diodes had better electron collection but significantly worse hole collection. The largest mean free absorption distances found for electrons and holes in this material were 200μm and 700μm, respectively. The hole absorption distance was only slightly less than the $\sim$ 1000 μm expected for trap-free GaAs. Therefore the concentration of hole traps in LEC SI-U GaAs is low. The electron absorption distance for a trap-free material, however, should be larger than the hole distance, due to the higher velocity of the carriers. This was not observed and the reduction was attributed to the deep levels in the material, and the EL2 defect in particular.

The electron charge collection was observed to increase for a voltage above V_{fd}, an effect that was assumed to be due to field-enhanced electron de-trapping. A correlation was observed between the high voltage current increase and the increase in charge collection which therefore supports this assumption.

A linear increase was observed with bias for the mip cce up to a bias of V_{fd}. This increase was due to the linear increase in high field 'active' region of the diode with bias. The mip cce measured at the maximum reverse bias for a 200 μm thick MCP diode was $75 \pm 5\%$. The Alenia diode had a very similar mip charge collection due to the poor electron collection.

The high voltage current characteristics of the SI-In doped diodes were very similar to those obtained from the MCP SI-U material. The hole charge collection was 83%, at 650 V, which was higher than that measured for SI-U detectors, but the electron cce was only 15%, in the plateau bias range of 100 - 450 V. The mip cce was very similar to a MCP SI-U device.

The deep levels present in both SI materials therefore affected the charge collection properties of the detectors.

The VPE diodes examined were shown to obey standard semiconductor theory. The barrier height was obtained from the current-voltage and current-temperature dependences. A value of 0.848 ± 0.005 V was obtained from the activation method, which is close to that quoted for titanium on n-type GaAs. The reverse current characteristic was examined to try to understand the cause of the extra current observed over that expected for such a barrier. Generation current was proposed for a bias below -10 V as the source of the extra current, which can be expected for a device with a large barrier height. At larger values of bias the diode did not follow standard theory and this was attributed to edge effects.

The capacitance measurement did not show a dependence on frequency and thus the concentration of deep levels in the VPE material was low. From the C-V measurements a value of $2.8 \pm 0.2 \times 10^{14}/\text{cm}^3$ was obtained for the doping density. This high doping density prevented the extension of the depletion region beyond 30 μm before breakdown occurred due to the high bias required (>200 V). Charge collection experiments were limited due to the small depletion region. The charge collection efficiencies obtained for electrons from alpha particle experiments and 60keV gammas were, however, close to 100%. If the doping concentration in the VPE could be reduced, and thus a larger depletion width obtained before breakdown, then detectors fabricated upon this material will make very good particle detectors with charge collection efficiencies close to 100%. The VPE material also has the advantage over other epitaxial material that it is available at thicknesses close to 200 μm at a cost that is not prohibitive for physics applications.

The effects of the irradiations upon both the current and charge collection characteristics of all three types of substrate were investigated.

The low voltage analysis was performed for SI-U diodes exposed to three proton fluences up to a maximum of 1.35×10^{14} /cm^2. The bulk resistivity of the material was seen to increase with proton radiation while the Schottky barrier height fell. The resistivity increase was assumed to be due to carrier removal via an increased trap concentration. Creation of an increased number of dislocations in the material, and thus of p-type zones, was suggested as an explanation of the reduction in the barrier height.

For the SI-U diodes the high voltage IV characteristic showed only slight degradation with fluence. The value of V_{fd} fell to between 2/3 and 1/2 of its pre-irradiation value, with the majority of the reduction occurring within the first few 10^{13} particles/cm^2. The reverse current increased by only a factor of about two after 1×10^{14} p/cm^2. The post-V_{fd} current was reduced for the MCP diodes, with the gradient in the IV curve falling with increasing fluence.

Noise measurements showed, for a fixed current, a reduction in noise with increasing proton fluence. At 100 nA, for example, the measured equivalent noise charge with a shaping time of 3 μs fell from 1600 electrons prior to irradiation to 323 electrons after 1.9×10^{14} p/cm^2. It was suggested that the reduction was due to the increased density of traps in the material.

As far as the changes in its electrical characteristics are concerned, SI-U GaAs has therefore been shown to be radiation hard for particle fluences greater than those expected for experiments at the LHC.

The charge collection efficiency of these detectors, however, was severely affected. The hole cce fell below that of the electrons before a fluence of 5×10^{13} p/cm^2 was reached. For a bias above V_{fd} an increase in both electron and hole cce was observed, but at a greater rate for the electrons. The mip charge collection allowed the effects of the three particle types to be compared. ISIS neutrons were shown to be the least damaging, while the pions were the most damaging, causing four times more damage. For a 200 μm thick detector reverse biased at 200 V, a 10000 electron signal response to a ^{90}Sr source was obtained after 1.4×10^{14} n/cm^2, 6.0×10^{13} p/cm^2, and only 3.0×10^{13} π/cm^2. The cce fell rapidly initially and then at a slower rate for higher fluences with the position of the change in gradient depending upon the particle type. The reductions in cce for all three particle types were correlated with the NIEL of the particles.

It was concluded that the SI-U GaAs detectors investigated here would not be able to deliver the required level of signal after the full 10 year lifetime of the ATLAS experiment. Low carbon SI-U GaAs material has been investigated by other groups as an alternative, possibly more radiation hard, substrate. The low carbon material has less ionised EL2 defects prior to irradiation and therefore the electron lifetime was larger than that found in standard SI-U GaAs. The detectors have shown a slight improvement in post-irradiation charge collection efficiencies, but, at present they are still not adequate for the the entire lifetime of the ATLAS experiment.

In irradiated standard SI-U LEC detectors, the forward current fell with fluence, allowing forward biased operation of the detector. The hole cce was seen to be similar to that under reverse bias. The response to electrons, however, had a large peak ($\approx$ 60%) for low forward bias (40 V) which fell as the bias was increased. At 100 V the forward and reversed bias electron charge collection were similar.

The effect of irradiating the detectors at -6 ± 4^oC had a slight effect on the mip charge collection efficiency, but the reverse current was observed to increase alarmingly. Current assisted annealing of two detectors was suggested to have occurred due to the increased cce observed for these diodes. Further experimentation is required, however, to verify these results.

Annealing studies were performed on irradiated detectors. Room temperature annealing over a duration of a year showed no increase in V_{fd} and a fall in reverse current. Annealing at 210°C in an oven in air reduced both the reverse current and the value of V_{fd}. The charge collection efficiency below V_{fd} increased for annealing times up to 5 hours. For example, the mip cce after 1×10^{14} p/cm^2 increased from 23% to 33% after a 5 hour anneal. Annealing for 33 hours killed the detectors.

Annealing at 450°C was performed with a rapid thermal anneal. This was expected to remove the arsenic antisite defects. The electron cce increased with anneal time, but the hole charge collection was hardly effected. The radiation induced electron traps were concluded to be arsenic antisite defects, but the identification of the hole traps is still not certain.

The effect of a fluence of 1×10^{14} p/cm^2 on the SI-indium doped samples increased the current and reduced V_{fd}. The mip cce, which was comparable to the undoped samples before irradiation fell to only 10 ± 1.5%, compared to 18 ± 1.5% for a SI-U detector, at an applied bias of 1000V. Therefore the SI-indium doped detectors were less radiation hard than the SI-U detectors.

After a fluence of 1.25×10^{14} p/cm^2 the VPE diode current increased dramatically from 90 nA to 1500 nA, for an applied bias of 200V, which represents an increase of more than an order of magnitude. The capacitance fell from 300 pF to 40 pF for a bias of -5 V. The proton fluence created a significant concentration of deep levels in the material which were responsible for the increase in the generation current and the change in the diode capacitance.

Charge collection from a VPE detector was considerably better than for the SI-U LEC devices both before and after the radiation fluence. The electron cce for a typical VPE diode fell from 100% before irradiation to 68% after a fluence of 1.25×10^{14} p/cm^2. The SI-U device measured at 200 V fell from $62 \pm 5\%$ to $11 \pm 3\%$, a reduction of 82%.

Therefore the better pre-irradiation characteristics and the low initial trap density of the VPE detector meant that the detectors were more radiation hard than the SI-U devices. If large quantities of VPE material with a lower initial free carrier concentration could be obtained at reasonable cost, then GaAs could be used as a radiation hard detector. The time scale for this, however, was considered too long to affect the decision made by the ATLAS collaboration with respect to the use of GaAs microstrips in the ATLAS inner detector.

Three distinct designs of microstrip detector were tested at the SPS. The Alenia detector (AL-W3-6) with a segmented Schottky side, integrated reach-through biasing and decoupling capacitors had the lowest leakage current density of 8 nA/mm^2 at 20°C. The breakdown voltage was close to -200 V, which was expected for the 200 μm thick device. The second Alenia detector, (AL-W3-8), with ohmic strips, suffered damage during bonding which reduced the breakdown voltage from -250 V to -170 V. The third detector, from Glasgow University, had a severe fabrication fault which limited the results that could be obtained with this device.

The best resolution, measured for the AL-W3-6 detector with a peaking time of 300ns, obtained for clusters of two of more strips, was 10.83 μm. Including all cluster sizes gave a value of 12.75 μm. The signal to noise was 14.8 and the detection efficiency was 94%. The resolution was better than pitch/$\sqrt{12}$, (= 14.4 μm), which is obtainable without charge sharing.

The ohmic strip detector gave very promising results with a resolution of 12.6 μm. The noise was larger for this device than with the AL-W3-6 detector, due to the increased capacitance and increased reverse current, due to the bonding problem. The cluster size was also increased, an effect that was concluded to be due to the lower electron mean free absorption distance in comparison to holes in LEC SI-U GaAs detectors.

Significant progress has been made over the last eight years in understanding and developing SI-U GaAs detectors. Detectors have been fabricated with very high minimum ionising particle charge collection efficiencies (typically > 70 %). The radiation induced reduction in the charge collection efficiency, however, is a major problem for the inclusion of GaAs detectors in an experiment at the LHC. Silicon detectors have not shown significant signal loss for fluences up to 1×10^{14} p/cm^2 and if the cooling of the inner detector can be achieved then the effects of room temperature annealing on the full depletion voltage will be controlled. Silicon based microstrip detectors could then be used in the forward positions of the ATLAS inner detector.

The development of GaAs detectors will continue at Glasgow University. X-ray imaging applications are being worked on at present to develop low dose imaging utilising the high atomic number of the material. VPE diodes and novel detector designs are also being investigated for possible radiation hard detectors for future experiments.

Appendix A

Properties of Si and GaAs

m_0 is the electron rest mass = 0.91095×10^{-30} kg.

The superscripts represent:

a Longitudinal effective mass.

b Transverse effective mass.

c Light-hole effective mass.

d Heavy-hole effective mass.

Properties	Silicon	GaAs
Crystal structure	Diamond	Zincblende
Band structure	Indirect	Direct
Atomic number	14	32
Atomic density (atoms/cm^3)	5.0×10^{22}	4.42×10^{22}
Density (g cm^{-3})	2.328	5.32
Dielectric constant ϵ	11.9	13.1
Bandgap at 300K (eV)	1.12	1.424
Electron Effective mass,	0.98^a	0.067
m^*/m_0	0.19^b	
Hole Effective mass,	0.16^c	0.082^c
m^*/m_0	0.49^d	0.45^d

Properties	Silicon	GaAs
Effective density of states in the conduction band, N_C (cm^{-3})	2.8×10^{19}	4.7×10^{17}
Effective density of states in the valance band, N_V (cm^{-3})	1.04×10^{19}	7.0×10^{18}
Intrinsic carrier density (cm^{-1})	1.45×10^{10}	1.79×10^{6}
Intrinsic resisitivity (Ωcm)	2.3×10^{5}	3.8×10^{8}
Electron mobility, μ_n (cm^{2}V^{-1}s^{-1})	1500	8500
Hole mobility, μ_p (cm^{2}V^{-1}s^{-1})	450	400
Minority carrier lifetime (s)	2.5×10^{-3}	$\sim 10^{-8}$
Energy to create an e-h pair (eV)	3.55	4.27
Most probable specific energy loss, $\frac{dE}{dx}_{mp}$, (keV μm^{-1})	0.28	0.57
Specific heat (J g^{-1} K^{-1})	0.7	0.35
Thermal conductivity at 300K (W cm^{-1} K^{-1})	1.5	0.46

All the data is taken from [1]. The values of the drift mobilities were obtained in the purest and most perfect materials available at the time the reference was published.

References

[1] S. M. Sze. *Physics of Semiconductor Devices.* John Wiley & Sons, 2nd edition, 1981.

[2] E. H. Rhoderick. *Metal-semiconductor contacts.* Clarendon Press, 1978.

[3] D. E. Holmes et al. *Applied Physics Letters*, 40(1982) 46.

[4] V. Prinz et al. *Proc. of the Fourth international conference on Deep Impurities in Semiconductors*, Eger, Hungary, 1983.

[5] K. Berwick et al. *Mat. Sci and Engineering*, B28(1994) 485.

[6] G. M. Martin et al. *Electronics letter*, 13(1977) 191.

[7] A. Mitonneau et al. *Review of Physics Applications*, 14(1979) 853.

[8] Proposal to Develop GaAs Detectors for Physics at the LHC. CERN, DRDC 90-58, 1990.

[9] ATLAS Collaboration. ATLAS Technical Proposal for a General-Purpose pp Experiment at the Large Hadron Collider at CERN. CERN, LHCC 94-43, 1994.

[10] G. Bellini et al. *Nuclear Instruments and Methods in Physics Research*, 107(1973) 85.

[11] J. Kemmer. *Nuclear Instruments and Methods in Physics Research*, 169(1980) 499.

[12] A. Peisert. Silicon Microstrip Detectors. In *Instrumentation in High Energy Physics*, editor F.Sauli, chapter 1, pages 1-79. World Scientific, 1992.

[13] R. Turchetta. *Nuclear Instruments and Methods in Physics Research*, A335(1993) 44.

[14] D. Froidevaux. The performance specifications of the ATLAS inner detector. ATLAS Internal Note, INDET NO-046, May 1994.

[15] K. Hahn and J. Ranft. *Phys. Rev., D*, 41(1990) 1462.

[16] A. Fasso et al. FLUKA92. *Proc. of the Workshop on simulating accelerator radiation environments*, Santa Fe, USA, 11-15 January 1994.

[17] G. Gorfine and G. Taylor. Particle fluxes and damage to silicon in the ATLAS inner detector. ATLAS Internal Note, INDET NO-030, November 1993.

[18] W. T. Anderson et al. Radiation induced damage in GaAs devices. *Proc. of the International Symposium on GaAs and related Compounds*, Heraklion, Greece, 1987.

[19] R. N. Hall. *Proc. IEE*, 106-B(17)(1959) 923.

[20] C. J. Hwang. *Phys. Rev. B*, 6(1972) 1355.

[21] S. Manolopoulos. *A Study of GaAs Detectors for Tracking in the ATLAS Experiment.* PhD thesis, Dept. Of Physics, University of Sheffield, December 1996.

[22] A.Vorobiev. Radiation Resistance of GaAs Structures Based on $\pi - \nu$ Junction. ATLAS Internal Note, INDET NO-036, February 1994.

[23] M. Toporowsky. *Development and Characterization of Tracking Detectors made form SI-GaAs for the LHC Experiments.* PhD thesis, Institute Of Physics, RWTH-Aachen, 1997.

[24] H.A. Bethe. Theory of the boundary layer of crystal rectifiers. MIT Radiation Lab., Report 43-12, 1942.

[25] C. Hilsum. *Semi-conducting III-V Compounds.* Pergamon Press, 1961.

[26] C. Look. *Electrical Characterisation of GaAs Materials and Devices.* John Wiley & Sons, 1992.

[27] J. R. Yeargan et al. *Journal of Applied Physics*, 39(1968) 5600.

[28] S. Makram-Ebeid. Defects in semiconductors. In *MRS*, editors J. Narayan and T. Y. Tan, page 495. North-Holland, 1981.

[29] A. G. Milnes. *Deep Impurities in Semiconductors*, pages 106-109. John Wiley & Sons, 1973.

[30] M. Toporowsky. Status of GaAs detectors at RWTH-Aachen. *Proc. of the 4th International Gallium-Arsenide Workshop and related compounds*, Aberfoyle, 1996. To be published in Nucl. Instr. and Meth A.

[31] I.R. Grant. Bulk growth of gallium arsenide. ICI Wafer Technology Ltd, Technical report, 1989.

[32] R.Bertin et al. *Nuclear Instruments and Methods in Physics Research*, A294(1990) 211.

[33] R. Adams. Low Pressure Vapour Phase Epitaxy Technologies. *Proc. of the 4th International Gallium-Arsenide Workshop and related compounds*, Aberfoyle, 1996. To be published in Nucl. Instr. and Meth A.

[34] V. O'Shea. Preliminary results for LP VPE X-ray detectors. *Proc. of the 4th International Gallium-Arsenide Workshop and related compounds*, Aberfoyle, 1996. To be published in Nucl. Instr. and Meth A.

[35] MCP Wafer Technology plc. 34 Maryland Road, Milton Keynes, Bucks. MK15 8HJ U.K.

[36] J. J. Thompson. *Semiconductor Science and Technology*, 5(1990) 596.

[37] LabView 4.0 National Instruments Corporation, USA.

[38] W. R. Leo. *Techniques for Nuclear and Particle Physics Experiments.* Spring-Verlag.

[39] S. Ramo. Currents Induced By Electron Motion. *Proc. of the I.R.E.*, pages 584-585, September 1939.

[40] J. Vaitkus. Private communication, November 1996.

[41] Z. Q. Fang. *Journal of Electronic Materials*, 22(11)(1993) 1361.

[42] D.S. McGregor et al. *Nuclear Instruments and Methods in Physics Research*, A343(1994) 527.

[43] M. Alietti et al. *Nuclear Instruments and Methods in Physics Research*, A355(1995) 420.

[44] A. Cola. A microscopic modelling of semi-insulating GaAs detectors. *Proc. of the 4^{th} International Gallium-Arsenide Workshop and related compounds*, Aberfoyle, 1996. To be published in Nucl. Instr. and Meth A.

[45] A. van der Ziel. Semiconductor Noise. In *Noise in Electron Devices*, editors L.D. Smullin and H.A. Haus, chapter 6, pages 311-343. John Wiley & Sons & Tech. Press of MIT, 1959.

[46] M. J. Buckingham. *Noise in electronic devices and systems.* John Wiley and Sons, 1983.

[47] K. M. van Vliet. *Physical Review*, 110(1958) 50.

[48] G. De Geronimo. *Review of Scientific Instruments*, 67(1996) 2643.

[49] B. Levit. *Nuclear Instruments and Methods in Physics Research*, A235(1985) 355.

[50] F. Dubecky et al. *Journal of Applied Physics*, 69(3)(1990) 1769.

[51] I. Strzalkowski et al. *Applied Physics Letters*, 28(6)(1976) 350.

[52] F. Dubecky et al. *Semiconductor Science and Technology*, 9(1994) 1654.

[53] J. Matheson et al. *Nuclear Instruments and Methods in Physics Research*, A362(1995) 297.

[54] J. C. Garth. *IEEE Transactions on Nuclear Science*, 32(6)(1985) 4382.

[55] E. Gatti. *Nuclear Instruments and Methods in Physics Research*, A225(1984) 608.

[56] V. A. J. van Lint. *Nuclear Instruments and Methods in Physics Research*, A253(1987) 453.

[57] K. Gill et al. *Nuclear Instruments and Methods in Physics Research*, A322(1992) 177.

[58] CERN-RD2 Collaboration. *Nuclear Instruments and Methods in Physics Research*, A344(1994) 228.

[59] V. Eremin et al. *Nuclear Instruments and Methods in Physics Research*, A360(1995) 458.

[60] F. Lemeilleur et al. *Nuclear Physics B*, 32(1993) 415.

[61] E. A. Burke. *IEEE Transactions on Nuclear Science*, NS-34(1987) 1220.

[62] J. Lindhard et al. *Mat. Fys. Medd.*, 33(10)(1963).

[63] T. F. Luera at al. *IEEE Transactions on Nuclear Science*, NS-34(6)(1987) 1557.

[64] A. M. Ougouag et al. *IEEE Transactions on Nuclear Science*, NS-37(6)(1990) 2219.

[65] A. van Ginneken. *Fermilab pre-print FN-522*, (1989).

[66] M. Huhtinen et al. *Nuclear Instruments and Methods in Physics Research*, A335(1993) 580.

[67] J.S. Meyer A. Chilingarov and T. Sloan. Radiation Damage due to NIEL in GaAs Particle Detectors. ATLAS Internal Note, INDET NO-134, 1996.

[68] M. Edwards et al. The Radiation Hardness Test Facility. Rutherford Appleton Laboratory, Technical Report RAL-90-065, August 1990.

[69] M. Tavlet et al. The PS-Acol Irradiation Facility at CERN. *Proc. of the First European conference on radiation and its effects on devices and systems, ESA-IEEE*, Universite Montpellier II, France, 1991.

[70] C. Furetta et al. Fluence and Dosimetric Measurements for a $\pi^{\pm}$ irradiation facility. *CERN Publication CERN-ECP/95-2*, (1995).

[71] E. Leon-Florian et al. Particle Fluence Measurements by Activation Technique for Radiation Damage Studies. *CERN Publication CERN-ECP/95-15*, (1995).

[72] N. K. Goswami et al. *Solid State Communications*, 40(1981) 473.

[73] R. Worner et al. *Applied Physics Letters*, 40(2)(1982) 141.

[74] D. S. McGregor. The investigation of Custom Grown Vertical Zone Melt SI Bulk Grown GaAs as a Radiation Spectrometer. *IEEE Transactions on Nuclear Science*, (1996). To be published.

[75] J. Vaitkus et al. Traps in GaAs detectors and electric field redistribution in excited SI-GaAs. *Proc. of the* 4^{th} *International Gallium-Arsenide Workshop and related compounds*, Aberfoyle, 1996. To be published in Nucl. Instr. and Meth A.

[76] F. Lemeilleur et al. *IEEE Transactions on Nuclear Science*, NS-39(1992) 551.

[77] D. V. Lang and L. C. Kimerling. *Lattice Defects in Semiconductors.* Inst. Phys. Conf. Series 23, 1975.

[78] J. Matthews. Bulk Radiation Damage in Silicon Detectors and Implications for ATLAS SCT. ATLAS Internal Note, INDET NO-118, December 1995.

[79] K. Thommen. *Physical Review*, 174(1968) 938.

[80] D. Pons et al. *Journal of Applied Physics*, 51(1980) 4150.

[81] O. Toker et al. Viking, A CMOS Low Noise Monolithic 128 Channel Front end for Si-strip Detector Readout. CERN, PPE 93-141, July 1993.

[82] A. Lang and J.P. Vanuxem. Sirocco II: A Silicon Strip Read-out CAMAC Controller with Flash ADC Input. CERN, EP-ELECTRONICS 90-01, 1990.

[83] S. M. Sze. *Physics of Semiconductor Devices*, pages 613-619. John Wiley & Sons, 2nd edition, 1981.

[84] P.J. Sellin et al. Punch Through Biasing Structures for GaAs Microstrip Detectors. In *3rd International Gallium-Arsenide Workshop*, editor J. Ludwig, San Miniato, March 1995. World Scientific. ISBN 981-02-2393-5.

[85] G. Cavalleri et al. *Nuclear Instruments and Methods in Physics Research*, 92(1970) 137.

[86] A. J. Weinstein. Silicon Tracking Conceptual Design Report. SCIPP 92/04, March 1992.

[87] E. Nygård et al. CMOS Low Noise Amplifier for Microstrip Readout Design and Results. CERN, PPE 90-142, October 1990.

[88] P. Sellin. Private communication, June 1995.